CATALYTIC CERAMIC CONVERSION OF Zr702 ALLOY SURFACES FOR COMBATING WEAR AND CORROSION

by

XINHE XIONG



UNIVERSITY OF BIRMINGHAM

A thesis submitted to the
University of Birmingham
for the degree of
DOCTOR OF PHILOSOPHY

School of Metallurgy and Materials
University of Birmingham
June 2023

UNIVERSITY OF
BIRMINGHAM

University of Birmingham Research Archive

e-theses repository

This unpublished thesis/dissertation is copyright of the author and/or third parties. The intellectual property rights of the author or third parties in respect of this work are as defined by The Copyright Designs and Patents Act 1988 or as modified by any successor legislation.

Any use made of information contained in this thesis/dissertation must be in accordance with that legislation and must be properly acknowledged. Further distribution or reproduction in any format is prohibited without the permission of the copyright holder.

Synopsis

Due to their attractive properties, Zr and its alloys are widely used in some industrial sectors including nuclear equipment and medical devices. However, their low hardness, high friction and poor wear resistance have prohibited their tribological and tribo-corrosion applications. Recently developed novel catalytic ceramic conversion treatment (CCCT or C3T) has been shown to successfully improve the tribological and tribo-corrosion properties of titanium alloys with significantly reduced treatment time and energy consumption, while effectively increasing the production efficiency as compared to the conventional ceramic conversion treatment (C2T). However, the feasibility of applying the C3T technique for improving the tribological and tribo-corrosion properties of Zr and its alloys has not been investigated. Therefore, this research aims to improve the mechanical, corrosion and wear properties of commercial grade Zr702 alloy by developing a new C3T technique tailored for Zr alloys.

In this research, the C3T method has been investigated for Zr702 alloy with pre-deposited films of Ag, V, Au, Pd, Ag/V and Ag/Pd in the temperatures range of 450 - 600 °C, with treatment times between 5 minutes and 60 hours. The surface morphology and the microstructure of the treated samples were fully characterised using optical microscopy, SEM/EDX, XRD, TEM and GDOES; the mechanical, corrosion and tribological properties were evaluated using nano-& micro hardness indentation, electrochemical corrosion tests, and tribo-tests, respectively.

The results have shown that the pre-deposited catalytic films can effectively speed up the ceramic conversion process to produce a significantly thicker zirconium oxide layer with finer columnar structure as compared to the zirconium oxide layer formed using the conventional C2T process. For the four catalytic elements investigated in this research, under 600°C for 10-hour treatment, the catalytic effects in terms of increasing the surface oxide layer thickness were observed in the following order of Ag>V>Pd>Au. Although the specific catalytic mechanism is element dependent, enhanced oxygen absorption and inward diffusion promoted by the refined columnar structure of the oxide layers are common features for all the C3T treatments. The optimal C3T conditions were found to be 550-600°C for 40-60 hours, especially for V and Au pre-deposited C3T. All C3T treated samples were shown to have improved corrosion properties in comparison with C2T treated samples. This was found to be associated with thick, dense and uniform oxide layer formed during the C3T, which can prevent the direct contact of aggressive ions attacking the metal surface. The Au pre-deposited C3T sample demonstrated the best anti-corrosion performance and was shown to reduce the corrosion rate to only about 2% and 3% that of the untreated and C2T samples respectively. The surface hardness was measured to increase from 150 HV for the untreated Zr702 to 1400 HV for the V pre-deposited C3T sample. The C3T was shown to reduce the coefficient of friction from 0.65 to less than 0.25 and provide two orders of magnitude reduction in the wear factor due to the formation of thick and dense oxide layers.

It is expected that the developed C3T technique can pave the way towards wider applications of Zr and its alloys especially under challenging tribological and tribo-corrosion environments.

Acknowledgements

First of all, I would like to thank my parents for their support in my decision to pursue an academic career and for their tremendous support to complete this degree. Despite the challenges posed by the Covid-19 pandemic, which prevented me from being able to see them for the past four years, they have consistently shown me patience, care and love. Their wisdom about life always guides me to find peace and hope during moments of homesickness and anxiety.

I would also like to thank my supervisors, Professor Hanshan Dong and Dr Xiaoying Li, for their continuous and careful guidance in my scientific research and academic exploration in the past few years. During the global pandemic, they also showed great support and care. I cannot thank them enough for the help they have given me over the past five years.

I also sincerely thank all the research staff, seniors and colleagues in the surface engineering group in the School of Metallurgy and Materials including Dr Zhenxue Zhang, Dr Xiao Tao, Dr Shaojun Qi, Dr Shiling Zhang, Dr Behnam Dashtbozorg, Dr James Alexander, Dr Yana Liang, Dr Zhiyuan Jing, Mr Fangzhou Shi, Mr Yepeng Yang, Mrs Yingdi Feng, Ms Chang Che and Mr Minhao Shen etc. I am truly grateful for the incredible encouragement, support, knowledge, and experience that I have received from them.

The technical support from the technicians from the School of Metallurgy and Materials has been fantastic. I am very appreciative of the effective training and

guidance received in operating various experimental instruments and using different research facilities from Mr Jaswinder Singh, Mr Paul Stanley, Mrs Terresa Morris, Mr Ludwig Schneider, Ms Amy Newell etc.

Finally, I am especially grateful to my girlfriend, Dr Yixin Wang, for her company, encouragement, and support during the completion of my PhD degree. I am deeply appreciative of the calmness and joy she has brought to me throughout this journey. My relatives and friends have also been incredibly supportive of me over the years. They have stayed connected with me, caring about my progress, wellbeing and constantly wishing me well.

Publication

Xiong X, Li X, Alexander J, Zhang Z, Dong H. A Novel Catalytic Ceramic Conversion Treatment of Zr702 to Combat Wear. Materials. 2023;16(5):1763. doi: 10.3390/ma16051763

Table of Contents

CHAPTER 1. INTRODUCTION 1

1.1 BACKGROUND 1

1.2 AIMS AND OBJECTIVES 2

1.3 THESIS STRUCTURE 3

CHAPTER 2. LITERATURE REVIEW 4

2.1 ZIRCONIUM AND ITS ALLOYS 4

2.1.1 Historic notes 4

2.1.2 Classification 6

2.1.3 Physical metallurgy 7

2.1.4 Properties and applications 8

2.1.4.1 Nuclear applications 8

2.1.4.2 Chemical industrial applications 12

2.1.4.3 Medical applications 12

2.1.5 Limitations 15

2.1.5.1 Wear 15

2.1.5.2 Corrosion and corrosion wear 19

2.2 SURFACE ENGINEERING OF ZIRCONIUM ALLOYS 24

2.2.1 Surface coating 25

2.2.1.1 Physical vapour deposition 25

2.2.1.2 Electroplating 26

2.2.1.3 Plasma electrolytic oxidation 27

2.2.2 Surface modification methods 31

2.2.2.1 Ion implantation 31

2.2.2.2 Laser assisted surface treatment 32

2.2.2.3 Thermochemical and electrochemical methods 33

2.2.2.4 Ceramic conversion treatment 34

2.3 OXIDATION OF ZIRCONIUM ALLOYS AND OXIDATION KINETICS 35

2.4 ELLINGHAM DIAGRAMS 41

2.5 CERAMIC CONVERSION TREATMENT (CCT OR C2T) 44

2.5.1 C2T 44

2.5.2 Catalytic ceramic conversion treatment (CCCT or C3T) 46

2.6 SUMMARY 48

CHAPTER 3. EXPERIMENTAL METHODOLOGY 50

3.1 MATERIALS SELECTED AND SAMPLE PREPARATION 50
3.2 CATALYTIC CERAMIC CONVERSION TREATMENT (C3T) 50
3.2.1 Pre-deposition of thin catalytic films 50
3.2.2 Ceramic conversion treatment 51
3.3 MICROSTRUCTURE CHARACTERISATION 54
3.3.1 Specimen preparation 54
3.3.2 Surface morphology observation and roughness measurement 55
3.3.3 X-ray diffraction (XRD) phase identification 56
3.3.4 TEM 57
3.3.5 Surface layer structure analysis 58
3.4 CORROSION TESTING 59
3.5 HARDNESS AND TRIBOLOGICAL PROPERTIES EVALUATION 61
3.5.1 Hardness 61
3.5.2 Tribological testing 63
3.5.3 Corrosion wear test 64

CHAPTER 4. RESULTS 66

4.1 PRE-SCREENING OF CATALYTIC CERAMICS CONVERSION TREATMENT 66
4.1.1 Microstructure of as-received Zr702 67
4.1.2 Surface morphology 67
4.1.3 Surface phase identification 75
4.1.4 Weight gain and layer thickness 78
4.1.5 Selection of the C3T treatments 83
4.2 MICROSTRUCTURE OF C3T TREATED ZR702 83
4.2.1 Microstructure of 600 °C/10h C3T treated samples 84
4.2.1.1 Surface morphology and surface roughness 84
4.2.1.2 Surface layer structures 87
4.2.2 C3T duration effect 90
4.2.2.1 Surface morphology 90
4.2.2.2 Weight gain and layer thickness 95
4.2.2.3 Oxide layer structure 97

4.2.3 Phase and microstructure analysis *102*
4.2.3.1 XRD 102
4.2.3.2 TEM characterisation of C2T and C3TAu samples 106
4.3 CORROSION BEHAVIOUR OF CERAMICS CONVERSION TREATED ZR702 113
4.3.1 Corrosion properties of Unt and C2T samples *113*
4.3.2 Samples of C3T with pre-deposition of Au *119*
4.3.3 Samples of C3T with pre-deposition of Ag *123*
4.3.4 Samples of C3T with pre-deposition of V *126*
4.3.5 Summary of E_{corr} and I_{corr} *127*
4.4 MECHANICAL AND TRIBOLOGICAL PROPERTIES OF C3T SAMPLES 129
4.4.1 Hardness of 600 °C C3T treated samples *129*
4.4.1.1 600 °C/10-hour treated C3T samples 129
4.4.1.2 C3T treatment duration effects 130
4.4.1.3 Hardness depth profiles 132
4.4.2 Coefficient of Friction *135*
4.4.3 Wear resistance of 600 °C/10-hour C3T samples under 21N load *136*
4.4.3.1 Wear factors 136
4.4.3.2 Wear tracks 138
4.4.4 Load effect on wear behaviour *143*
4.4.4.1 Wear factors 143
4.4.4.2 Wear track morphologies 146
4.4.5 Wear behaviour of selected C3T samples in NaCl solution *156*
4.4.5.1 Wear factors 156
4.4.5.2 Wear tracks 157

CHAPTER 5. DISCUSSION 160

5.1 CATALYTIC EFFECTS AND MECHANISMS 160
5.1.1 C3T with pre-deposition of Ag (C3TAg) *160*
5.1.2 C3T with pre-deposition of V (C3TV) *165*
5.1.3 C3T with pre-deposition of Pd (C3TPd) *167*
5.1.4 C3T with pre-deposition of Au (C3TAu) *168*
5.1.5 Treatment duration on the catalytic effects *170*
5.2 CORROSION PROPERTIES IMPROVEMENT 171
5.2.1 Corrosion behaviour of Unt sample *171*

5.2.2 Anti-corrosion performance of C2T sample *175*
5.2.3 Anti-corrosion performance of C3T samples *176*
5.3 IMPROVED MECHANICAL AND TRIBOLOGICAL PROPERTIES 179
5.3.1 Mechanical and tribological properties of Unt and C2T samples *179*
5.3.1.1 Hardness improvement 179
5.3.1.2 Tribological property enhancement 180
5.3.2 Mechanical and tribological properties of C3T samples *183*
5.3.2.1 Hardness improvement 183
5.3.2.2 Tribological property enhancement 185
5.3.3 Wear in NaCl solution *189*
CHAPTER 6. CONCLUSIONS AND FUTURE WORK 192
6.1 SUMMARY AND CONCLUSIONS 192
6.2 SUGGESTED FUTURE WORK 197
REFERENCES 199

List of Figures

Figure 2.1-1 Zircon (Zirconium silicate ($ZrSO_4$)) [8].....4
Figure 2.1-2 (a) The experimental determined temperature-pressure phase diagram for zirconium; (b) The phase change of the zirconia in different temperature ranges [21, 22]. 7
Figure 2.1-3 Zirconium alloys used in nuclear reactors. (a) and (b) images of fuel assemblies for nuclear reactors; (c) and (d) schematic draw of fuel assemblies structure and rod cross section. [26, 27, 28, 29]. 11
Figure 2.1-4 Examples of the zirconium applications in medical implants: (a) Total hip replacement (THR); (b) Total knee replacement (TKR); and (c) Z-Systems Z-Look3 Evo implant (Ceramic Teeth implant) [30]. 14
Figure 2.1-5 The schematic diagram of adhesive wear mechanism [41]. 16
Figure 2.1-6 The three wear modes of abrasive wear in cross sectional profiles: (a) ploughing mode, (b) wedge forming mode (c) cutting mode [45]. 17
Figure 2.1-7 The abrasive wear mechanisms: (A) two-body abrasion, (B) third-body abrasion [45]. 18
Figure 2.1-8 The degree of the wear calculated from the 2D scan of the groove [45]. 18
Figure 2.1-9 The degradation of the zirconia ceramics: (a) the ageing mechanisms; (b) the smaller grain size produces leads to less phase transformation, and thus less ageing of zirconia ceramics; (c) more yttria (stabilizer) content for zirconia ceramics leading to less phase transformation, and thus less ageing [49, 51]. 22
Figure 2.1-10 The wear surfaces of (a) untreated Zr705 alloy, and (b) Zr705 alloy ceramic conversion treated under 600°C/3 hours [43]. 23
Figure 2.2-1 The PEO process summary in schematic draw [68]. 28
Figure 2.2-2 Schematic draw of the PEO coated aluminium sample [58].....28
Figure 2.2-3 The improved wear and corrosion properties shown on PEO coated Zr alloy compared to uncoated substrate. (a) (ii), (iii) and (iv) represent the 2D scan of the wear tracks of PEO coated samples, having less wear volume compared to (i) the uncoated substrate. (b) the polarisation curves of PEO coated samples ZF1, ZF2 and ZF3 and uncoated substrate [53]. ...30

Figure 2.2-4 The SEM images and EDS lines scan after brush plating process (a) and (b); and LSA process (c) and (d) [77]. 33
Figure 2.3-1 (a) The Equilibrium phase diagram for Zr-O system; (b) The main phase transformation in the Zr-O system [81]. 36
Figure 2.3-2 The Oxidation kinetics for α-Zr (a) and β-Zr (b) [84].....40
Figure 2.4-1 The Ellingham diagram for some oxides, showing the reactions of different metals. The open and solid circle refers to melting and boiling of the metals, whereas the open triangles are melting points of oxides [87]. ..43
Figure 2.5-1 The surface cross sections of Ti6Al4V alloy after (a) C2T treated at 620 °C for 85 hours. (b) C3T (pre-deposition film of Ag) treated at 620 °C for 3 hours and (c) C3T (pre-deposition of Ag/Pd) treated at 620 °C for 5 hours [3, 90, 94, 95]. 45
Figure 2.5-2 The cross-sectional SEM images of (a) Zr705 alloy treated under 600 °C for 30 hours (b) Zr702 alloy treated under 600 °C for 30 hours [43]. 46
Figure 3.2-1 The Close Field Unbalanced Magnetron Sputtering Ion Plating Equipment (Teer Coating Ltd.) set up [99]. 51
Figure 3.3-1 The Differences between arithmetic average roughness value R_a (a) and data points range R_t (b), where R_z represents mean roughness depth and R_{z1max} represents maximum roughness depth [100].....56
Figure 3.3-2 The further sample preparation procedure for TEM characterisation. 58
Figure 3.4-1 The schematic draw of the electrochemical test set up. 61
Figure 3.5-1 The Vickers hardness measurement [104]. 62
Figure 3.5-2 The schematic draw of the reciprocating wear tests. 64
Figure 3.5-3 The schematic draw of the corrosion wear tests. 65
Figure 4.1-1 The observation of (a) as ground Zr702 alloy visually, and (b) the PFIB milled Zr702 alloy sample under the SEM revealing its microstructure. 67
Figure 4.1-2 The visual observation of (a) as ground (left), and Au pre-deposited (right) of Zr702 alloy; and (b) no pre-deposition (left) and Au pre-deposited (right) and then ceramic conversion treated sample surface. 68
Figure 4.1-3 Visual observations – the colour change of the samples surface after 10-hour treatment. 69

Figure 4.1-4 The 2D thickness profile of Ag element deposited on Silicon wafer. 71
Figure 4.1-5 The coloured SEM reveals the deposited layer of (a) Ag; (b) V; (c) Pd; (d) Au; (e) Ag/V and (f) Ag/Pd on the silicon wafer and the thickness was measured accordingly. 73
Figure 4.1-6 SEM observation of the deposition of (a) Ag, (b) V, (c) Pd, (d) Au, (e) AgV and (f) AgPd on silicon wafer.....74
Figure 4.1-7 Au deposited on (a) Si wafer and on (b) Zr702 surface. 75
Figure 4.1-8 The XRD analysis of the samples after the C2T and C3T (single element deposition) process, samples treated at 600 °C for 10 hours. 76
Figure 4.1-9 The XRD analysis of the samples after the C3T (pre-deposited with Ag, V and Ag/V) process, samples treated at 600 °C for 10 hours. 77
Figure 4.1-10 The XRD analysis of the samples after the C3T (pre-deposited with Ag, Pd and Ag/Pd) process, samples treated at 600 °C for 10 hours. .77
Figure 4.1-11 The weight change of the samples after 10-hour ceramic conversion treatment with and without pre-deposition (None, C2T) as a function of treatment temperatures. 80
Figure 4.1-12 The oxide thickness of the samples after 10-hour ceramic conversion treatment with (C3T) and without pre-deposition (None, C2T) as a function of treatment temperatures. 82
Figure 4.2-1 SEM images showing the surface morphology of the ceramic conversion treated samples. 85
Figure 4.2-2 The surface roughness values in R_a and R_t of ceramic conversion treated samples, comparing with the untreated sample. 87
Figure 4.2-3 The cross-sectional SEM images showing the surface layer structure for samples of (a) C2T; (b) Ag6010; (c) Pd6010; (d) V6010 and (e) Au6010; The EDX analysis of the surface and cross section is outlined in (f).....89
Figure 4.2-4 SEM images showing surface morphology of the samples Ag6010, Ag6020, Ag6040 and Ag6060. 91
Figure 4.2-5 SEM images showing surface morphology of the samples V6010, V6020 and V6060. 92
Figure 4.2-6 SEM images showing surface morphology of the samples Au6000 (5 mins), Au6005, Au6010, Au6020, Au6040 and Au6060. 94

Figure 4.2-7 The weight change of the pre-deposited with Ag, V and Au, and ceramic conversion treated at 600 °C for the treatment time ranging from 5 mins to 60 hours. 95
Figure 4.2-8 The oxide thickness of the samples after ceramic conversion treatment with (C3T) and without pre-deposition (None, C2T) at the same temperature 600 °C as a function of treatment time ranging from 5 mins to 60 hours. 97
Figure 4.2-9 The cross-sectional SEM images of Ag, V and Au pre-deposited samples treated under 600 °C at 20 hours and 60 hours. 99
Figure 4.2-10 The cross-sectional SEM images of V6060 sample with (a) the EDX mapping and (b) line-scan analysis. 101
Figure 4.2-11 The XRD analysis of the short time (5mins) C3T treated Au pre-deposited samples at 600 °C comparing with the Unt sample. 103
Figure 4.2-12 The XRD analysis of the longer time (40 hours) C3T treated Au pre-deposited samples at 600 °C comparing with the Unt sample. 104
Figure 4.2-13 The XRD analysis of the Au pre-deposited samples after the C3T treatment, samples treated at 600 °C for different periods of time, i.e. Au6000 (5 mins), Au6005 (5 hours), Au6010 (10 hours), Au6020 (20 hours), Au6040 (40 hours) and Au6060 (Au6060), comparing with the Unt sample. 105
Figure 4.2-14 TEM microstructure of C2T5010 (a) surface oxide layer structure, interface and substrate; corresponding SAD patterns of (b) surface oxide layer, and (c) horizontally grown grain interface layer 107
Figure 4.2-15 TEM microstructure of C3T6010 (a) surface oxide layer structure and corresponding SAD patterns of (b) top surface layer, and (c) dominant columnar oxide layer. d) TEM image of C2T in the same scale bar to a) for columnar grain width comparison. 109
Figure 4.2-16 High-angle annular dark-field scanning transmission electron microscopy (HAADF-STEM) analysis of C3TAu6040 sample: STEM image of the surface layer at the top area and corresponding elements mappings as indicated. 110
Figure 4.2-17 (a) TEM microstructure and SAD pattern of C3TAu6040, showing lateral cracks, related to the formation of t-ZrO2 phase, and (b) optical

image of the C3TAu6040 sample (polished without etching), revealing typical layer structures. 111
Figure 4.3-1 The polarisation curves of Unt and C2T samples. 114
Figure 4.3-2 The SEM images of corroded Unt sample surface after the electrochemical test showing (a) intergranular corrosion and (b) & (c) pitting corrosion. 116
Figure 4.3-3 The SEM images of C2T6010 sample surface after the corrosion test. (a), (b) and (c) located outside the tested aera, (d) and (e) located inside the tested area. 118
Figure 4.3-4 The polarisation curves of selective Au pre-deposited sample treated (Au6005, Au6010, Au6020, Au6040 and Au6060) with different treatment durations compared with the C2T sample. 119
Figure 4.3-5 The SEM images of corroded (i.e. (b), (d) and (f)) and uncorroded (i.e. (a), (c) and (e)) surface for Au6010, Au6040 and Au6060 samples respectively after the corrosion test. 121
Figure 4.3-6 The SEM images of Au6005 and Au6020 sample surface after the corrosion test. (a) the surface of Au6005 sample showing the unevenness of gold deposition; (b) and (c) the corroded surface of Au6005 and Au6020 sample. 122
Figure 4.3-7 The polarisation curves of selective Ag pre-deposited sample treated (Ag6010, Ag6020 and Ag6040) with different time compared with the C2T sample. 123
Figure 4.3-8 The corrosion morphology of Ag6020 and Ag6040 samples: (a) presents the uncorroded surface and (b) presents the corroded surface of Ag6020 samples. (c) shows the surface of Ag6040, the corroded area is marked out and the detailed features in this area are shown in (d) and (e). 125
Figure 4.3-9 The polarisation curves of selective V pre-deposited sample treated (V6010, V6020 and V6020) with different time compared with the C2T sample. 126
Figure 4.3-10 The SEM images of (a) V6010 and (c) V6040 samples surface before and after the corrosion test (i.e. (b) presents the corroded surface for V6010, and (d) presents the corroded surface for V6040, where (a) and (c) presents uncorroded surface). 127

Figure 4.4-1 Surface hardness of C2T and C3T samples treated under 600 °C/10h, compared with the untreated sample. 130
Figure 4.4-2 Surface hardness of C3T Au pre-deposited samples treated under 600 °C for different period of time ranging from 5 mins to 60 hours, compared with the untreated sample.....132
Figure 4.4-3 (a) Hardness depth profiles of C3T Au6040 sample and C2T6040 sample and (b) GDOES composition depth profiles of the C3T Au6040 sample. 134
Figure 4.4-4 Dynamic Coefficient of Friction (CoF) curves for all C3T samples tested under the normal load of 21N, together with the CoF curves for C2T and Unt samples for comparisons. 135
Figure 4.4-5 (a) 2D wear track profiles scanned by profilometer of Unt, C2T and selective samples with pre-deposition layers (Ag6010, V6010, Pd6010 and Au6010) treated under the condition of 600 °C/10h after the wear test under the load conditions of 21N, 30 mins (3600 cycles); (b) The wear factors of the C3T samples treated at 600 °C/10h. 137
Figure 4.4-6 The SEM images of the wear tracks formed on different samples: (a) Unt; (b) C2T6010; (c) Au6010; (d) Ag6010; (e) V6010 and (f) Pd6010. 139
Figure 4.4-7 The SEM observation on the wear tracks of (a) C2T; (b) Ag6010; (c) V6010; (d) Au6010; (e) Table summarises the EDX point ID chemical analysis results in wt% in the wear tracks in (a), (b), (c) and (d). 142
Figure 4.4-8 The effect of wear test loads on the wear factors (log) of Au pre-deposited C3T samples treated at 600 °C for 5, 10, 20 and 40 hours, C2T sample treated at 600 °C for 10 and 40 hours, and the untreated sample for comparison. 145
Figure 4.4-9 SEM images of samples Unt after wear test under 21N, (a) at the bottom of the wear track, (b) on the surface of the counterpart WC-Co ball with EDX elements distribution.....148
Figure 4.4-10 SEM images of samples Unt after wear test under 45N, (a) at the bottom of the wear track with EDX analysis, (b) surface of the counterpart WC-Co ball with EDX elements distribution. 149
Figure 4.4-11 The wear track profiles of 5-hour and 10-hour C3TAu samples after wear tested under 21N (a) and 45N (b). 150

Figure 4.4-12 SEM images of the wear track of Au6005 sample wear tested under the normal load of 21N ((a), (c) and (e)) and 45N ((b), (d) and (f)). 152
Figure 4.4-13 (a) The colour chem SEM image reveals the inside of the wear track for Au6020 sample wear tested under the load of 45N. (b) and (c) present the surface counterpart WC-Co ball and the EDX chemical analysis via colour chem SEM image. 154
Figure 4.4-14 The colour chem SEM image reveals (a) & (b) the wear track of Au6040 sample wear tested under the load of 45N, (a) zooming in the part highlighted in (b) showing the wear features inside the wear track for Au6040 sample. (c) presents the surface counterpart WC-Co ball and the EDX chemical analysis via colour chem SEM image. 155
Figure 4.4-15 The wear factor (log) comparisons between Unt sample, C2T and C3T Au pre-deposited samples in different treatment time, tested in dry and wet conditions. 156
Figure 4.4-16 SEM images of (a) the WC-Co ball surface sliding against the Unt sample after the corrosion wear test; (b), (c) and (d) reveal the wear track and wear features of the untreated Zr702 sample after the corrosion wear test. 158
Figure 4.4-17 SEM images of the inside of the wear tracks and wear features of the C2T6010 samples after wear tests in dry conditions (a) and wet condition (b). 159
Figure 5.1-1 A more comprehensive Ellingham diagram showing the ease of the Ag_2O reduction [89]. 164
Figure 5.1-2 Schematic diagram showing the palladium monolayer with adsorbed oxygen atoms in relaxed structures [131]. 167
Figure 5.2-1 SEM image of oxide layer formed on (a) sponge zirconium during the corrosion process after 69 days exposure in hot water (360 °C); (b) crystal bar Zr after 3 days exposure and (c) Zircaloy-4 after 75 days of exposure [134, 135]. 173
Figure 5.2-2 Schematic diagrams of initiation of pitting via (a) penetration and (b) film breaking mechanisms [138]. 175
Figure 5.2-3 The polarisation curves of selected treated (Ag6010, V6010, Au6010, C2T6010) and untreated Zr702 samples. 178

Figure 5.3-1 The colour chem SEM image showing inside of the wear track of Unt sample under 45N, indicating high oxygen contents. 182

List of Tables

Table 2.1-1: The compositions of common Reactor-grade zirconium alloys and Commercial-grade zirconium alloys [14, 15, 16]. 6
Table 2.1-2: List of structural materials compared to zirconium in tensile property and neutron absorption property.....9
Table 2.1-3 Properties comparisons between commercial Zr alloy Zr702 (R60702) and commercial Ti alloy (Grade-1) [30].....13
Table 2.2-1: Scope of surface engineering methods of Zr alloys [2, 57, 58].....24
Table 2.2-2: Table summarised the applications and substrate of PEO [68].....29
Table 2.3-1: The oxygen diffusion coefficient of α-Zr and zirconia in different temperature ranges [82, 83]. 37
Table 3.1-1: The chemical composition (wt%) of Zr 702 alloy. 50
Table 3.2-1: Treatment conditions and the sample codes. 53
Table 3.3-1: The sample grinding and polishing process. 54
Table 4.1-1: Table summarises the thickness measurement of different elements deposited on silicon wafer. 72
Table 4.1-2: Summary of phase constituents identified after the ceramic conversion treatment of each sample under the condition of 600 °C/10 hours.....78
Table 4.3-1: Summary of the corrosion potential E_{corr} and corrosion current density I_{corr}, with calculated corrosion rate in mpy. 128
Table 4.4-1: The wear factor results of untreated Zr702, C2T and C3T (Au pre-deposited) samples under different load conditions (21N vs. 45N).....145
Table 4.4-2: The wear factor results of untreated Zr702, C2T and C3T Au pre-deposited samples under different wear conditions - Dry vs. Wet, with same normal load 21N and numbers of cycles (30min/3600 cycles).....157

List of Abbreviations

C2T – Ceramic conversion treatment

C3T – Catalytic ceramic conversion treatment

CCCT – Catalytic ceramic conversion treatment

CCT – Ceramic conversion treatment

CoF – Coefficient of friction

EDX – Energy-dispersive X-ray spectroscopy

FIB – Focused ion beam

GDOES – Glow-discharge Optical Emission Spectroscopy

PVD – Physical vapour deposition

SAD – Selected area diffraction

SEM – Scanning electron microscope

STEM – Scanning transmission electron microscope

TEM – Transmission electron microscopy

XRD – X-ray diffraction

Chapter 1. Introduction

1.1 Background

Zirconium and its alloys are widely used in the nuclear industry as structural materials in nuclear reactors mainly due to their low neutrons absorption rate. Zirconium alloys are also commonly used for the medical implants such as knee/hip replacements and dental implants as a result of their bio-inertness and bio-corrosion resistance. However, zirconium and its alloys are also characterised by low hardness (i.e. 150 HV[1]), low wear resistance and high friction. Hence it is imperative to improve the mechanical, tribological and corrosion properties of zirconium and its alloys for wider industrial applications, which forms the basis of this research study.

Some surface engineering methods have been reported including energy beam surface alloying, physical vapour deposition (PVD), and electroplating to combat the wear of Zr and its alloys. However, energy beam alloying has been shown to result in poor surface finish whilst PVD and electroplating approaches commonly lead to poor interface bonding and low load bearing capacity. An advanced surface ceramic conversion treatment (CCT or C2T) has been developed in the past two decades based on thermal oxidation and has been successfully applied to titanium alloys to improve their tribological and corrosion properties, and the C2T has also been explored for zirconium alloys. However, the C2T method requires long treatment durations (usually 50-200 hours [2]) to achieve the desirable properties enhancement, which is extremely energy consuming. Recent studies have demonstrated that by applying a catalytic film prior to the CCT of titanium alloys, the oxidation process can be sped up and the treatment time can be reduced down to 8 hours, thus forming the

foundations of the so-called catalytic ceramic conversion treatment (i.e. C3T) [3, 4]. However, the feasibility of applying the C3T technique to improve the mechanical, tribological and corrosion properties of Zr and its alloys has not been explored.

1.2 Aims and Objectives

The aims of this PhD research are to develop a cost-effective and environmentally friendly surface technology to enhance the corrosion and tribological properties of Zr702 alloy, and to study the role and the mechanism of pre-deposited noble metal film in catalytic ceramic conversion treatment (C3T) of Zr702 alloy. The scientific and technological objectives of this PhD research can be summarised as follows:

1) To investigate the effect of pre-deposited thin films of Ag, V, Pd, Au on the C3T behaviour of Zr702 alloy;
2) To identify the optimal C3T conditions (metal film, temperature & time) for C3T to generate high-quality surface oxide layers with the shortest time and/or the lowest temperature;
3) To fully characterise the surface morphology, layer microstructure, chemical composition and phase constituents of the treated materials;
4) To evaluate the mechanical, tribological and corrosion properties of the C3T treated Zr702 alloy; and
5) To study the mechanisms involved in C3T of Zr702 alloy to advance scientific understanding.

1.3 Thesis Structure

This thesis consists of 6 chapters and follows the normal PhD thesis structure. The thesis starts with an introduction (Chapter 1) to the background and importance of this research, research motivation and the gaps to be filled, and the structure of the thesis. Chapter 2 reviews the current literature on Zr and its alloys, oxidation and surface engineering, and the development and current status of ceramic conversion technique to identify the research gap to be filled. Chapter 3 is devoted to the description of the materials, treatments and the equipment used for microstructural characterisation and property evaluation. The experimental results are reported in detail in Chapter 4, which are then discussed in Chapter 5 to advance scientific understanding and to contribute to new knowledge. The thesis finishes with a summary and conclusions and suggestions for future work (Chapter 6).

Chapter 2. Literature review

2.1 Zirconium and its alloys

2.1.1 Historic notes

Zirconium is naturally found occurring in about 30 mineral species [5]. The mineral *zircon* is one of the best-known compounds of zirconium (Zr), which has been known from the ancient times and is even found to be mentioned in biblical writings along with its variations. It is believed that the name zircon was originated from the word *zargono* or the word *zargun* in Arabic languages. The meanings for both words are similar and are used for the description of the colour of certain gemstones. Figure 2.1-1 shows a typical zircon. The elemental zirconium was first discovered in 1789 while analysing a *jargon* from Sri Lanka and was named as Zirkonerde (zirconia) by the German chemist Martin Heinrich Klaproth [5, 6, 7, 8]. Klaproth failed to isolate the pure zirconium and Humphry Davy also failed in 1808 trying to use electrolysis method to isolate [5, 9].



Figure 2.1-1 Zircon (Zirconium silicate ($ZrSO_4$)) [8].

In 1824, the Swedish chemist, Baron Jöns Jacob Berzelius became the first person to isolate an impure zirconium metal, which was achieved using a heating method to heat the mixtures of potassium and potassium hexafluorozirconate (K_2ZrF_6) in an iron

tube. In 1925, an ‘iodide decomposition process’ (also known as the ‘Van Arkel–de Boer process’ or the ‘crystal-bar process’) was developed by Dutch chemists Anton Eduard van Arkel and Jan Hendrik de Boer to thermally decompose the zirconium tetraiodide to produce pure metallic zirconium [5, 6, 7, 10]. In 1947, the Kroll process was developed by the Luxembourgish metallurgist, William Justin Kroll, by using magnesium to reduce the zirconium tetrachloride by heating both reactants at 700 °C in vessels [11].

The development of zirconium based alloys was heavily linked to the applications of zirconium and its alloys in the nuclear industry [12]. In late 1940s, in order to develop the nuclear-propelled ships and submarines, a metal that had good level of corrosion resistance and would be able to maintain the integrity at high temperatures and the environment of intense radiation for long time, and would not absorb neutrons, was needed for nuclear reactions. Kaufman at MIT and Pomerance at Oak-Ridge found out in laboratory by separating the hafnium content from zirconium that, the pure zirconium absorb very low level of neutrons, which led to the decision made by Admiral H.G. Rickover from the US Navy to select zirconium as the structural material in the pressurised water reactors (PWR) for nuclear submarines. The research focused on the production of the material and then aimed on developing high purity zirconium, however, the higher purity material revealed lower corrosion resistance as compared with the impure ones. As a result, the first stage to develop the zirconium alloys was to consider the ‘impurities’ that would be able to enhance the corrosion resistance. One of the most effective ‘impurities’ was found to be tin (Sn), which was shown to simultaneously achieve good corrosion resistance, strength and fabricability. This alloy was later named as *Zircaloy-1* (Contain 2.5wt% tin).

The *Zircaloy-2*, *Zircaloy-3* and *Zircaloy-4* were developed later with lower content of tin but with additions of other elements including iron, chromium and nickel [12, 13].

2.1.2 Classification

Hafnium and zirconium are in the same column on the periodic table, with the same charge and similar size and thus possess similar properties. It becomes difficult to separate hafnium from the natural zirconium [7]. Commercial grade zirconium and its alloy contains 1 to 3 wt% of hafnium but reactor-grade zirconium only contains almost negligible amount of hafnium [6]. The common zirconium alloys are summarised in Table 2.1-1.

Table 2.1-1: The compositions of common Reactor-grade zirconium alloys and Commercial-grade zirconium alloys [14, 15, 16].

Alloy (UNS grade)	Composition wt%											
	Zr+Hf (min)	Hf	Sn	Nb	Fe	Cr	Ni	O	Fe+Cr	H (max)	N (max)	C (max)
Reactor-grade zirconium alloys												
Zircaloy-2 (R60804)	-	0.10	1.20-1.70	-	0.07-0.20	0.05-0.15	0.03-0.08	0.1-0.14	-	0.0025	0.0080	0.027
Zircaloy-4 (R60804)	-	0.10	1.20-1.70	-	0.18-0.24	0.07-0.13	-	0.1-0.14	-	0.0025	0.0080	0.027
Zr-2.5Nb (R60904)	-	0.005	-	2.40-2.80	<0.15	-	-	0.09-0.13	-	0.0010	0.0065	0.027
Commercial-grade zirconium alloys												
Zr702 (R60702)	99.2	4.5	-	-	-	-		0.16 max	0.2 max	0.005	0.025	0.05
Zr704 (R60704)	97.5	4.5	1.0-2.0	-	-	-		0.18 max	0.2-0.4	0.005	0.025	0.05
Zr705 (R60705)	95.5	4.5	-	2.0-3.0	-	-		0.18 max	0.2 max	0.005	0.025	0.05

2.1.3 Physical metallurgy

Being known as the lustrous, silver and malleable metal at room temperatures, pure zirconium is soft and ductile, while alloyed zirconium is hard and brittle [9]. It has a high melting (1854°C, 2127 K) and boiling (4406°C, 4679 K) point [5, 9]. Pure zirconium exhibits HCP (Hexagonal closed packed) structure and has a c/a ratio of 1.593 at 865.85 °C (1139 K)[17].

In the heating process of zirconium, the HCP (α-Zr) structure of the pure zirconium transforms to BCC structure (β-Zr) when the temperature reaches 1139 K (865.85 °C) at the pressure of 1 atm [18, 19]. By heating the zirconia to 1443.15K (1170 °C), the zirconia in monoclinic phase will transform into tetragonal phase, accompanied by a 5% reduction volume [20]. Figure 2.1-2 shows the structural and phase changes of zirconium and zirconia in the heating process: (a) phase diagram of zirconium; and (b) phase change of zirconia.

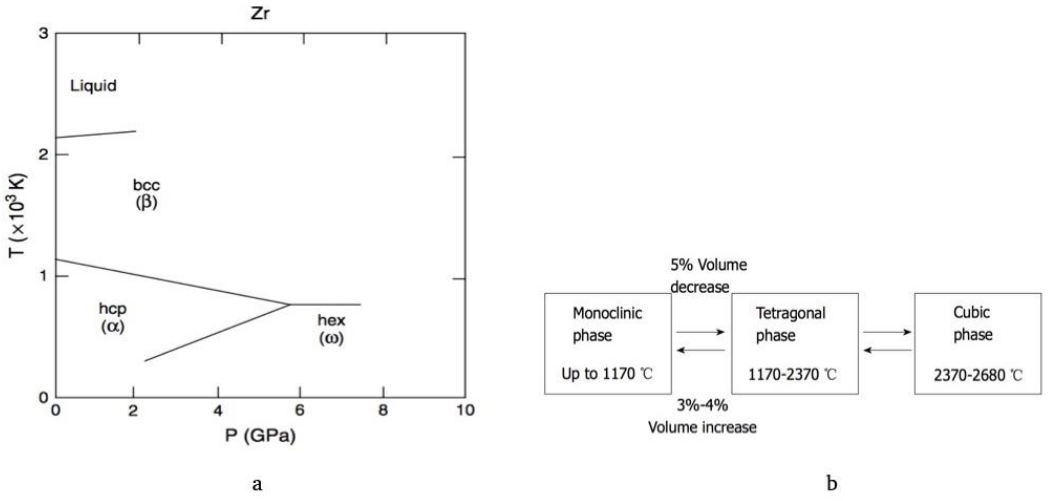


Figure 2.1-2 (a) The experimental determined temperature-pressure phase diagram for zirconium; (b) The phase change of the zirconia in different temperature ranges [21, 22].

2.1.4 Properties and applications

As mentioned in the Section 2.1.1, zirconium and its alloys have significant applications in the nuclear industry, which also in turn promotes the development of zirconium and its alloys. The low absorption cross section for neutrons makes it an idea solution in nuclear energy application. The zirconium alloy tubing used in the nuclear reactors could be longer than 100,000 metres. More than 90% of zirconium metal production is reported to be used in commercial nuclear power generation nowadays [5, 6].

Apart from being largely used in nuclear industry, zirconium and its alloys, and other zirconium compounds are also widely used in medical applications (body implants etc.), chemistry industry and high temperature environment (the aerospace industry etc.) due to their good corrosion resistance, low coefficient of thermal expansion (CTE), high melting points, non-toxicity and good biocompatibility [2, 20, 23, 24].

2.1.4.1 Nuclear applications

Compared to other structural materials listed in Table 2.1-2, it is obvious that zirconium-based alloys have much less neutrons absorption per unit. Although beryllium has lower neutrons absorption per unit than zirconium, the poor ductility especially after exposure to radiation, limits its use in the nuclear industry [25]. Zircaloy was the nuclear-grade zirconium alloy firstly developed to meet the needs in nuclear submarines by separating hafnium from zirconium to obtain even lower neutrons absorption and by adding element tin to improve its corrosion resistance [12].

Table 2.1-2: List of structural materials compared to zirconium in tensile property and neutron absorption property.

Base Metal	Ultimate Tensile Strength at 300°C[a]	Macroscopic Cross Section for Thermal Neutrons [b]	Relative Neutron Absorption For Given Design Stress
	MPa	Σc, cm^2/cm^3	
Zirconium	900	.01	1
Iron	1100	.17	14
Nickel	1100	.31	25
Titanium	1000	.26	28
Aluminium	90	.014	14
Magnesium	90	.005	5
Beryllium	180-350[c]	.001[c]	0.25-0.50

a) Based on presently available high strength alloys

b) Probable value for high strength alloy designed to minimise neutron absorption

c) For unalloyed beryllium

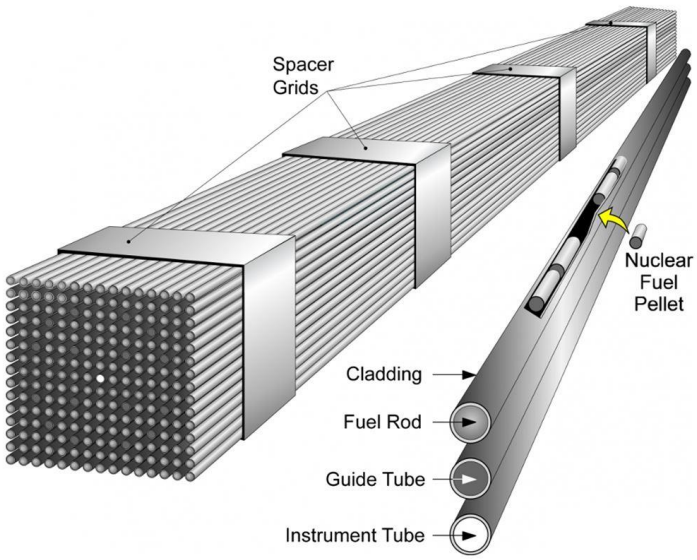
The long-term high temperature water corrosion testing of Zircaloy-1 showed that the corrosion rate did not, as expected, slow down with increasing time, instead, the corrosion rate increased at a specific time and then remained constant and such specific time did not show advantages compared to the unalloyed material. Then Zircaloy-2 was developed by adding iron and nickel for high temperature corrosion resistance. Having almost same level of tensile properties as compared to Zircaloy-1, Zircaloy-2 was tested to have higher high temperature corrosion resistance. The Zircaloy-3 was developed based on the experiences of developing Zircaloy-1 and Zircaloy-2, trying to lower the content of tin but to increase the content of iron for further enhance the high temperature corrosion resistance. However, Zircaloy-3 showed lower mechanical properties compared with Zircaloy-2. Zircaloy-4 is the 'nickel free Zircaloy-2' having as good corrosion resistant properties as Zircaloy-2

but with 50% of the hydrogen absorption. Consequently, in selecting structural materials in reactors, zircaloy-2 and zircaloy-4 are popular options [12].

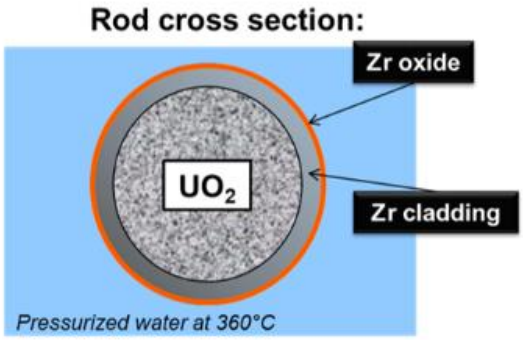
Apart from Zircaloy (Zr-Sn alloy), the ZrNb alloys (E110, E125, M5, Zr-2.5%Nb) and multicomponent alloys such as E635, ZIRLO, NDA, MDA, etc, are also widely used in nuclear applications, particularly in the fuel rods and the spacer grids as parts of the fuel assemblies in the nuclear reactors. Figure 2.1-3 (a) shows the image of the fuel assemblies using zirconium alloys in building nuclear reactors [26], The schematic drawings of fuel assemblies and fuel rod (Figures 2.1-3 (b) and (c)) reveal the applications of zirconium and its alloys as cladding material, providing the cover to the fuel rod in the nuclear reactor [27, 28].



(a) (b)



(c)



(d)

Figure 2.1-3 Zirconium alloys used in nuclear reactors. (a) and (b) images of fuel assemblies for nuclear reactors; (c) and (d) schematic draw of fuel assemblies structure and rod cross section. [26, 27, 28, 29].

2.1.4.2 Chemical industrial applications

In the chemical processing industry, commercial grade containing hafnium is used rather than nuclear grade. The corrosion resistance of zirconium and its alloys is due to the tightly adherent and protective oxide film which provides corrosion resistance by protecting the metal-oxide interface. It is reported that zirconium and its alloys are resistant to most organic acids, strong alkalis and seawater. The corrosion rates under corrosive attack of nitric acid (HNO_3), sulfuric acid (H_2SO_4), and hydrochloric acid (HCl) with impurities are generally under 5 mpy (milli-inches per year) [5, 15]. Compared to other metals, zirconium has better corrosion resistant compared to stainless steel but worse than tantalum [25].

2.1.4.3 Medical applications

Cobalt-chrome (Co-Cr), titanium (Ti) and tantalum (Ta) and its alloys are the major materials developed for medical implants, however, the drawbacks including adverse effect entailed from the release of metal ions (i.e., Ni, Co and Cr), the high density of Ta (16.4 g cm^{-3}) making titanium and titanium alloys become a more ideal metal selection for implants application [30, 31, 32].

Recently, it has been reported that zirconium-based alloys are considered as the more promising material because intrinsic bone-like apatite layer was found to form on the surface in the body environment. This apatite layer is crucial for the adhesion of the implants onto the bone and the growth of new bones on top of the implant surface at

the early stage of the implantation. Zirconium and titanium are both in group 4 of the periodic table (same number of outer shell valence electrons), and the properties and characteristics for both metals and their alloys as well as their oxides are very similar. They also share properties such as bio-inertness, excellent bio-corrosion resistance which are key properties in medical implants applications. Zirconium alloys on some occasions particularly in medical implants applications have even better crucial properties than titanium alloy. For example, despite titanium having higher hardness and Young's modulus, zirconium has even better corrosion resistance and it has a lower level of intrinsically magnetic susceptibility (1.3×10^{-6} cm^3g^{-1}) compared to titanium (3.2×10^{-6} cm^3g^{-1}), which is less than 50% of titanium and much lower than other implants metals as well. The magnetic susceptibility for implants materials is important in high Tesla MRI diagnoses (Magnetic Resonance Imaging) diagnostics because high magnetic susceptibility can lead to heat generation, dislocation of implants and low-quality images. The following table (Table 2.1-3) compares the basic properties between commercial grade zirconium (Zr702, R60702) and commercial grade of titanium (Grade-1) [30, 33].

Table 2.1-3 Properties comparisons between commercial Zr alloy Zr702 (R60702) and commercial Ti alloy (Grade-1) [30].

Elements	Oxygen content [wt%]	Atomic number	Atomic weight	Valence electron	Melting point [°C]	Boiling point [°C]	Density [g cm^{-3}]	Tensile strength [MPa]	Yield strength [MPa]	Elongation at break [%]	Young's modulus [GPa]	Shear modulus [GPa]	Magnetic susceptibility 10^{-6} [cm^3 g^{-1}]
CP Zr	≤0.16	40	91.224	4	1852	4377	6.7	440	240	18	88	35.3	1.3
CP Ti Grade 1	≤0.18	22	47.867	4	1668	3287	4.51	240	170	24	102.7	44	3.2

The zirconium-based alloy used in medical implants such as total knee replacement (TKR) and total hip replacement (THR) is called *Oxinium* (oxidised Zr-based alloy, Zr–2.5Nb, wt%), which was developed and used in 1997 and 2002 respectively. The

Oxinium implants have been shown to function for 20-25 years, which provides 10 years longer lifetime compared with Co-Cr alloys and polyethylene implants [30]. The application of Oxinium in implants THR and TKR are shown in Figures 2.1-4 (a) and (b). Zirconia is also widely used for dental applications such as prosthetic teeth. Figure 2.1-4 (c) demonstrates a Z-systems implant, which is one of the varieties of zirconia based dental implant systems. The good biocompatibility and mechanical properties (high bending and tensile strength [34]) of zirconia make it a perfect choice for the dental implants. More importantly, it also presents with tooth-like colour and remains inert in body fluids [24, 30, 34]. Zirconium compounds are also used for phosphorous pollution control in public health applications, and for clinical applications including hemofiltration, haemodialysis and peritoneal dialysis via Zr-containing sorbents and wearable kidneys design and construction [24, 35].

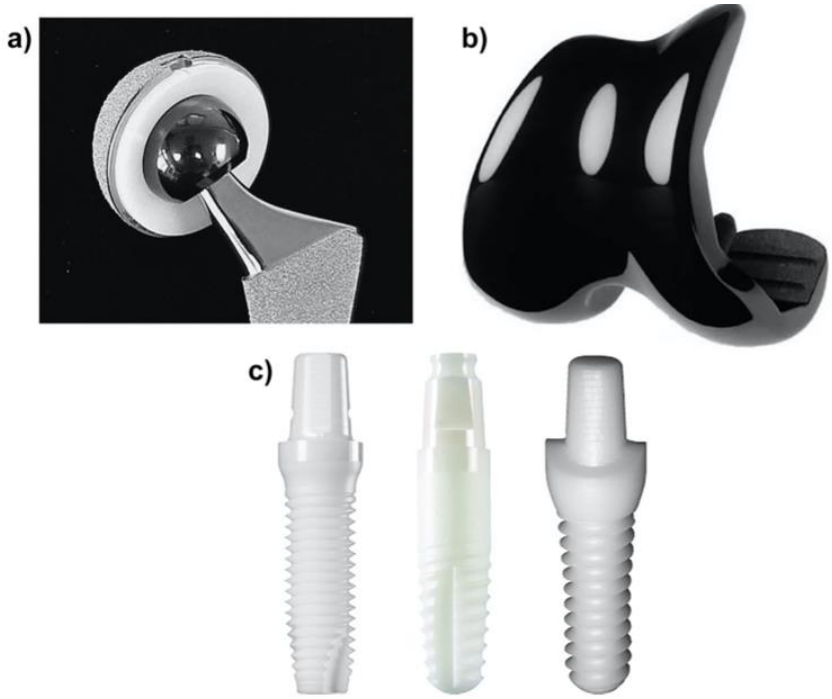


Figure 2.1-4 Examples of the zirconium applications in medical implants: (a) Total hip replacement (THR); (b) Total knee replacement (TKR); and (c) Z-Systems Z-Look3 Evo implant (Ceramic Teeth implant) [30].

2.1.5 Limitations

Despite the good properties, the drawbacks of zirconium and its alloys could prohibit their wider use in the above fields and other areas. These drawbacks include, but are not limit to, low hardness, poor wear resistance and high friction. The hardness of an annealed zirconium sample is measured as 150 HV [1]. Zirconium also has relatively low resistance to abrasion and has the tendency to gall, which creates problems under mechanically and tribologically demanding applications [36].

2.1.5.1 Wear

The wear of metals could be defined as the plastic displacement and the removal of surface and near-surface material, and the wear debris are formed from the detached particles. Mild and severe wear would cause different size of the particles in wear debris. Mild wear produces smooth and smaller wear debris with the particle size typically ranging from 0.01 μm to 1 μm, whereas the severe wear produces roughened worn surface and larger wear debris with sizes ranging from 20 μm to 200 μm [37]. The wear rate, which is used to quantified wear, is independently of the materials contact area, but can be affected by the factors including the applied load, temperature, lubrication etc [38, 39]. Adhesive wear and abrasive wear are the common wear types in the wear of metals.

Adhesive wear is characterised by material transfer during the frictional contact from one surface to another surface, leaving the pits, voids, cavities or valley on the top of

the surface [40]. This is caused by stronger adhesive bonds compared to the cohesive bond in the weaker material, and is generally observed when metals in contact have similar chemical composition, or the contact surfaces are clean without oxide layer, i.e. in vacuum or inert environments [37]. The adhesive wear mechanism is demonstrated in Figure 2.1-5. The bond junction is broken in the continued motion of the surfaces, causing the wear particles formed usually from the weaker material. The removed material may adhere to the other surface [41]. Severe adhesive wear could also cause galling [42]. The adhesive wear tendency of a ductile metal depends on a few factors, which includes surface hardness, nature of deformation (plastic or elastic), chemical activity (d-bond character) and chemical similarity of contacting surfaces (metallurgical compatibility) [43].

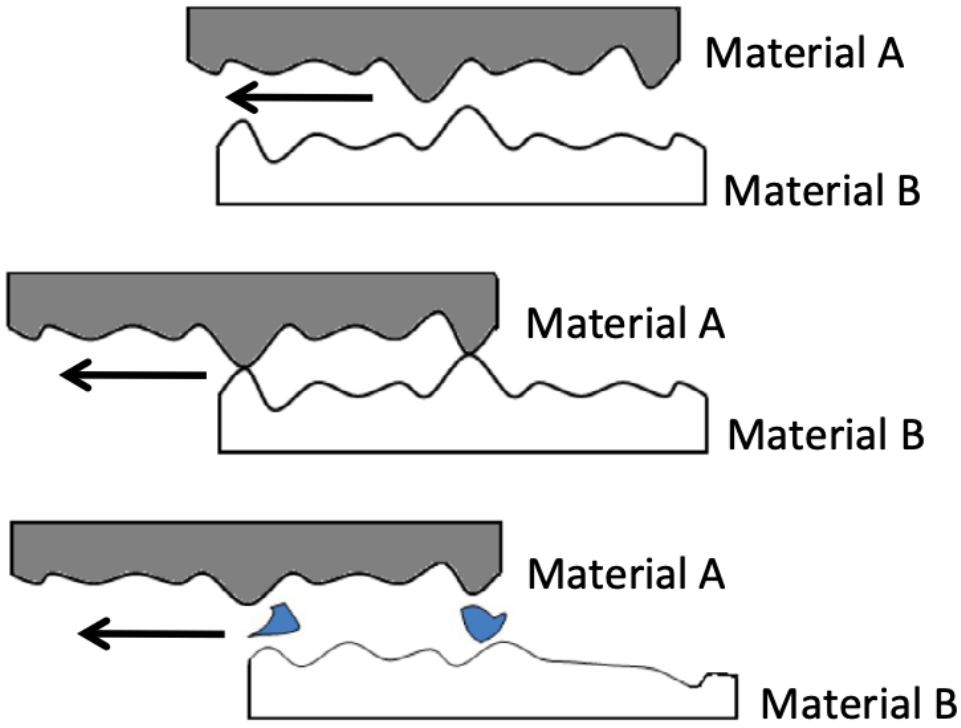


Figure 2.1-5 The schematic diagram of adhesive wear mechanism [41].

Abrasive wear occurs when the harder body or grain sliding against the soft solid surface [37, 44]. As shown in Figure 2.1-6, the abrasive wear results in three abrasive modes, which are ploughing, wedge forming and cutting modes [37, 45]. Based on the amount of the material remained at the sides of the groove, the cutting mode (Figure 2.1-6 (c)) shows that a much larger part of the groove volume is lost, as compared to the ploughing mode. The wedge forming mode is between ploughing and cutting, as shown in Figure 2.1-6 (b), in which part of the groove volume is lost and part remains at the sides [45].

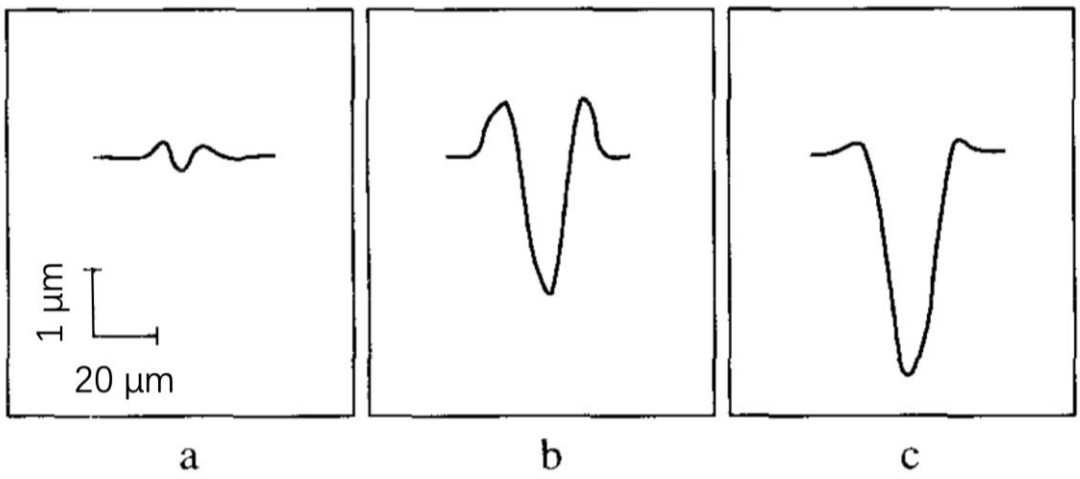


Figure 2.1-6 The three wear modes of abrasive wear in cross sectional profiles: (a) ploughing mode, (b) wedge forming mode (c) cutting mode [45].

Abrasive wear could also be classified as two-body abrasive wear and third-body abrasive wear (Figure 2.1-7). The typical example of two-body abrasive wear is grinding, cutting or machining, where abrasive marks are left on one surface (soft material) by the other surface (hard material). The third-body abrasive wear has abrasive marks occurring on both surfaces, and the harder abrasive particles may embed into the soft surface [37, 41].

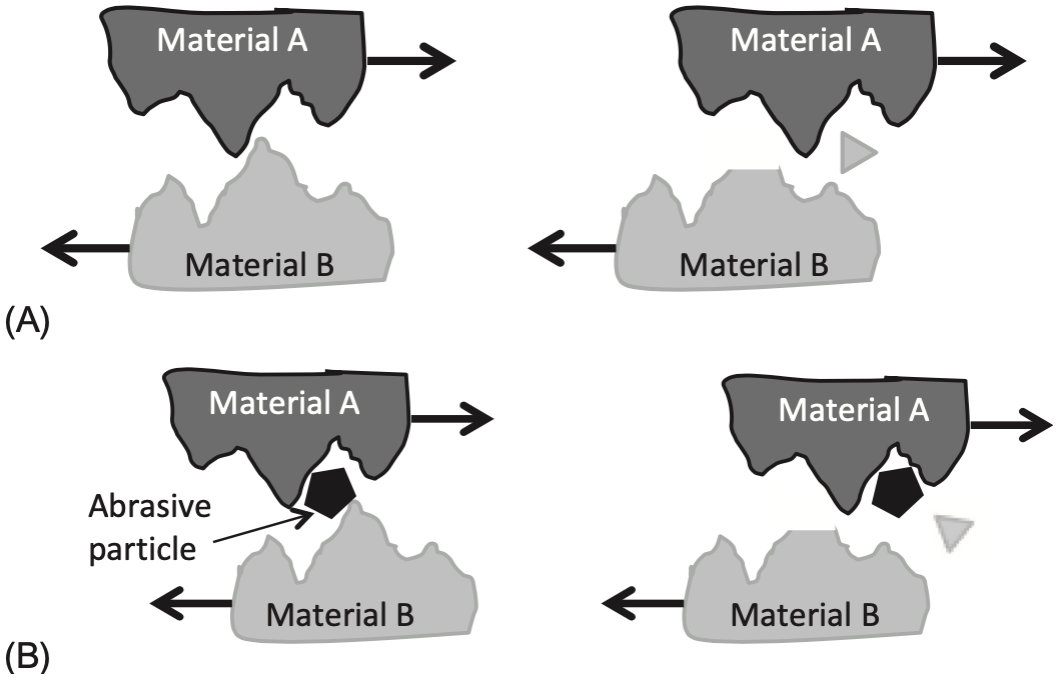


Figure 2.1-7 The abrasive wear mechanisms: (A) two-body abrasion, (B) third-body abrasion [45].

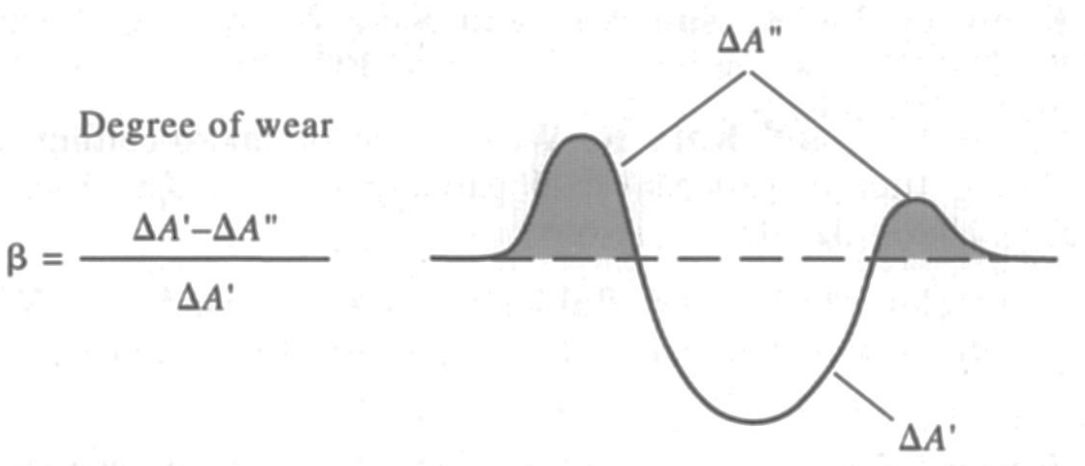


Figure 2.1-8 The degree of the wear calculated from the 2D scan of the groove [45].

As shown in Figure 2.1-8, the degree of the wear could be expressed as β, which can be calculated via the equation:

$$\beta = \frac{\Delta A' - \Delta A''}{\Delta A'} \qquad \text{(Equation 2.1)}$$

where *ΔA'* and *ΔA''* represent the area of the groove and the material on the sides in 2D scan [45]. The typical way to effectively reduce the abrasive wear is to use abrasive-resistant material or applying coatings, changing the design or preventing the intrusion of hard grains [44].

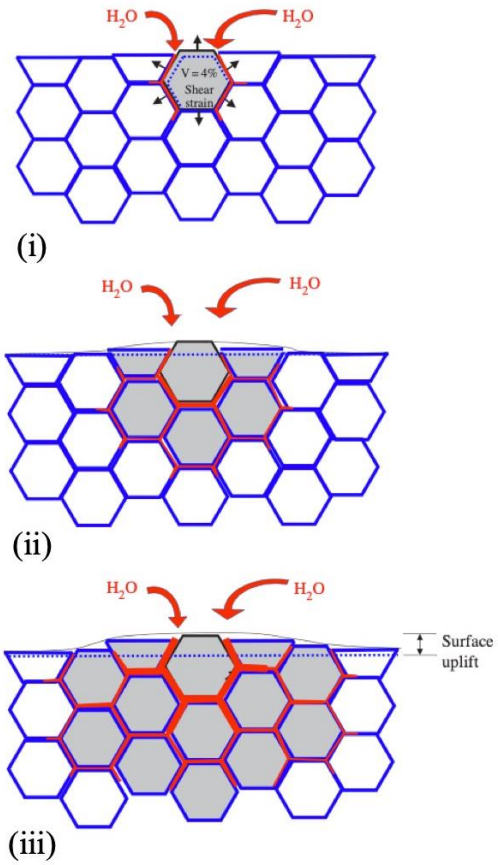
Zirconium has strong cold welding and high junction strength in sliding against metal surfaces due to its very low d-bond character (high chemical activity) and high metallurgical compatibility, and it also has high ductility, which make zirconium and its alloys have strong adhesive wear/galling tendency. High wear rates, particularly in abrasive wear, can be attributed to the low hardness of zirconium and its alloys [43].

2.1.5.2 Corrosion and corrosion wear

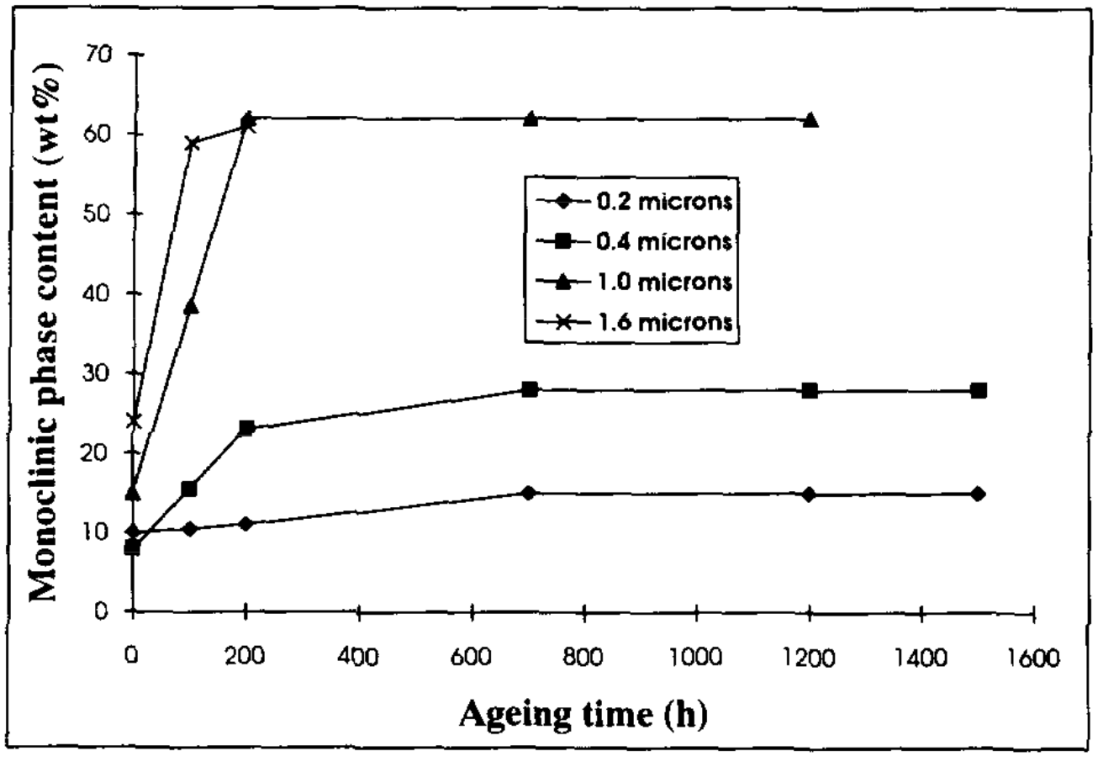
Even though zirconium and its alloys have relatively good corrosion resistance under various corrosive attacks including in high-temperature steam [46], stress corrosion cracking (SCC) of zirconium and Zircaloy-4 was reported in halide aqueous solutions (1 M NaCl, 1 M KBr and 1 M KI) at potentials higher than the pitting potential testing with an initial strain rate (SR) between 4.6×10^{-6} to 2.5×10^{-2} s^{-1} [47]. SCC of Zr has also been reported when it is in boiling nitric acid at corrosion potential of 0.8V for 17% HNO_3, 0.1V for 70% HNO_3 and at an open circuit potential in 94% HNO_3, under the testing strain rate of 4.17×10^{-6} s^{-1} [48].

The zirconia ceramics used as medical implant, are also sensitive to low temperature degradation (LTD) leading to its limitation of roughening and fatigue failure [49]. The yttria stabilised tetragonal zirconia (YTZP) is used in the implant application as it

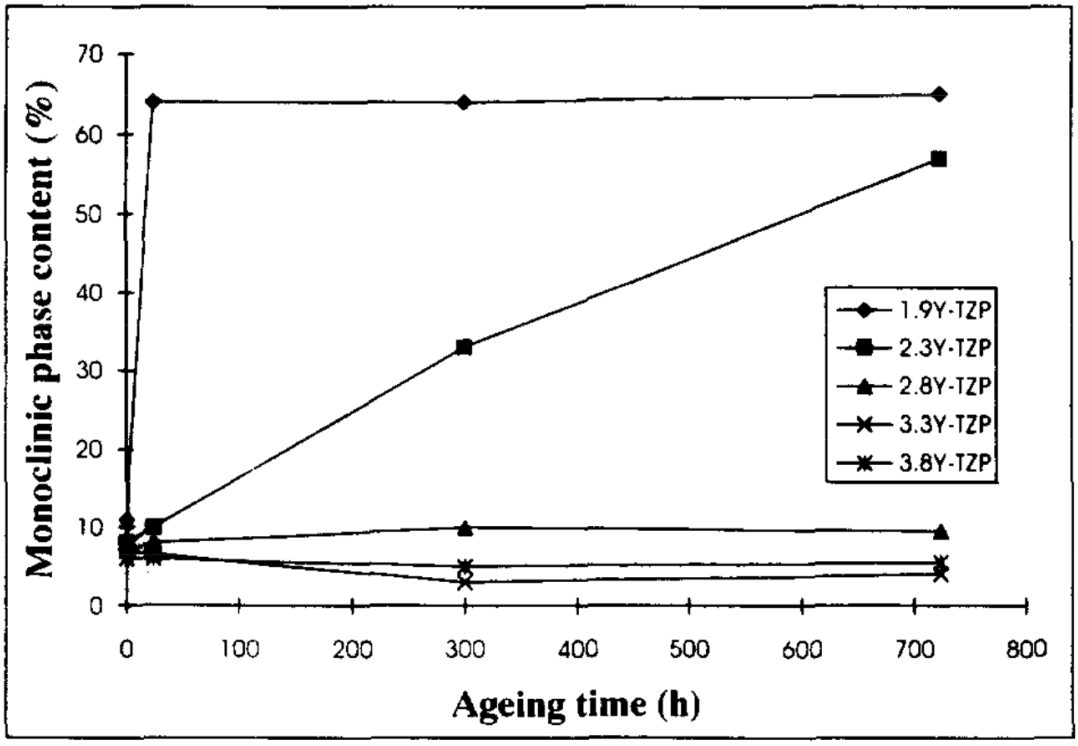
has high strength, high fracture toughness (linked to the tetragonal-monoclinic phase transformation) and low wear rates, however, the delayed failure in vivo was still found as the results of crack propagation. The additions of carbon nanotubes (CNT) has been proposed for improving the lifetime [50, 51]. In presence of humid air, water or water vapour in the temperature range of 65 °C -500 °C, the ageing of zirconia ceramics stabilised with yttria, ceria, calcia or magnesia occurs because of the surface transformation from tetragonal (metastable) to the monoclinic phase, which is the stable structure of zirconia ceramics at room temperature [49, 50, 51]. The relationship of the grain size with the transformation and the stabiliser content with the transformation have been discovered (as illustrated in Figures 2.1-9 (b) and (c)): the decrease of grain size and increase of stabiliser content could slow down the ageing [51]. This also means that larger grain size, low stabiliser content and residual stresses etc. can cause a disequilibrium state initiating the phase transformation. The volume increase arises from the transformation of the grains, causing the adjacent grains being stressed up and thus microcracking occurs, which gives the space for water to penetrate (Figure 2.1-9 (a)) [49].


H2O
H2O
V = 4%
Shear
strain
(i)
H2O
H2O
(ii)
H2O
H2O
Surface
uplift
(iii)

(a)


Monoclinic phase content (wt%)
70
60
50
40
30
20
10
0
0
200
400
600
800
1000
1200
1400
1600
Ageing time (h)
0.2 microns
0.4 microns
1.0 microns
1.6 microns

(b)



(c)

Figure 2.1-9 The degradation of the zirconia ceramics: (a) the ageing mechanisms; (b) the smaller grain size produces leads to less phase transformation, and thus less ageing of zirconia ceramics; (c) more yttria (stabilizer) content for zirconia ceramics leading to less phase transformation, and thus less ageing [49, 51].

Corrosion wear occurs in lubricated wear conditions, which is caused by the chemical reactions between the worn surface and the lubricating medium [37]. When investigating the corrosion response of prior abrasion of Ti based alloys, Komotori et al. [52] reported that the ceramics conversion treated Ti-6Al-4V alloy performs the best corrosion wear resistance under potentiodynamic and cyclic polarisation (CP) procedure conducting in de-aerated 0.89 wt.% NaCl at 37°C comparing to the as-received PVD TiN coated Ti-6Al-4V alloy and SP700 (Ti-4.5Al-3V-2Fe-2Mo) alloy. This was attributed to the dense, stable and wear resistant TiO_2 oxide layer formed [43]. Figure 2.1-10 illustrates the comparisons between the untreated zirconium alloy (Zr705) and ceramic conversion treated Zr705 alloy after reciprocating sliding wear tests in 3.5 wt% NaCl solution, which shows the severe adhesive craters and fractured adhesion junctions with parallel abrasive wear grooves (Figure 2.1-10 (a)). The ceramic conversion treated Zr705 alloy only showed shallow abrasive wear grooves and the wear resistant, calculated through the wear volume loss, showing 220 times improvement compared to the untreated Zr705 alloy [43].

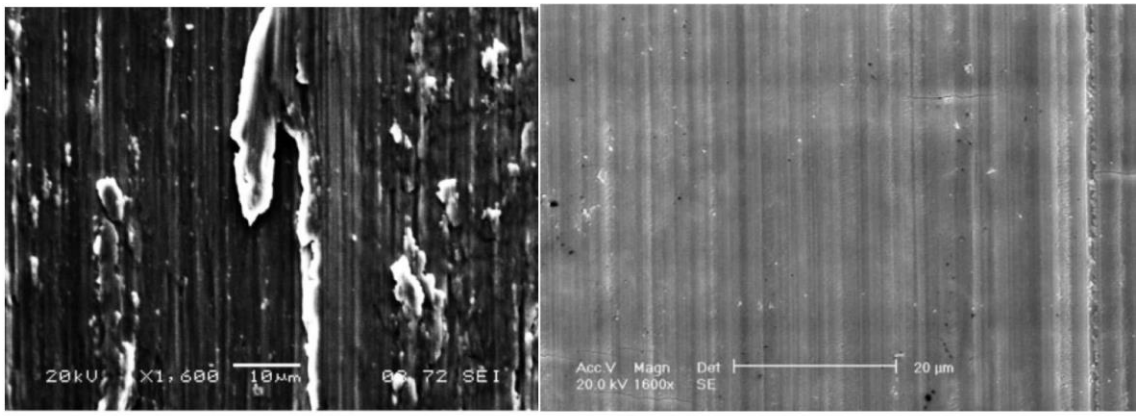


Figure 2.1-10 The wear surfaces of (a) untreated Zr705 alloy, and (b) Zr705 alloy ceramic conversion treated under 600°C/3 hours [43].

2.2 Surface engineering of zirconium alloys

As summarised in the following table (Table 2.2-1), the different surface engineering methods such as vapour deposition (PVD and CVD), ion implantation, laser treatment, etc,[53, 54, 55, 56] have been developed to improve the properties of Zr and its alloys. Many of these techniques require high temperatures and the thickness of the modified layer is typically thin (within several thousands of angstrom), which can only be used in light load wear conditions.

Table 2.2-1: Scope of surface engineering methods of Zr alloys [2, 57, 58].

	Methods	**Findings**	**Drawbacks**
Surface coating	Physical vapour deposition (PVD)	Deposition of zirconia or zirconium nitride to increase wear resistance	• Difficult for PVD to deposit on the sample with complex dimensions. • PEO is not cost-effective. • For most surface coating methods, poor bonding strength between the layer and surface. Low load bearing capacity.
	Plasma electrolytic oxidation (PEO)	Zirconium oxide obtained on the zirconium alloy surface, enhanced the wear and corrosion resistance.	
	Electroplating	Copper, nickel and iron electroplating, corrosion resistance improved	
Surface modification methods	Ion implantation	To produce surface layer within the substrate for properties improvements	•Very thin case generated sensitive to ion dose and substrate temperatures
	Laser assisted surface treatment		•Localised high temperature, •Distortion at high temperatures •Zr-hydrides formed
	Thermochemical and electrochemical methods		•Detrimental oxidation on the equipment; •Boundary between oxide layer and substrate

2.2.1 Surface coating

2.2.1.1 Physical vapour deposition

Physical vapour deposition (PVD) is a variety of methods to transfer material from a solid or liquid source, as a vapour gas or sputtered species form and condense them on to the substrate surfaces as thin films. The thickness of the layer deposited onto the substrate can range from a few to thousands of angstroms. The PVD is capable of depositing many organic and most inorganic materials in various forms. The PVD can be categorised as vacuum evaporation, sputter deposition, arc vapour deposition and ion plating [57].

The vacuum evaporation is a cost-effective method to deposit high purity films from high purity source material in high vaporisation rates. However, it is difficult to deposit many alloy compositions and compounds. It is unable to obtain good surface coverage and uniform thickness on artifacts with complex surface and dimensions and the deposited coating is characterised by weak bonding to the substrate. The sputter deposition is more often used in applying wear-resistant coatings; however, the sputtering rate is low, and the target materials are expensive. It also has the problems to obtain uniform thickness films. Alloy materials can be vapourised readily via arc vapour deposition. The arc vapour deposition (AVID) is used to deposit wear resistant coatings as well, which includes the deposition of TiN, ZrN and HfN [57, 59]. The arc vapour ion deposition process utilizes the metal ion bombardment to ion etches and heats the substrate surface following the deposition of films onto the clean biased substrate [59].

Ion plating is a hybrid process combining sputtering with evaporation. Oxides, nitrides, carbides etc. can be formed on the surface in reactive ion plating through acceleration of reactive species including nitrogen and oxygen produced by the plasma [57]. Molarius et al. [60] has reported the method to use reactive ion plating to produce ZrN coating. An electron beam gun was used for the evaporation of the Zr metal [61]. In terms of quality of film obtained, the ion plating method improves the surface coverage; however the variation of properties found on the surface are linked to the non-uniform ion bombardment and the substrate may be heated excessively during the process [57, 62]. Microscopic defects such as pinholes were found in the coatings produced by the ion plating. The pinholes can lead to the rapid corrosion, and the material underneath can be corroded, resulting in the complete failure of the coating. Methods include pulsing of nitrogen flow, substrates rotation, sputtering period separation etc. have been studied and discussed to improve the corrosion resistance [63]. However, PVD, coatings are normally thin (a few microns) and the Zr substrate is relatively soft. Hence, the load bearing capacity of PVD coated Zr and its alloys is limited by the 'thin-ice' effect. Another major technical limitation of PVD coatings for Zr alloys is the low bonding due to the oxide films present on the active Zr surface before PVD.

2.2.1.2 Electroplating

Similar to PVD, electroplating is a method to produce coatings, but this is achieved via reduction reactions of the cation, and the coating is obtained on the cathode. Schickner, Beach and Faust [64] developed a method to produce adherent electroplates on zirconium surface. The plated zirconium showed bonding

enhancement from 6000 psi to 50,000 psi [64]. However, the zirconium and its alloys are reported to be difficult to coat using electroplating, as the oxide film is easily formed on the surface acting as a 'barrier' to the substrate for further electrochemical reactions [65].

Electroplating process can only work for electricity conductive materials. In addition electroplated film always have impurities such as added chemicals, added particles, cathodic products, hydroxides and bubbles [66].

2.2.1.3 Plasma electrolytic oxidation

Plasma electrolytic oxidation (PEO) is a relatively new surface treatment method to form oxide layers on some metals (such as Al, Mg, Ti, Zr etc.) mainly via intensive electrochemical reactions. The oxide layers obtained are thick and dense and could primarily provide enhancement of wear and corrosion resistance. Other properties including thermal stability, bioactivity and biocompatibility could also be improved. Originated from anodic oxidation of metals, the PEO process is operated under the high electric potentials and the environment of acidic electrolytes, and the process is schematically shown in Figure 2.2-1. The process consists of electrochemical reactions, plasma chemical reactions, and thermal oxygen diffusion reactions, producing a three-layer structure of the coatings obtained (porous outer layer, dense intermediate layer and thin inner layer). The coatings grow both outward and inward to the substrate, as Figure 2.2-2 illustrates a structure of oxide grown via PEO on 1060 Al substrate. As a result, the coating obtained from PEO generally have good adhesion to the substrate [58, 67].

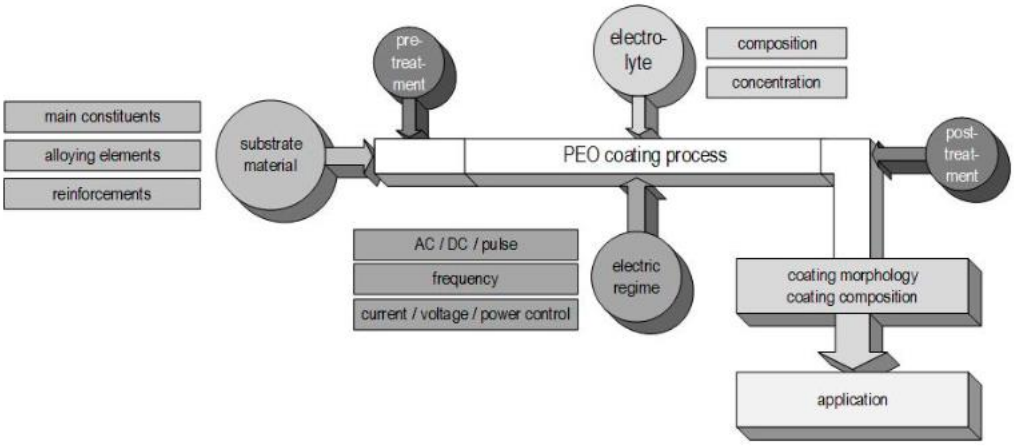
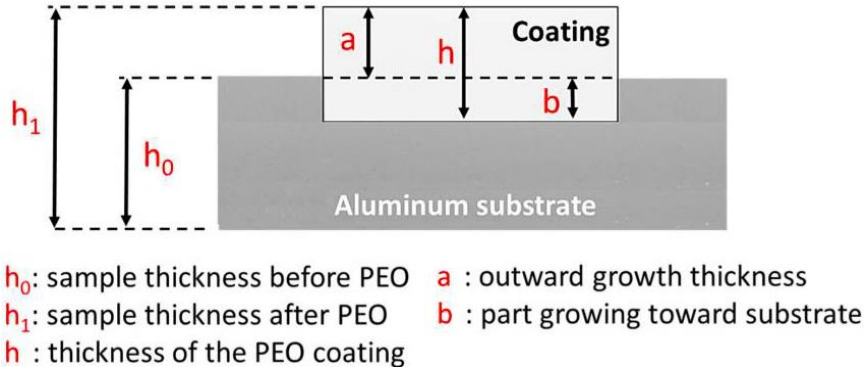


Figure 2.2-1 The PEO process summary in schematic draw [68].



h_0: sample thickness before PEO
h_1: sample thickness after PEO
h : thickness of the PEO coating
a : outward growth thickness
b : part growing toward substrate

Figure 2.2-2 Schematic draw of the PEO coated aluminium sample [58].

Due to the facts that it can produce good adhesive oxide coating, with improved properties to the substrate, the PEO is used in various areas and can be grown on different substrates, as summarized in Table 2.2-2 [68].

Table 2.2-2: Table summarised the applications and substrate of PEO [68].

Application/Motivation	Substrate
Corrosion and wear protection	Al, Mg, Ti, Zn, brass, Fe/Steel, Nb, Be, Ta, c-graphite materials
Adjustment of radiation behavior improved thermal emission, lowered absorbance lowered optical reflection	Ti, Mg
Decorative purpose (by coloring)	Al, Mg
Improvement of thermal isolation	Al
Medical Issues Formation of hydroxyapatite (HA) for improved bioactivity Adjustment of the degradation in contact with body tissue	Zr, Ta, Mg, Ti, Mg
only selective scientific description photoluminescence Catalytic activity	Hf, Fe

Wang et al.[53] reported PEO of Zr–2.5 wt.% Nb alloy. The thickness of the coatings obtained was measured in the range of 7–15 μm. All the PEO coated samples revealed improved properties in wear and corrosion resistance, as shown in Figure 2.2-3 [53]. Sezgin Cengiz et al. [69] also reported the formation of a crystalline hydroxyapatite (HA) coating on zirconium substrate using PEO method, which is promising in the biomedical applications.

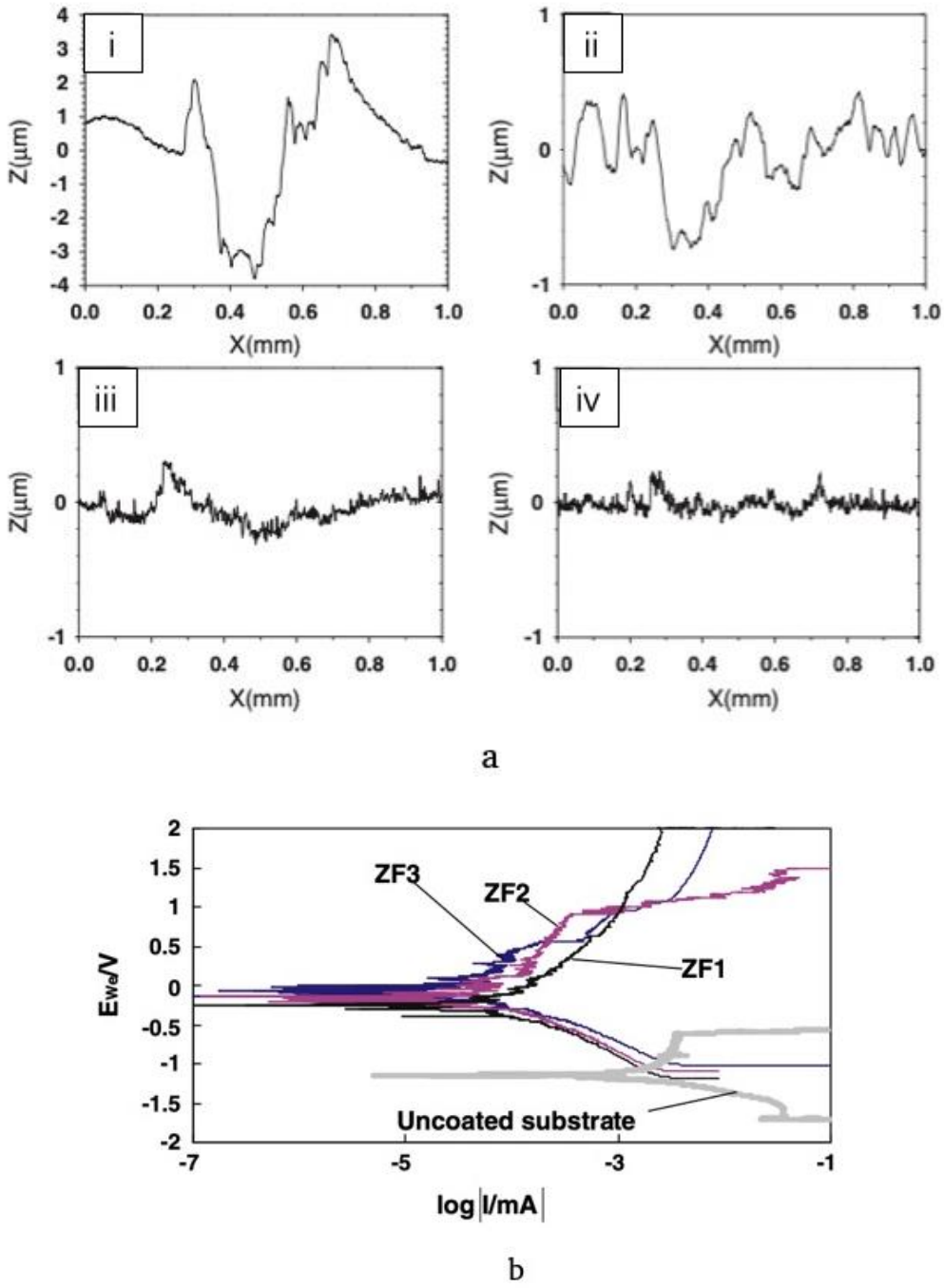


Figure 2.2-3 The improved wear and corrosion properties shown on PEO coated Zr alloy compared to uncoated substrate. (a) (ii), (iii) and (iv) represent the 2D scan of the wear tracks of PEO coated samples, having less wear volume compared to (i) the uncoated substrate. (b) the polarisation curves of PEO coated samples ZF1, ZF2 and ZF3 and uncoated substrate [53].

Although the PEO method can effectively improve the properties of Zr-based materials, there are some associated technical limitations. The PEO method involves complex process and reactions, leading to high energy consumption and high cost. In addition, after PEO the treated Zr surface became rough [68, 70].

2.2.2 Surface modification methods

2.2.2.1 Ion implantation

Ion implantation is a surface modification method that accelerates the ions of the element towards the target to purposely change the surface chemistry and properties of the original material. Peng et al. [55] reported lanthanum ion implantation to modify the oxidation behaviour of zirconium. The oxidation behaviour of ion implanted zirconium was shown to have been improved [55]. Research also showed that the Mg-implantation into zirconium and titanium enhanced the bioactivity [71].

Some other researchers used the ion implantation techniques, particularly the nitrogen ion implantation to improve the corrosion resistance Zircaloy-4 alloy [72, 73, 74]. The temperature dependence was found in the distribution of nitrogen, oxygen and carbon during the implantation process, and the corrosion resistance of the implanted Zircaloy-4 was also affected by the implantation temperature. ZrO_2 was found to be mainly distributed at the outer layer followed by ZrN [72]. Apart from the temperature, localised corrosion potential also corresponds with the ion dose. At certain condition (ion does: 5×10^{-17} ions cm^{-2}, 400°C), the best corrosion resistance was achieved because of the formation of a thick ZrO_2 layer with less defects under this condition [74]. Low substrate temperatures of 100 °C or 200 °C and

temperatures at 500 °C may degrade (rather than improving) the corrosion properties [73, 74].

2.2.2.2 Laser assisted surface treatment

Laser assisted surface treatment is a process to produce fine microstructure of the metals for wear and corrosion resistance enhancements. The principle of the process is to melt a small surface volume of the materials via the laser beam, followed by the rapid cooling. This is referred to laser surface melting (LSM), which showed the improvement of corrosion resistance in acidic environments (10% $FeCl_3$ solution) [75]. A study by Lee et al. [76], on laser surface alloying (LSA) to form an alloy system of Zr-Nb-Sn-Fe-Cr (thickness of 170-300μm formed) on Zircaloy-4, also indicated the improvements of the corrosion in chloride solution and mechanical property (i.e. microhardness); however, it was found that the corrosion resistance was reduced under steam at 400°C [76].

Chen et. al. [77] presented a study on combining the electroplating technique and laser surface alloying. Following the brush plating of Cr on commercial Zr alloy (CP Zr, Zr702), the specimen was treated using a pulsed laser for alloying Cr on the surface. Figures 2.2-4 (a) and (b) demonstrated the SEM image and EDS line scans of the brush plated specimen, and it can be seen that after the brush plating, a Cr coating with thickness of 22 μm was obtained. The microstructures of the LSA treated specimen were characterised and the microhardness was measured. The LSA formed five zones from the top of the surface down to the Zr alloy matrix with melted zones MZ-1 and MZ-2, and solid-state phase transformation zones SSPTZ-1 and

SSPTZ-2, and finally the Zr alloy matrix, as shown in Figures 2.2-4 (c) and (d). The EDS line scans (Figure 2.2-4 (d)) confirmed the effective Cr alloying achieved mainly in the melted zones (MZs) rather than in the solid-state phase transformation zones (SSPTZs), which may be due to the lower temperatures in SSPTZs limiting the diffusion of Cr. Due to the solid solution strengthening and grain refinement, the Zr alloy after LSA treatment was found to have significant hardness improvement, around 2.4 times that of the Zr alloy matrix [77].

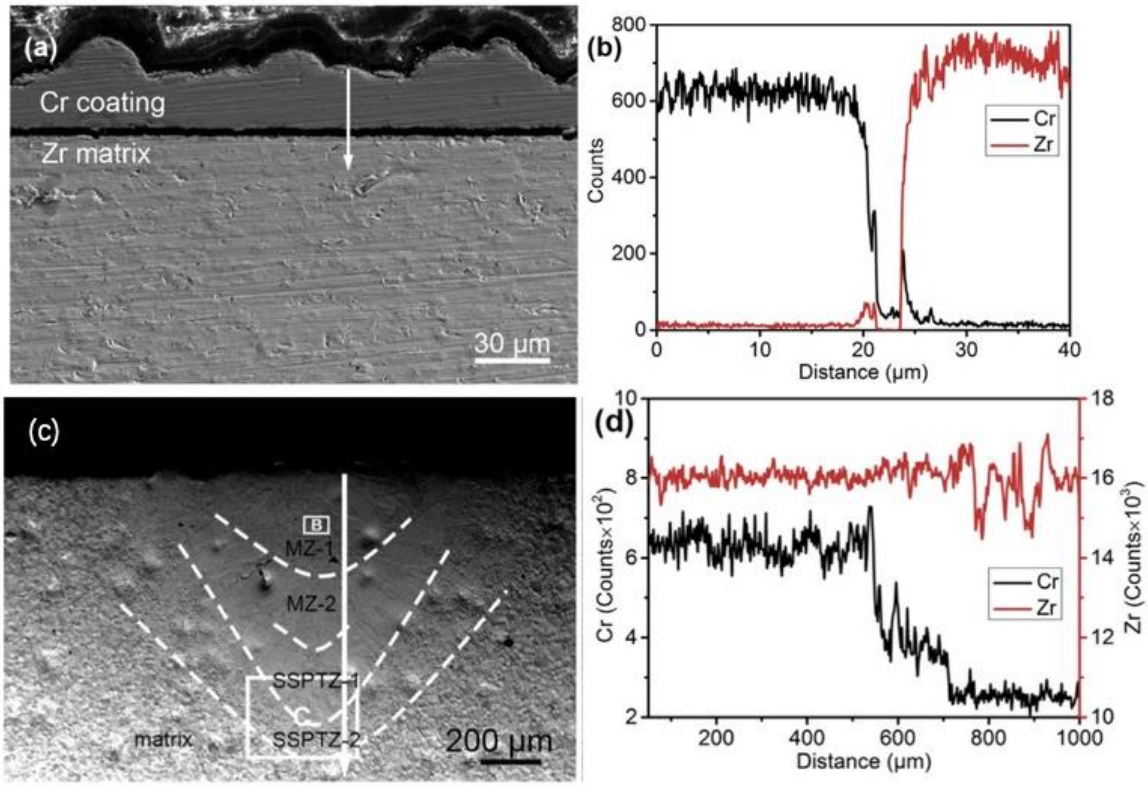


Figure 2.2-4 The SEM images and EDS lines scan after brush plating process (a) and (b); and LSA process (c) and (d) [77].

2.2.2.3 Thermochemical and electrochemical methods

The high wear resistance, high hardness, physical and chemical stability of zirconium nitrides imply that surface nitriding of zirconium and its alloy could be a promising

method to improve these properties. It is feasible to use this method on large scale complex surfaces and the composition can be controlled. The electrochemical nitriding of Zr follows the equation scheme of:

$$N^{3-}=N_{adsorbed}+3e^{-} \quad \text{(Equation 2.2)}$$

$$N_{adsorbed}+xZr=Zr_xN \quad \text{(Equation 2.3)}$$

The nitride ions were oxidised to adsorbed nitrogen atoms, which reacted with the zirconium surface to form zirconium nitride [78]. Recently, the surface nitriding technique has been used to improve the surface hardness of Zr-based metallic glass (MG). The MG surfaces have been irradiated by a fibre nanosecond pulsed laser system in a reaction chamber with nitrogen to avoid oxidation and to introduce the ZrN phase [79, 80]. A recent research by Hong et al. [80] indicated that the surface hardness of the MG could be improved to 2 times the original value of as-cast MG, which has been attributed to the generation of ZrN phase [80]. Distortion at high treatment temperature and the very thin layer formed are the major drawbacks of this technique [2].

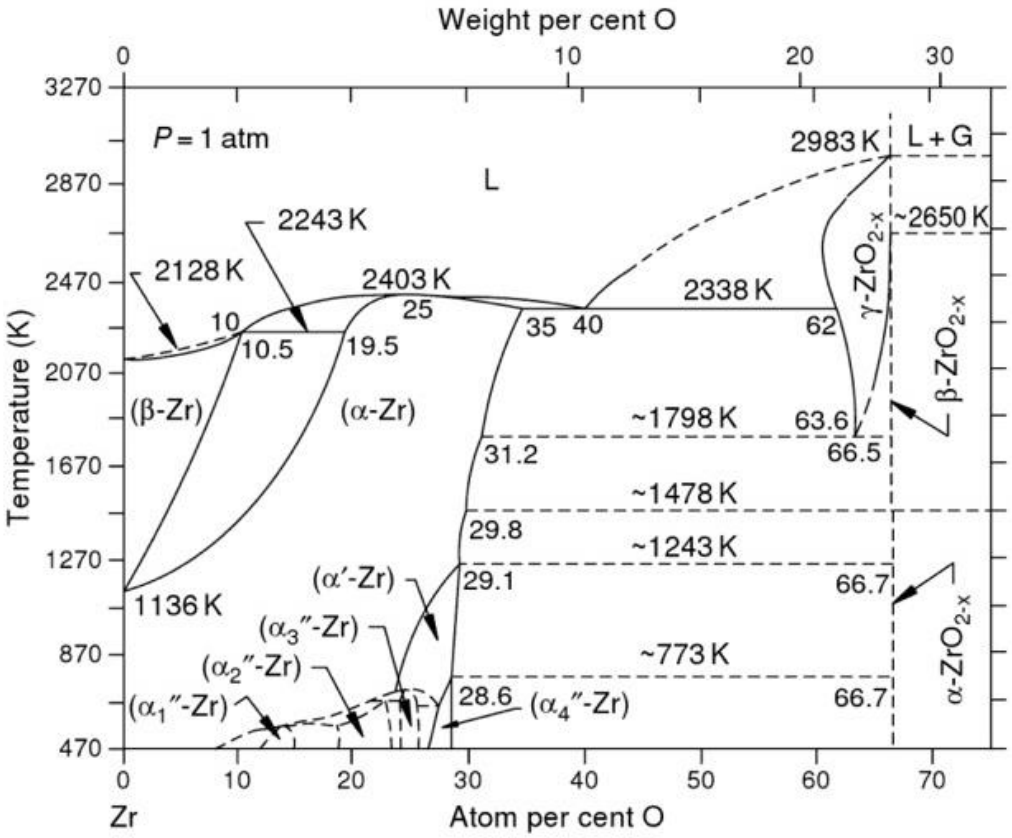
2.2.2.4 Ceramic conversion treatment

The ceramic conversion treatment (CCT or C2T) is the process which is capable to improve the properties of titanium alloys and zirconium alloys including hardness, wear properties, corrosion properties etc. based on thermal oxidation. Details will be explained in the later sections. This research is focused on further exploring this technique on Zr702 alloy, particularly the catalytic effects of pre-deposition elements before the CCT (or C2T) treatment.

2.3 Oxidation of zirconium alloys and oxidation kinetics

When zirconium and its alloys are placed in air, zirconia will be formed naturally as a thin film on the surface. The formation of the zirconia is crucial to the corrosion properties of zirconium and its alloys [2]. Apart from naturally formed zirconia, there are multiple ways used for zirconia synthesis. The common methods are combustion synthesis of zirconyl nitrate and ion exchange, as well as other methods including solid-state reaction, sol-gel synthesis, glycothermal processing, pechini method and wet chemical method [50]. In additional to the corrosion resistance enhancements, as mentioned above, zirconia is widely used as medical implant and in high temperature environment based on its advantageous properties such as very good thermal stability and low thermal conductivity.

The Zr-O phase diagram is shown in Figure 2.3-1 (a), and the key points along with the phase change is listed in Figure 2.3-1 (b). The oxygen solubility is high, and as evidenced from the phase diagram, the maximum solubility of oxygen in α-Zr is 35 at%, whereas for β-Zr is 10 at%. Below the eutectic temperature 2338K for α-Zr, and below the peritectic temperature of 2243K for β-Zr, the oxygen solubility limit is increased as the temperature increases. The phases of ZrO_{2-x} shown in the phase diagrams, referring to Zirconia (ZrO_2) also explain the phase transformation showing in Figure 2.1-2 (b).



a

Phase reaction	Type of reaction	Temperature (K)	Composition (at.% O)
$L \longleftrightarrow \beta Zr$	Melting	2128	0
$L \longleftrightarrow (\alpha Zr)$	Congruent	2403 ± 10	25 ± 1
$L \longleftrightarrow \gamma ZrO_{2-x}$	Congruent	2983 ± 15	66.6
$L \longleftrightarrow (\alpha Zr) + \gamma ZrO_{2-x}$	Eutectic	2338 ± 5	$(40 \pm 2)(35 \pm 1)(62 \pm 1)$
$L + (\alpha Zr) \longleftrightarrow (\beta Zr)$	Peritectic	2243 ± 10	$(10 \pm 0.5)(19.5 \pm 2)$ (10.5 ± 0.5)
$L + \gamma ZrO_{2-x} + G$		2983	(~ 66.6) (~ 66.6) (~ 100)
$\gamma ZrO_{2-x} \longleftrightarrow (\alpha Zr) + \beta ZrO_{2-x}$	Eutectoid	~ 1798	(63.6 ± 0.4) (31.2 ± 0.5) (66.5 ± 0.1)
$\beta ZrO_{2-x} \longleftrightarrow (\alpha Zr) + \alpha ZrO_{2-x}$		~ 1478	(~ 66.5) (29.8 ± 0.5) (~ 66.5)
$\gamma ZrO_{2-x} + \beta ZrO_{2-x} + G$		~ 2650	(~ 66.6) (~ 66.6) (~ 100)
$\beta ZrO_{2-x} + \alpha ZrO_{2-x} + G$		~ 1478	(~ 66.6) (~ 66.6) (~ 100)
$\gamma ZrO_{2-x} \longleftrightarrow \beta ZrO_{2-x}$	Congruent	~ 2650	66.6
$\beta ZrO_{2-x} \longleftrightarrow \alpha ZrO_{2-x}$	Congruent	~ 1478	66.6
$\beta Zr \longleftrightarrow \alpha Zr$	Allotropic	1136	0

b

Figure 2.3-1 (a) The Equilibrium phase diagram for Zr-O system; (b) The main phase transformation in the Zr-O system [81].

The oxidation of zirconium and its alloys follows the reaction:

$$Zr+(1-x/2)O_2 \rightarrow ZrO_{2-x} \qquad \text{(Equation 2.4)}$$

When the oxide is formed, the metal/oxide interface is where the reaction takes place for further oxidation. The oxygen from the environment needs to diffuse to the interface for reactions and therefore only a part of the oxygen can arrive for reactions when other parts are dissolved. The oxygen diffusion coefficient varies for α-Zr and zirconia under different temperature ranges (see Table 2.3-1), where D is in $m^2 s^{-1}$, R=8.314 J mol^{-1} K^{-1}, T is in K [82].

Table 2.3-1: The oxygen diffusion coefficient of α-Zr and zirconia in different temperature ranges [82, 83].

Temperature ranges	Oxygen diffusion coefficient, D $m^2 s^{-1}$	Temperature ranges	Oxygen diffusion coefficient, D
α-Zr		zirconia	
300 °C -600 °C	$D = 0.594 \cdot 10^{-14} \cdot \exp[-197237/RT]$	150 °C -500 °C	$D = 679 \cdot 10^{-18} \cdot \exp[-131524/RT]$
650 °C -850 °C	$D = 444 \cdot 10^{-4} \cdot \exp[-214016/RT]$	400 °C -850 °C	$D = 105 \cdot 10^{-7} \cdot \exp[-122474/RT]$

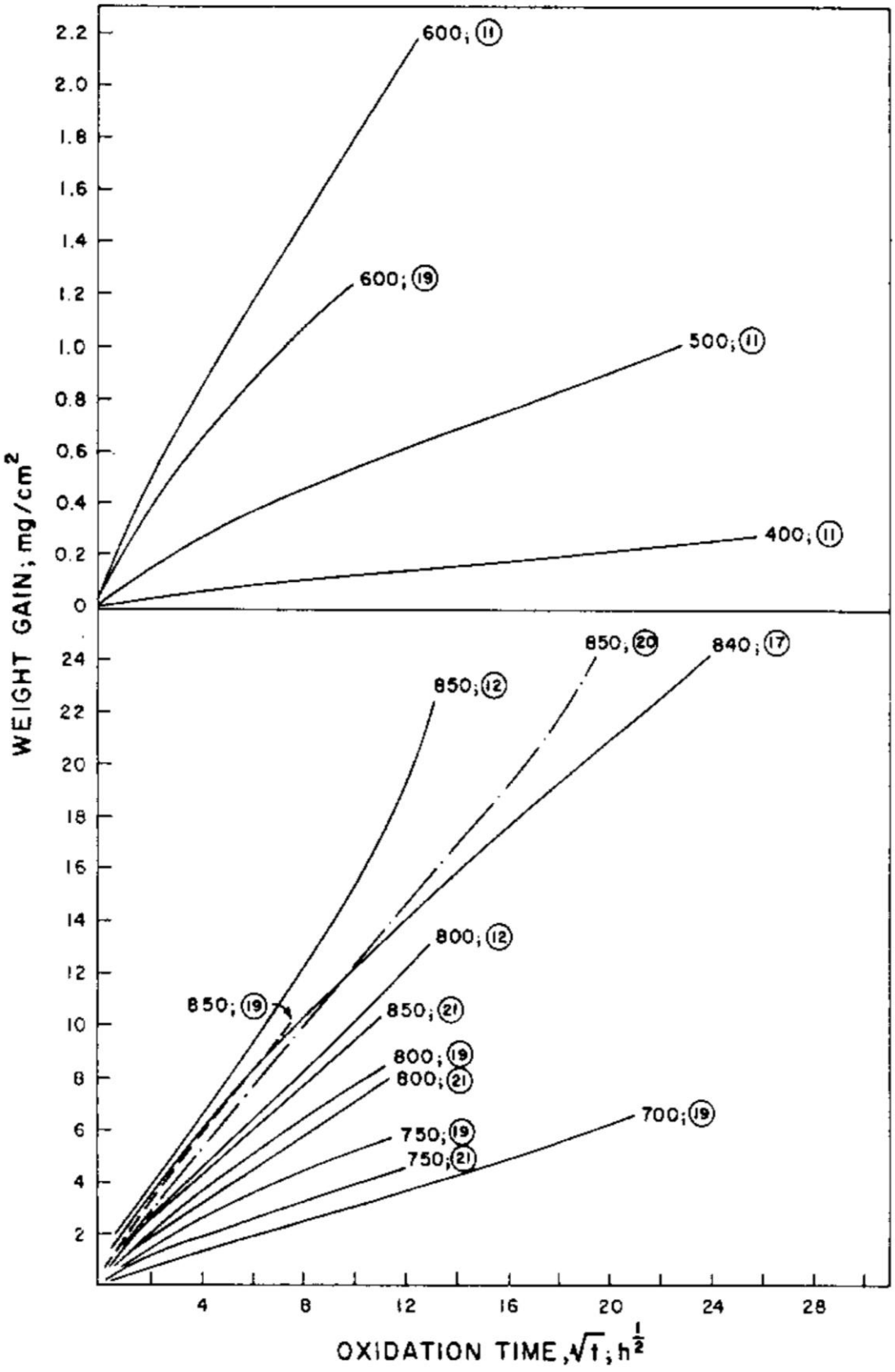
The oxidation rate has also been excessively studied, and can be expressed as

$$\Delta m=(K_c t)^{\frac{1}{3}} \cdot k_c t^{\frac{1}{3}} \qquad \text{(Equation 2.5)}$$

for the temperature range between 350 °C - 950 °C for abraded specimens, where Δm is the oxygen uptake per unit area, t is the oxidation time, K_c and k_c are the cubic rate constants. The parabolic relationship is applied for chemically polished samples, which can be expressed as

$$\Delta m=A+(K_p t)^{\frac{1}{2}}=A+k_p t^{\frac{1}{2}} \qquad \text{(Equation 2.6)}$$

where A stands for a constant, K_p and k_p are parabolic rate constants. It is believed that the smoother the surfaces, the slower the oxidation rate [84]. For example, it was found by Hussey and Schmeltzer [84, 85] that abraded samples and chemically polished samples oxidised at different rates, with the chemically polished sample showing less extent of oxidation. It was also found that annealed zirconium samples were oxidised at more rapidly than the un-annealed samples [84]. The oxidation kinetics data is plotted in Figure 2.3-2 for α-Zr (a) and β-Zr (b).


WEIGHT GAIN; mg/cm²
OXIDATION TIME, √t; h^½
600; (11)
600; (19)
500; (11)
400; (11)
850, (20)
840; (17)
850; (12)
800; (12)
850; (19)
850; (21)
800; (19)
800; (21)
700; (19)
750; (19)
750; (21)

(a)

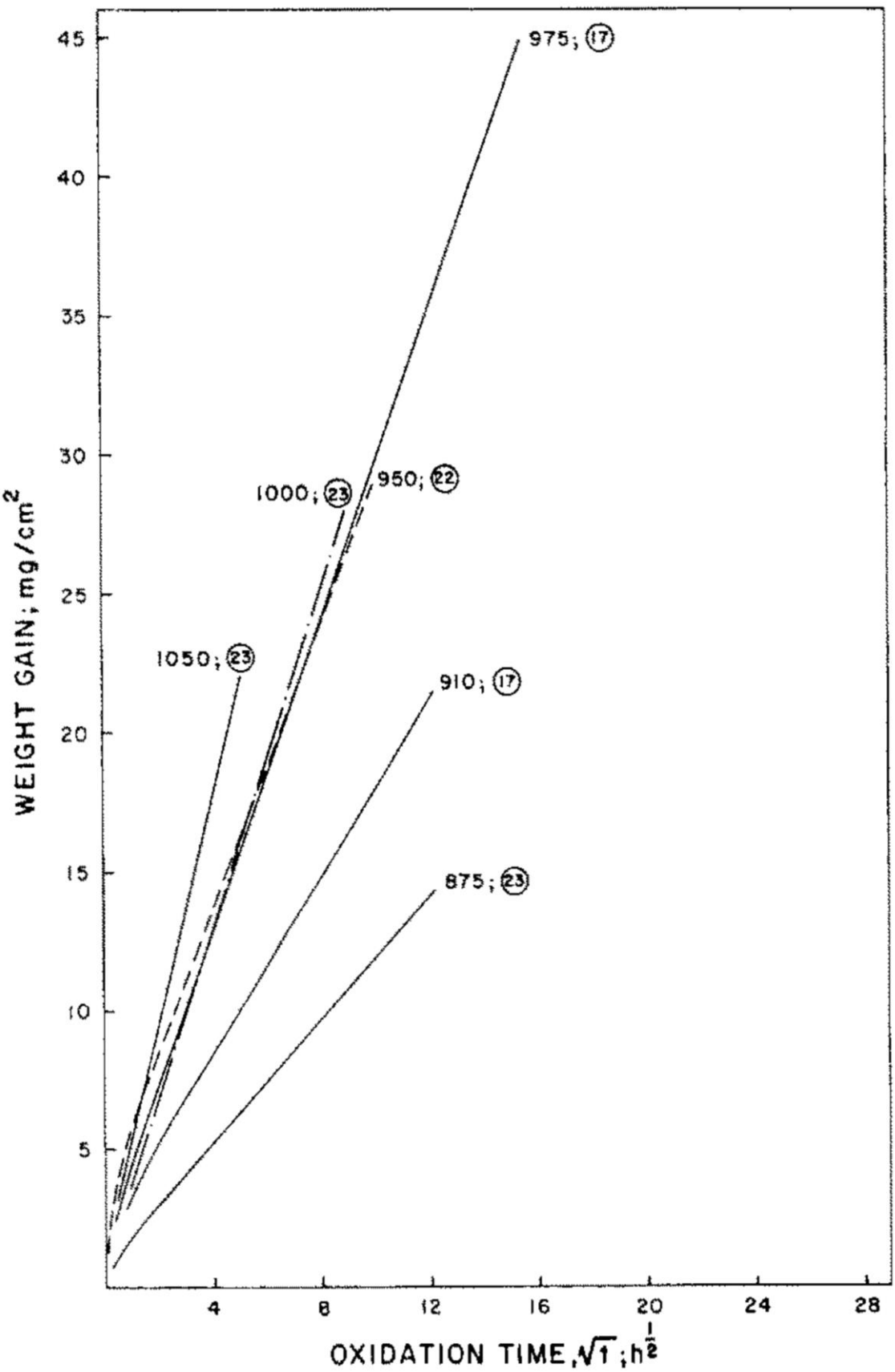


Figure 2.3-2 The Oxidation kinetics for α-Zr (a) and β-Zr (b) [84].

2.4 Ellingham diagrams

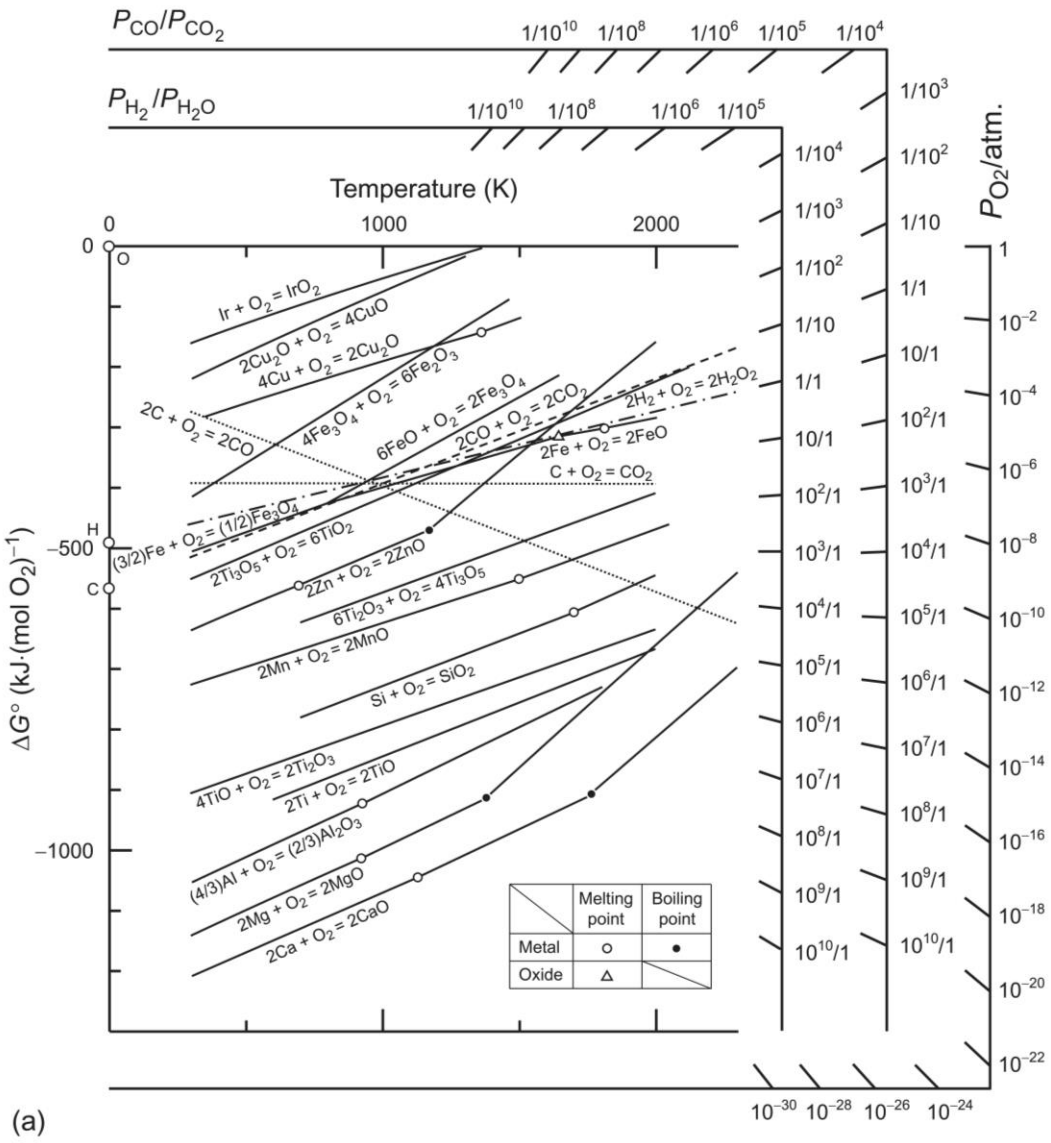
Based on the experimentally determined variations of standard Gibbs energy change of a compound (ΔG_f°), the diagrams (as shown in Figure 2.4-1) were constructed by Ellingham [86] in 1944 for oxides and sulphides revealing the approximate linear relationship between ΔG_f° and temperatures with no phase transformations occurred [87]. The ΔG_f° can be expressed as

$$\Delta G_f^\circ = \Delta H_f^\circ - T\Delta S_f^\circ \qquad \text{(Equation 2.7)}$$

where ΔH_f° is enthalpy change, and ΔS_f° is the entropy change and *T* is temperature. This expression can also be simplified by considering A and B as constants in a specified range.

$$\Delta G_f^\circ = A + BT \qquad \text{(Equation 2.8)}$$

where A is ΔH_f°, B is negative of ΔS_f° [87]. The Ellingham diagram assumes that there is enough oxygen in the environment to allow the reactions to take place [88]. The diagrams have been commonly used to determine the ease of the reduction from the metallic oxide to metal, and to determine equilibrium partial pressure of oxygen at a given temperature as well as the CO/CO_2 ratio needed for reduction. The stability of the oxide with temperature could be expressed via the position of the line. The higher position of the line indicates more noble metals and unstable oxides, resulting easier reduction to occur comparing those reactions located lower down in the diagrams. It also implies that a metal can reduce other metal oxides located above that line [89]. For example, as $Zr + O_2 = ZrO_2$ line is below $2Pd + O_2 = 2PdO$ line and having a big gap between the lines, which means that zirconium can effectively reduce PdO to metallic Pd.


P_{CO}/P_{CO_2}
P_{H_2}/P_{H_2O}
Temperature (K)
0
1000
2000
ΔG° (kJ·(mol O_2)$^{-1}$)
P_{O_2}/atm.
O
H
C
$Ir + O_2 = IrO_2$
$2Cu_2O + O_2 = 4CuO$
$4Cu + O_2 = 2Cu_2O$
$2C + O_2 = 2CO$
$4Fe_3O_4 + O_2 = 6Fe_2O_3$
$6FeO + O_2 = 2Fe_3O_4$
$2CO + O_2 = 2CO_2$
$2H_2 + O_2 = 2H_2O_2$
$2Fe + O_2 = 2FeO$
$C + O_2 = CO_2$
$(3/2)Fe + O_2 = (1/2)Fe_3O_4$
$2Ti_3O_5 + O_2 = 6TiO_2$
$2Zn + O_2 = 2ZnO$
$6Ti_2O_3 + O_2 = 4Ti_3O_5$
$2Mn + O_2 = 2MnO$
$Si + O_2 = SiO_2$
$4TiO + O_2 = 2Ti_2O_3$
$2Ti + O_2 = 2TiO$
$(4/3)Al + O_2 = (2/3)Al_2O_3$
$2Mg + O_2 = 2MgO$
$2Ca + O_2 = 2CaO$
Melting point
Boiling point
Metal
Oxide

(a)

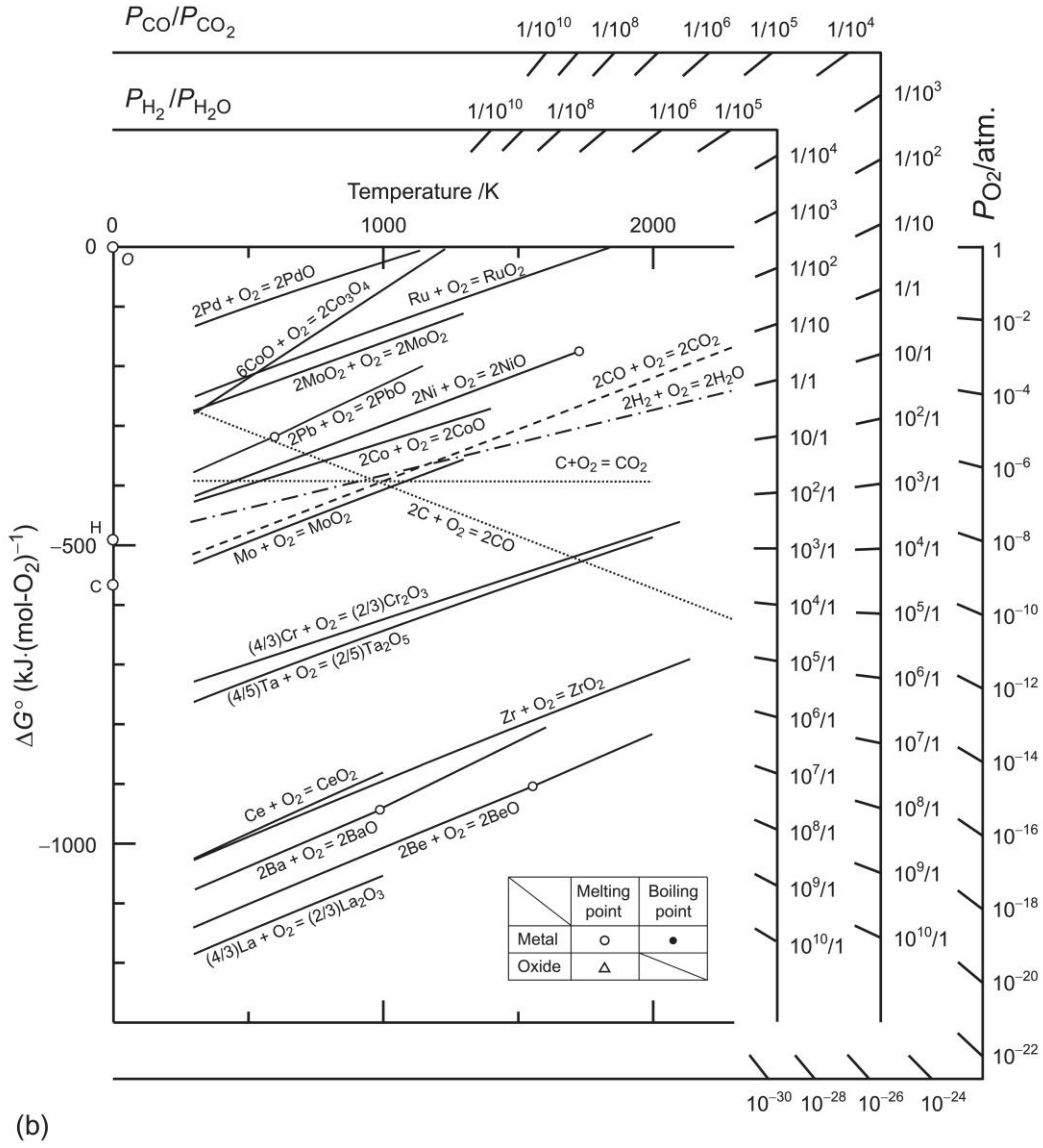


Figure 2.4-1 The Ellingham diagram for some oxides, showing the reactions of different metals. The open and solid circle refers to melting and boiling of the metals, whereas the open triangles are melting points of oxides [87].

The analysis from the Ellingham diagram is based on thermodynamics theory, without considering the reactions kinetics. The prediction of the ease of the reaction can sometimes end up with a slow reaction experimentally [88]. The Ellingham diagram can be particularly interesting and important in explaining the mechanism and reactions occurred during the catalytic ceramic conversion treatment (CCCT, or C3T) process, which will be further discussed in the later chapters.

2.5 Ceramic conversion treatment (CCT or C2T)

2.5.1 C2T

The surface ceramic conversion treatment (CCT) is the surface treatment method based on thermal oxidation. It is also named as C2T in order to distinguish it from C3T (catalytic ceramic conversion treatment), which will be introduced in the next chapter. The C2T technique was first developed for titanium and its alloys. The technique involves thermal treatment of the alloys to obtain the dense, oxide film on the top of the substrate and formed oxygen diffusion zone (ODZ) underneath. Onto the Ti6Al4V, a thin oxide layer of 1-2 μm can be grown (as shown in Figure 2.5-1 (a) [90]), which leads to significant improvements of tribological properties, anti-corrosion properties and biocompatible properties [90, 91, 92]. The surface hardness can be improved to 10.6 GPa from around 3.0 GPa for untreated Ti6Al4V [93]. The coefficient of friction can be reduced to less than 50% of the values of untreated sample under both dry and lubricated conditions for titanium alloys. The wear rate of the treated sample shows two orders magnitude reduction compared to the untreated ones. Galling occurred at low loads (6-18N) for untreated Ti6Al4V alloy but no galling observed even at a high load to 200N. The adhesive and abrasive wear of untreated sample changed to mild abrasive wear after the C2T process [94]. The significant improvements in these properties are primarily because of the formation of the oxide layer and ODZ for hardening the material.

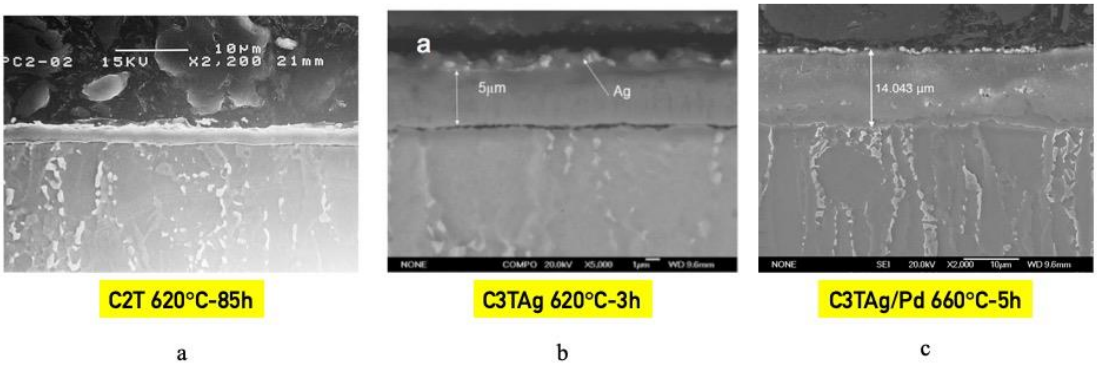


Figure 2.5-1 The surface cross sections of Ti6Al4V alloy after (a) C2T treated at 620 °C for 85 hours. (b) C3T (pre-deposition film of Ag) treated at 620 °C for 3 hours and (c) C3T (pre-deposition of Ag/Pd) treated at 620 °C for 5 hours [3, 90, 94, 95].

Recent research has applied the success of this technique from titanium alloys onto the zirconium alloys, based on the facts that both alloys share a range of similar properties and in the past research always compared two materials or studied them simultaneously. Ji et al. [43] has ceramic conversion treated the Zr702 and Zr705 alloys under 400°C-700 °C and with the different treatment time ranging from 3 hours to 30 hours. The oxide thickness obtained was measured to be between ~3 μm and ~30 μm depending on the treatment conditions (as shown in Figure 2.5-2). Among the treatment conditions used in this research, the higher treatment temperature and/or longer treatment duration formed thicker oxide layers. The wear resistance of the treated samples was tested in 3.5wt% NaCl solution, showing significant improvements after the CCT in most of the treatment conditions. The results have shown that the oxide layer formed on Zr705 alloy is thicker (almost double thickness, as shown in Figures 2.5-2 (a) and (b)) than the oxide layer on the Zr702 alloy for the same treatment conditions, and that the hardness of the Zr705 alloy is higher than that of the Zr702 alloy. This indicates the stronger response of Zr705 alloy to CCT

treatment, which can be explained by the presence of richer β phase due to the Nb content in Zr705 alloy providing a shortcut for oxygen diffusion. The Zr705 alloy surface was more effectively hardened compared to Zr702 alloy because of the formation of niobium oxide in the ZrO_2 in Zr705 [43].

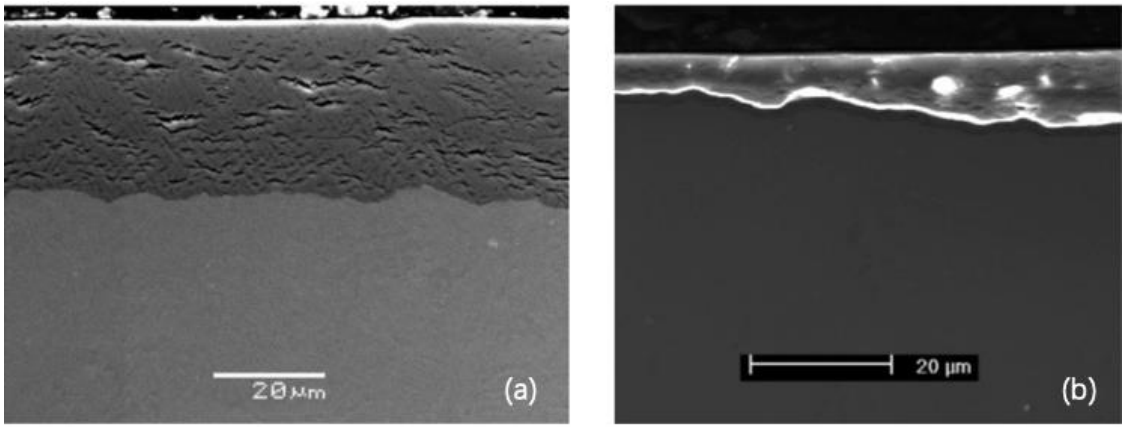


Figure 2.5-2 The cross-sectional SEM images of (a) Zr705 alloy treated under 600 °C for 30 hours (b) Zr702 alloy treated under 600 °C for 30 hours [43].

Zhang [2] has also applied the C2T approach to commercial grade Zr702 alloy and nuclear grade zircaloy-4. It was also found that the oxide layer thickness increased with the treatment temperature in the range of 400°C-800°C and duration from 10 hours to 200 hours. The enhanced properties are very similar to the findings on titanium alloys: the hardness was improved to 14 GPa-16 GPa depending on the types of alloys; about 50% reduction in coefficient of friction (CoF); improved corrosion resistance; and hundreds to thousands of times improvements in the wear resistance, as compared to the untreated zirconium alloys.

2.5.2 Catalytic ceramic conversion treatment (CCCT or C3T)

One of the major limitations of the C2T technique is that it requires a relatively long processing time period (50-200 hours) to obtain a reasonably thick ceramic layer for

tribological applications [2], which requires excessive energy consumption and is inefficient for the industrial production.

Recently, Alexander et al. [4] and Zhang et al. [3] have found that a pre-deposited thin Ag, Au or combinations of Ag/Pd layer could greatly speed up the CCT process of Ti6Al4V at 620 °C and other temperatures as well. The treatment time for the C3T process on Ti6Al4V alloy can be greatly reduced from 60-80 hours to only 8 hours at 620°C to generate a compact and hard surface oxide layer with excellent tribological properties. The oxide produced by C3T is much thicker (5-100 μm) than the layer thickness (1-2 μm) obtained from the C2T process (as shown in Figures 2.5-1 (b) and (c)). As the efficiency is enhanced, the C3T technique is promising for producing even better properties with significantly reduced treatment time and energy consumption, and therefore is more feasible for industrial applications. For example, for the anti-bacterial efficacy, it is reported the C2T treated Ti64 samples produced 50% reduction in CFUs (average number of viable colony-forming units) whereas the Ag C3T treated sample produced 93% compared with the untreated ones [4].

Research by Chen and Goodman [96] proposed that gold is able to activate the oxygen directly due to structural effects and support effects. The bilayer structure of gold was found to be more active in catalytic oxidation than the monolayer structure of gold, which fully wets (covers) the oxide support. In addition, research by Behm et al. [97] reported the linear relationship of the total surface oxide with the oxide support/Au nanoparticles interfacial peripheral sites number, indicating support in the gold interface as oxygen can play a leading role in activation. The pre-deposition of a combination of two elements, such as vanadium with silver, can produce a synergetic

effect in accelerating the formation of a good quality surface oxide layer on CP-Ti [98].

However, there is still a knowledge gap on applying the C3T technique to zirconium-based alloys and the optimal conditions (i.e. most effective pre-deposited layer, treatment temperatures and treatment time) for the C3T of Zr alloys still need to be investigated, which has directed the aims and purposes of this PhD study.

2.6 Summary

Zirconium and its alloys are widely used in the areas of nuclear industry, medical industry and chemical process due to their excellent properties including non-toxicity, low neutrons absorption cross section, high corrosion resistance and excellent biocompatibility. However, the technical limitations of low hardness, low wear resistance and high friction of zirconium and its alloys are barriers for their wider uptake. Although some surface engineering methods such as physical vapour deposition (PVD) and surface modification approaches have been investigated, limited progress has been made to meet the challenging requirements for effectively improved tribological and corrosion properties with minimum post-machining and high cost-effectiveness.

The ceramic conversion treatment method could produce an oxide layer on top of the Zr alloys with an oxygen diffusion zone (ODZ) formed underneath, which has contributed to the improved hardness, wear resistance and corrosion properties. However, this method requires long treatment time and only very thin adherent oxide

layer can be produced, and consequently it is characterised by high energy consumption and low production efficiency. By pre-deposition a thin metal film onto the titanium alloy, the oxidation process can speed up, and the dense and thick oxide layers can be formed.

As titanium and zirconium are both group 4 elements on periodic table and shares similar properties but no literature has reported on applying new C3T technique to zirconium-based alloys. Therefore, a comprehensive study on transferring the catalytic ceramic conversion treatment technique onto the zirconium alloys substrate is needed, which forms the aims of this PhD research to develop and to study the C3T of Zr alloys, for the purpose of enhancing the corrosion, tribological and wear properties.

Chapter 3. Experimental methodology

3.1 Materials selected and sample preparation

To avoid influence of Nb content on the oxidation behaviour[43], a Nb free commercial grade Zr702 alloy (also known as commercial purity Zr alloy or simplified as CP Zr) was selected as the substrate material for this research. The chemical compositions of Zr702 alloy are listed in Table 3.1-1. The samples were cut from a Zr702 alloy bar (24mm in dimeter) using the Struers Accutom-50 cutting machine (Rotherham, UK) to coupons of 4.5 mm in thickness followed by grinding with abrasive SiC papers from grade 240 to grade 1200. The samples were cleaned with soapy water and acetone in an ultrasonic bath.

Table 3.1-1: The chemical composition (wt%) of Zr 702 alloy.

Element / Material	Zr+Hf, max	Hf, max	Fe+Cr, max	C, max	O, max
Zr702	99.2	4.5	0.20	0.05	0.16

3.2 Catalytic ceramic conversion treatment (C3T)

3.2.1 Pre-deposition of thin catalytic films

Thin films of various elements or combinations were deposited on the surface of each sample prior to the catalytic ceramic conversion treatment (C3T). For comparison purpose, no thin film was pre-deposited on the surface of some samples prior to the C2T surface treatment. These films of silver (Ag), vanadium (V), palladium (Pd) or the combinations Ag/V, Ag/Pd was obtained by physical vapour deposition (PVD) via

the Close Field Unbalanced Magnetron Sputtering Ion Plating Equipment (Teer Coating Ltd., Worcestershire, UK). The sputtering targets of specific elements (Ag, V and Pd) were installed and the samples were placed on the sample holder as shown in Figure 3.2-1. The sputtering process was carried out in an evacuated environment. The target current/deposition time were 1A/3min, 1.5A/5min and 1A/3min for Ag, V and Pd targets respectively. The gold (Au) thin film was obtained by using the Emscope SC 500 (Hertfordshire, UK) sputter coater with a current of 25 mA for 180s. The layer thickness of the pre-deposition film was controlled to be in the range of 50-500 nm by adjusting the deposition time.

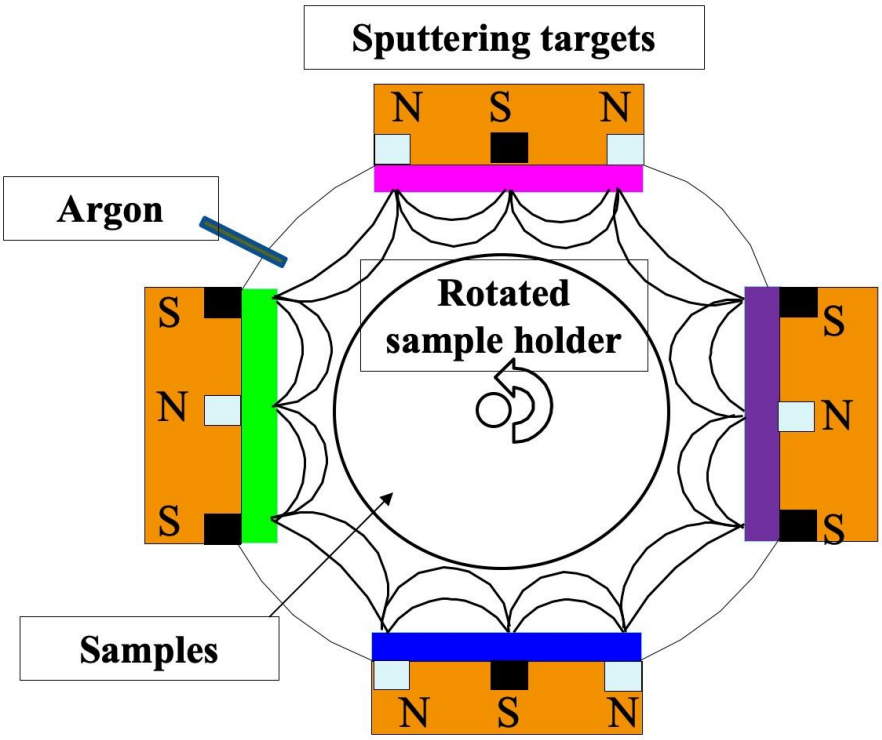


Figure 3.2-1 The Close Field Unbalanced Magnetron Sputtering Ion Plating Equipment (Teer Coating Ltd.) set up [99].

3.2.2 Ceramic conversion treatment

The Ag, V, Pd, Ag/V, Ag/Pd and Au pre-deposited (for C3T) and un-coated (for C2T) samples were placed in the Muffle furnace (Elite Thermal Systems Limited,

Leicestershire, UK) for ceramic conversion treatment. As introduced in the previous sections, the pre-deposited layers could act as the catalyst to accelerate the oxidation of Zr based alloys. To investigate the catalytic effects of these pre-deposited films and the temperature dependence, these samples were treated at temperatures of 450, 500, 550 and 600 °C for a fixed treatment time of 10 hours as shown in Table 3.2-1. Based on the initial results from these samples, which will be further explained in the later sections, Ag and V pre-deposited samples were selected for treatment in longer time (20 hours, 40 hours and 60 hours) and Au pre-deposited samples were selected for shorter (5mins, 5 hours) and longer (20 hours and 40 hours) time treatments to further investigate the catalytic effect of gold. The heating ramp rate for all treatments was 8 °C/min and the samples were cooled down in the furnace once the treatment finished. All the samples and the treatment conditions are listed in Table 3.2-1. The code of the C3T treated samples started with the catalytic element(s) followed by treatment temperature and time. For example, the code Au6040 stands for C3TAu treated at 600 °C for 40 hours. The only exception is for the short-time (5 min or 0.08 hours) and 600 °C C3TAu treated sample the code is Au6000. The samples without any surface treatment are named as untreated sample, simplified as Unt. The samples with no pre-deposition layer but ceramic conversion treated is named as C2T samples. The Unt and C2T samples provide the reference for comparisons of C3T treated samples, especially understanding the catalytic effects of pre-deposition layers and the properties enhancement.

Table 3.2-1: Treatment conditions and the sample codes.

Different pre-deposition layer, different temperatures, same treatment time (10 hours)				
Sample info	Pre-deposition	Temperature/°C	Time/hours	Sample Codes
C3TAg	Ag	450, 500, 550, 600	10	Ag4510, Ag5010, Ag5510, Ag6010
C3TV	V	450, 500, 550, 600	10	V4510, V5010, V5510, V6010
C3TPd	Pd	450, 500, 550, 600	10	Pd4510, Pd5010, Pd5510, Pd6010
C3TAg/V	Ag/V	450, 500, 550, 600	10	AgV4510, AgV5010, AgV5510, AgV6010
C3TAg/Pd	Ag/Pd	450, 500, 550, 600	10	AgPd4510, AgPd5010, AgPd5510, AgPd6010
C3TAu	Au	450, 500, 550, 600	10	Au4510, Au5010, Au5510, Au6010
C2T	None	450, 500, 550, 600	10	C2T4510, C2T5010, C2T5510, C2T6010
Unt	-	-	-	Unt
Same pre-deposition layer, same temperature (600 °C), different treatment time				
C3TAg	Ag	600	10, 20, 40, 60	Ag6010, Ag6020, Ag6040, Ag6060
C3TV	V	600	10, 20, 40, 60	V6010, V6020, V6040, V6060
C3TAu	Au	600	0.08 (5 mins), 5, 10, 20, 40, 60	Au6000, Au6005, Au6010, Au6010, Au6040, Au6060
C2T	None	600	0.08 (5 mins), 5, 10, 20, 40, 60	C2T6000, C2T6005, C2T6010, C2T6010, C2T6040, C2T6060

3.3 Microstructure characterisation

3.3.1 Specimen preparation

After surface treatment (C2T and/or C3T), the samples were cut using the Struers Accutom-50 from the treated surfaces of the coupon samples to prepare for the specimens for microstructure characterisation. The cut pieces were then mounted in conductive Bakelite using the OPAL 480 hot mounting press machine for the SEM examination of the cross-sectional layer structure. The mounted samples were ground with abrasive SiC papers from grade 240 to grade 2500 and polished with the diamond suspensions on the MD-Mol and MD-Chem polishing cloth. The grinding and polishing processes, which includes the three major steps of plane gridding (PG), fine grinding (FG) and oxide polishing (OP), is outlined in Table 3.3-1. The samples were cleaned with soapy water and acetone in an ultrasonic bath after each step.

Table 3.3-1: The sample grinding and polishing process.

Step	Plane Grinding (PG)	Fine Grinding (FG)	Oxide Polishing (OP)
Surface	Silicon carbide paper	MD-Mol	MD-Chem
Abrasive Type Size	Silicon carbide	Diamond 3 microns	Colloidal Silica
Suspension	Water	DP suspensions	Activated colloidal for final polishing
Speed, rmp	300	150	150
Force, N	40	150	60
Time, min	Grade 2500 until Plane	10	5

3.3.2 Surface morphology observation and roughness measurement

The microstructure of the as-received material was observed using the Helios PFIB G6 Field Emission SEM (FE-SEM). The surface morphology of the treated samples was observed visually under Scanning Electron Microscopes (SEMs) via FEI Quanta 3D FEG FIB-SEM and TF Apreo 2S HiVac, Hitachi TM-3030 and Jeol 7000F. The selection of above SEMs was based on the information and images to obtain, i.e. Hitachi TM-3030 was used mainly for instant observation of the surface layer and the TF Apreo 2S HiVac was used to obtain colour chem SEM images. All the SEMs are equipped with EDX (Energy dispersive X-ray spectroscopy) for chemical compositions analysis. The surface layer examinations, wear tested samples including the counterparts (WC-Co balls) and the surface of the selected samples after the corrosion test (which will be explained in later section) were also studied using the SEM/EDX.

The Ambios XP-200 stylus profilometer (USA) was used for surface roughness measurement. The surface roughness values R_a (arithmetic average roughness) and R_t (data points range) were measured before and after the treatment, and the average values of three measurements were recorded and reported. The standard error was calculated and used for error bars. The differences between R_a and R_t are demonstrated in Figure 3.3-1. The arithmetical mean R_a value could not represent the individual peaks or valleys, and therefore measuring both R_a and R_t values could give more comprehensive information on the roughness values and distribution [100].

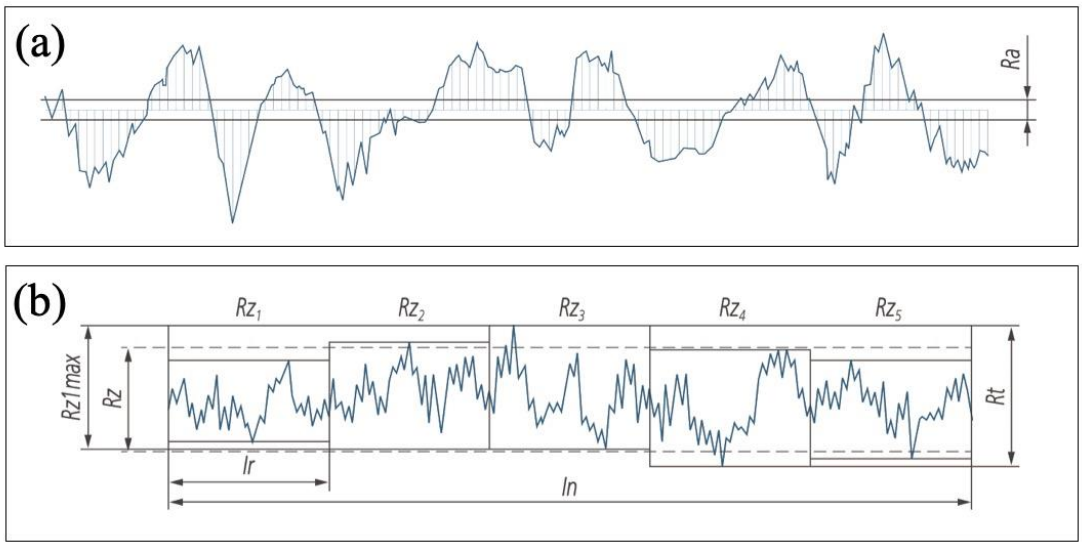


Figure 3.3-1 The Differences between arithmetic average roughness value R_a (a) and data points range R_t (b), where R_z represents mean roughness depth and R_{z1max} represents maximum roughness depth [100].

3.3.3 X-ray diffraction (XRD) phase identification

The collimated beam of X-rays is diffracted by the crystalline phases in XRD based on the Bragg's law, which can be expressed as

$$2d\sin\theta=n\lambda \qquad \text{(Equation 3.1)}$$

d is the spacing between diffracting planes, θ is the incident angle, *n* is diffraction factor, and λ is the wavelength of the X-ray beam [101]. The XRD was used in this research to identify the crystalline phases after the C2T/C3T oxidation process. The samples were all characterised via X-ray diffraction (XRD) scans (Normal Scan Mode – coupled, 2θ ranges from 10°to higher 2θ positions i.e. 80°) using the Proto AXRD (Wrocław, Poland) device. The HighScore [102] software (Malvern Panalytical Ltd., UK) was used to analyse and identify the phase constituents.

3.3.4 TEM

Some selected samples were further prepared for characterisation under Transmission Electron Microscopy (TEM) for crystal structural and microstructural information. As very thin samples are required in TEM for better spatial resolution in TEM imaging, the samples were prepared in the multiple stages as shown in Figure 3.3-2. The treated samples were cut using a Struers Accutom-50 from the top of the treated surface and the side, so that multiple slats in dimensions of 1 mm × 0.5 mm × 3mm containing parts of the treated surface were taken from the original treated samples. Two slats were then glued together using G-1 epoxy by placing the treated surface facing each other. By gluing together, the two slats could be ground to thin slide at the same time in the next stage and the glue could provide the protection of the treated surface in the following grinding process to avoid the treated surface (i.e., coating) to be removed accidentally. The glued slabs were manually ground on the abrasive SiC paper grade 1200 with the grinder (Gatan Inc.) from the cross-sectional direction to ensure the thickness was ground from 0.5 *mm* to less than 50 μm (at the point the corners of the slabs started fading). A vernier calliper was used during and after the grinding process to check the thickness. The glued slabs were then cleaned and detached by soaking in acetone to separate the two thin slides. The separated thin slides were then transferred to the focused ion beam (FIB, FEI Quanta 3D, USA) for milling to a thickness less than 100 *nm* before TEM analysis. The Joel 2100 electron microscope (LaB6, 200 kV, Japan) was employed for the TEM imaging. The TEM (STEM) mode of GEI Philips Tecnai F20 instrument (FEG, 200 kV, USA) was used for high angle annular dark field (HAADF) imaging and EDX analysis.

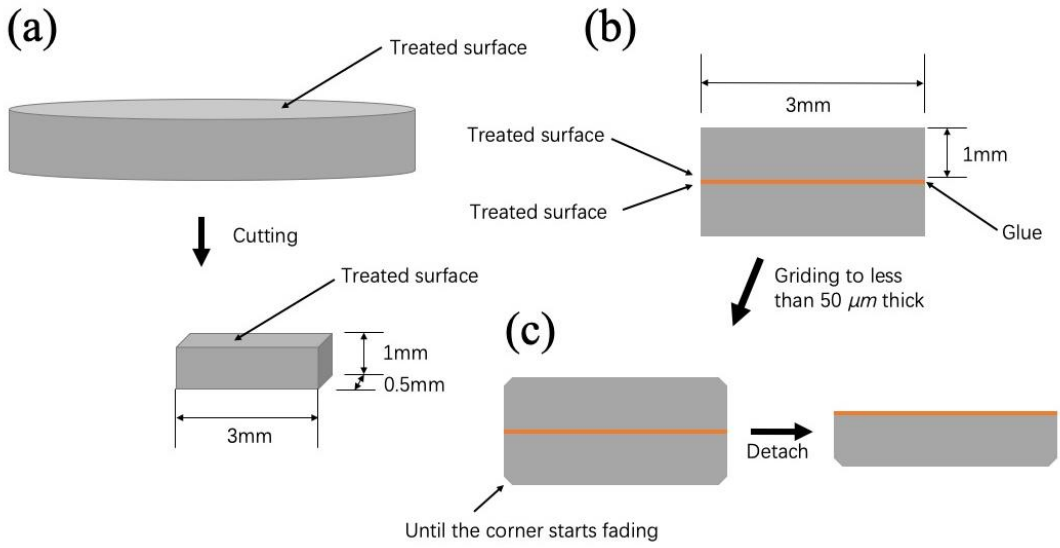


Figure 3.3-2 The further sample preparation procedure for TEM characterisation.

3.3.5 Surface layer structure analysis

The prepared cross-sectional samples were characterised under the FEI Quanta 3D FEG FIB-SEM, Hitachi TM-3030 and Jeol 7000F Scanning Electron Microscopes (SEMs) equipped with energy-dispersive X-ray spectroscopy (EDX, Oxford), to obtain the information including oxide layer thickness, layer structures (including compositional measurements of the sample via EDX point ID, line scans and mapping) and the quality of the surface layers. The *Image J* software was used to measure the layer thickness of the cross-sectional samples, and the average value of five measurements are reported. The standard error was calculated and used for error bars.

The oxygen content profile along the depth of selected sample after the ceramic conversion treatment process was further studied via the glow-discharge optical emission spectroscopy (GDOES) using the GDA 650 HR analyser (Spectruma

Analytik GmbH, German). The direct current (DC) mode (1000 V, 14 mA) was selected to operate the test under an argon working gas environment at 335 Pa. The collected data was calibrated based on the crater depth measurements obtained using the Ambios XP-200 stylus profilometer and analysed via the WinGDOES 5.0 software based on its built-in database.

3.4 Corrosion testing

The corrosion behaviour of untreated and C2T/C3T treated samples was evaluated using electrochemical testing as it is a fast and sensitive process for corrosion measurement. The test kits and interface 1000-06014 from Gamry Instruments (USA) were used for this three-electrode electrochemical test. The electrolyte used in this test is 3.5wt% sodium chloride (NaCl) aqueous solution, which was prepared more than 24 hours before the corrosion test by mixing 35g of NaCl salt with 965 mL deionised water in the volumetric flask. Before the test, the corrosion cell was cleaned with running water and deionised water. The testing kits including the corrosion cell were dried before the start if the test to avoid the current overload during the test.

The test kits set up including the electrode connection is shown in Figure 3.4-1. The platinum coated rod, i.e., the counterpart electrode (CE), and Saturated Calomel (Hg_2Cl_2) reference electrode (RE) were immersed into the testing electrolyte filled in the testing corrosion cell where the RE was positioned very close to the working electrode (WE). The working electrode (WE) was connected to the tested sample by placing the sample below the corrosion cell filled with the testing electrolyte, so that

the sample surface is exposing to the testing electrolyte with a tested area of 0.503 cm^2. The Open Circuit Potential (OCP, or E_{OC}) represents the potential difference of the WE and RE in the electrolyte and is the 'starting point' for the electrochemical corrosion. The E_{OC} needs to be stable to ensure that the corroding system is at the steady state before the test begins. Longer OCP time allows the sample to stabilise in the corrosive environment, and thus more likely the OCP is steady before the potentiodynamic polarisation scan starts. In each test of this research, the OCP was run for 1800s and reached the steady state prior to the potentiodynamic polarisation scans. If the OCP was found to not be steady near the end of 1800s, the test was stopped and restarted. The range for the potentiodynamic polarisation scans was from -0.5 V vs. E_{OC} to 1.5 V vs. E_{OC}, with a scan rate of 1 mV/s. In this mixed potential system, the potential and current relationship can be presented as the Bulter-Volmer Equation, which is:

$$I=I_a+I_c=i_{corr}(e^{(2.3(E-E_{OC})/\beta_a)}-e^{(-2.3(E-E_{OC})/\beta_c)})$$

(Equation 3.2)

where I is the cell current (A), E is the applied potential (V), β_a and β_c are the anodic and cathodic Tafel constants (V). The graphical representation of the Bulter-Volmer Equation is so-called the Tafel curves. By applying the Tafel fit to the polarisation curves using the Gamry Echem Analyst software, the corrosion current i_{corr} was measured from the Tafel curves obtained in the test and the corrosion rate (in the unit of milli-inches per year, mpy) can be calculated from i_{corr} via the following equation [103]:

$$\text{Corrosion rate (mpy)}=0.13I_{corr}(\mu A/cm^2)(EW)/d$$

(Equation 3.3)

$$I_{corr}=i_{corr}/A \qquad \text{(Equation 3.4)}$$

Where I_{corr} is the corrosion current density in $\mu A/cm^2$, A is the area in cm^2, EW is equivalent weight, d is the density g/cm^3 [103]. The test was operated at room temperature (20 °C) and repeated for no less than three times to ensure the reliability and repeatability of the data obtained. After each test, the sample and the corrosion cell were cleaned with deionised water and dried. The tested samples were later observed under the SEM/EDX for corrosion features (i.e., pitting and crevice corrosion) on the sample surface.

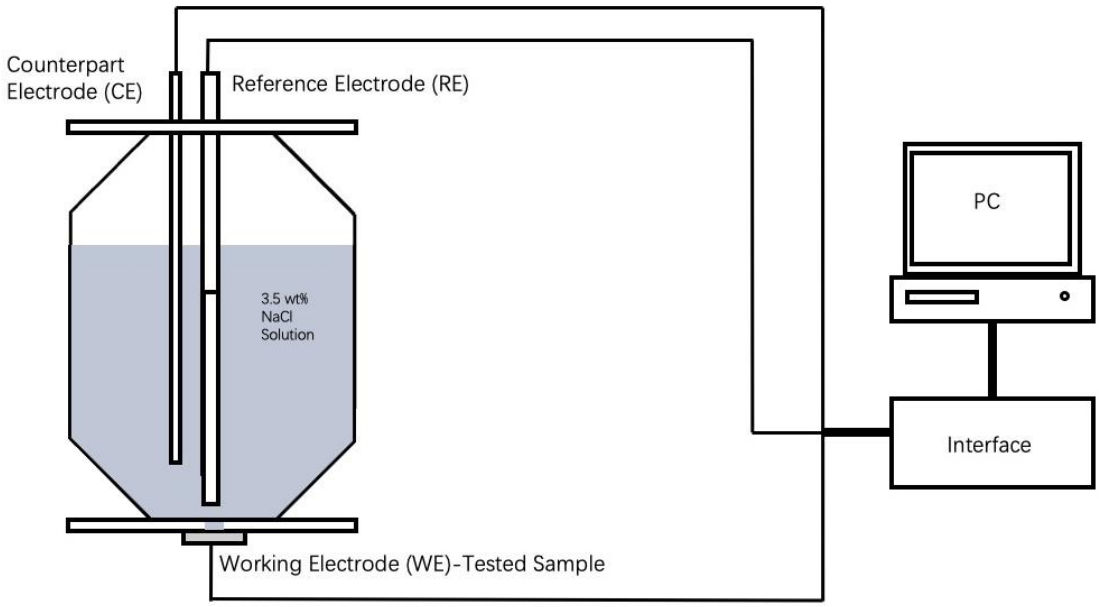


Figure 3.4-1 The schematic draw of the electrochemical test set up.

3.5 Hardness and tribological properties evaluation

3.5.1 Hardness

The surface hardness of the treated samples was measured by the Mitutoyo MVK-H1 Vickers microhardness tester (Japan) and Zwick/Roell hardness tester (Germany) under the load of 50 g and 100 g, with a few tests using 25g load. The standard block (757.3HV0.3) was used first to confirm the calibration. The angle of the diamond indenter is 136°, the d_1 and d_2 are the length of the diagonal of the indents as shown in

Figure 3.5-1. The Vickers microhardness could be therefore calculated based on the following equations:

$$d=\frac{d_1+d_2}{2} \qquad \text{(Equation 3.5)}$$

$$HV=\frac{F}{A}==0.1891\frac{F}{d^2} \qquad \text{(Equation 3.6)}$$

where d is the average length of d_1 and d_2, F is the applied force and A is the surface area. The Vickers hardness values are generally reported in the form of xxHVyy, where xx is the hardness number, HV is the hardness scale and yy is the load in *kgf*. The test is repeated and the average value of five indents are reported. The standard error was calculated and used for error bars.

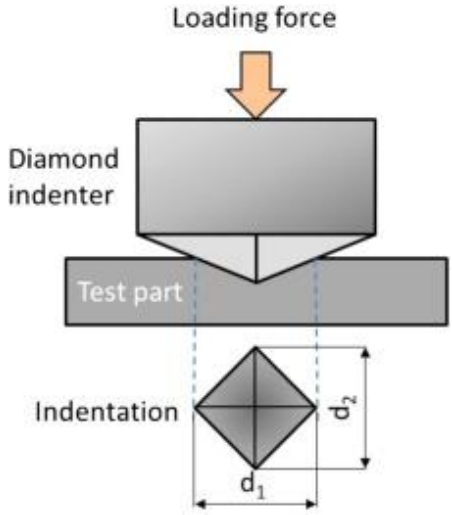


Figure 3.5-1 The Vickers hardness measurement [104].

The Nanoindentation was conducted using the NanoTest Vantage nanoindentation machine (Micro Materials Ltd, UK) with a pyramid Berkovich indenter for selected samples to investigate the hardness variations along the depth of the ceramic conversion treated samples.

3.5.2 Tribological testing

Both friction tests and wear tests were performed under the dry/unlubricated condition. Both tests were repeated at least twice to ensure the reliability and repeatability of the data obtained.

The friction behaviour of the both the treated and untreated samples was investigated by the Phoenix TE-79 multi-axis tribology machine (UK). A tungsten carbide ball (8mm in diameter) acted as the counterpart to slide against the surface of the sample mounted on the sample holder, with the applied load of 20N for 1000 cycles. The counterpart and the sample holders were cleaned with acetone prior to the tests. The sliding stroke was 5 mm and the sliding speed was 5 mm/s. The coefficient of friction (CoF) vs number of cycles graph was obtained via the Compend 200 software and the average CoF value was calculated.

A homemade reciprocating sliding wear tester was used for the wear tests as it could apply larger loads compared to the Phoenix TE-79 multi-axis tribology machine. A tungsten carbide ball (12mm in diameter) was used as the counterpart in the wear tests (as shown in Figure 3.5-2) under the load of 21N and 45N for 3600 cycles (equivalent to 30 mins) with sliding stroke of 5 mm. The wear tracks were 2D scanned via the Ambios XP-200 stylus profilometer in the direction which is perpendicular to the sliding direction, to obtain the 2D graph and the wear area value (in μm^2). The scans were repeated for three times and the average wear area was calculated and reported. The standard error was calculated and used for error bars. The wear factor (i.e., wear rate) k (in $m^3/m \cdot N$, 10^{-16}) of the samples was calculated according to the following equation:

$$k=\frac{V}{F\cdot s}=\frac{5000A}{18F\times 100} \qquad \text{(Equation 3.7)}$$

where A is the wear area (μm^2), F is the applied load (N), V is the wear volume and s is the sliding distance. The worn surface and the counterpart were further characterised under SEM observation and EDX analysis for revealing the wear features and wear mechanisms.

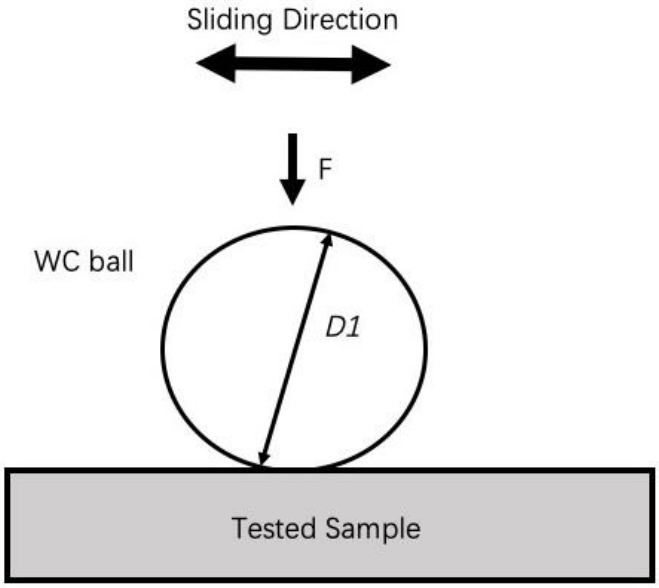


Figure 3.5-2 The schematic draw of the reciprocating wear tests.

3.5.3 Corrosion wear test

In addition to the electrochemical corrosion test and the reciprocating wear tests, the reciprocating wear tests were also performed in 3.5wt% NaCl solution to investigate the corrosion-wear resistance of the treated samples under the wet conditions to simulate wear in presence of sea water and for possible future biomedical applications in the body. The test was performed on the homemade reciprocating sliding wear tester with the same conditions for the reciprocating wear tests above but only tested under a normal load of 21N. As shown in Figure 3.5-3, a pipette dropper was used to

continuously adding the solution, to ensure the sample surface and the counterpart were fully immersed in the solution throughout the test. Each test was operated for 30 mins (3600 cycles). The wear area and wear rates were measured and calculated using the Ambios XP-200 stylus profilometer and the wear rate was evaluated with Equation 3.7. Data obtained was also compared with the wear data obtained under dry conditions. The wear tracks and the counterparts were characterised under SEM and EDX for understanding wear features and wear mechanisms.

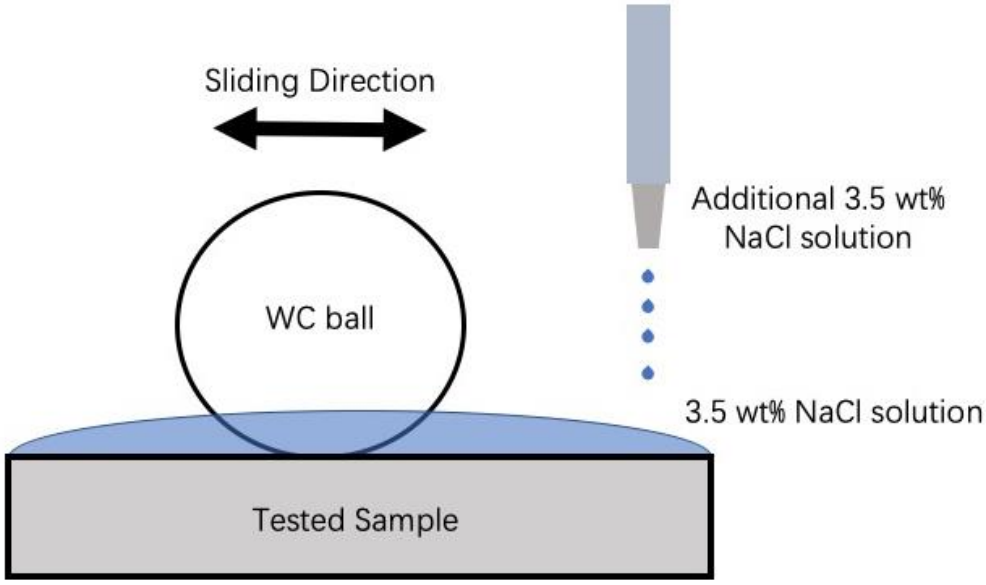


Figure 3.5-3 The schematic draw of the corrosion wear tests.

Chapter 4. Results

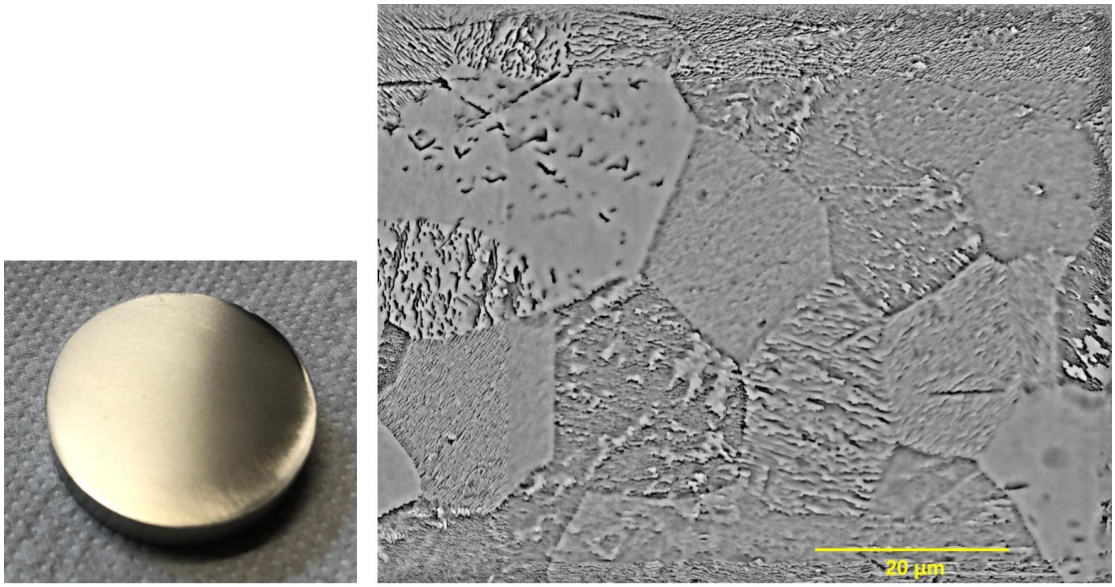
In this chapter, the results will be reported in the following sections. The microstructure of the as-received materials and the initial characterisation outcomes for the screening of the C3T treatments including visual observation, SEM morphology, weight change, surface roughness, and phase constituents of Zr702 alloy are reported in Section 4.1. More detailed microstructure characterisation results, i.e., surface layer structures, XRD and TEM results, of the selected samples are reported in Section 4.2, demonstrating the impact of pre-deposition elements and treatment duration on the catalytic effects. The corrosion test results are presented in Section 4.3. Section 4.4 presents the mechanical and tribological properties, which includes hardness, coefficient of friction, and the wear properties under different wear conditions.

4.1 Pre-screening of catalytic ceramics conversion treatment

The microstructure of as-ground Zr702 and the samples after the pre-deposition of the elements were examined and analysed in the first stage. Samples were also analysed after the ceramic conversion treatment comparing with the pre-deposited Zr702 samples from the first stage to provide some initial information, to identify the optimal pre-deposition (i.e., single element deposition vs. duplex co-deposition) and treatment conditions (optimal treatment temperature and duration) for more in-depth systematic studies.

4.1.1 Microstructure of as-received Zr702

As shown in Figure 4.1-1 (a), the untreated Zr702 sample appears in the colours of light and shining grey. The microstructure of the Zr702 sample was observed more closely under SEM imaging after milling using the Plasma FIB (PFIB) (Figure 4.1-1b)), revealing the small near-equiaxed grains in the microstructure with the grain size of about 15 µm.



(a) (b)

Figure 4.1-1 The observation of (a) as ground Zr702 alloy visually, and (b) the PFIB milled Zr702 alloy sample under the SEM revealing its microstructure.

4.1.2 Surface morphology

One as-ground Zr702 alloy sample was partially covered by a conductive tape before the pre-deposition of Au, and the colour change of due to Au deposition on the Zr702 surface can be clearly seen on the sample surface after the conductive tape is removed. The pre-deposition of Au on the Zr702 changed from the light and shinning grey colour (left) to the goldish and greenish colour (right) as shown in Figure 4.1-2

(a). The ceramic conversion treatment changes the goldish and greenish colour to darker golden colour with no presence of the light green colour anymore, which is shown in Figure 4.1-2 (b) (right). The left part of Figure 4.1-2 (b), with no pre-deposition before the treatment, shows a colour change to the darker grey colour.

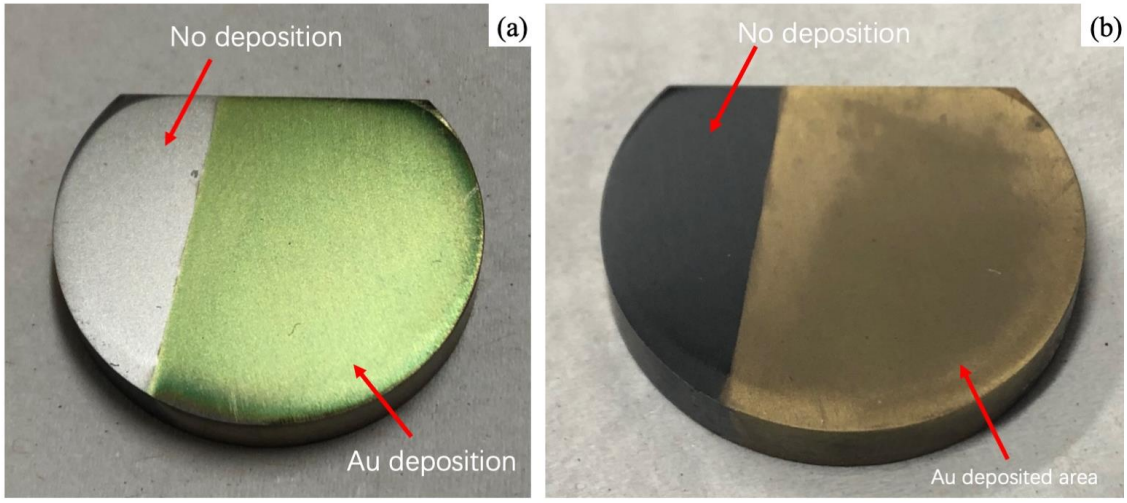


Figure 4.1-2 The visual observation of (a) as ground (left), and Au pre-deposited (right) of Zr702 alloy; and (b) no pre-deposition (left) and Au pre-deposited (right) and then ceramic conversion treated sample surface.

As shown in Figure 4.1-3, the ceramic conversion treatment has changed the colour of these samples depending on the pre-deposited elements (Ag, V and Pd) and the treatment temperature. When treated at a low temperature of 450 °C for 10 hours, the colour of the C3T treated surfaces depends on the type of the pre-deposited elements. The Ag, V and Pd pre-deposited samples appeared a silver grey, shinning purple and navy-blue colours respectively as shown in Figure 4.1-3. However, these colours start to fade when treated at 500 °C and disappeared completely when treated at the even higher temperature (550 °C and 600 °C), leaving only the dark grey colour for all the samples. No significant change of colour can be observed for the samples without any pre-deposition after C2T for 10h at different temperatures ranging from 450 °C to 600 °C.

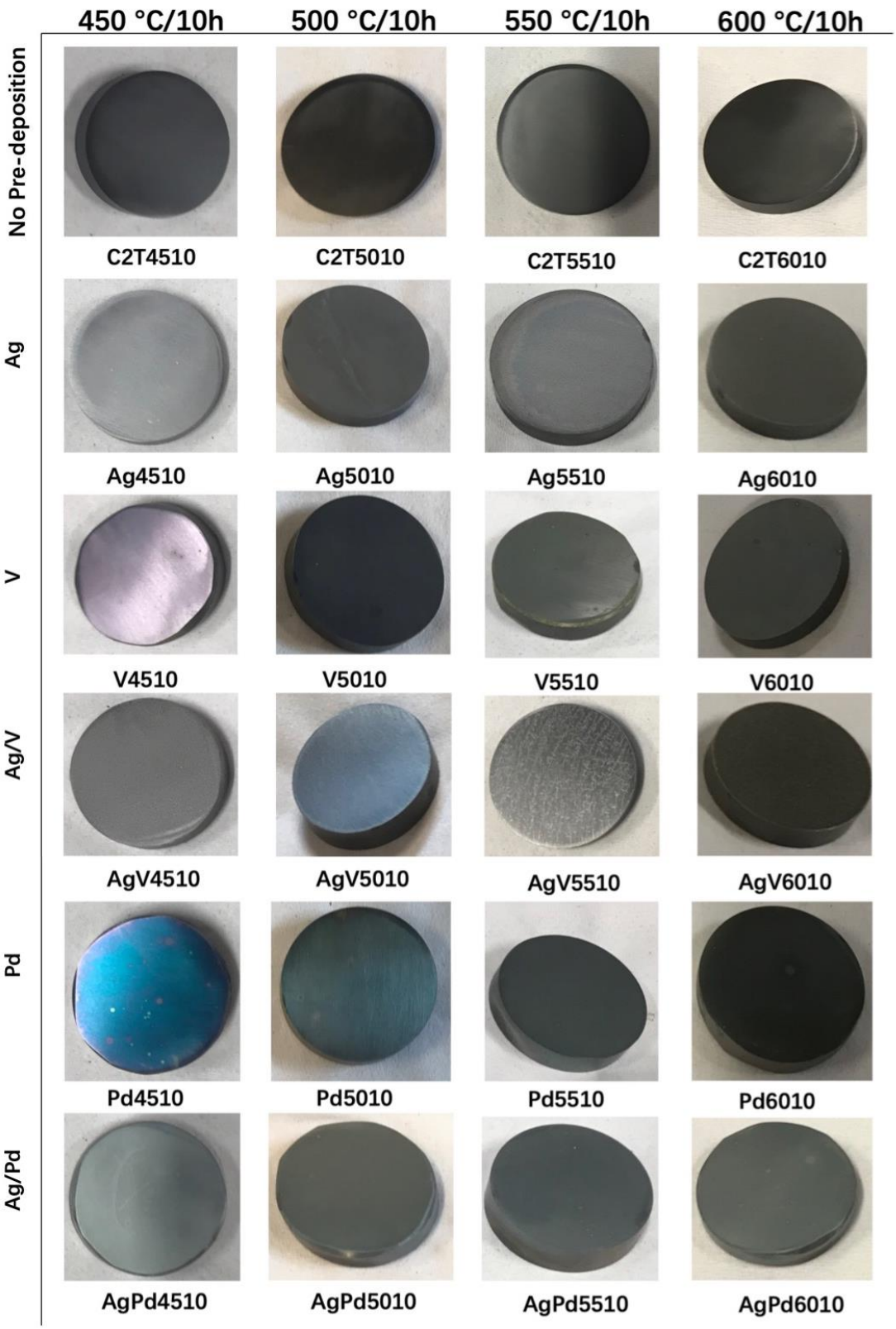


Figure 4.1-3 Visual observations – the colour change of the samples surface after 10-hour treatment.

In order to measure and monitor the thickness of the pre-deposited metallic layer, a silicon wafer was also placed in the PVD chamber together with the Zr702 samples, so that the elements were also deposited on the silicon wafer for the measurement of layer thickness. The layer thickness was measured in two ways. Firstly, part of the pre-deposited film was removed by carbon adhesive discs, and the 2D thickness profile was obtained by a profilometer. As shown in Figure 4.1-4, the thickness profile of the Ag pre-deposited silicon wafer indicates that the thickness of the pre-deposited layer ranges between 0.2 to 0.3 μm. Secondly, the silicon wafer deposited with a specific element was fractured so that the cross-sectional view of the silicon wafer could be revealed under SEM, and the thickness of the deposited layer was measured from the SEM images. Figure 4.1-5 shows the coloured SEM images with EDX mapping and the layers could be clearly identified and measured. The thickness measured from the 2D thickness profile and from the coloured SEM images are summarised in Table 4.1-1. In general, these two methods provided reasonably close thickness values although some variation was observed.

The morphology of deposited elements on silicon wafer has also been observed under the SEM, as shown in Figure 4.1-6. The Ag deposition appears to be consisted of the bubble shape particles with the size smaller than 100 nm in dimeter on the surface (Figure 4.1-6 (a)). The deposition of V (Figure 4.1-6 (b)) and Pd (Figure 4.1-6 (c)) on silicon wafer produced smoother surface and no apparent features observed, particularly for the V deposition. The Au deposition (Figure 4.1-6 (d)) produced patches of the planar and island-like structures closely adjacent to each other. The duplex co-deposition shows the combination of the morphology of each element, i.e. the bubble shape like particles become more obvious to see in either Ag/V co-

deposition (Figure 4.1-6 (e)) and Ag/Pd (Figure 4.1-6 (f)) co-deposition. All depositions showed smooth and even distribution of the elements on silicon wafer. Figure 4.1-7 compares SEM images of the deposited Au elements on silicon wafer and on the ground Zr702 sample surfaces. The planar and island like structures were also spotted on the Zr702 sample surface above the grinding traces (as shown in Figure 4.1-7 (b)). As a result, it can be concluded that the surface morphology of the deposited elements should share the same features both on the Zr702 sample surface and on the silicon wafer surface.

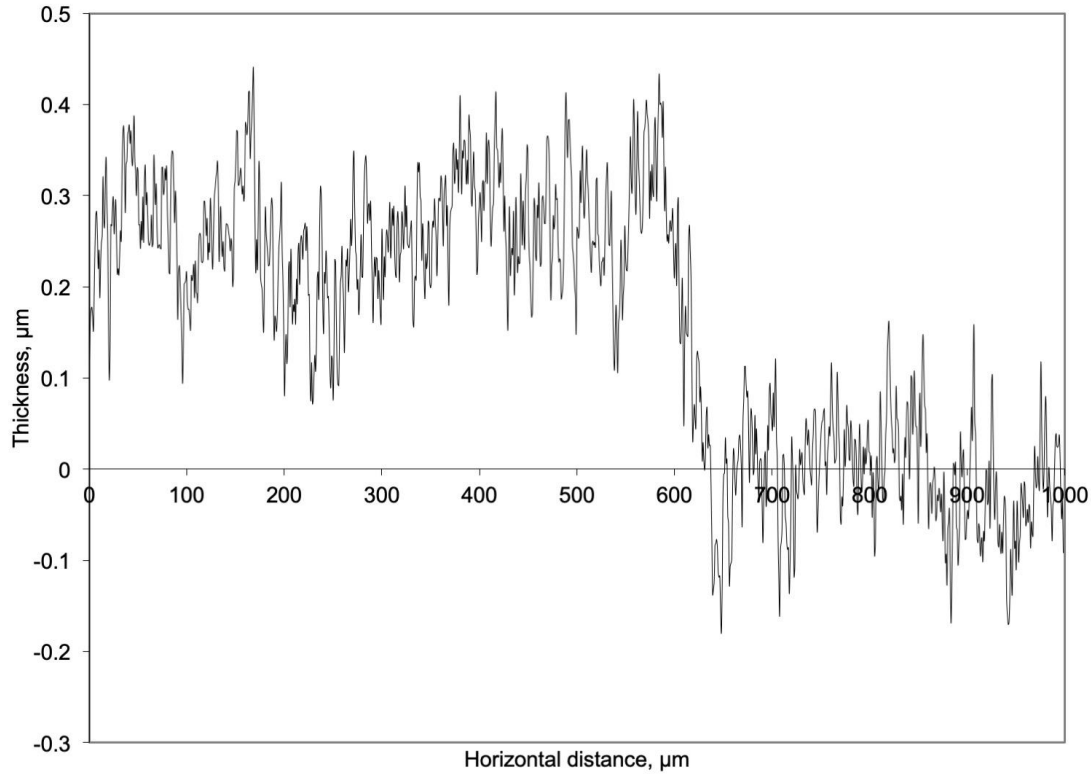


Figure 4.1-4 The 2D thickness profile of Ag element deposited on Silicon wafer.

Table 4.1-1: Table summarises the thickness measurement of different elements deposited on silicon wafer.

Elements deposited	Thickness measured from thickness profile, μm	Thickness measured from SEM images, μm
Ag	~0.20-0.30	0.248
V	~0.05-0.15	0.062
Pd	~0.20-0.30	0.165
Au	~0.04	0.071
Ag/V	~0.10-0.30	0.314
Ag/Pd	~0.10-0.30	0.433

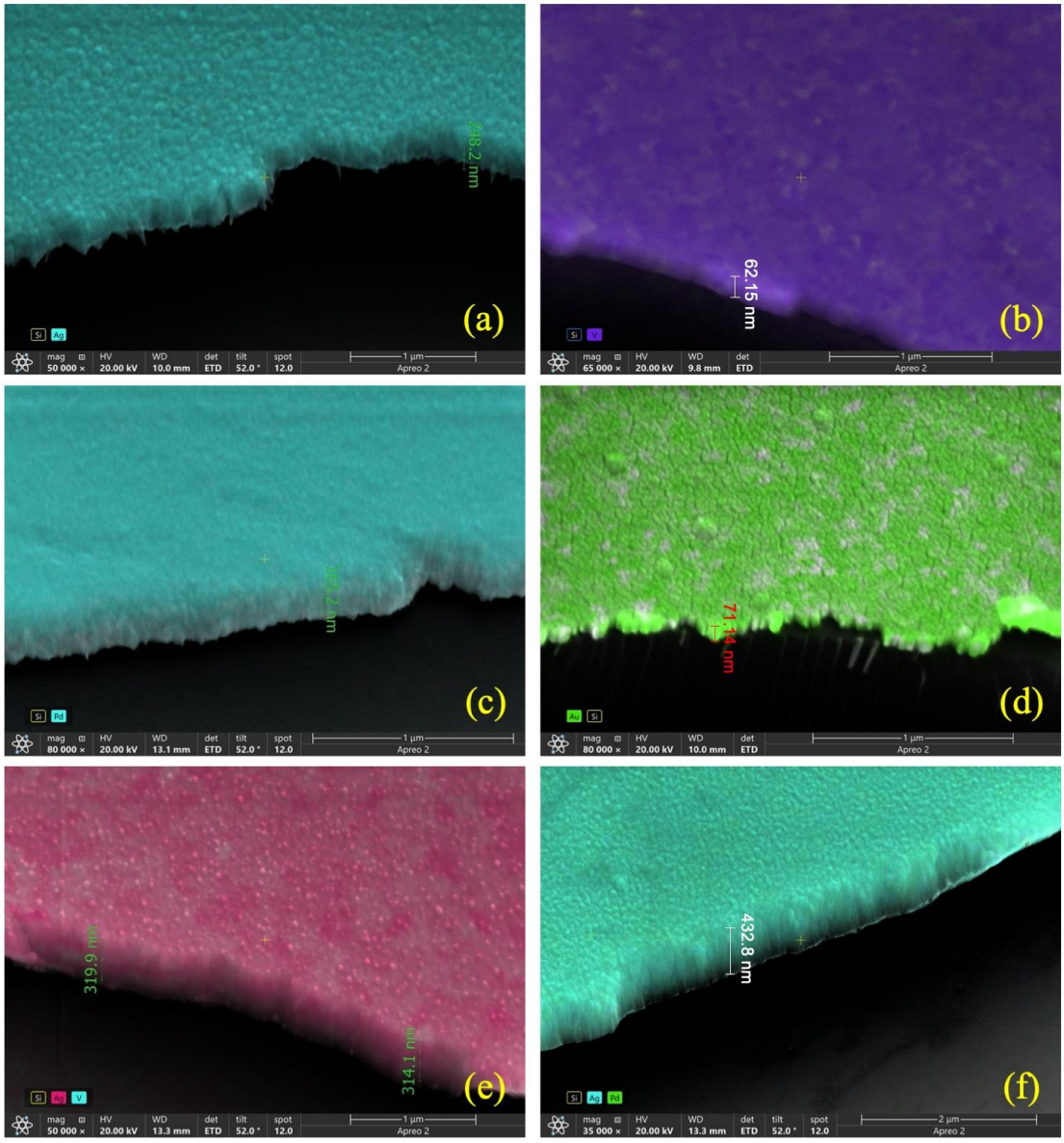


Figure 4.1-5 The coloured SEM reveals the deposited layer of (a) Ag; (b) V; (c) Pd; (d) Au; (e) Ag/V and (f) Ag/Pd on the silicon wafer and the thickness was measured accordingly.

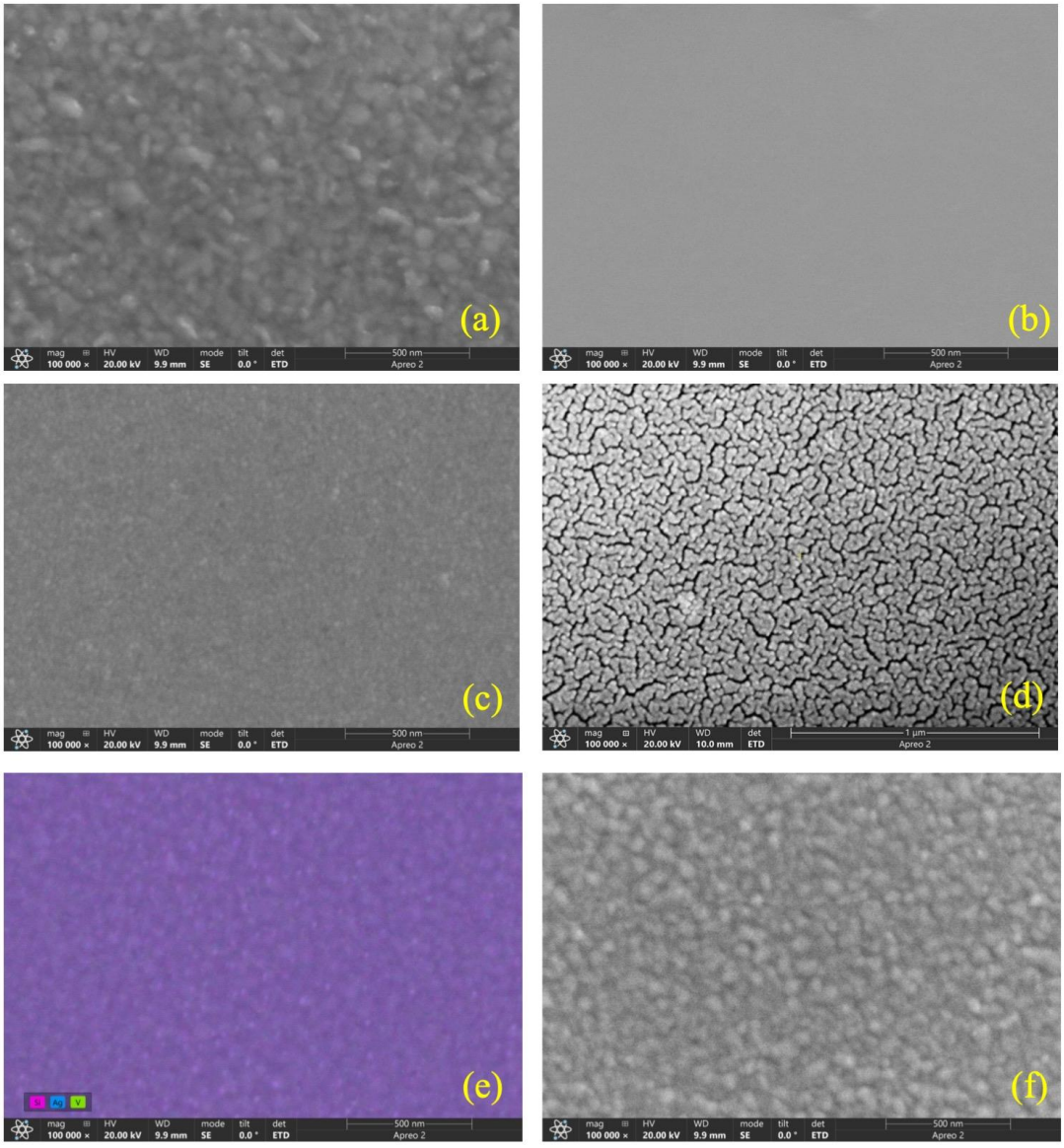


Figure 4.1-6 SEM observation of the deposition of (a) Ag, (b) V, (c) Pd, (d) Au, (e) AgV and (f) AgPd on silicon wafer.

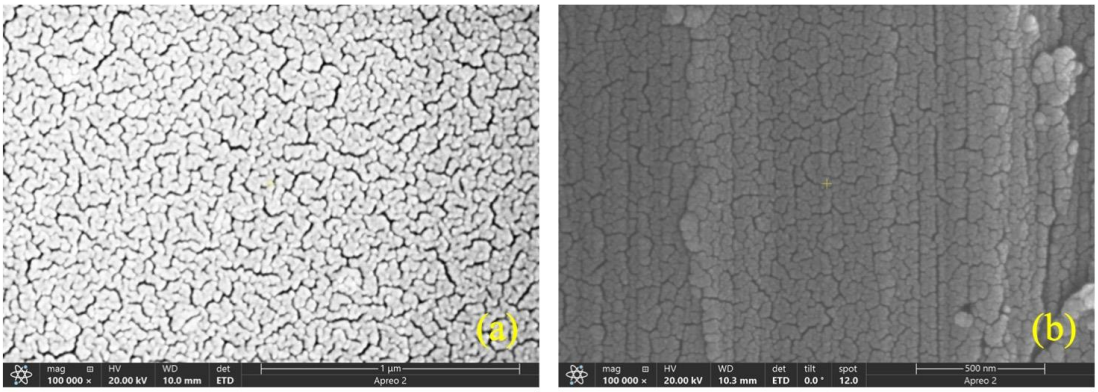


Figure 4.1-7 Au deposited on (a) Si wafer and on (b) Zr702 surface.

4.1.3 Surface phase identification

Figure 4.1-8 shows the XRD patterns of the C2T and single element pre-deposited C3T samples after 600 °C, 10-hour treatment. The characteristic peaks of m-ZrO_2 are marked in Figure 4.1-8 with dash lines at 2θ positions of 24°, 28.2°, 34.3° etc. Such features were identified on all the samples. The double dot dash lines marked in Figure 4.1-8 represent the α-Zr peaks, detected from the samples with no or thin surface layers (i.e., C2T and Au6010 samples)

Evidenced by the peak of (001) at 2θ position of 20.7 °, the V6010 sample showed the formation of a vanadium pentoxide (V_2O_5) phase. The peak around 2θ positions of 34 ° was identified as (101) of PdO phase for Pd6010 sample. The Ag_2O (200) and pure silver phases were identified for Ag6010 sample as indexed in Figure 4.1-8. The dendrite-like grains were analysed under EDX revealing the O/Ag ratio of 1/8 (see Figure 4.2-3), which implies the inclusion of Ag and Ag_2O phases in the dendrite-like grains. The (111) peak of fcc gold phase at 2θ position of 38.2 ° was identified from Au6010 sample.

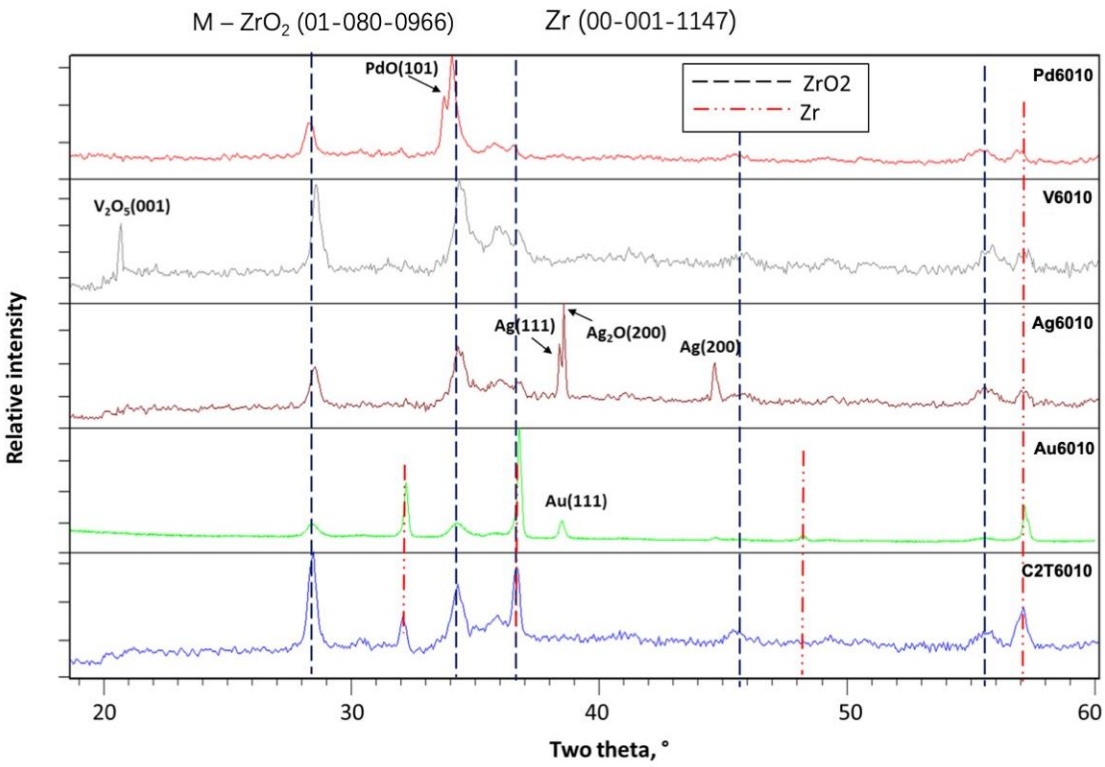


Figure 4.1-8 The XRD analysis of the samples after the C2T and C3T (single element deposition) process, samples treated at 600 °C for 10 hours.

Figure 4.1-9 and Figure 4.1-10 show the XRD patterns of single element (Ag, V and Pd) pre-deposited C3T samples comparing with co-deposited (Ag/V and Ag/Pd) C3T samples after 600 °C, 10-hour treatment. Comparing the features of single element Ag and V deposited samples, the characteristic peaks at 2θ position of ~18.3°, 25.8°, 32.6°, 38.6°, 44.5° and 53.5° were identified as AgO_3V phase for Ag/V pre-deposited sample (Figure 4.1-9). As evidenced in Figure 4.1-10, both PdO and $(Pd, Ag)_3O_4$ phases were identified on the Ag/Pd pre-deposited sample at 2θ position around of 39.2° and 45.5°. The phases constituents after the C2T and C3T process for the single and co-deposition samples are summarised in Table 4.1-2.

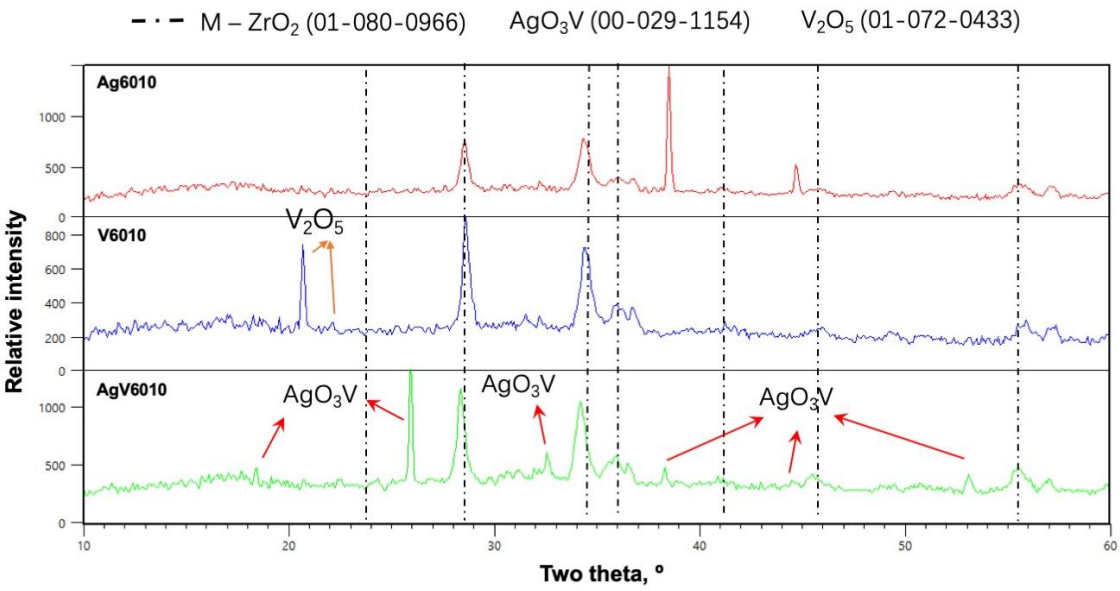


Figure 4.1-9 The XRD analysis of the samples after the C3T (pre-deposited with Ag, V and Ag/V) process, samples treated at 600 °C for 10 hours.

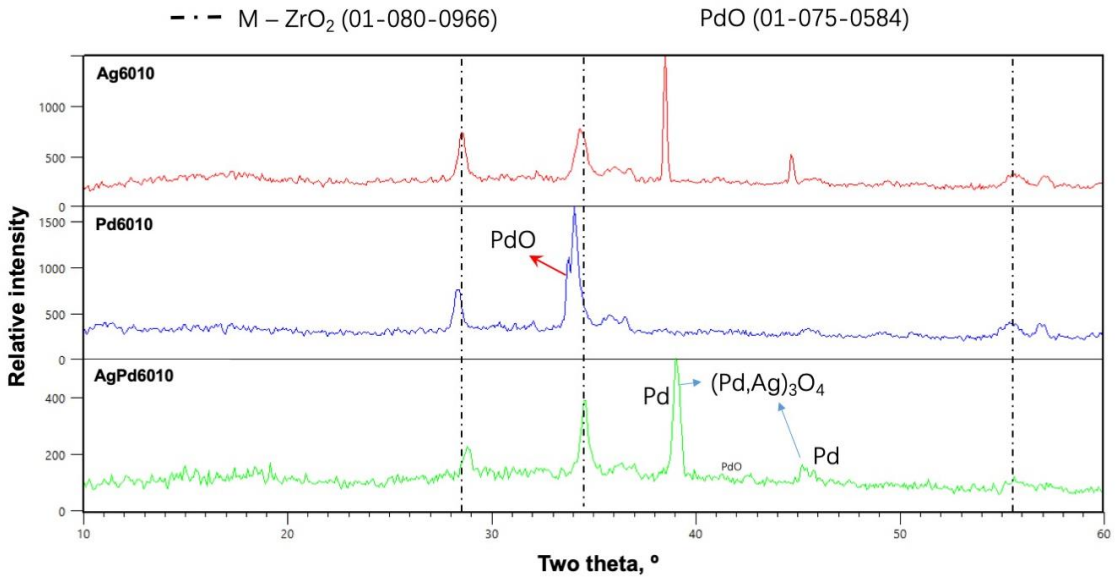


Figure 4.1-10 The XRD analysis of the samples after the C3T (pre-deposited with Ag, Pd and Ag/Pd) process, samples treated at 600 °C for 10 hours.

Table 4.1-2: Summary of phase constituents identified after the ceramic conversion treatment of each sample under the condition of 600 °C/10 hours.

	C2T6010	**Ag6010**	**V6010**	**AgV6010**	**Pd6010**	**AgPd6010**	**Au6010**
600 °C/10h	ZrO_2	ZrO_2 Ag_2O	ZrO_2 V_2O_5	ZrO_2 AgO_3V	ZrO_2 PdO	ZrO_2 PdO, $(Pd,Ag)_3O_4$	ZrO_2 Au

4.1.4 Weight gain and layer thickness

The change in weight can reflect the addition of the weight generated mainly due to the formation of oxide layer during the ceramic conversion treatment. After the treatment at temperatures ranging from 450-600 °C for 10 hours, the weight change of the samples treated is plotted in Figure 4.1-11. It is clear when treated for 10 hours, the weight gain after ceramic conversion treatment increased with the treatment duration for both C3T (with pre-deposition) and C2T (none pre-deposition) samples. However, it is also evident that the pre-deposition of these elements, either single (Ag, V, Pd and Au) or mixed (Ag/V and Ag/Pd), can increase the weight gain after the same ceramic conversion treatment as compared with the sample without (None) pre-deposition. For the samples with the same pre-deposition elements, more weight is gained as the treatment temperature goes up.

It is of interest to find that the catalytic effect of the pre-deposited element is also highly temperature dependent. When treated at low temperature of 450 °C, Pd showed the highest level of catalytic efficacy whilst Ag and Au revealed little if any catalytic efficacy. When treated at 500 °C, except for Ag, no significant difference in weight gain can be observed when the experimental errors are considered for all other

single elements (V, Pd and Au) with a very similar weight gain around 5 mg. Overall, the single element deposited samples showed low catalytic efficacy when treated at or below 500 °C, and no significant difference in weight gain could be observed for samples with different elements when the experimental errors are considered as all these samples showed a very similar low degree of weight gain (less than 5 mg).

However, once the treatment temperature was increased to above 500 °C, the weight gain of the Ag pre-deposited sample jumped from 3.5 mg to 9.9 mg (almost 200% increase), and the Pd pre-deposition produced the highest weight gain (13.4 mg) among all the single element pre-deposited samples when treated at high temperature of 600 °C, as compared to Ag (12.1 mg), V (12.4 mg) and Au (10.1 mg).

For the samples pre-deposited with two elements (Ag/V and Ag/Pd), when treated at relatively high temperature some co-deposited sample showed more weight change (i.e., AgV6010 and AgPd5510) compared to single element deposited samples suggesting synergic effect. For example, Ag/Pd showed a large increase in weight change from 4.7 mg to 11.6 mg when the treatment temperature increased from 500°C to 550 °C. The Ag/V pre-deposited sample showed most significant change at 600 °C (14.1 mg), up from the 7.6 mg weight change at 550 °C. However, the opposite was also observed for AgV5510 and AgPd6010 and the potential mechanism involved will be discussed in Chapter 5.

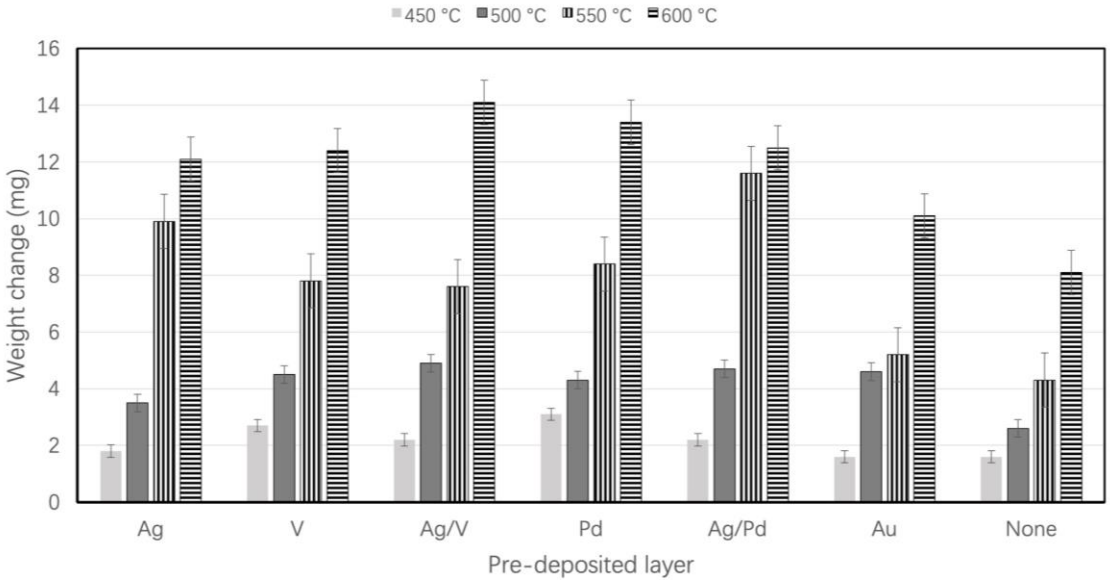


Figure 4.1-11 The weight change of the samples after 10-hour ceramic conversion treatment with and without pre-deposition (None, C2T) as a function of treatment temperatures.

It should be mentioned that although the weight change is mainly associated to the formation of the surface oxide layer, other factors including oxygen inward diffusion etc. can also affect the weight gain after the ceramic conversion treatment. Furthermore, it is difficult, if not impossible to precisely prepare the samples with the same dimensions and the surface areas after the cutting and grinding, which may affect the weight gain data above. Hence, the change of weight is only an estimation of the possible change of surface oxide layer thickness during the treatment. Consequently, the surface layer thickness was measured from the cross-sections of the surface treated samples.

The sample layer thickness of these C3T samples, measured from the cross-sectional SEM images, is plotted in Figure 4.1-12 as a function of different treatment temperatures compared with the no pre-deposition (C2T) samples. Very similar to the

trend of the weight gain shown in Figure 4.1-11, the thickness of the surface oxide layer formed during the final ceramic conversion treatment increased with the treatment temperature for all C3T and C2T samples. The samples with pre-deposited elements (C3T) produced thicker surface oxide layers compared to the samples with no pre-deposition of elements (C2T). Hence it can be concluded that the pre-deposition of such metal films as Ag, V, Pd and Au prior to the final treatment can speed up the formation of the surface oxide layers thus demonstrating significant catalytic effects.

It can be seen from Figure 4.1-12 that the thickness of the surface oxide layer formed on Pd pre-deposited sample is very thin (< 1 μm) when treated at 450 °C whilst all other C3T samples produced a surface oxide layer in between 1 and 2 μm. When treated at 500 °C, the oxide thickness is between 2 and 3 μm apart from V pre-deposited samples which is slightly over 3 μm. The co-deposited (Ag/V, Ag/Pd) samples showed a slightly thicker oxide layer after 450 °C treatment as compared to single element deposited sample, but this trend was not found when treated at 500 °C.

The largest variation in catalytic efficacy was observed for the C3T samples treated at 550 °C. As depicted in Figure 4.1-12, Ag, Pd and V pre-deposition effectively increased the surface oxide layer thickness to 5.8, 4.7 and 4.2 μm respectively from 2.3 μm for the C2T samples, which is 2.5, 2.0 and 1.8 times that of the C2T samples. The Au pre-deposited samples showed relatively less increase in the thickness of the surface oxide layer compared with other pre-deposited samples, particularly when treated at 500 and 550°C. The surface oxide layer thicknesses for all C3T samples are increased to the largest extent at 600°C, ranging from about 5.3-6.3 μm, which is 96-

133% increase as compared to the oxide thickness of the C2T sample treated at the same temperature of 600°C.

Judged by the average value, the co-deposited samples, AgV6010 and AgPd5510, showed the thicker surface oxide layer compared to other samples treated under the same treatment conditions (temperature and time). However, it should be noted that the difference is not significant when the experimental errors are considered. In addition, co-deposition is more complicated and not so cost-effective as compared with deposition of single element. Therefore, the co-deposited samples do not show any appreciable technical or economical advantage over the single element pre-deposition.

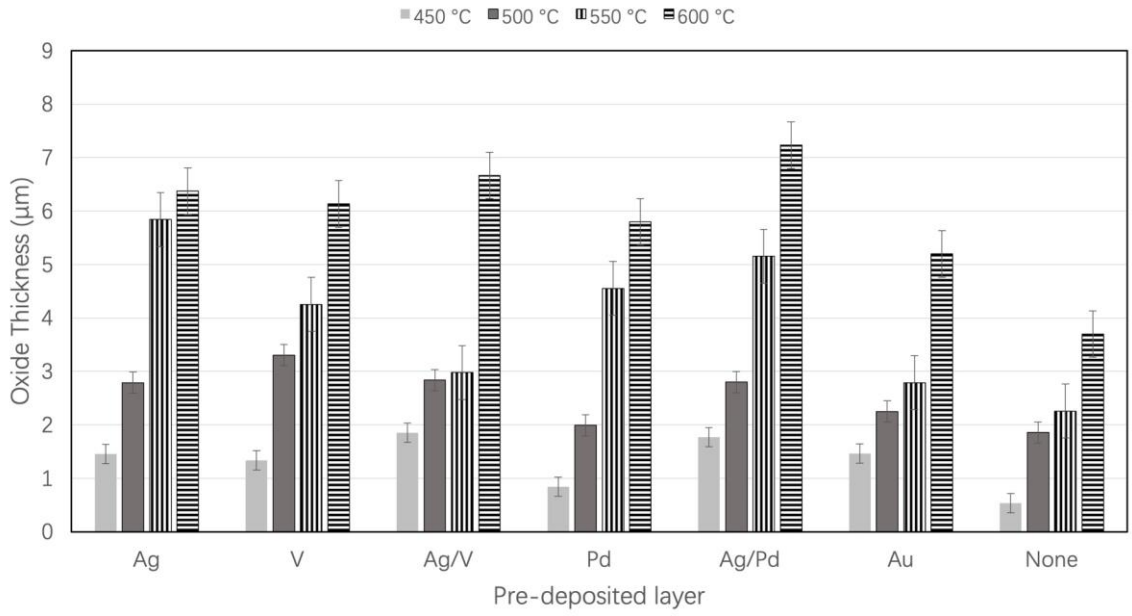


Figure 4.1-12 The oxide thickness of the samples after 10-hour ceramic conversion treatment with (C3T) and without pre-deposition (None, C2T) as a function of treatment temperatures.

4.1.5 Selection of the C3T treatments

The first stage of the experimentation was designed for screening promising C3T treatment conditions mainly based on the sample weight gain after the treatment and the surface oxide layer thickness measurements. As stated above, in terms of surface oxide layer thickness, the co-deposited samples (Ag/V and Ag/Pd) do not show appreciable technical and economic advantages as compared to the single element (Ag, V, Pd, Au) deposited samples. Consequently, the main research was focused on the investigations of the catalytic ceramics conversion treatment of single element deposited (i.e., Ag, V, Pd and Au) samples to study their catalytic performance and their effect on property. In addition, as reported above, the pre-deposited elements revealed the strongest catalytic effect during the ceramic conversion treatment temperature at 600 °C and therefore in the second stage (main stage) of the research the treatment temperature is fixed at 600 °C and the effect of treatment time on the catalytic effect and properties enhancement have been investigated.

4.2 Microstructure of C3T treated Zr702

In this section, the evolution of microstructures of the single element pre-deposited samples treated at 600 °C for 10 hours is reported first followed by the effect of treatment duration at 600 °C.

4.2.1 Microstructure of 600 °C/10h C3T treated samples

4.2.1.1 Surface morphology and surface roughness

Detailed SEM observations have been carried out to observe the change of surface morphology of the samples after the ceramic conversion treatment. As shown in Figure 4.2-1 (a), the vertical grinding traces can be clearly observed on the as-prepared Unt sample surface. All the ceramic conversion treated sample surfaces revealed different surface features mainly depending on the pre-deposition prior to the ceramic conversion treatment.

As shown in Figure 4.2-1 (b), the C2T6010 sample (without pre-deposition) formed some patches of lumps above the grinding traces. Some fine particles covered the Au6010 sample surface (Figure 4.2-1 (c)). Most of the particles were measured to be in the range of 200-400 nm in diameter, with a few bigger particles with the sizes between 0.8-1.1 μm in diameter. The surface morphology of the Pd pre-deposited and ceramic conversion treated Pd60010 (Figure 4.2-1 (d)) shares some common features with Au6010, but the surface particles are extremely fine (about 150 nm) and evenly covered the whole surface. Multi-directional needles (length of 5μm) were observed on the top pf the V6010 sample (Figure 4.2-1 (e)), which may correspond to the formation of the vanadium oxide (as will be confirmed in the later sections through the XRD analysis). The Ag pre-deposited and ceramic conversion treated Ag6010 revealed very different surface morphology. As depicted in Figure 4.2-1 (f), the silver particles tend to agglomerate to columnar-dendrite-like grains (50 μm in length and 10 μm in width) after the ceramic conversion treatment.

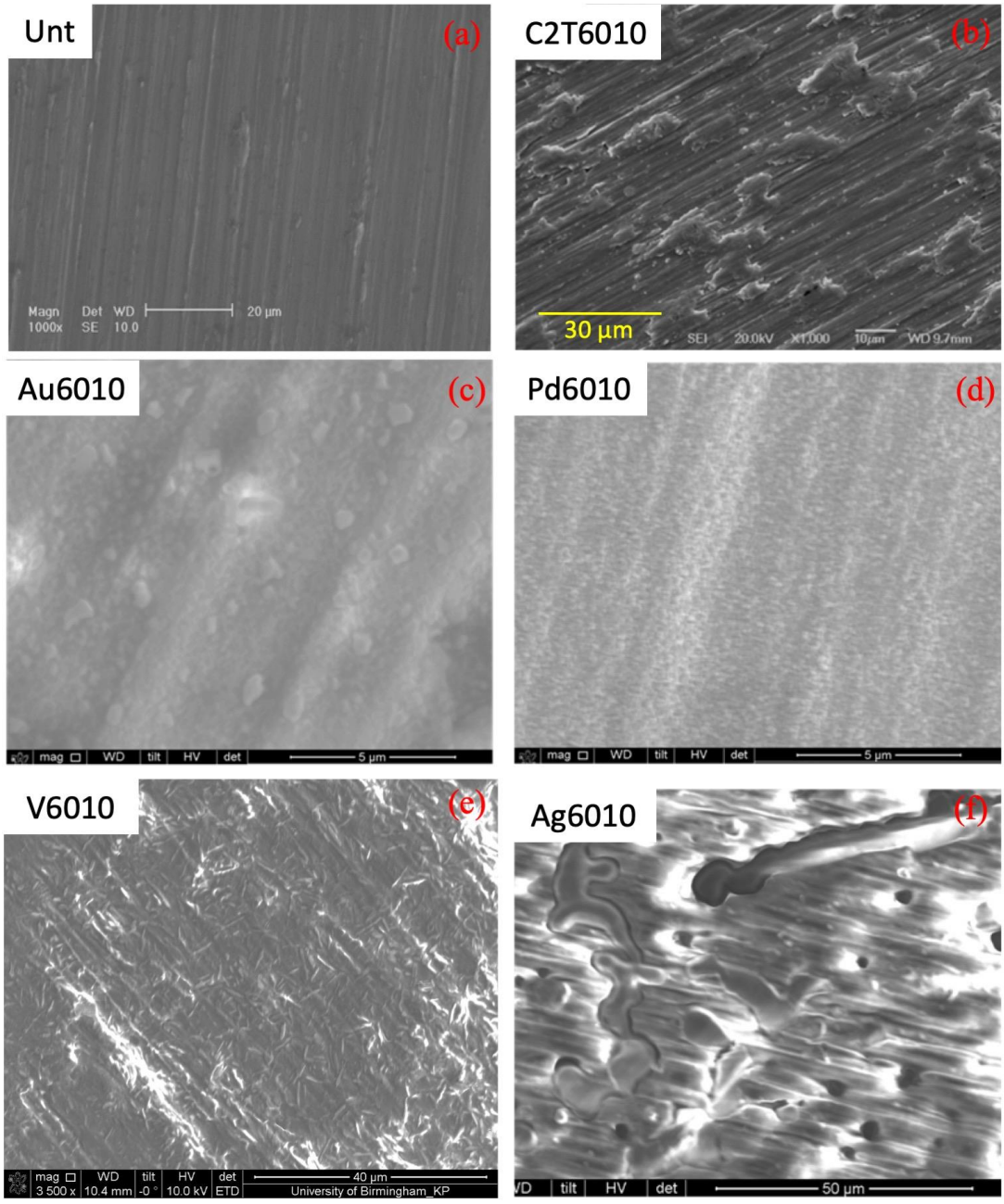


Figure 4.2-1 SEM images showing the surface morphology of the ceramic conversion treated samples.

As has been discussed in Chapter 2, surface roughness has been measured in R_a (arithmetic average roughness) and R_t (maximum and minim data points range), and the surface roughness of all the samples are compared in Figure 4.2-2). It can be seen from the figure that after the ceramic conversion treatment at 600 °C for 10 hours, the R_a values of all the treated samples are more or less increased as compared to the

untreated Unt sample with the Ag6010 sample being much rougher than all other samples.

However, major difference in surface roughness is more clearly indicated by the R_t values. As shown in Figure 4.2-2, the Ag6010 sample demonstrates a largest increase in R_t value of 4.11 μm, which is caused by the agglomerated silver particles on the surface as discussed above. In contrast, the V6010 sample showed the lowest R_t value of 0.34 μm, only 1/5 of the value of C2T. This implies that the fine needle shaped vanadium oxides are finely dispersed and embedded into the grinding traces and grooves (Figure 4.2-1 (e)), and this phenomenon becomes more obvious when treated for longer durations (Figure 4.2-5 (b) and Figure 4.2-5 (c)). The slightly increased R_t values of Pd6010 and Au6010 might be related to the formation of very fine PdO (identified by the XRD in Section 4.1.3) and the presence of the fine Au particles (as shown in Figure 4.2-3 and Figure 4.2-6).

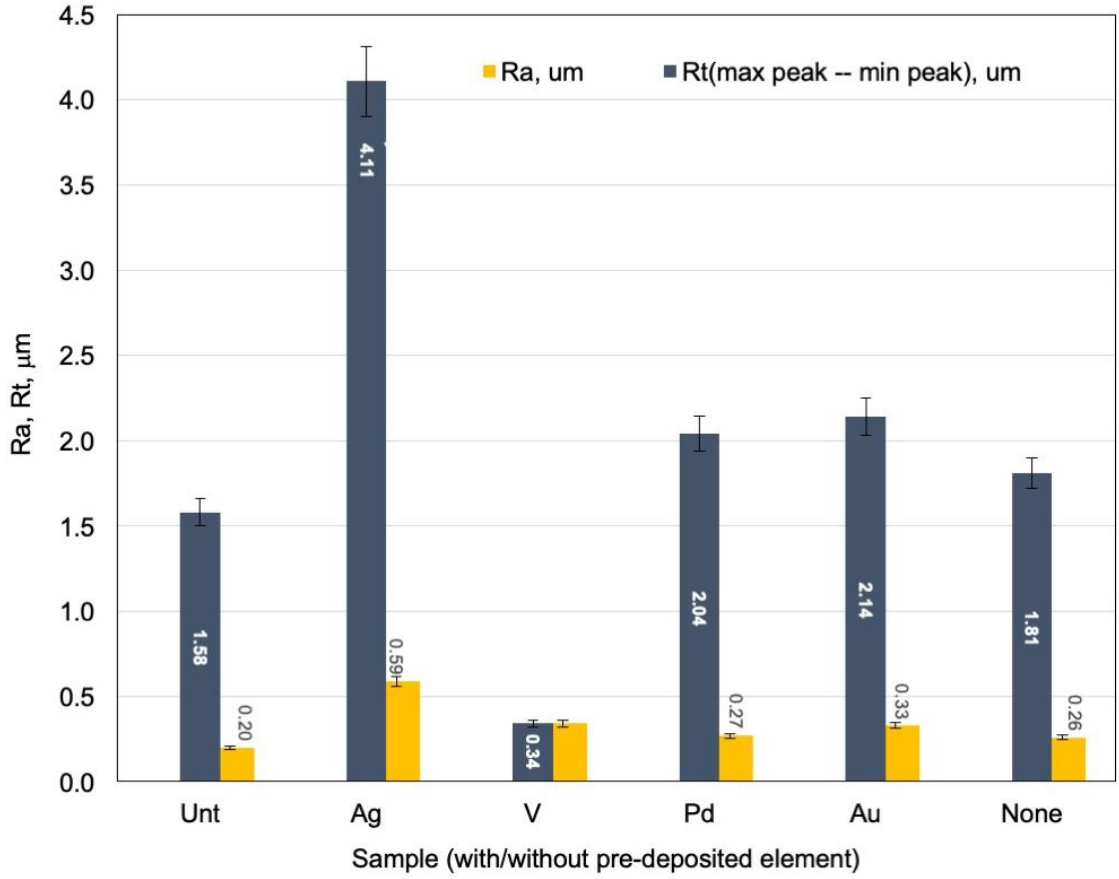


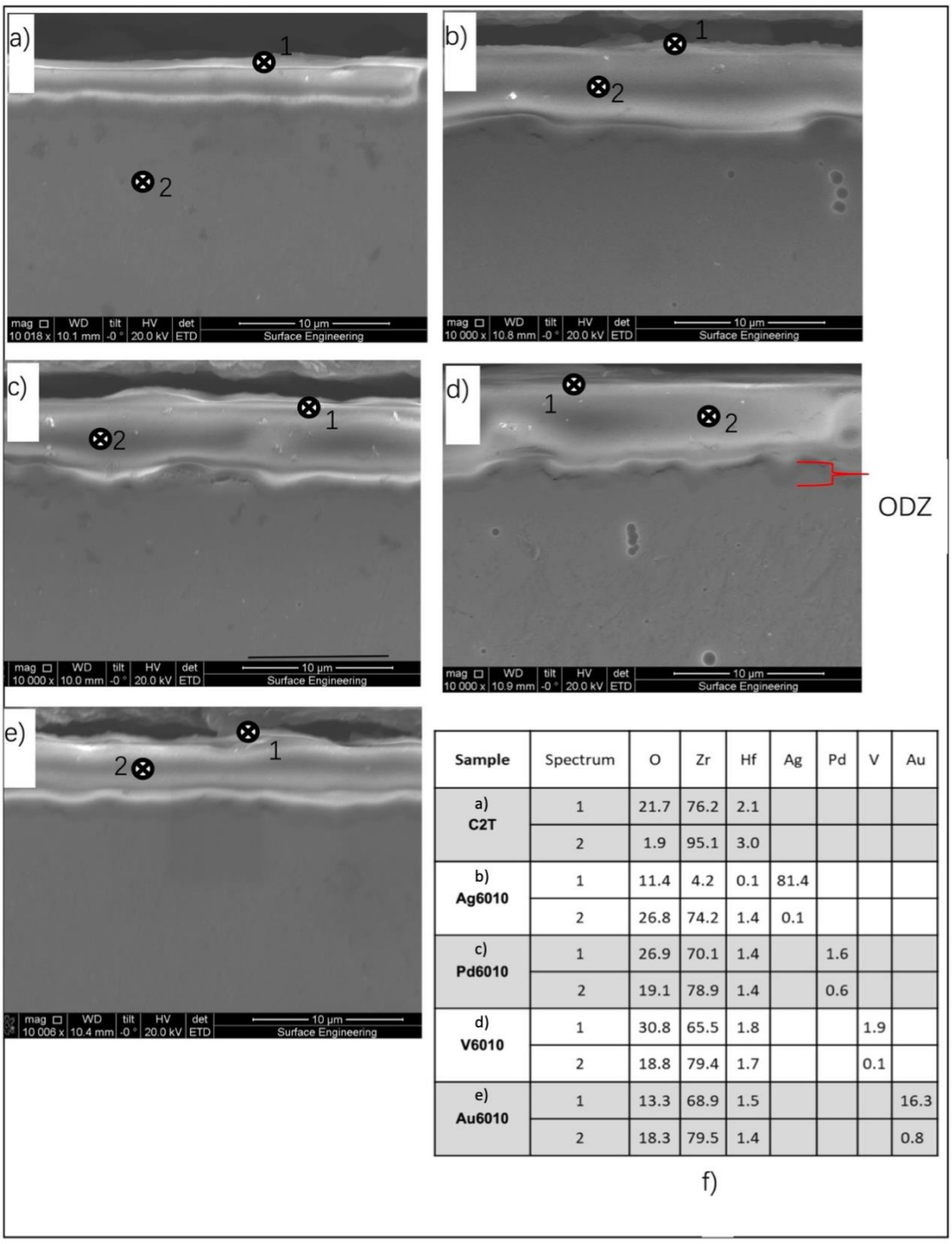
Figure 4.2-2 The surface roughness values in R_a and R_t of ceramic conversion treated samples, comparing with the untreated sample.

4.2.1.2 Surface layer structures

As reported in Section 4.1, the surface of the Zr702 samples was converted into ZrO_2 after the ceramic conversion treatment. In addition to ZrO_2, Ag_2O, V_2O_5, and PdO were also formed on the C3T treated samples pre-deposited with Ag, V and Pd respectively. In addition to the oxide layer thickness, the layer structure is also scientific interesting for advancing the understanding of the oxide layer formation and for the understanding of the property enhancement in later sections.

The cross-sectional SEM images of the samples treated at 600 °C for10 hours are shown in Figure 4.2-3. These SEM images clearly demonstrated that the C3T sample layer structure consists of an outmost surface, oxide layer and then an interface to the substrate. The formation of the oxide layer is implied by the XRD analysis (Section 4.1.3) and confirmed by the high oxygen content probed by EDX results (Figure 4.2-3 (f)) in such regions. Compared to the C2T samples, all C3T samples developed much thicker oxide layer.

As illustrated and marked in Figure 4.2-3 (d), an oxygen diffusion zone (ODZ) can be observed for all the treated samples underneath the oxide layer. The ODZ is usually a few microns (~2 μm) thick. After the treatment, the content of the pre-deposited elements, Pd and V, are moderately higher (1.6 wt% and 1.9 wt% respectively) on the outmost surface compared to their contents in the oxide layer. However, high levels of the pre-deposited elements are detected from the Ag and Au pre-deposited samples, which are 81.4 wt% and 16.3 wt% respectively. This is supported by the findings in the previous section and are linked to the agglomeration of Ag to dendrite-like grains on the top of the surface and the granular grains observed on Au pre-deposited sample (Figure 4.2-1).



Sample	Spectrum	O	Zr	Hf	Ag	Pd	V	Au
a) **C2T**	1	21.7	76.2	2.1				
	2	1.9	95.1	3.0				
b) **Ag6010**	1	11.4	4.2	0.1	81.4			
	2	26.8	74.2	1.4	0.1			
c) **Pd6010**	1	26.9	70.1	1.4		1.6		
	2	19.1	78.9	1.4		0.6		
d) **V6010**	1	30.8	65.5	1.8			1.9	
	2	18.8	79.4	1.7			0.1	
e) **Au6010**	1	13.3	68.9	1.5				16.3
	2	18.3	79.5	1.4				0.8

f)

Figure 4.2-3 The cross-sectional SEM images showing the surface layer structure for samples of (a) C2T; (b) Ag6010; (c) Pd6010; (d) V6010 and (e) Au6010; The EDX analysis of the surface and cross section is outlined in (f).

4.2.2 C3T duration effect

Apart from the effect of temperatures, the treatment duration can also affect the C3T process and the catalytic effect of the pre-deposited elements. Therefore, the effects of treatment duration were investigated for some selected treatments.

4.2.2.1 Surface morphology

Figure 4.2-4 shows the sample surface morphology of Ag pre-deposited Ag6020, Ag6040 and Ag6060 samples after the treatment at 600 °C for 20, 40 and 60 hours respectively compared to the 10-hour treated Ag6010. The SEM images reveal very similar surface morphology, but these long-time treated samples exhibited a greater degree of agglomeration of silver with increasing the treatment time particularly when treated for 40 hours and 60 hours, which is 2-3 times compared to the sample treated for 10 hours.

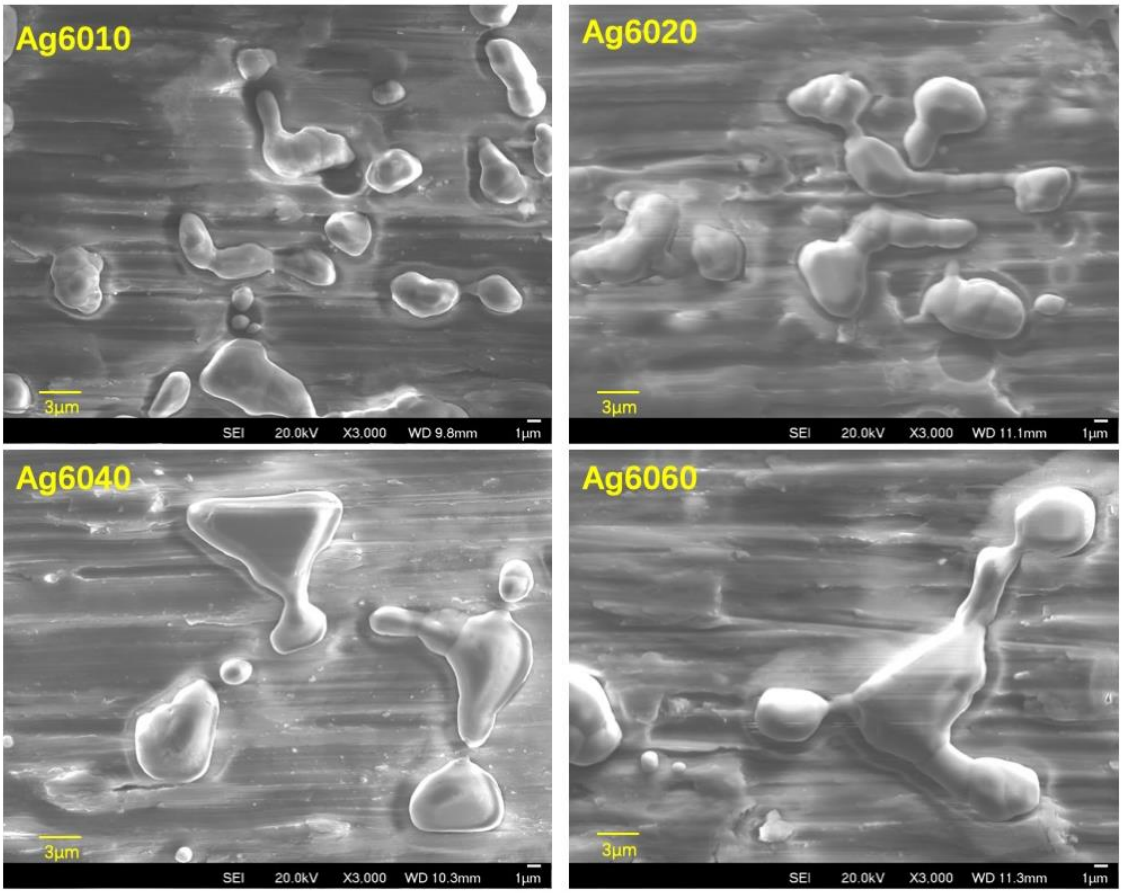


Figure 4.2-4 SEM images showing surface morphology of the samples Ag6010, Ag6020, Ag6040 and Ag6060.

The vanadium oxide needles observed on the V6010 keep presenting on the top of the surface when the treatment time increases (20 hours and 60 hours, see Figure 4.2-5), but these needles are found to be more embedded into the grinding traces on the Zr702 alloy surface when treated for longer duration compared to what is observed on V6010.

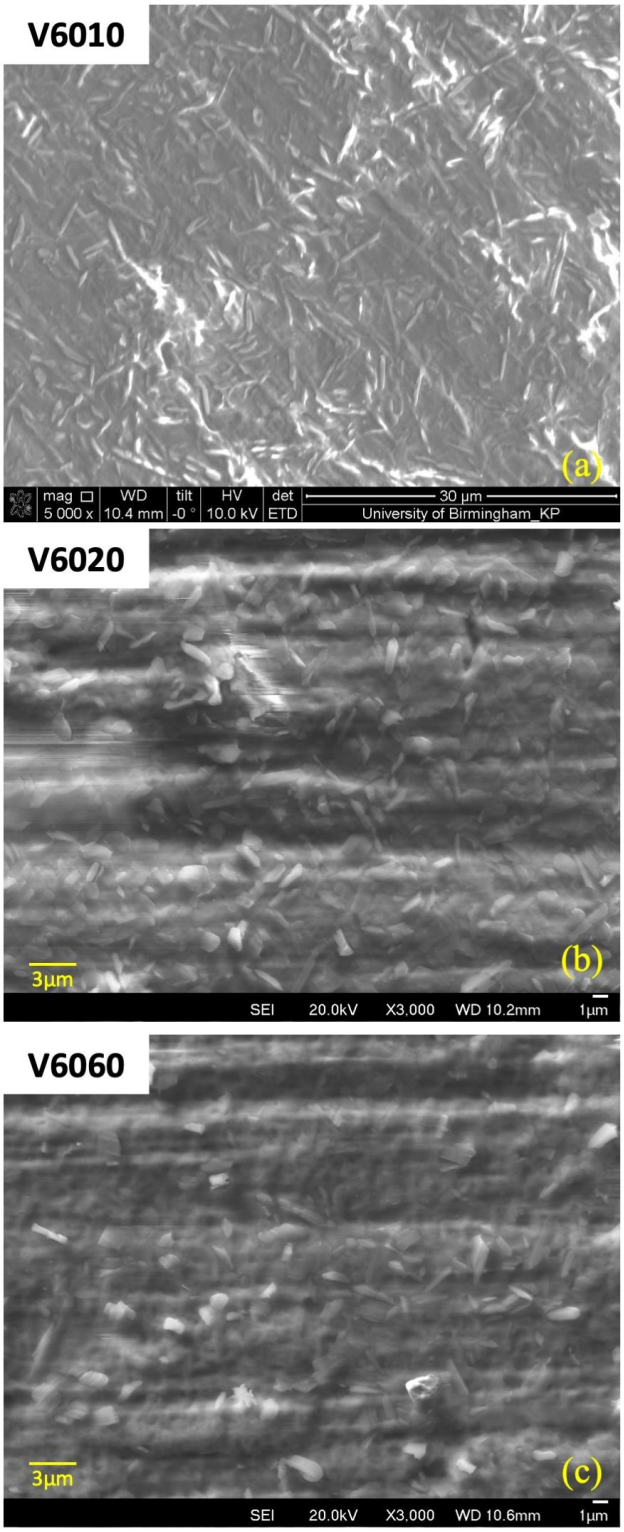


Figure 4.2-5 SEM images showing surface morphology of the samples V6010, V6020 and V6060.

In order to better study the evolution of the pre-deposited Au during ceramic conversion treatment, the Au pre-deposited samples were treated for 5 mins, 5 hours, 10 hours, 20 hours, 40 hours and 60 hours. Figure 4.2-6 demonstrates the changes of the surface morphology of Au pre-deposited samples as a function of different periods of treatment time. A few very small Au particles (confirmed via EDX) appeared on the 5 minutes treated Zr702 alloy surface. In general, when increasing the treatment time from 5 minutes to 60 hours, gold particles appeared to become more densely and evenly distributed on the surface. The effects of the treatment duration will be discussed in the following sections.

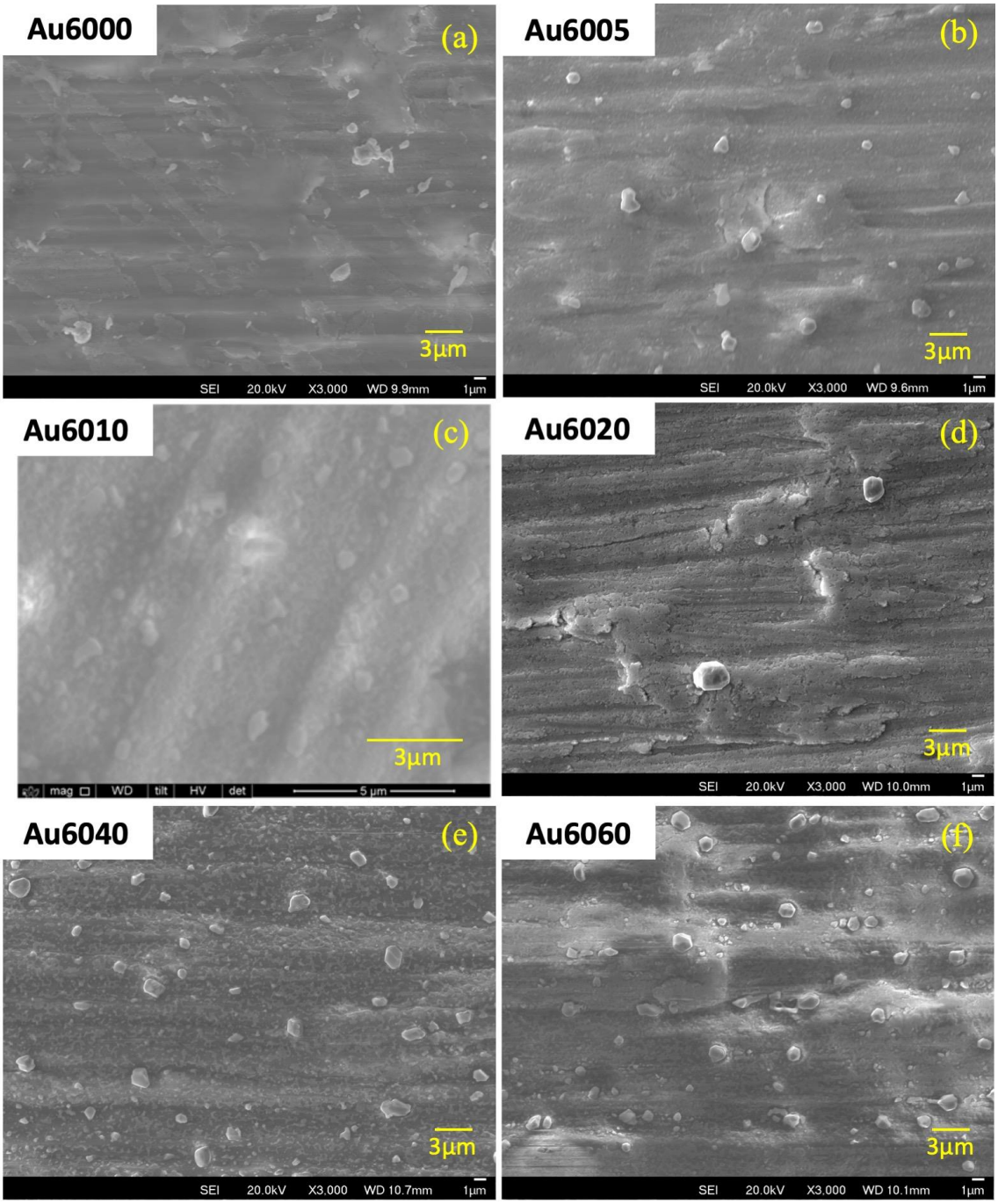


Figure 4.2-6 SEM images showing surface morphology of the samples Au6000 (5 mins), Au6005, Au6010, Au6020, Au6040 and Au6060.

4.2.2.2 Weight gain and layer thickness

Figure 4.2-7 compared the selected single element(s) (Ag, V and Au) pre-deposited samples treated at 600 °C but different treatment duration (5mins to 60 hours), to investigate how the treatment time affects the weight change. The sample with no pre-deposition layer (i.e., C2T) was not included in view of the small weight change for the sample and the relatively large experimental error, but the C2T sample is included in the comparison of the surface layer thickness in Figure 4.2-8. It can be seen that, the weight of these three types of samples increases with the treatment time up to 40 hours. The weight gain of the 40-hour treated sample doubles that of the 10-hour treated sample. However, further increase of the treatment time to 60 hours lead to less weight gained, which differs from the results of the layer thickness (Figure 4.2-8) directly measured from the cross-section of the samples. Comparing the pre-deposited elements, V shows the most weight gain as compared to Ag and Au when treated for 10 hours, 20 hours, 40 hours and 60 hours.

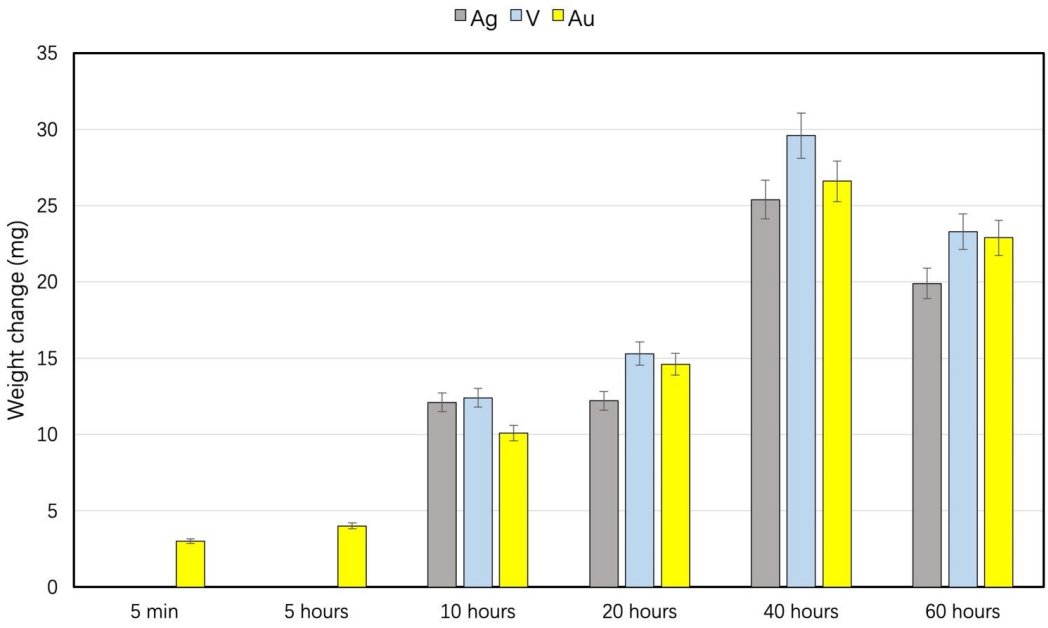


Figure 4.2-7 The weight change of the pre-deposited with Ag, V and Au, and ceramic conversion treated at 600 °C for the treatment time ranging from 5 mins to 60 hours.

The observation that weight gain is less when treated for 60 hours than for 40 hours might imply possible surface layer spallation for the 60-hour treated samples. However, this was not seen in the thickness measurement. As shown in Figure 4.2-8, the surface layer thickness increases with the increase of treatment duration of Ag, V and Au pre-deposited samples. It is evident in Figure 4.2-8 that pre-deposition of these three elements can effectively increase the surface oxide layer thickness after the same ceramic conversion treatment as compared with the samples with no pre-deposition (C2T). Figure 4.2-8 clearly shows that long treatment time such as 40 hours and 60 hours can produce very thick oxide layers. For example, when ceramic conversion treated for 40 hours, the pre-deposited sample produced surface oxide layer twice (for Ag and V) or nearly three times (for Au) of the thickness when compared to the sample without pre-deposition. When treated for 60 hours, the V6060 sample produced surface oxide layer about four times that of the C2T6060 sample whereas the surface oxide layer of Au6060 is almost five times that of the C2T6060 sample.

More specifically, Au outperformed Ag and V with the largest increase of the surface layer thickness when treated at 20, 40 hours and 60 hours. When treated for 60 hours, the layer thickness of Au pre-deposited sample is 31.5 μm, which is 6 times the thickness of the C2T sample when treated for 10 hours. The oxide layer thickness of Ag and V pre-deposited samples are quite similar when treated for 10 hours, 20 hours and 40 hours, but the 60-hour treatment resulted in the V pre-deposited sample having a thickness (27.3 μm) almost doubled that of the Ag6060 sample (14.5 μm).

The chart was also used to study the efficiency and effectiveness of C3T techniques for promoting the formation of the surface oxide layer. For example, the chart shows that treating C2T sample at 600 °C for a long treatment of 60 hours produced the same thickness level of Ag6010 and Au6010. This demonstrates a reduction of treatment time from 60 hours to 10 hours, i.e., 83% reduction of time and hence the less energy consumption. This phenomenon implies the great level of acceleration in the oxidation process with pre-deposition of Au.

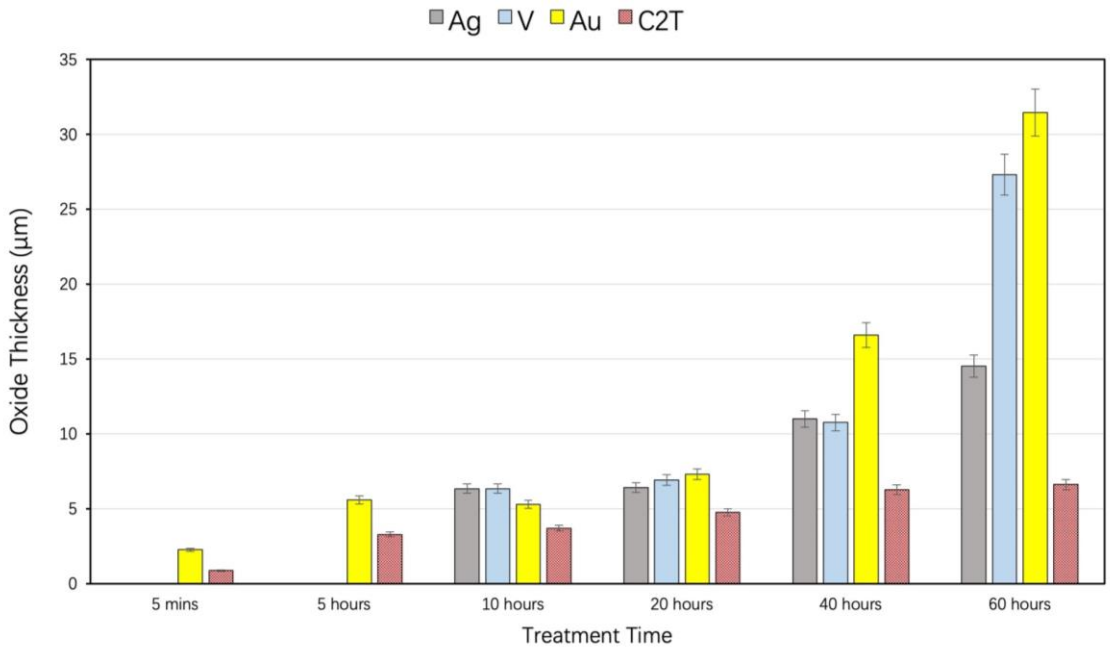


Figure 4.2-8 The oxide thickness of the samples after ceramic conversion treatment with (C3T) and without pre-deposition (None, C2T) at the same temperature 600 °C as a function of treatment time ranging from 5 mins to 60 hours.

4.2.2.3 Oxide layer structure

Figure 4.2-9 compares the cross-sectional SEM images of Ag, V and Au pre-deposited samples treated under 600 °C for 20 hours and for long treatment time of 60 hours. The very long treatment time produced the thickest oxide layer; however, more tiny pores and cracks within the oxide layers could be observed for those

samples treated for 60 hours, resulting relatively poorer quality oxide layer as compared to the denser oxide layer formed by 20-hour treatment.

Figure 4.2-10 displays the results of EDX analysis of the V6060 sample in both line scan and mapping. The results revealed higher oxygen content at the outmost surface than inside the oxide layer and the high V content at the outmost surface. Almost no V was found inside the oxide layer and the substrate, similar with the findings for the V6010 sample (Figure 4.2-3 (d) - spot 2), which indicates that the pre-deposited V element is unlikely to diffuse into the oxide layer.

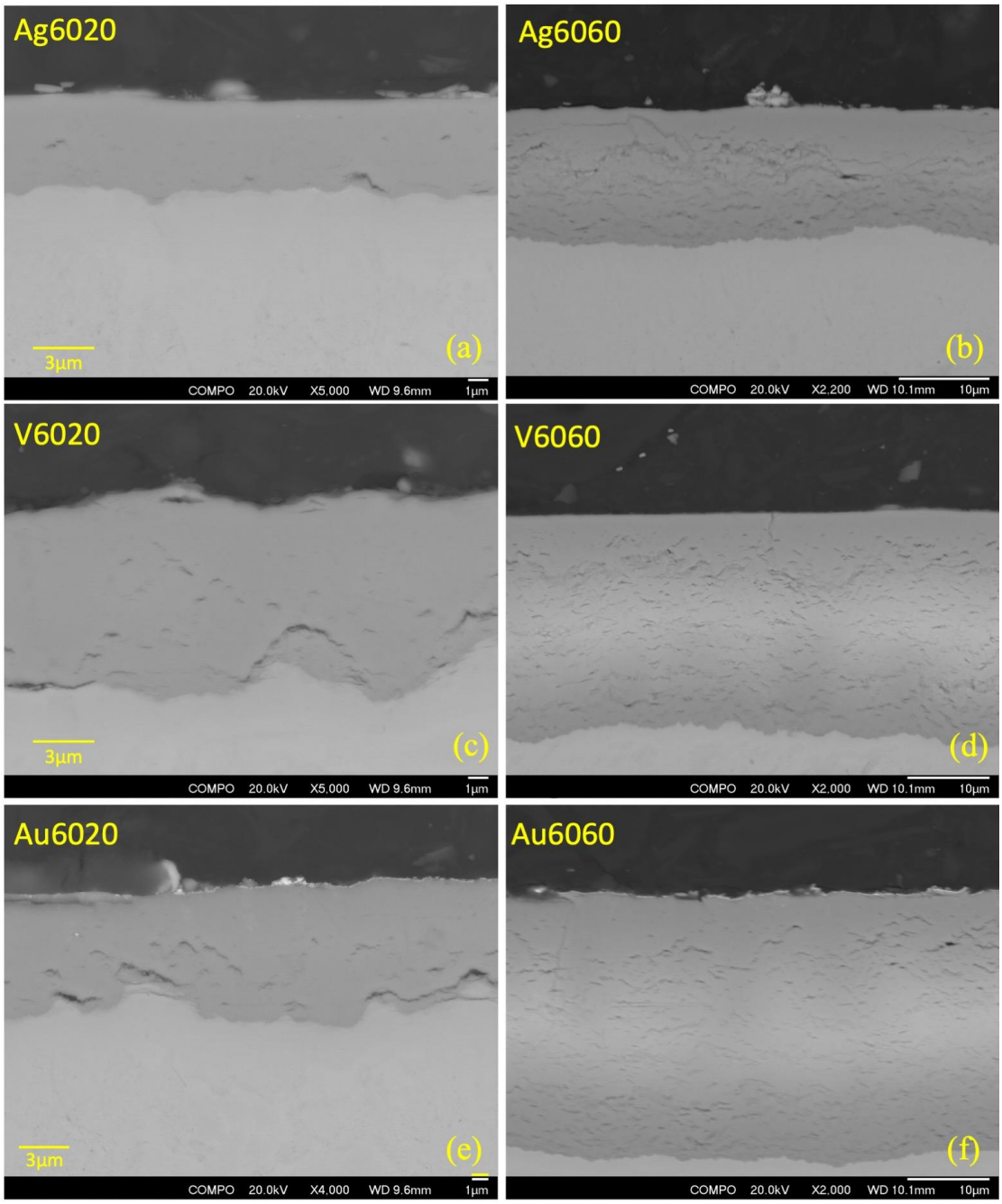
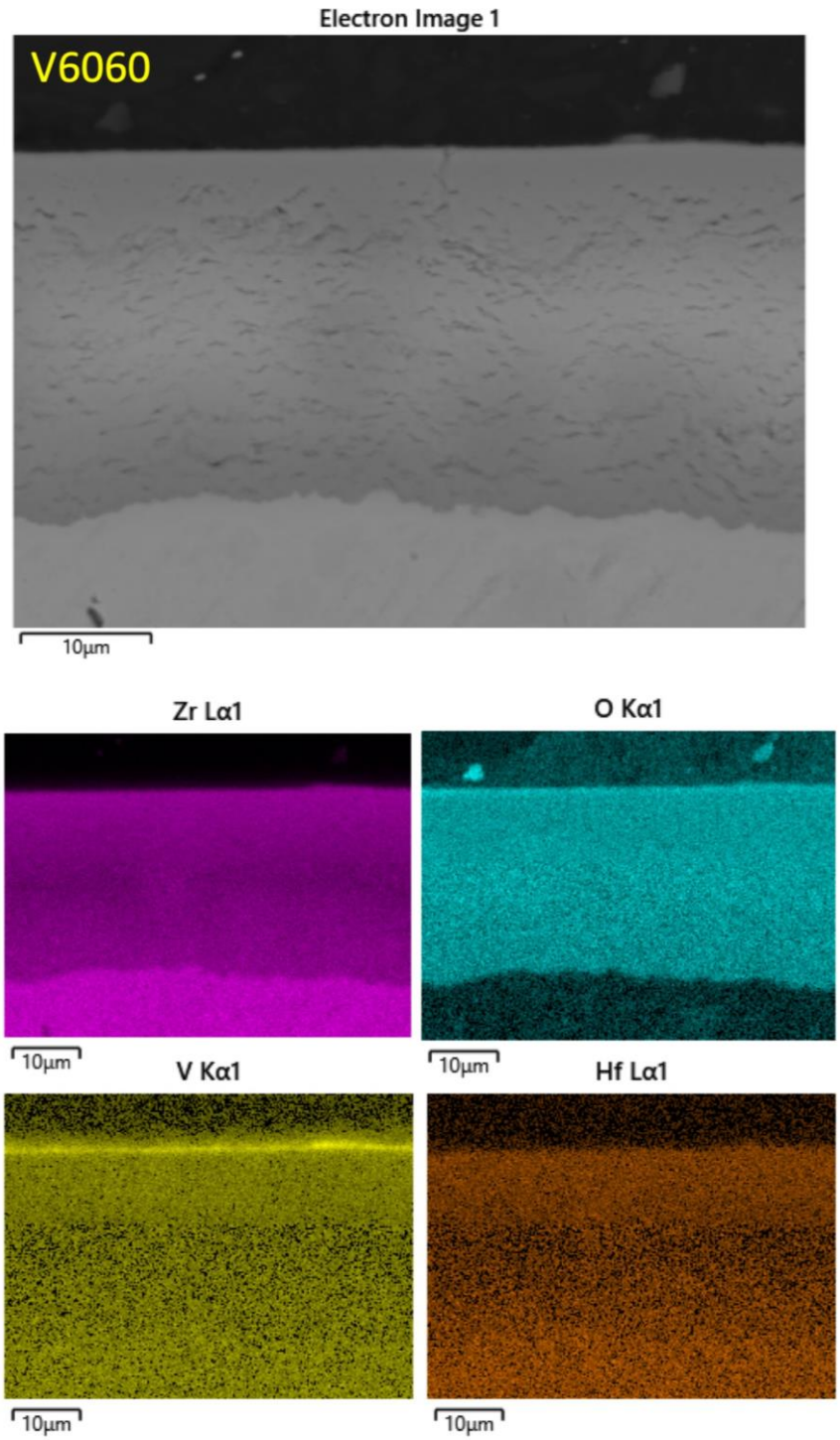
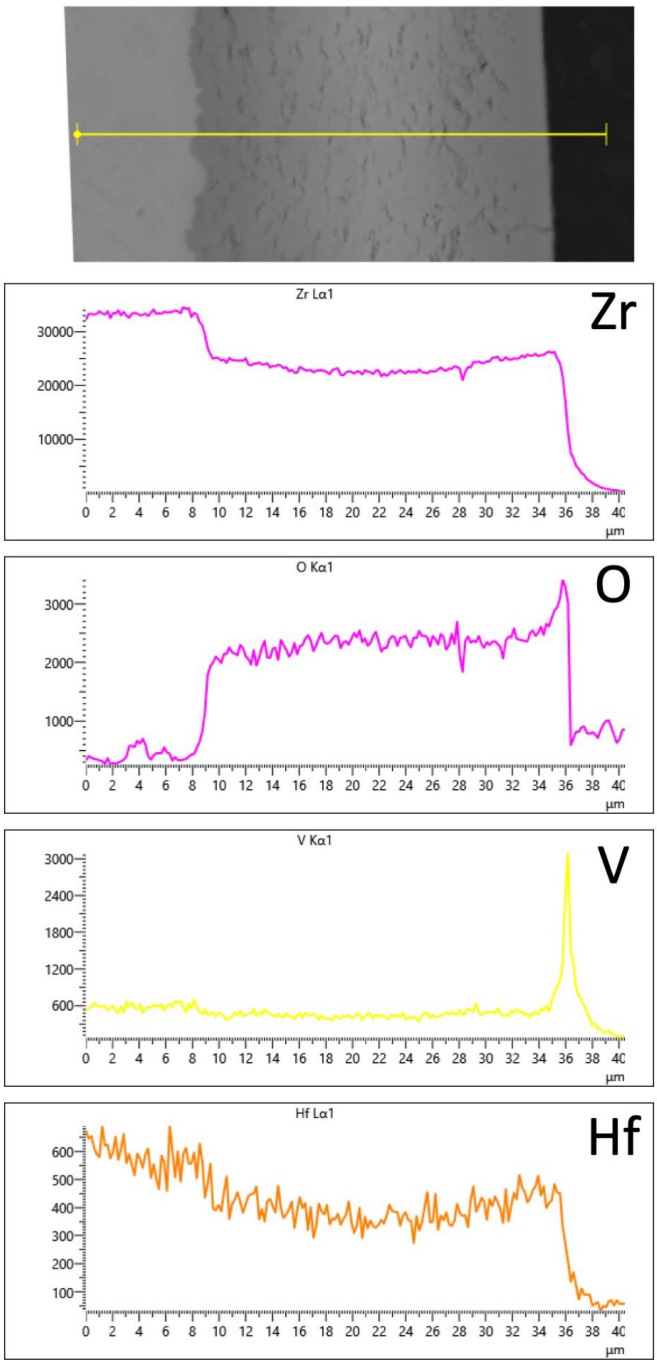


Figure 4.2-9 The cross-sectional SEM images of Ag, V and Au pre-deposited samples treated under 600 °C at 20 hours and 60 hours.


Electron Image 1
V6060
10µm
Zr Lα1
10µm
O Kα1
10µm
V Kα1
10µm
Hf Lα1
10µm

(a)



(b)

Figure 4.2-10 The cross-sectional SEM images of V6060 sample with (a) the EDX mapping and (b) line-scan analysis.

4.2.3 Phase and microstructure analysis

Phase identification of 10-hour treated samples were presented in Section 4.1.3 and the phases detected are summarised in Table 4.1-2. It is revealed that the main oxide phase formed is the monoclinic ZrO_2 and other oxides related to the deposited elements, such as Ag_2O, V_2O_5 and PdO, are also detected from related samples. XRD scans were carried out on samples treated for different time periods and the resulting patterns are similar with the ones taken from the 10-hour treated samples in terms phase constitutes but varied intensity of the diffraction peaks, reflecting the oxide layer thickness of the samples. In this section, detailed XRD analysis of different time periods, 600°C treated Au pre-deposited C3T samples will be presented. Further TEM characterisation of C3T Au6010, C3T Au6040 compared with C2T5010 samples will show detailed layer microstructures of the surface layers.

4.2.3.1 XRD

The XRD patterns of the 5 minutes (at 600 °C) treated C3T sample with Au pre-deposition, Au6000, are presented in Figure 4.2-11 comparing with the Unt sample. The fcc Au (111) peak was observed at 2θ position of 38.2 °. Comparing with the Zr phase peaks of the Unt sample, the m-ZrO_2 phases detected were compared with the Zr phase peaks of Unt sample at 2θ positions of 28.2° and 34.3° etc., indicating the efficient catalytic effect of Au on oxidation in short period of time.

	NO.	Ref. Code	Chemical Formula	Crystal System
	1	01-089-4892	Zr	Hexagonal
	2	01-089-9066	ZrO_2	Monoclinic
	3	00-001-1172	Au	Cubic
	4	00-014-0534	(ZrO_2)	Tetragonal

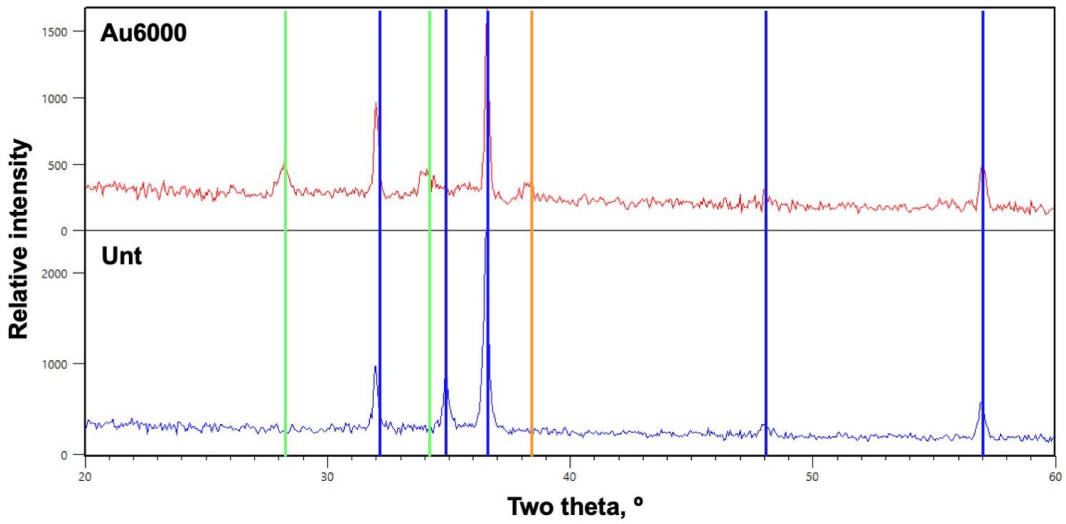


Figure 4.2-11 The XRD analysis of the short time (5mins) C3T treated Au pre-deposited samples at 600 °C comparing with the Unt sample.

Figure 4.2-12 presents the XRD patterns of 40-hour (at 600 °C) treated C3T sample with Au pre-deposition, Au6040, comparing with the Unt sample. No characteristics Zr peaks have been observed for the Au6040 sample. Apparent fcc Au (111) peak was observed at 2θ position of 38.2 °. The dominant peaks are related to the m-ZrO_2 and it was found that with the longer treatment time, there are more new detected peaks corresponding to m-ZrO_2 as compared with the XRD patterns of the Au6000 sample. As shown in Figure 4.2-11, the m-ZrO_2 peaks were not only observed at 28.2° and 34.3° but also observed at higher 2θ positions of 35.8°, 45.6° and 55.5° etc. The tetragonal t-ZrO_2 peaks were hardly seen according to the XRD patterns, but the existence of the t-ZrO_2 was confirmed in the TEM results, which is presented in the next section.

	NO.	Ref. Code	Chemical Formula	Crystal System
	1	01-089-4892	Zr	Hexagonal
	2	01-072-1699	ZrO_2	Monoclinic
	3	00-089-3697	Au	Cubic
	4	00-014-0534	(ZrO_2)	Tetragonal

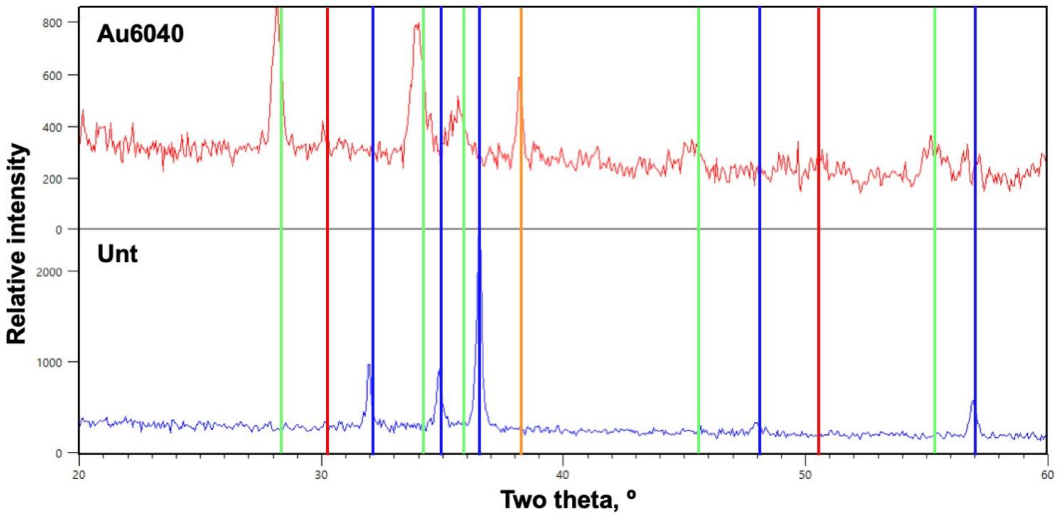


Figure 4.2-12 The XRD analysis of the longer time (40 hours) C3T treated Au pre-deposited samples at 600 °C comparing with the Unt sample.

Figure 4.2-13 outlines the XRD patterns of all the Au pre-deposited C3T samples treated at 600 °C with different treatment time periods, ranging from 5 mins to 60 hours. The C3T XRD patterns are compared with the Unt sample. With the increase of the treatment time, it was found that the Zr peaks disappear, particularly when treated for 20 hours and longer. The strong m-ZrO_2 peaks were seen for the C3T samples with longer treatment time above 5 hours. The increased intensity of the m-ZrO_2 peaks and the disappear of the Zr peaks indicate the increase of the surface oxide layer thickness.

	NO.	Ref. Code	Chemical Formula	Crystal System
	1	01-089-4892	Zr	Hexagonal
	2	01-089-9066	ZrO_2	Monoclinic
	3	00-001-1172	Au	Cubic
	4	00-014-0534	(ZrO_2)	Tetragonal

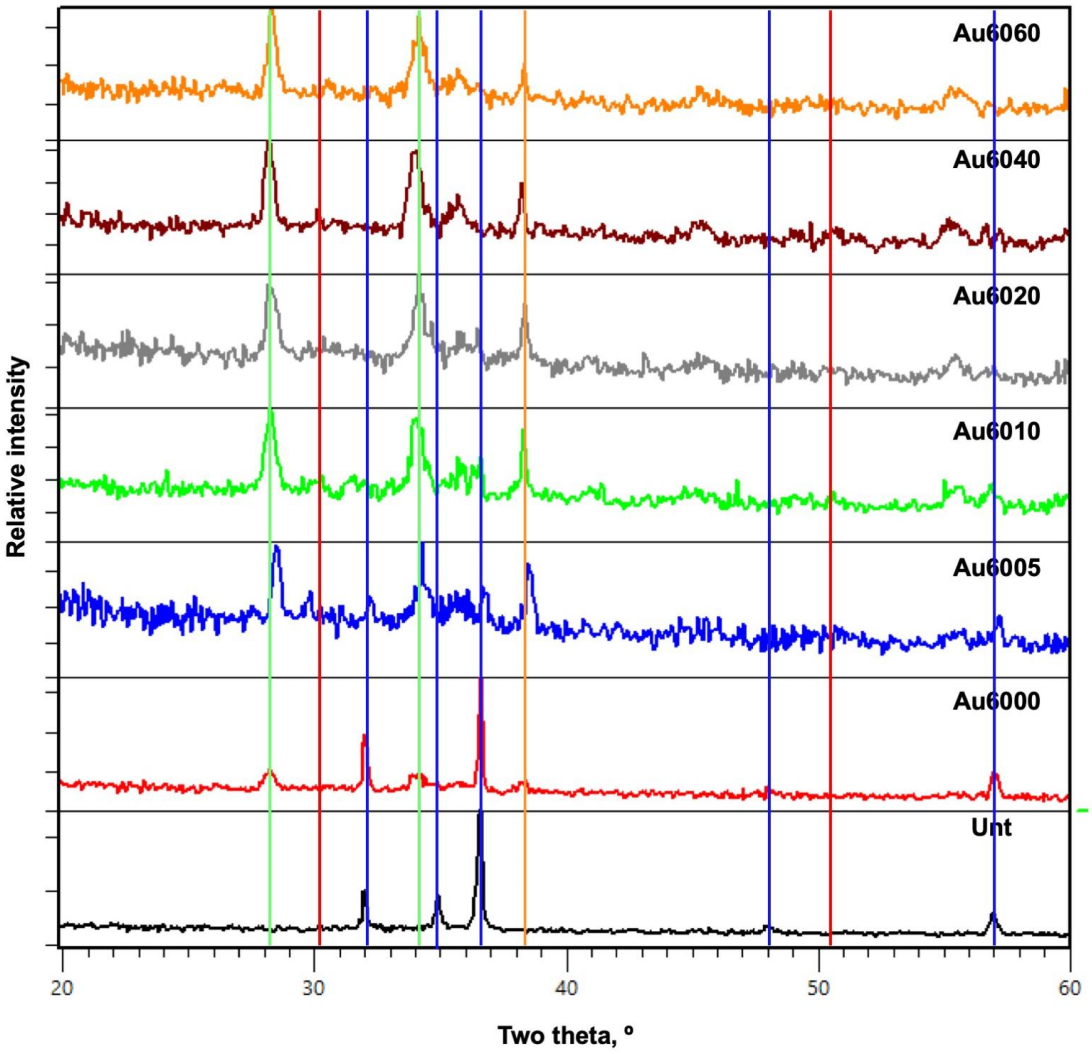


Figure 4.2-13 The XRD analysis of the Au pre-deposited samples after the C3T treatment, samples treated at 600 °C for different periods of time, i.e. Au6000 (5 mins), Au6005 (5 hours), Au6010 (10 hours), Au6020 (20 hours), Au6040 (40 hours) and Au6060 (Au6060), comparing with the Unt sample.

4.2.3.2 TEM characterisation of C2T and C3TAu samples

Samples of C2T5010, C3T Au6010 and C3T Au6040, were selected for TEM characterisation to investigate the detailed layer structures for typical C2T and C3T samples.

Figure 4.2-14 shows TEM microstructure and corresponding selected area diffraction patterns of C2T sample. It shows that the treated surface is composed of a fine columnar structured layer, oriented in perpendicular to the sample surface and a horizontally grown grain interface layer along the oxide/matrix interface (Figure 4.2-14 (a)).

The corresponding SAD patterns taken from the oxide layer revealed a ring pattern (Figure 4.2-14 (b)) and the indexing of the rings revealed a preponderance of the monoclinic ZrO_2 (m-ZrO_2) phase with a trace of the tetragonal ZrO_2 (t-ZrO_2) phase planes, as evidenced by the bright dense rings for the former and weak diffused rings for the latter, although the latter are superimposed with the former. The indexing for the oxide diffractions is in good agreement with the indexing of the X-ray diffraction patterns as has reported in Figure 4.1-8.

Figure 4.2-14 (c) is a diffraction pattern taken from the horizontally grown grain interface layer. Indexing of this SAD pattern identified B=$[0001]_{Zr}$ and a $[2\bar{1}\bar{1}0]$ $ZrO_{0.35}$, zirconium substoichiometric phase i.e., $ZrO_{0.35}$, with a preferred orientation of $[2\bar{1}\bar{1}0]_{ZrO_{0.35}}$ // $[0001]_{Zr}$, (0002)//($\bar{1}$010). It is also observed that the diffraction spots of the Zr are elongated and diffused, indicating a high density of the defects in the area beneath the oxide layer. This is contributed from the residual stress between the

oxide layer and the substrate and the diffused-in oxygen in the interstitial space of the HCP Zr crystal, or diffusion zone.

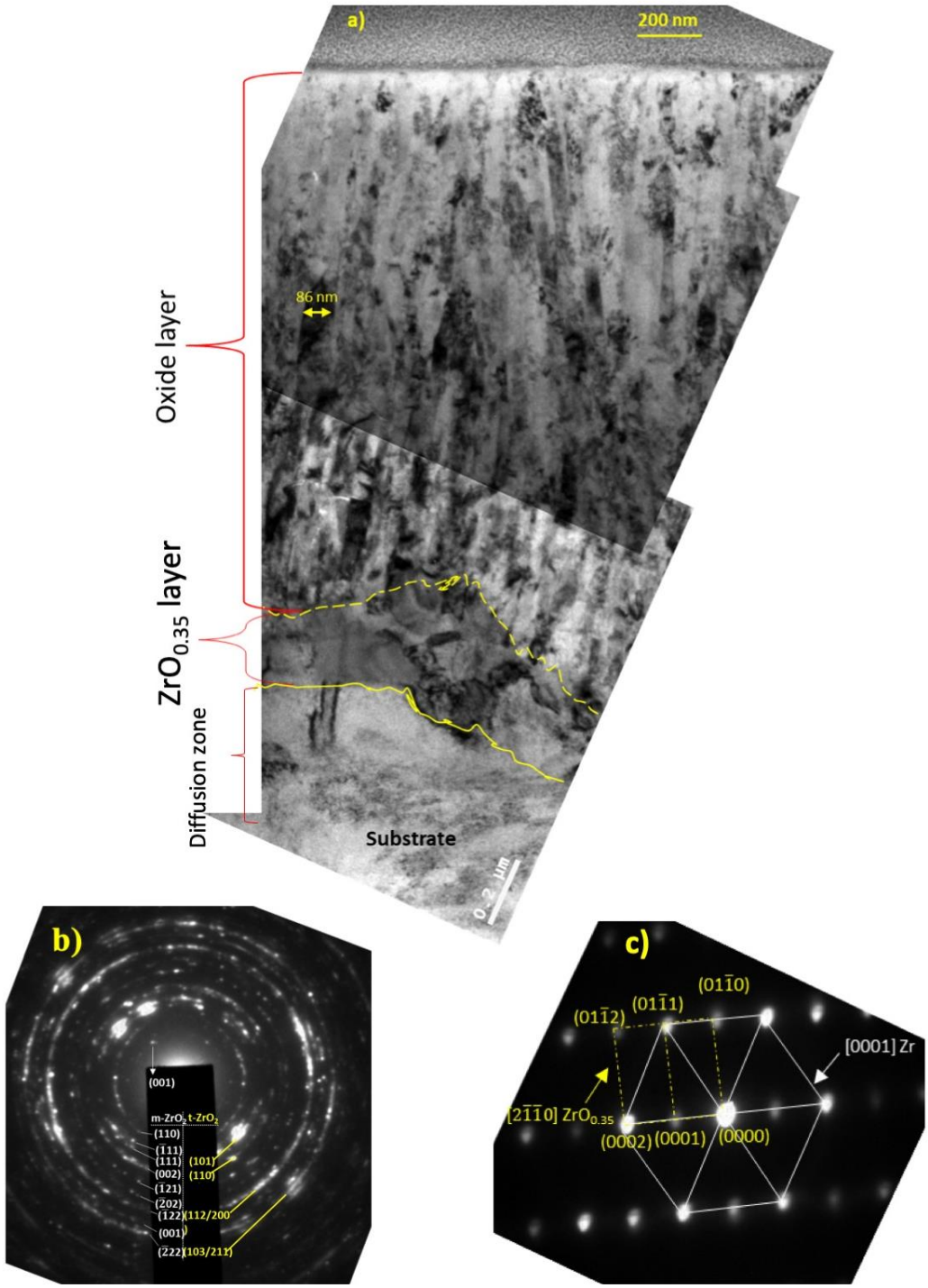


Figure 4.2-14 TEM microstructure of C2T5010 (a) surface oxide layer structure, interface and substrate; corresponding SAD patterns of (b) surface oxide layer, and (c) horizontally grown grain interface layer.

Figure 4.2-15 shows a typical TEM microstructure of C3TAu sample at the top-most area of the oxidised layer. It can be seen that there is a dark contrasted layer at the top of the columnar oxide layer. SAD patterns taken from the top dark contrasted layer revealed diffused/broaden ring pattern, which can be indexed to fcc phases of Pt and Au (Figure 4.2-15 (b)) as their d-spacings are very close. Analysis of the SAD patterns from the columnar structure indicates the monoclinic structure of ZrO_2 as evidence in Figure 4.2-15 (c). However, some faint rings of a tetragonal ZrO_2 phase cannot be ruled out, as they are superimposed with the m-ZrO_2 as indicated in Figure 4.2-14 (b). Further STEM observation with EDX mapping was carried out to further investigate the top-layer structures. Figure 4.2-16 presents the outcome of the high-angle annular dark-field scanning transmission electron microscopy (HAADF-STEM) image and the elements mapping of the corresponding area. It can be seen that the top layer is enriched in gold, and underneath this layer, Au is distributed discretely across the layer with some areas enriched with Au. Based on the SAD pattern analysis and the STEM mapping, it can be concluded that the top thin layer is a gold enriched m-ZrO_2 layer as no other phases can be identified from SAD patterns taken from the top layer areas.

Compared with the columnar oxide layers formed on C2T and C3T samples, it is observed that the columnar width of the C2T is about 86 nm, while for C3TAu, it is only about 30nm in width as indicated in Figures 4.2-15 (a) and (d), nearly 1/3 of the width of C2T. This implies the catalytic effect of Au on the ceramic conversion of Zr702 alloy. Detailed discussion will be given in Section 5.1.

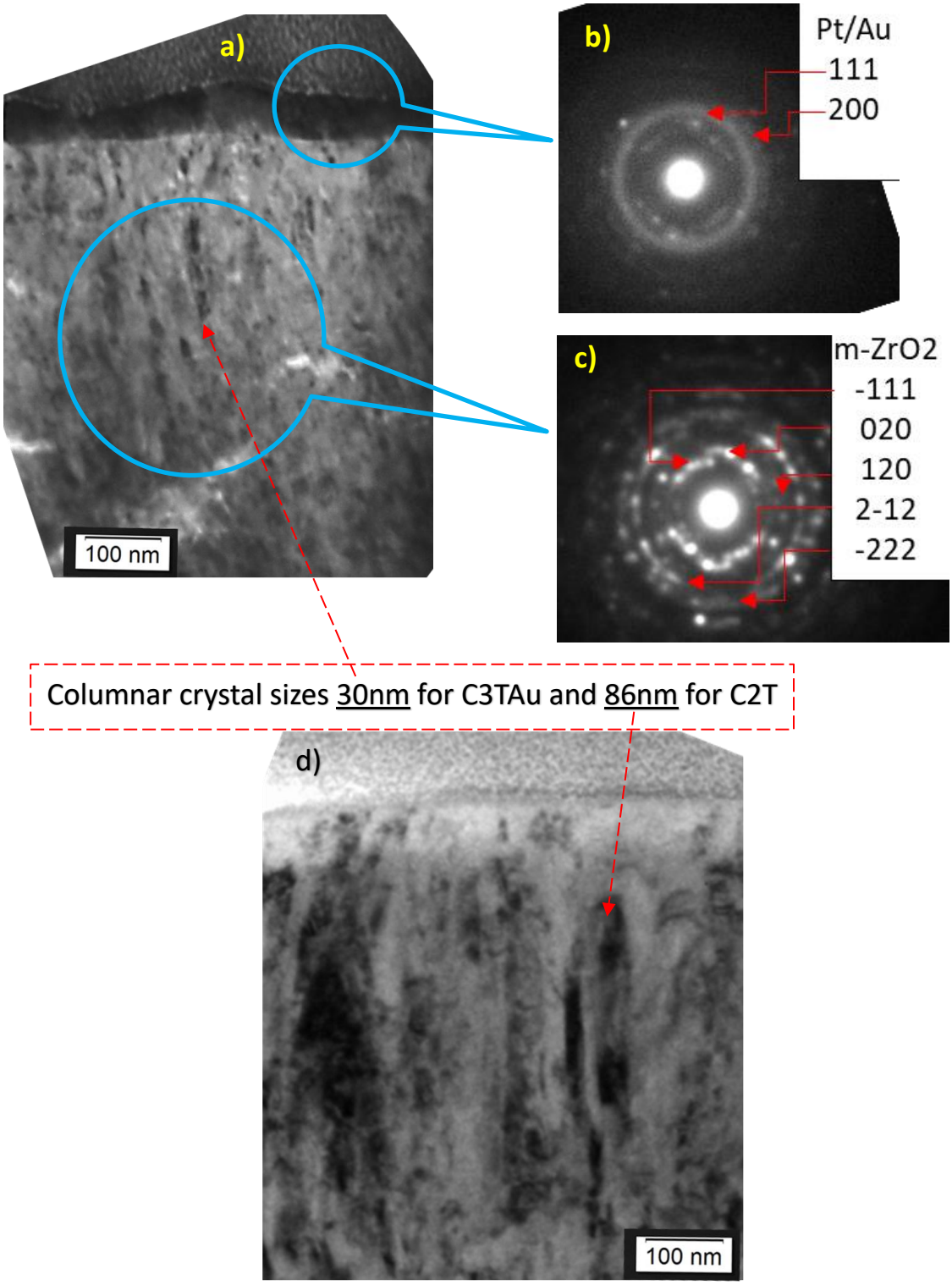


Figure 4.2-15 TEM microstructure of C3T6010 (a) surface oxide layer structure and corresponding SAD patterns of (b) top surface layer, and (c) dominant columnar oxide layer. d) TEM image of C2T in the same scale bar to a) for columnar grain width comparison.

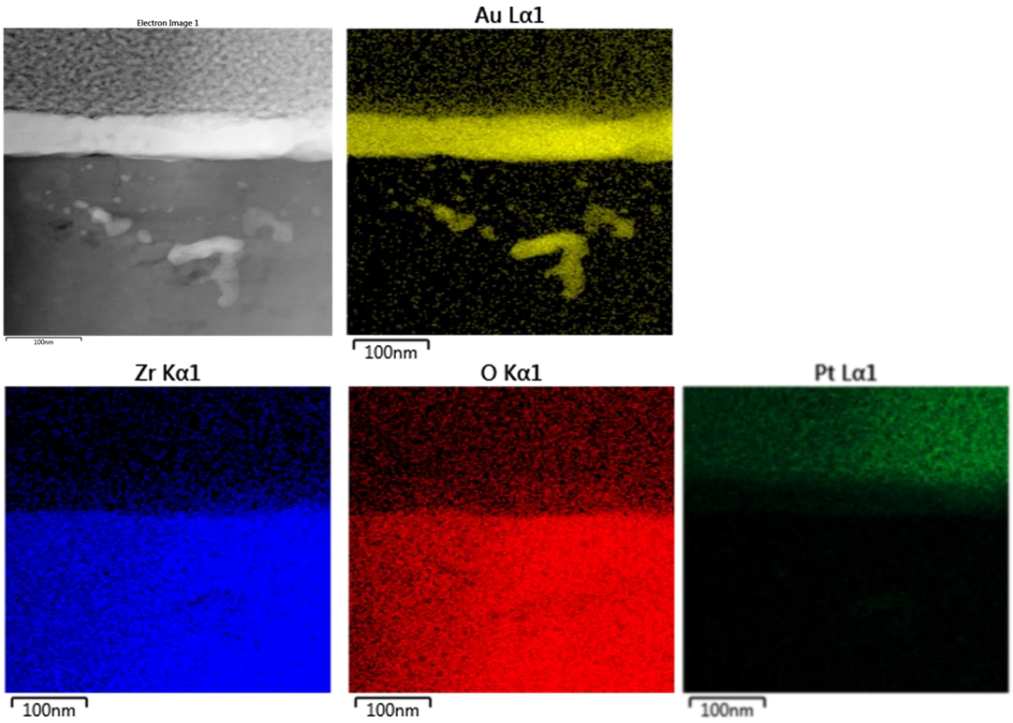
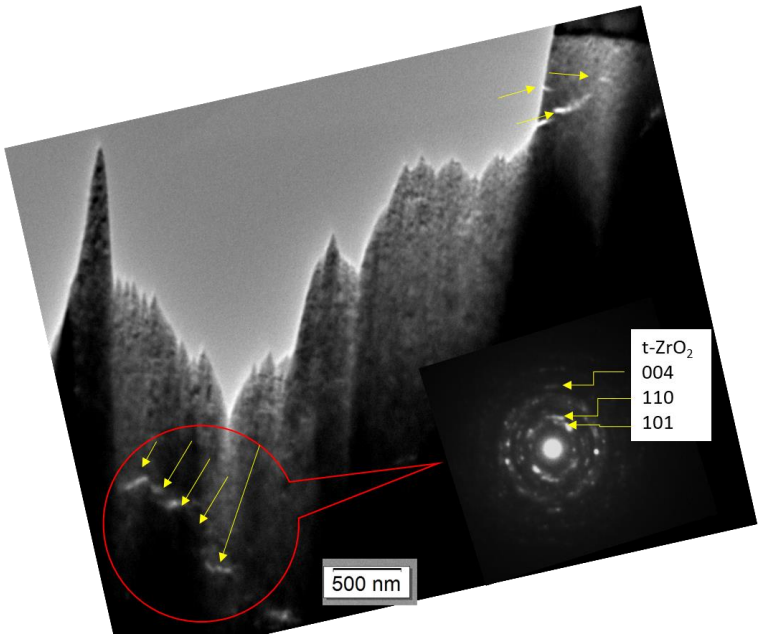
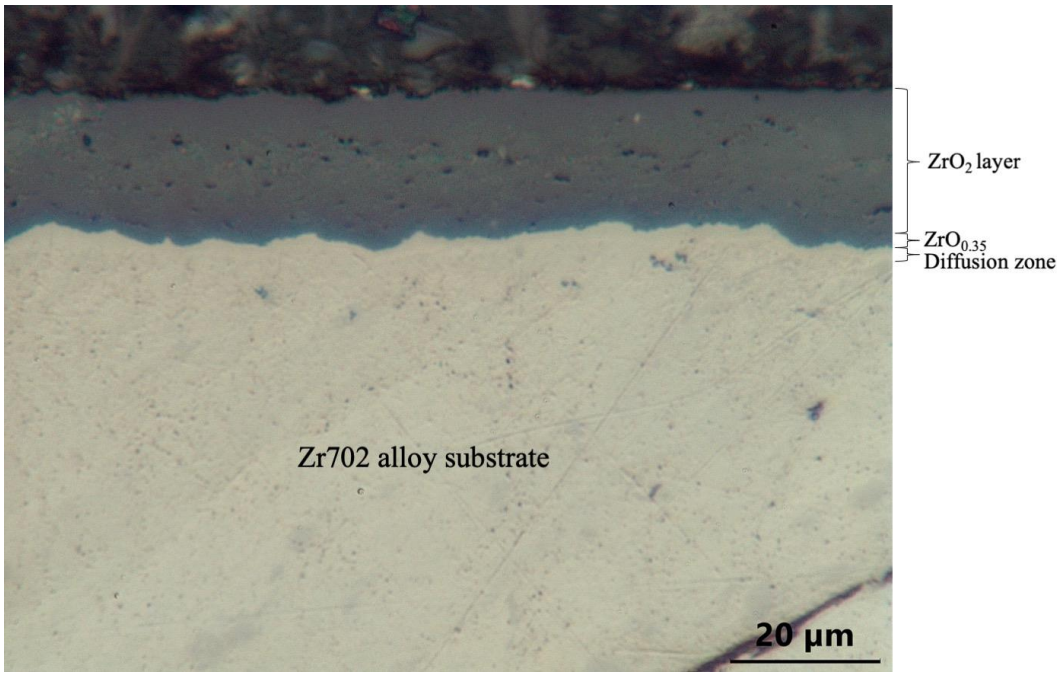


Figure 4.2-16 High-angle annular dark-field scanning transmission electron microscopy (HAADF-STEM) analysis of C3TAu6040 sample: STEM image of the surface layer at the top area and corresponding elements mappings as indicated.



(a)



(b)

Figure 4.2-17 (a) TEM microstructure and SAD pattern of C3TAu6040, showing lateral cracks, related to the formation of t-ZrO2 phase, and (b) optical image of the C3TAu6040 sample (polished without etching), revealing typical layer structures.

Figure 4.2-17 shows TEM microstructure within a relatively large area of sample C3TAu6040. Some lateral cracks (parallel to the oxide/matrix interface), 50-250 nm in length, were observed within the oxide layer (as denoted by arrows in Figure 4.2-17), which were also shown in SEM images (Figure 4.2-9). Similar features were also observed from C2T sample (Figure 4.2-14). SAD patterns took from these areas show some intermittent rings and calculated d-spacings are corresponding to the t-ZrO2 phase (see inserted SAD pattern in Figure 4.2-17)). As it is well known that the t-ZrO_2 is a high temperature oxide, which forms when oxidised above 1200°C. However, high stress induced t-ZrO_2 under low temperature of 350-415°C were observed by researchers [105, 106]. It is stated that the initiation of this tetragonal oxide is close to the oxide/metal interface, as the expansion of the surface oxide induced a highest residual stress here. However, the stresses in the oxide decrease with increasing distance to the oxide/metal interface [107, 108, 109] during the oxidation process, causing the tetragonal oxide grains to transform into monoclinic grains. As discussed in Section 2.1, the transfer of t-ZrO_2 to m-ZrO_2 accompanies 3-4% volume increase (Figure 2.1-2 (b)). There will be a substantial increase in the stress levels when the transformation occurs, causing the existing cracks to propagate and form a continuous band of cracks.

It needs to be emphasised that the lateral cracks observed under current C3T conditions are in a moderate state as neither apparent surface cracks nor spallation caused by the lateral cracks were observed on the samples examined, as evidenced by the optical image of C3TAu6040 sample shown in Figure 4.2-17 (b). This optical image also shows clearly the layer structures, especially the interface layers, of the C3TAu: 1) ZrO_2 layer (including top ZrO_2 with rich gold as shown in Figure 4.2-15

(a); 2) a bluish zirconium substoichiometric phase $ZrO_{0.35}$ layer, and 3) an oxygen diffusion zone of Zr(O), revealing smooth white feature, resulted from the increased hardness within this zone as indicated in Figure 4.4-3.

4.3 Corrosion behaviour of ceramics conversion treated Zr702

As stated in the last chapter, the corrosion behaviour of ceramic conversion treated Zr702 alloy has been investigated by the electrochemical testing of the treated surfaces in 3.5 wt% NaCl solution. The polarisation curves are obtained and analysed, the tested areas are observed under the SEM to study the anti-corrosion behaviours and the relevant mechanisms involved, and the corrosion rate (in the unit of milli-inches per year, mpy) is calculated. The results are reported in this section through comparing the corrosion behaviour of C3T samples with the Unt and C2T samples.

4.3.1 Corrosion properties of Unt and C2T samples

According to electrochemical theory, the electrochemical behaviour of a tested surface can be judged by the potentiodynamic polarisation curves obtained from the electrochemical tests: the more positive the corrosion potential (E_{corr}) is and the smaller the corrosion current density (I_{corr}) is, the better corrosion properties the sample will have [2, 110]. The E_{corr} and I_{corr} values were measured by applying Tafel fit to the polarisation curves using the Gamry Echem Analyst software, as outlined in Section 3.4. Summary of the E_{corr} and I_{corr} values including the full list of the data are reported in Section 4.3.5. The potentiodynamic polarisation curves were plotted

between the logarithms of corrosion current lg(*i*) and potential in voltage against reference voltage of reference electrode (Vf (V vs. ref)).

The potentiodynamic polarisation curves for the Unt and C2T samples are shown in Figure 4.3-1. The sudden increase in the corrosion current density of the Unt sample in the anodic zone of the curve at a potential of about 0.54 V_{SCE} (Voltage against Supersaturated Calomel Electrode (SCE)) is an indication of severe pitting of the sample. With further increase of the potential, the corrosion current continues to increase and remains at a high value. The localised pitting corrosion will destruct the untreated sample surface, mainly caused by action of the chloride ions as pitting agents. In contrast, no pitting occurred on the C2T sample because no pitting potential could be identified from the C2T polarization curve. Although the C2T sample exhibits slightly more negative E_{corr} than that for the untreated Unt sample, the corrosion current density of the former is consistently lower than that of the latter.

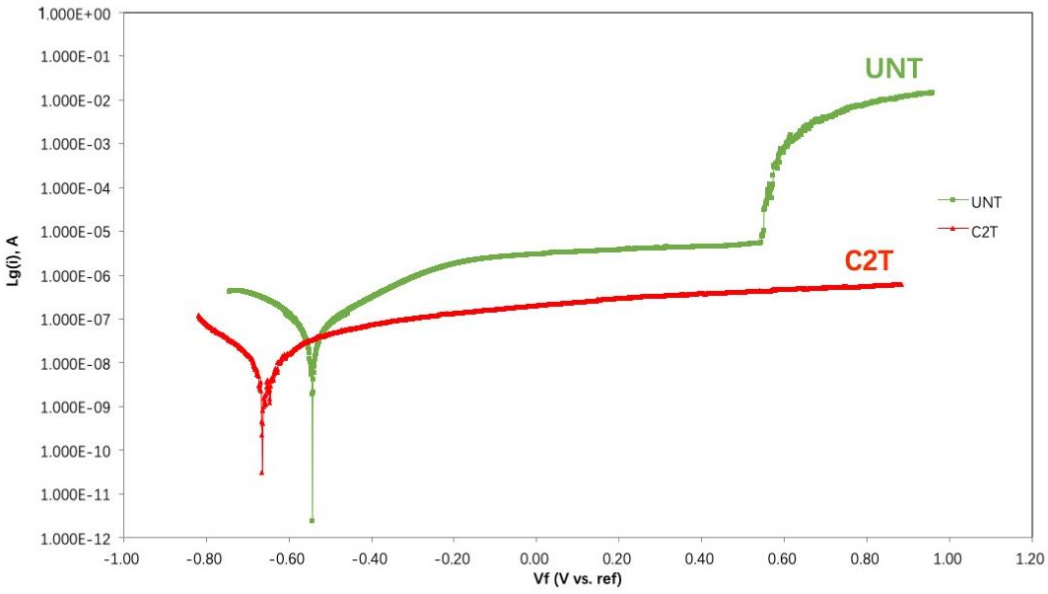


Figure 4.3-1 The polarisation curves of Unt and C2T samples.

The post-test SEM observation of the corroded surface of the untreated sample has been carried out and the surface morphology of the corroded surfaces are shown in Figure 4.3-2. Figure 4.3-2 (a) shows part of the corroded surface where some NaCl particles could be seen on the tested surface with some tiny pits and cracks observed, which indicate the intergranular corrosion of the untreated surfaces. Figure 4.3-2 (b) shows the corrosion pit formed in the untreated sample surface, with a diameter of 1.6mm. Higher magnification images (Figure 4.3-2 (c)) taken inside the corrosion pit revealed lamellar morphology inside with many micro pits.

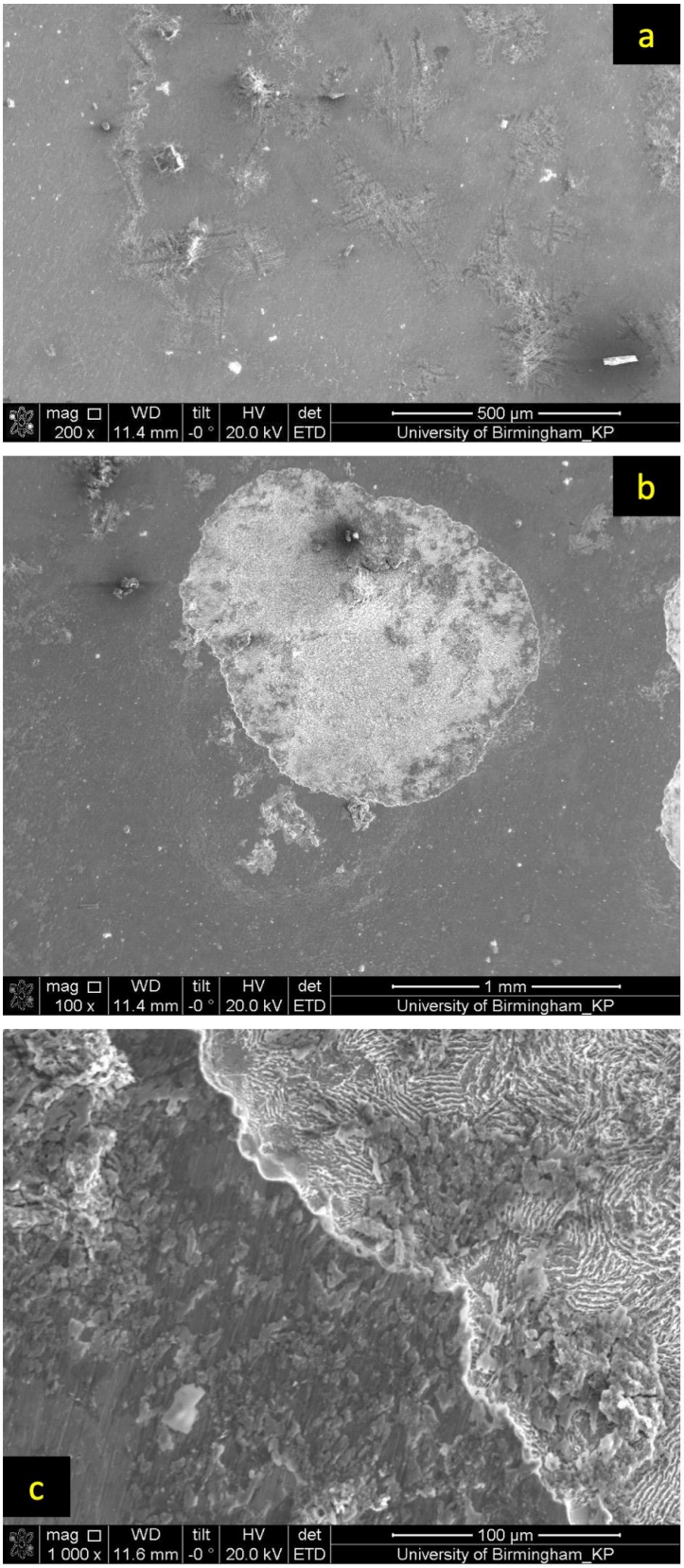


Figure 4.3-2 The SEM images of corroded Unt sample surface after the electrochemical test showing (a) intergranular corrosion and (b) & (c) pitting corrosion.

The SEM images of the corroded surface of C2T sample are shown in Figure 4.3-3. The edge of the corroded area is marked by a yellow dash line as shown in Figure 4.3-3 (a). No appreciable differences could be found from the tested surface as compared with the as-treated surface outside the tested area. In Figure 4.3-3, (b) and (c) present the features of un-tested part of the sample surface whereas (d) and (e) present the features of the tested area of the sample surface. It can be seen that mild uniform corrosion morphology was observed on the corroded surface; apart from this no other major differences can be observed between the untested (i.e., uncorroded) part and the corroded part. It thus can be concluded that the C2T treated surfaces possess better corrosion properties as compared to the untreated sample. The formation of the ZrO_2 ceramic layer should provide a barrier to corrosion, thus protecting the zirconium alloy substrate from the attack of the corrosion solution with Cl^- anions.

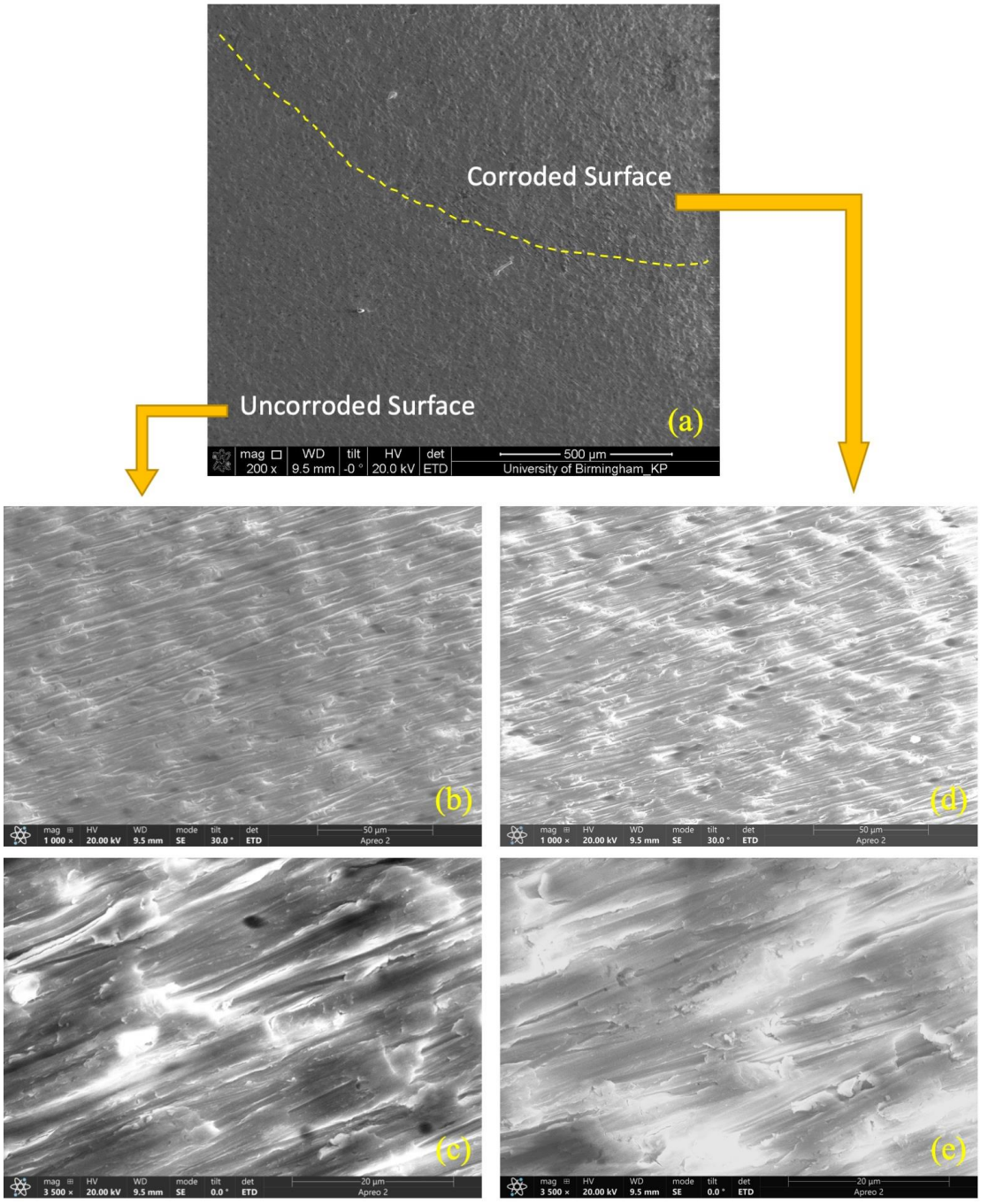


Figure 4.3-3 The SEM images of C2T6010 sample surface after the corrosion test. (a), (b) and (c) located outside the tested aera, (d) and (e) located inside the tested area.

4.3.2 Samples of C3T with pre-deposition of Au

The potentiodynamic polarisation curves of Au pre-deposited samples treated at 600 °C but with different treatment durations (5 hours, 10 hours, 20 hours, 40 hours and 60 hours) are put into a group to compare (Figure 4.3-4), along with the C2T sample. It can be seen from the figure that Au6010, Au6040 and Au6060 have very small I_{corr} values (only 3.2%, 5.5% and 4.5% of the I_{corr} value of C2T); however, the E_{corr} values for these samples are relatively negative compared to Au6005 sample. Au6040 has similar E_{corr} value (-657.0 mV) to the C2T (-655.0 mV) but with much smaller I_{corr} value. In general, the C3T Au pre-deposited samples have either more positive E_{corr} or smaller I_{corr} compared with the C2T sample, and no pitting potential (no corrosion current density rise) can be identified on the curves, showing improved corrosion properties. Furthermore, Au6005 and Au6060 have both more positive E_{corr} and smaller I_{corr} values indicating that these samples demonstrated even better anti-corrosion properties in all Au pre-deposited samples and also the C2T sample in terms of E_{corr} and I_{corr}.

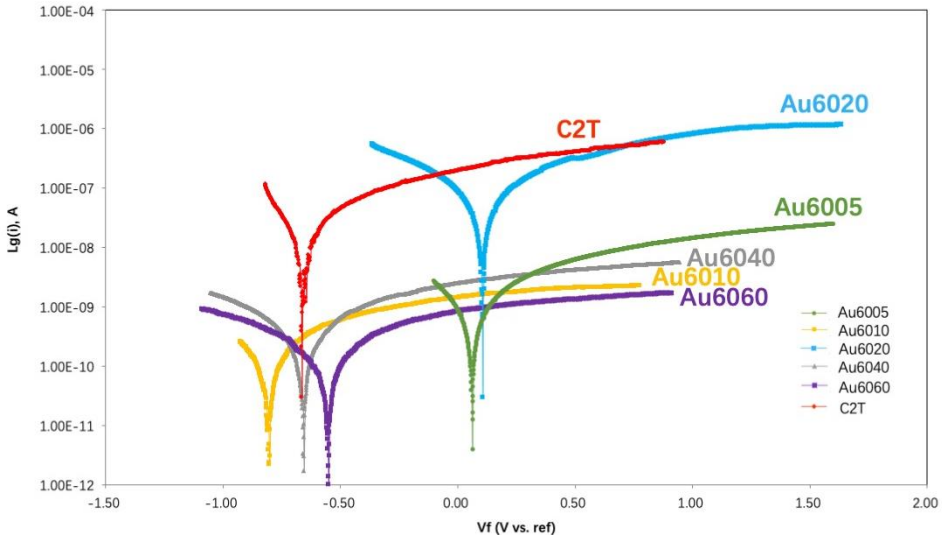


Figure 4.3-4 The polarisation curves of selective Au pre-deposited sample treated (Au6005, Au6010, Au6020, Au6040 and Au6060) with different treatment durations compared with the C2T sample.

Figure 4.3-5 shows the SEM observations on the sample surface of the Au6010, Au6040 and Au6060 samples after the electrochemical tests. The SEM images in the left column (i.e. Figures 4.3-5 (a), (c) and (e)) were taken on the untested (i.e. uncorroded area), whereas the other images (i.e. Figures 4.3-5 (b), (d) and (f)) were taken on the corroded areas. As exemplified in Figure 4.3-5, nearly identical surface morphologies have been observed before and after the electrochemical tests for all the C3T Au pre-deposited samples, except for the Au6060 sample. After the test, superficial thin oxide layer corrosion was observed from the Au6060 sample surface (Figure 4.3-5 (f)). The initial minor corrosion could be related to the cracks formed during long duration oxidation treatment, evidenced in Figure 4.2-9 (f) and Figure 4.3-5 (f) marked by red arrows. However, the corrosion curve indicates the best corrosion behaviour in terms of the lowest corrosion current density and highest corrosion potential, which is most probably related to the dense oxide layer beneath the top cracked layer.

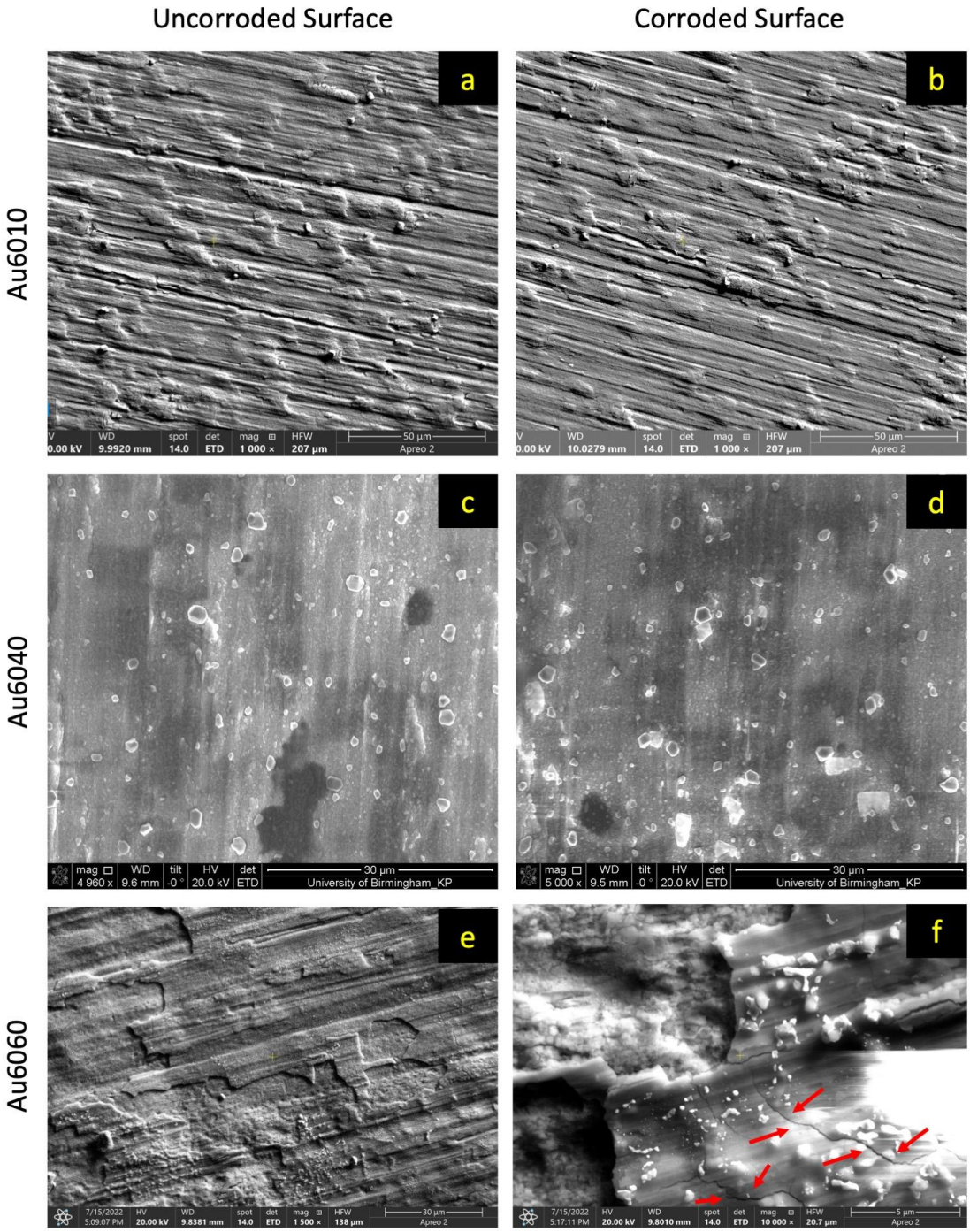


Figure 4.3-5 The SEM images of corroded (i.e. (b), (d) and (f)) and uncorroded (i.e. (a), (c) and (e)) surface for Au6010, Au6040 and Au6060 samples respectively after the corrosion test.

As noted above, the polarisation curves of Au6005 and Au6020 position further to the right than the other curves for other C3T Au pre-deposited samples and C2T sample. The much more positive E_{corr} values of Au6005 and Au6020 samples may be related to the high concentration of pre-deposition of Au, which is a noble metal. The corrosion tested areas of Au6005 and Au6020 are rich in gold as evidenced by colour chem SEM images shown in Figures 4.3-6 (b) and (c). The high concentration of the Au on the Zr702 alloy surface may lead to better protection of the zirconium substrate underneath.

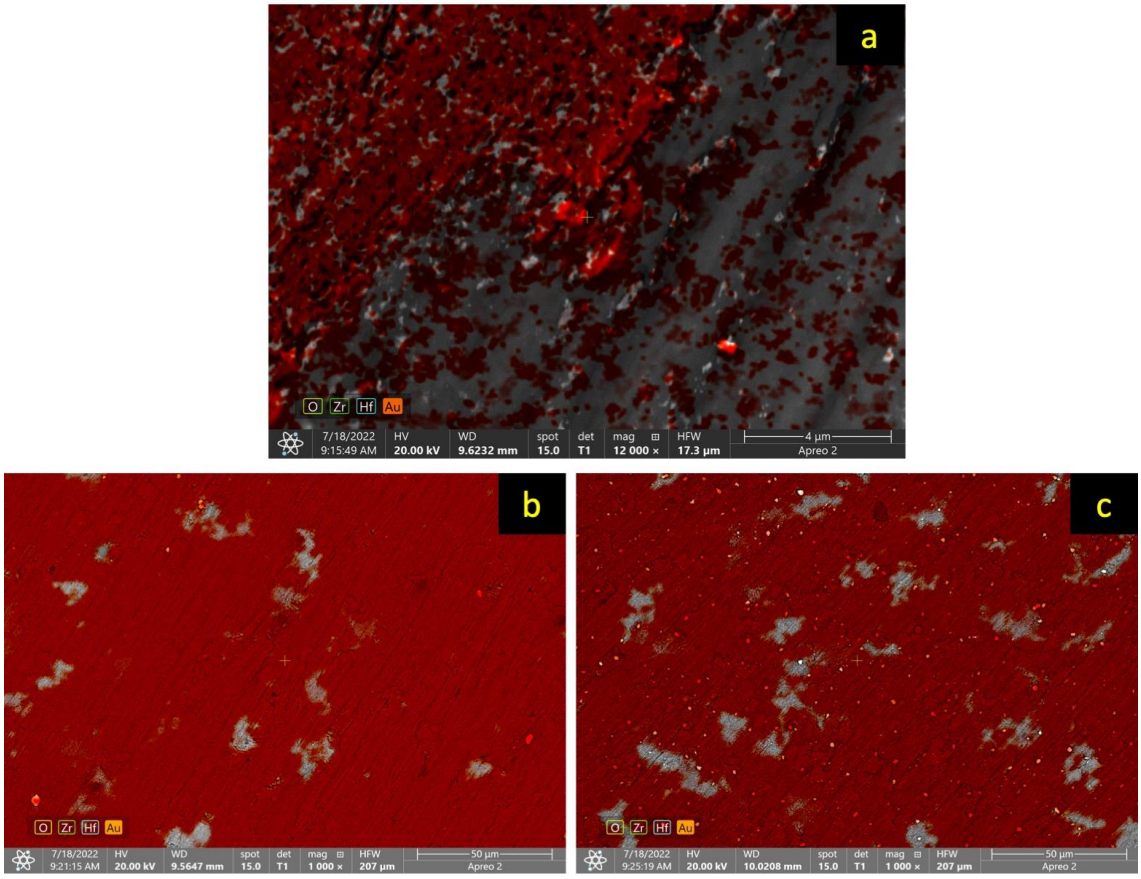


Figure 4.3-6 The SEM images of Au6005 and Au6020 sample surface after the corrosion test. (a) the surface of Au6005 sample showing the unevenness of gold deposition; (b) and (c) the corroded surface of Au6005 and Au6020 sample.

Generally, all C3T Au pre-deposited samples showed good anti-corrosion behaviours. Au6005, Au6010, Au6020 and Au6040 samples share very similar features and very

identical surface morphology observed between the corroded and uncorroded surface from the SEM images. Superficial thin oxide layer corrosion has been observed on Au6060, which is caused by the cracks formed in long time oxidation, but it did not cause an increase of the corrosion current density in the polarisation curve.

4.3.3 Samples of C3T with pre-deposition of Ag

As shown in Figure 4.3-7, the potentiodynamic polarisation curves of Ag pre-deposited samples treated at 600 °C but with different treatment time (10 hours, 20 hours and 40 hours) are put into a group to compare with the C2T sample. Clearly, all Ag pre-deposited samples were found to show more positive E_{corr} values (-545.0 mV for Ag6010, -535.0 mV for Ag6020 and -639.0 mV for Ag6040) than C2T (-655.0 mV). Ag6020 and Ag6040 have even smaller I_{corr} values and with more positive E_{corr} values, demonstrating better anti-corrosion properties than short duration treated (20 hours) C3T Ag sample and C2T sample in terms of E_{corr} and I_{corr}.

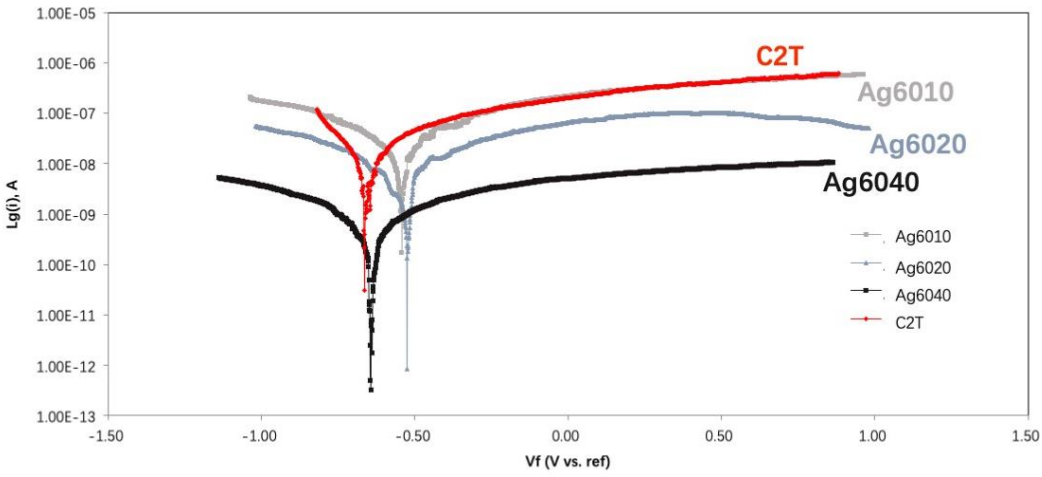


Figure 4.3-7 The polarisation curves of selective Ag pre-deposited sample treated (Ag6010, Ag6020 and Ag6040) with different time compared with the C2T sample.

Figure 4.3-8 shows the results of SEM observations on the corroded and uncorroded surfaces of Ag6020 and Ag6040 after the corrosion test. Figures 4.3-8 (a) and (b) compares the uncorroded area and corroded area of Ag6020 sample, showing no apparent surface morphology change, with only minor features of uniform corrosion observed from the corroded surface.

The orange dashed line in Figure 4.3-8 (c) marks out the uncorroded area (left) and the corroded area (right) of Ag6040 samples after the corrosion test. Figures 4.3-8 (d) and (e) zooms into the detailed features spotted in the corroded area of Ag6040 sample. A few shallow patches of mild corrosion areas have been observed in the corroded area of Ag6040 sample as shown in Figure 4.3-8 (d), which might be caused by the surface layer defects after long time oxidation. The localised corrosion (corrosion pit length around 100 μm and width 52 μm) was observed (Figure 4.3-8 (e)) for Ag6040 sample.

Therefore, the Ag6020 possesses the best anti-corrosion properties across the C3T Ag pre-deposited samples when considering both the E_{corr} and I_{corr} and the subsequent corrosion morphology.

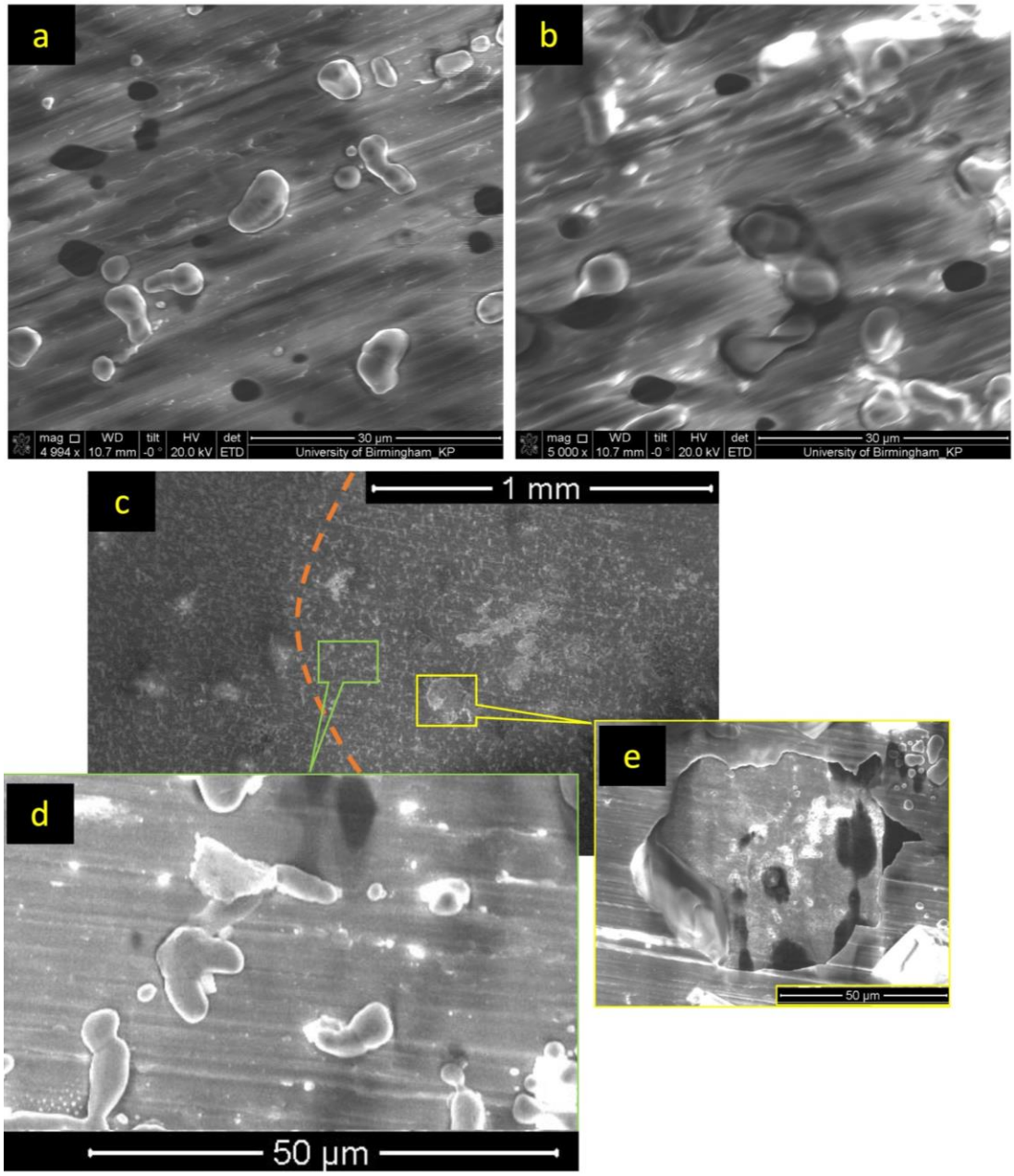


Figure 4.3-8 The corrosion morphology of Ag6020 and Ag6040 samples: (a) presents the uncorroded surface and (b) presents the corroded surface of Ag6020 samples. (c) shows the surface of Ag6040, the corroded area is marked out and the detailed features in this area are shown in (d) and (e).

4.3.4 Samples of C3T with pre-deposition of V

Figure 4.3-9 includes the potentiodynamic polarisation curves of V pre-deposited samples treated at 600 °C for 10 hours, 20 hours and 40 hours along with the C2T for comparison. Compared with C2T, V6010 has similar E_{corr} but slightly larger I_{corr}. V6020 sample has a much smaller value of I_{corr} but with the 'more negative' E_{corr}. In terms of both E_{corr} and I_{corr}, V6040 sample outperforms all other V pre-deposited samples as it is the only sample in this group having both more positive E_{corr} and smaller value of I_{corr}.

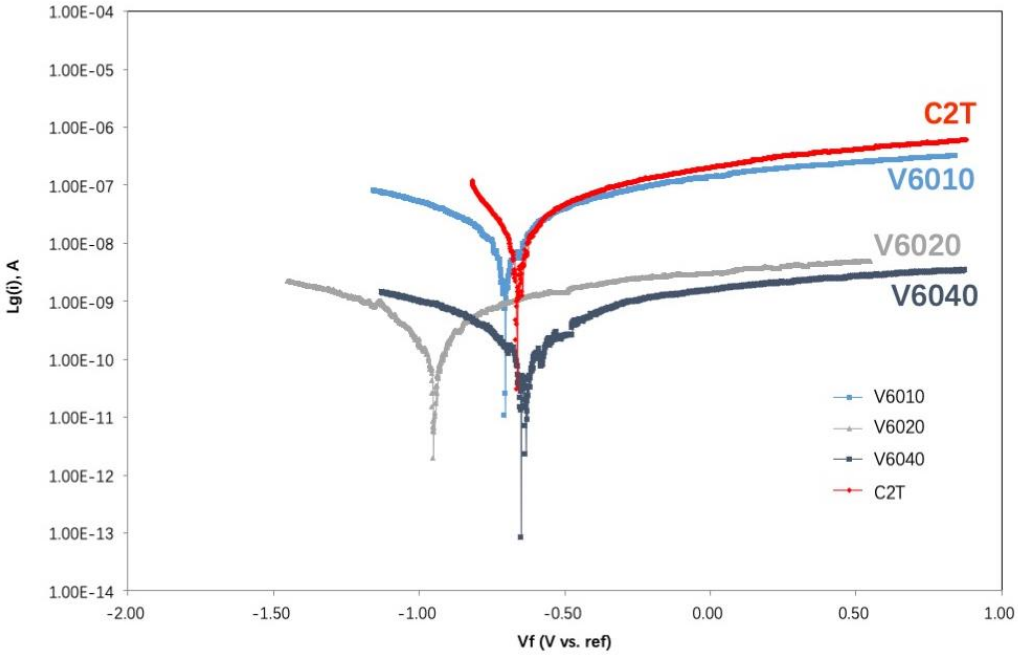


Figure 4.3-9 The polarisation curves of selective V pre-deposited sample treated (V6010, V6020 and V6020) with different time compared with the C2T sample.

The Figure 4.3-10 shows the corrosion morphology of the uncorroded and corroded surfaces of the V6010 and V6040 samples. Both samples in Figure 4.3-10 show nearly identical surfaces for uncorroded and corroded area and exhibit very good corrosion resistance. No localised corrosion (i.e., corrosion pits) or any other major corrosion features have been observed on the surface of these samples. The

differences of E_{corr} and I_{corr} of V6040 with other samples could be caused by the different morphology of vanadium oxide formed during different durations as shown in Figure 4.3-10.

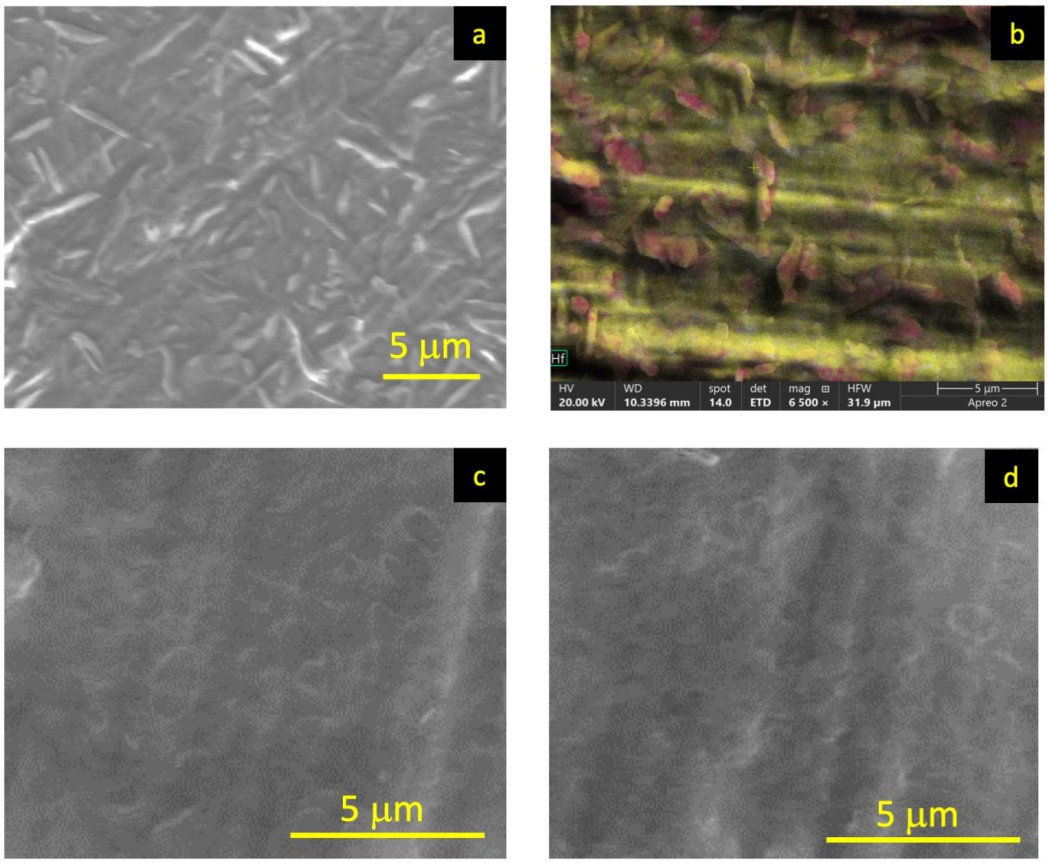


Figure 4.3-10 The SEM images of (a) V6010 and (c) V6040 samples surface before and after the corrosion test (i.e. (b) presents the corroded surface for V6010, and (d) presents the corroded surface for V6040, where (a) and (c) presents uncorroded surface).

4.3.5 Summary of E_{corr} and I_{corr}

Table 4.3-1 summarises the corrosion potential E_{corr} and corrosion current density I_{corr} values obtained by applying the Tafel fit, and the corrosion rate in mpy is calculated. In terms of calculated corrosion rate, the C2T sample shows less corrosion rate compared to the untreated samples, and most of the C3T samples show about 20 times to 40times reduction in corrosion rates as compared with the Unt sample apart from

Ag6010, Au6020 and V6010 showing higher corrosion rates. However, as stated above, according to the SEM observation on the corroded surface of these three samples, nearly identical surface between corroded area and uncorroded area were observed on these samples and no localised corrosion observed, except for the Ag6040 sample, which presented with obvious and severe corrosion pits.

Comparing all the tested samples, Au6010 sample exhibits the best in anti-corrosion properties.

Table 4.3-1: Summary of the corrosion potential E_{corr} and corrosion current density I_{corr}, with calculated corrosion rate in mpy.

Sample code	**E_{corr}, mV**	**I_{corr}, A/cm^2**	**Corrosion rate, mpy**
Unt	-543.0	99.90e-9	45.64e-3
C2T	-655.0	75.60e-9	34.55e-3
Ag6010	-545.0	944.0e-9	431.4e-3
Ag6020	-535.0	4.750e-9	2.169e-3
Ag6040	-639.0	5.930e-9	2.708e-3
Au6005	67.00	5.760e-9	2.634e-3
Au6010	-805.0	2.440e-9	1.114e-3
Au6020	107.0	257.0e-9	117.4e-3
Au6040	-657.0	4.160e-9	1.901e-3
Au6060	-559.0	3.390e-9	1.547e-3
V6010	-698.0	378.0e-9	172.8e-3
V6020	-946.0	2.840e-9	1.296e-3
V6040	-628.0	2.970e-9	1.355e-3

4.4 Mechanical and tribological properties of C3T samples

The C3T samples have been investigated on their surface hardness, hardness depth profiles along the depth, the coefficients of frictions and the wear properties, figuring out the effects of C3T on property enhancement. The results will be outlined based on the considerations of comparing the roles of the different pre-deposited elements and the treatment duration, and the data will be compared with C2T and Unt samples as well.

4.4.1 Hardness of 600 °C C3T treated samples

4.4.1.1 600 °C/10-hour treated C3T samples

The surface Vickers hardness values of 600 °C/10-hour treated samples are plotted in Figure 4.4-1. The Vickers hardness values are measured under the loads of 0.1, 0.05 and 0.025 kg and are compared with the untreated sample. According to the results, the ceramic conversion treatments with pre-deposited layer produced a surface hardened layer with the surface hardness between 950 to 1400HV. It has also been found that except for the untreated surface, the hardness values are lower when measured under 100g (HV0.01) than measured under 50g (HV0.05). Low hardness 400HV0.05-0.1 was measured for C2T sample with a surface layer less than 4 μm (but still twice that of the surface hardness of the untreated sample). A high value of 1000HV0.025 was measured for C2T sample when further reducing the load to 0.025kg.

It can be also seen that the surfaces of the C3T samples are all much harder than that of the C2T surface. This could be mainly due to the significantly increased surface oxide layer thickness (see Figure 4.1-12). However, the oxide layer thickness for Ag6010, V6010 and Pd6010 samples is very similar but the hardness of V6010 (C3TV) and Pd6010 (C3TPd) samples, 1380 and 1280HV0.05, respectively, is higher than Ag6010 (1014HV0.05). Hence, the measured high surface hardness could be also related to the formation of the oxide of V_2O_5 and PdO on the surfaces, which were identified via XRD reported in Section 4.1.3.

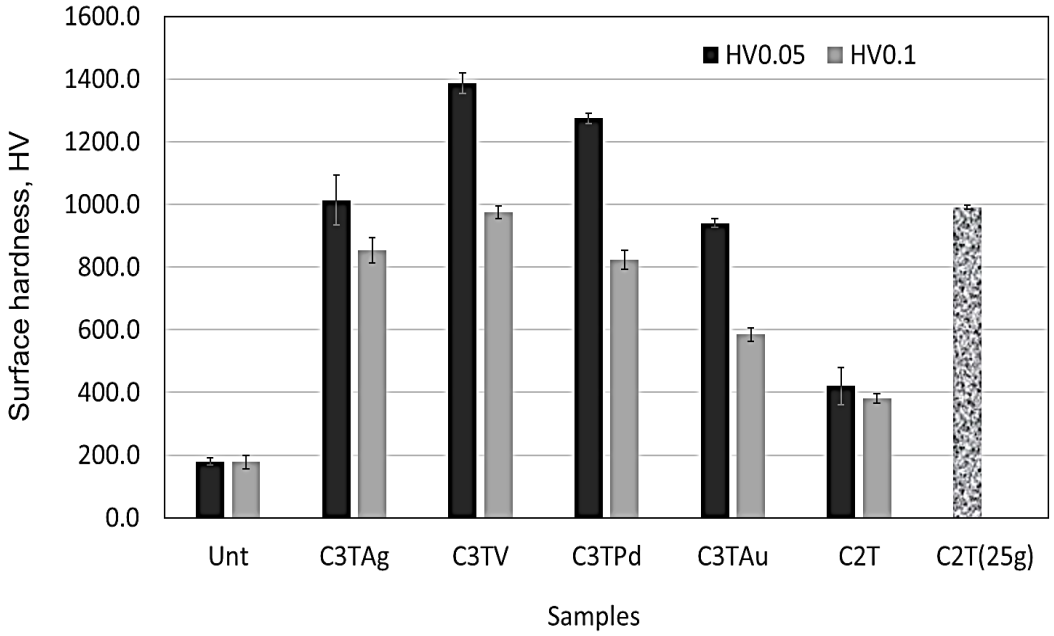


Figure 4.4-1 Surface hardness of C2T and C3T samples treated under 600 °C/10h, compared with the untreated sample.

4.4.1.2 C3T treatment duration effects

The surface Vickers hardness values of C3T Au pre-deposited samples treated at 600 °C for different period of time, from 5 mins to 60 hours, are plotted in Figure 4.4-2.

The Vickers hardness values were measured under loads of 0.1 and 0.05 kg compared with that of the untreated sample. According to the results, the ceramic conversion treatment with Au pre-deposited layer produced a surface hardened layer with the surface hardness between 920 to 1100HV. In general, the surface thickness measured under both loads increased as the treatment duration increased. Lower surface hardness was measured with heavier loads for most of the samples, e.g., 455HV0.1 for Au6005, and for Au6010 as has been shown in Figure 4.4-1 and discussed above. Au6000 (5mins treatment) only produced limited improvement on the surface hardness compared to Unt sample, from 183HV0.05 to 211HV0.05, where the layer thickness formed for Au6000 is thin (2.258 μm). Samples with similar oxide layer thickness tend to have very identical surface hardness values for treatment time no more than 10 hours, particularly found with the lower load of 0.05 kg. For example, the surface hardness for Au6005 is 938HV0.05 and 950HV0.05 for Au6010, where the thickness for these samples is 5.586μm 5.28μm respectively. Further increase of the treatment duration above 10 hours further improved the surface hardness, but such trend was slowed down when the treatment duration was above 40 hours, as the 40-hour treated sample had similar surface hardness values compared to 60-hour treatment under both loads. The surface hardness for Au6040 and Au6060 is 1316HV0.05 and 1319HV0.05 (or 1050HV0.1 and 1090HV0.1) respectively, despite the 60-hour treatment increased the surface layer thickness to almost twice (31.463 μm) that of the Au6040 (16.601 μm). This will be further discussed in Chapter 5.

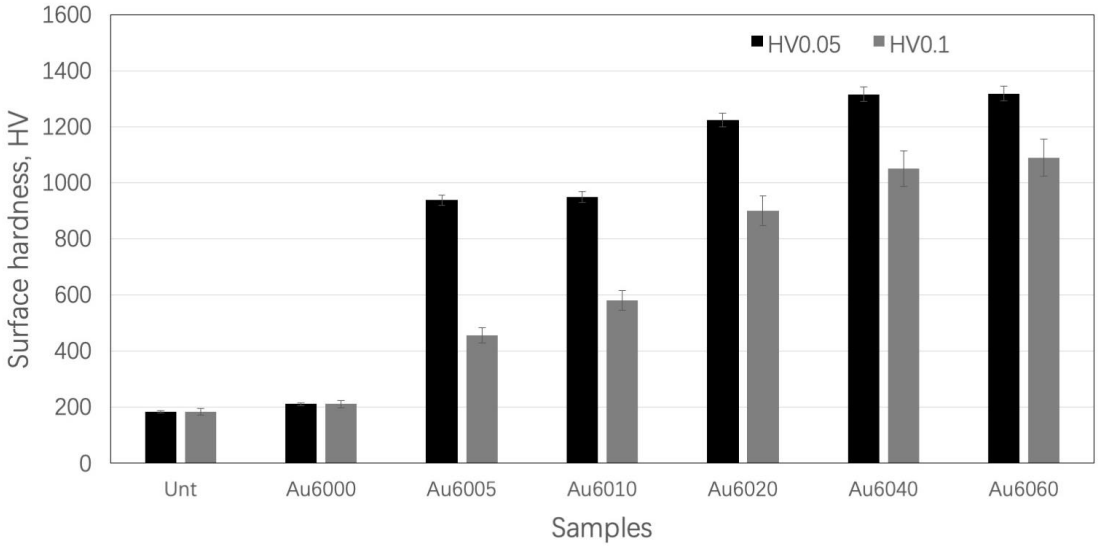


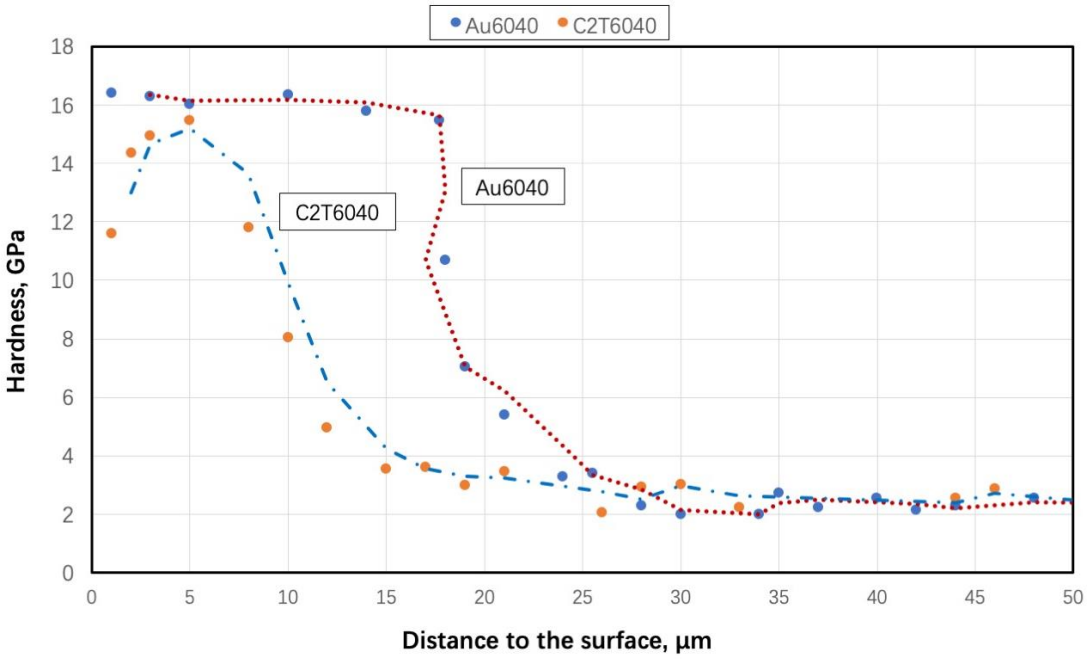
Figure 4.4-2 Surface hardness of C3T Au pre-deposited samples treated under 600 °C for different period of time ranging from 5 mins to 60 hours, compared with the untreated sample.

4.4.1.3 Hardness depth profiles

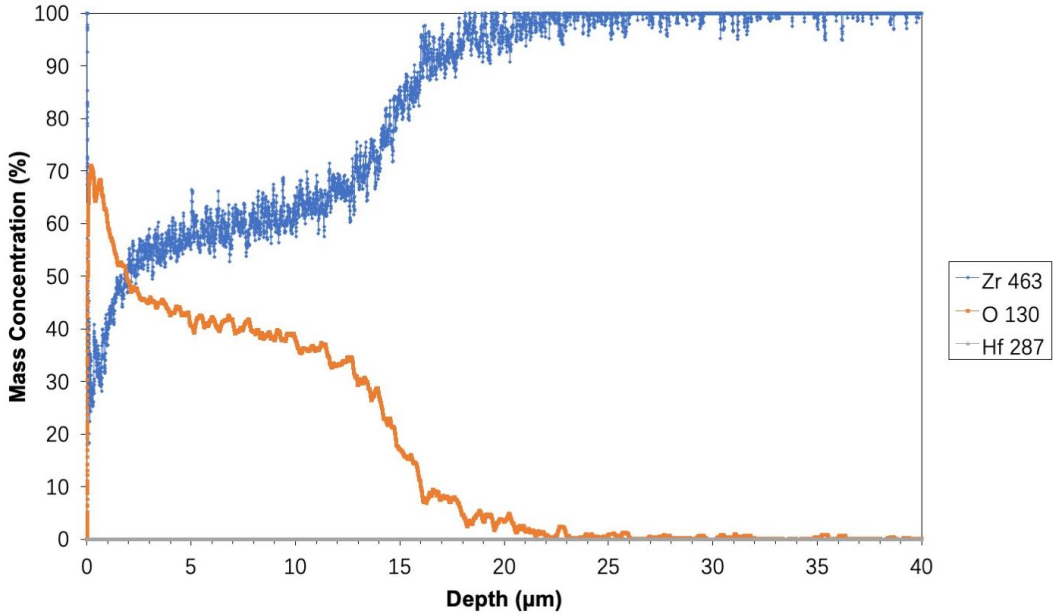
The cross-sectional hardness of selective C3T Au pre-deposited sample and C2T sample treated at 600 °C for 40 hours are obtained from the nanoindentation and plotted in Figure 4.4-3 (a) along the depth of the samples. As shown in Figure 4.4-3, the highest hardness value for the C3T Au6040 sample is at near-surface area (16.408 GPa) and remains almost constant between 15.47-16.3 GPa along the depth until the depth of 17.7 μm. The line then followed a sudden drop and then finally dropped to a steady hardness value of the Zr substrate (between 2-3 GPa) from the depth of 28 μm onwards. The zone with gradually reduced hardness with depth between 17 and 28 μm is the oxygen diffusion zone (ODZ) as revealed by GDOES oxygen depth profiling as shown in Figure 4.4-3 (b). The depth of the ODZ identified by nanoindentation method differs slightly from that by GDOES because they work on different physics principles.

The hardness values of C2T6040 increased from 11.61 GPa to 15.46 GPa as the depth increased to 5 μm, which is the highest obtained hardness value for the C2T6040 sample. The hardness values then dropped to a similar range as the near surface hardness value of 11.80 GPa at the depth of 8 μm. The ODZ is then followed until the depth reaching about 19 μm and finally remained constant at the Zr substrate hardness value of 2-3 GPa.

In Figure 4.2-8, the oxide layer thickness was measured as 6.3 μm for C2T6040 sample and 16.6 μm for Au6040 sample. By comparing the hardness changes along the depth of both samples and the oxide layer thickness measured, the high hardness value plateau of Au6040 sample or the hardness increase plateau of C2T6040 sample before the ODZ reached the similar depth of the oxide layer thickness, which indicates the high hardness values was attributed to the oxide formation. The varied hardness value near the top oxide layer of C2T6040 sample may link to the formation of the defects (such as pores and microcracks) formed within the layer. Both samples have similar depth of the hardness decreasing zone (HDZ) about 11 μm indicates the similar thickness of the oxygen diffusion zone (ODZ). The HDZ could be explained as the effects of strong solid solution hardening of oxygen in zirconium.



(a)



(b)

Figure 4.4-3 (a) Hardness depth profiles of C3T Au6040 sample and C2T6040 sample and (b) GDOES composition depth profiles of the C3T Au6040 sample.

4.4.2 Coefficient of Friction

Figure 4.4-4 shows the dynamic curves of the coefficient of friction (CoF) of Unt, C2T and 600 °C/10h treated C3T samples sliding with the WC-Co ball counterpart under a load of 20N for 1000 cycles. The CoF of the untreated Zr702 sample was around 0.15 at the beginning and increased gradually to 0.68 after 400 cycles and remained steadily for the rest of the cycles in the test. In contrast, significant reduction of CoF to 0.15-0.27 range can be seen for all ceramic conversion treated samples. This could be attributed to the ceramic layers formed during the ceramic conversion, which can reduce the metallurgical compatibility to the WC-Co counterpart surface and hence the adhesion. However, it is noted that Pd6010 and V6010 show high values within 100 and 450 cycles, respectively. This is believed to be caused by the high hardness of the surfaces, which will be further discussed in the later section.

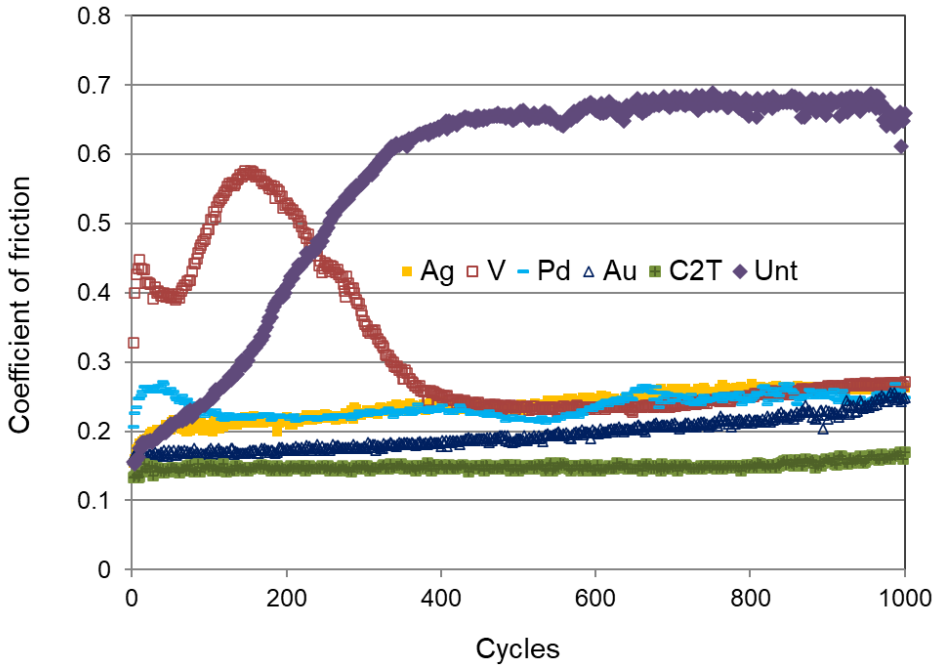


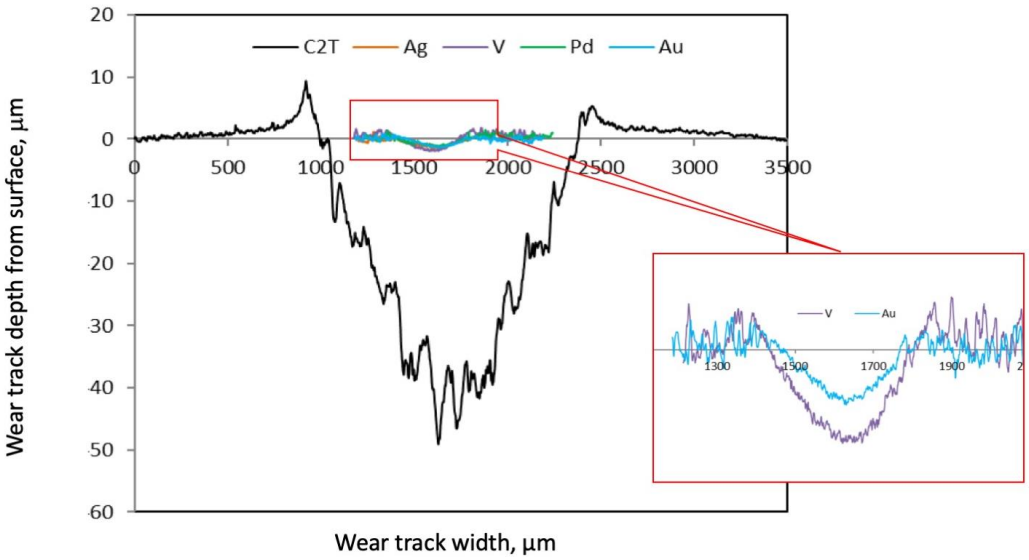
Figure 4.4-4 Dynamic Coefficient of Friction (CoF) curves for all C3T samples tested under the normal load of 21N, together with the CoF curves for C2T and Unt samples for comparisons.

4.4.3 Wear resistance of 600 °C/10-hour C3T samples under 21N load

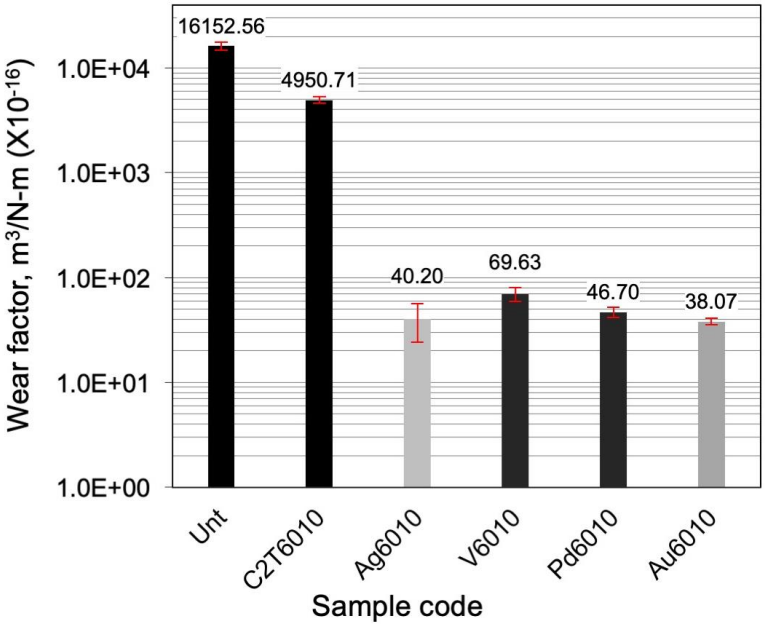
The 600 °C/10-hour C3T treated samples were tested against the counterpart WC-Co ball under 21N for 30 mins (3600 cycles), compared with the C2T and Unt sample tested under the same conditions. The wear factors were calculated based on the 2D scan of the wear tracks (Figure 4.4-5 (a)). The wear tracks have been observed under the SEM to understand the wear features and mechanisms.

4.4.3.1 Wear factors

Figure 4.4-5 (b) compares the wear factors of the treated (C3T and C2T) and the untreated samples. It can be seen from Figure 4.4-5 (b) that under the wear condition, the C3T samples significantly increased wear resistance of Zr702 material with the wear factor only about 0.24% to 0.43% that of Unt sample and about 2 orders of magnitude lower than that of C2T sample. The wear factors for all these C3T samples are very similar although a marginally increased performance of the wear resistance was observed in the orders of V6010, Pd6010, Ag6010, and Au6010 between these samples.



(a)



(b)

Figure 4.4-5 (a) 2D wear track profiles scanned by profilometer of Unt, C2T and selective samples with pre-deposition layers (Ag6010, V6010, Pd6010 and Au6010) treated under the condition of 600 °C/10h after the wear test under the load conditions of 21N, 30 mins (3600 cycles); (b) The wear factors of the C3T samples treated at 600 °C/10h.

4.4.3.2 Wear tracks

The SEM images of the wear tracks are shown in Figure 4.4-6. The width of the wear tracks for C3T treated samples is in the range of 0.3 mm to 0.5 mm (Figures 4.4-6 (c), (d), (e) and (f)), whereas it is around 1.6 mm for the C2T wear track (Figure 4.4-6 (b)) and around 3.6 mm wide for the Unt sample (Figure 4.4-6 (a)). All the C3T treated samples in general show much narrower wear tracks compared to the C2T and Unt as evidenced in Figure 4.4-5. As shown in Figure 4.4-5 (a), the depth of the wear tracks formed in the C3T treated samples is only a few microns whereas the C2T treated sample reaches as deep as ~45 μm. More specifically, among the C3T treated samples, the wear track formed in Au6010 is the shallowest. Overall, all the C3T treatments are found to have significant reduction in the wear area.

The wear tracks have been observed under SEM to study the mechanism involved. Typical adhesive wear feature, galling and tearing of the Zr materials can be seen for the untreated Zr702 alloy (Figure 4.4-6 (a)), which is caused by the strong tendency to adhesion of Zr due to its ductile nature. The severe wear was observed on C2T sample after wear testing under the current wear conditions. Large wear debris was found in the wear tracks with a few furrows with great depth as shown in Figure 4.4-7 (a). This is because the thin surface oxide layer can be removed easily during the reciprocating sliding process, and then the hard fragments of the removed oxide acted as the third body to cause excessive abrasive wearing of the soft substrate materials.

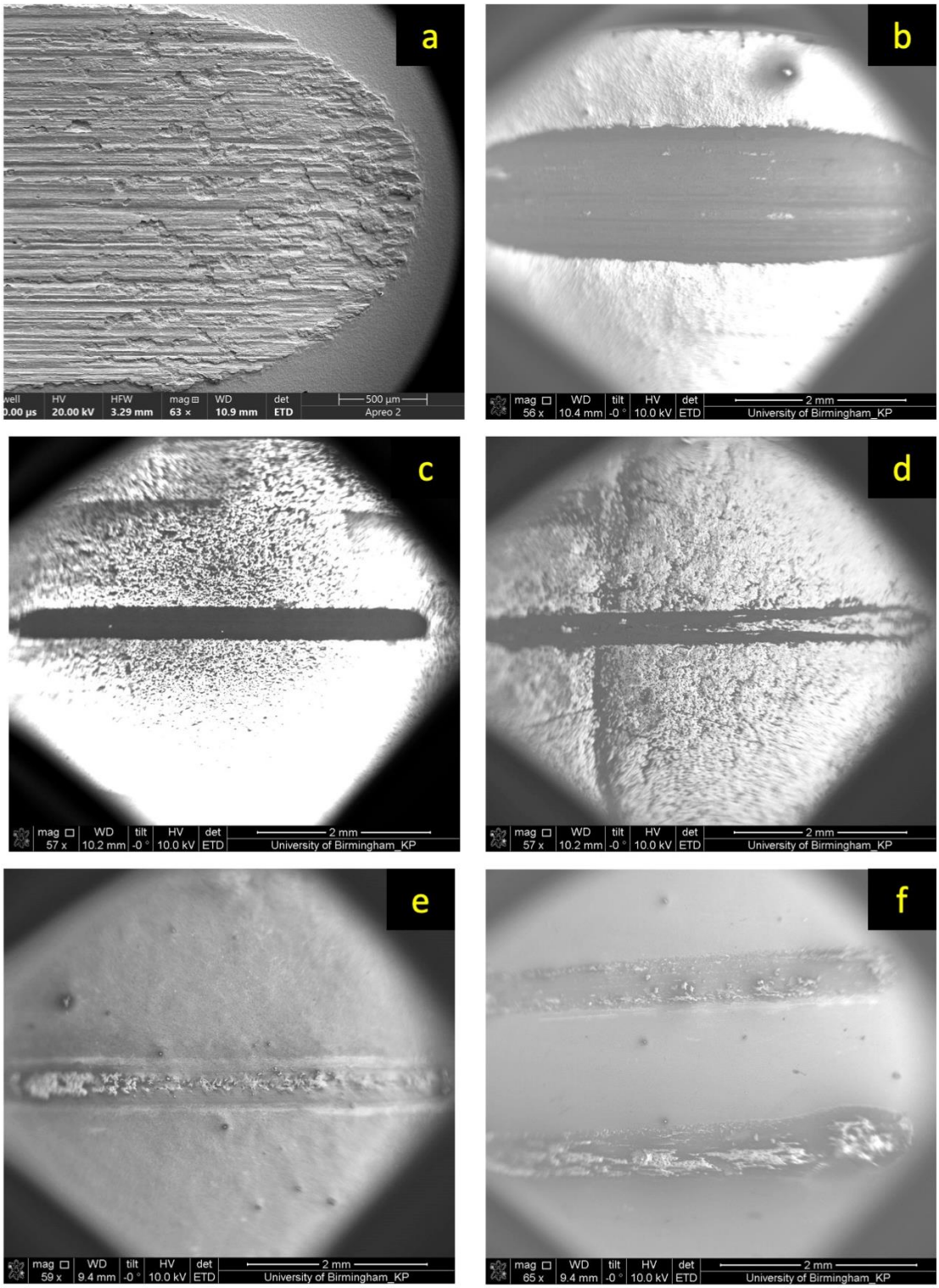


Figure 4.4-6 The SEM images of the wear tracks formed on different samples: (a) Unt; (b) C2T6010; (c) Au6010; (d) Ag6010; (e) V6010 and (f) Pd6010.

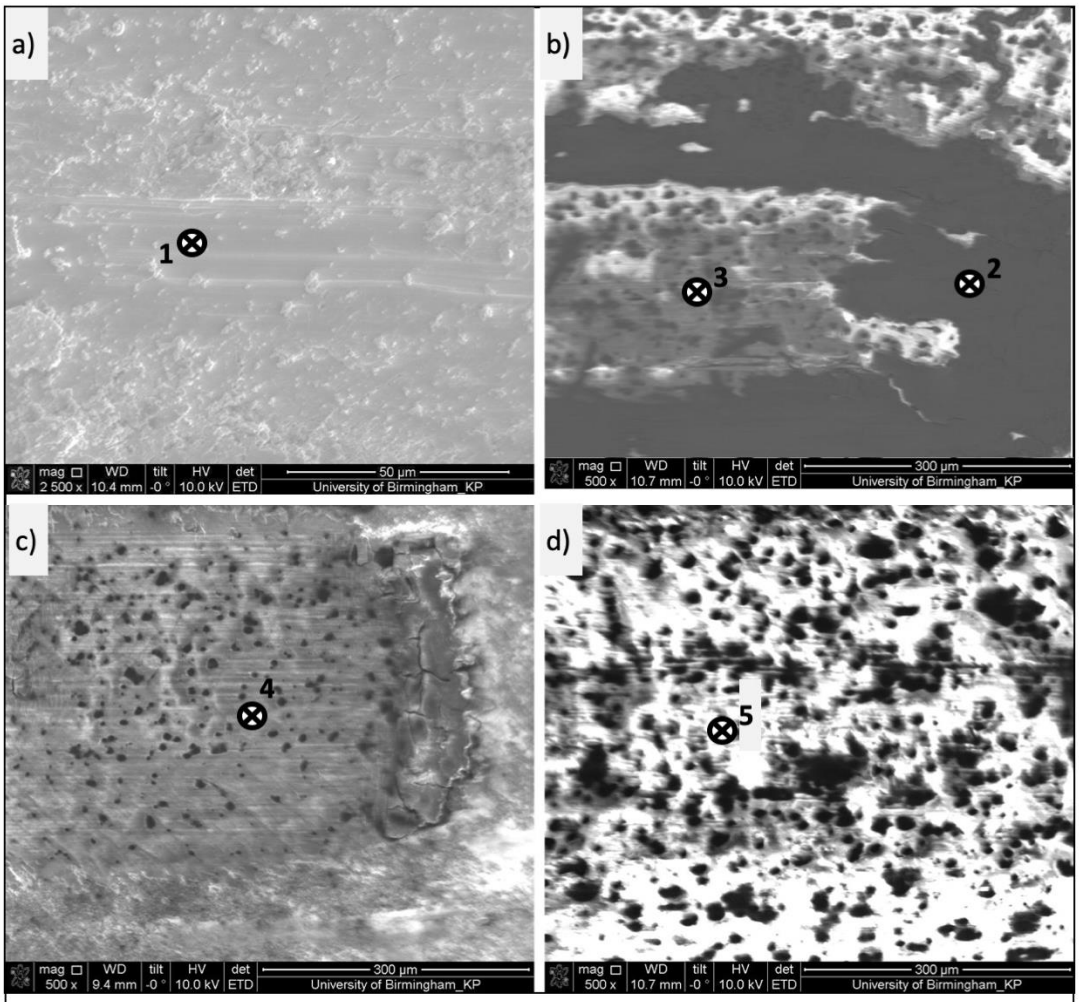
The wear morphologies observed from the wear tracks of the C3T samples differ greatly from that of the Unt and C2T samples. Shallow and flat wear tracks with a few debrides and mild furrows as exemplified in Figures 4.4-6 (c)-(f) and Figures 4.4-7 (b)-(d) were observed for all the C3T samples tested. Specifically, the wear tracks formed on Ag6010 sample were partially covered with black patches as shown in Figure 4.4-7 (b), and EDX analysis of these black patches revealed high content of Ag and W. This implies that the surface dendrite like Ag and AgO_2 particles protruding from the surface as shown in Figure 4.2-1 were worn off by the WC-Co ball during the reciprocating sliding process at the beginning, and then the worn off materials were compacted during the cyclic sliding process between the contacting parts, thus forming a self-lubricating film with soft Ag. The high Zr and O contents (see Figure 4.4-7 (e)) measured from spectrum 3 in Figure 4.4-7 (b) also support the micro-cutting effects of the hard asperities on WC-Co ball to the exposed ZrO_2 hard surface. Because of the similar hardness of the tribo-pair (HV1328 for WC-Co and HV1350 for ZrO_2)[111], the abrasive wear is mild. Furthermore, when silver or silver oxide were worn out, and the debris were imbedded in the silver rich black patch, self-lubricating film was formed during the cyclic sliding processes. The wear damage of these third-body particles to the surface of the Ag6010 samples is therefore reduced.

As depicted in Figure 4.4-7 (d), the wear track characteristics of Au6010 are similar to Ag6010, but with smaller, self-lubricant patches and less furrows. In addition, less wear debris from the WC-Co ball would be expected because of the smaller R_a and R_t values of Au6010 than Ag6010 sample and hence reduced the asperities of the ZrO_2,

which is evidenced by the lower W content detected from the black patch areas 5 (Au6010) than from area 2 (Ag6010).

The wear mechanism of V6010 and Pd6010 samples are different from that for the Ag6010 and Au6010. This could be attributed the superficial-surface oxides of V_2O_5 and PdO formed on the V6010 and Pd6010 samples respectively achieving the high hardness. The high friction coefficient of the tribo-pairs (Figure 4.4-4) of V6010/WC-Co and Pd6010/WC-Co at the early stage (Figure 4.4-4) and the high content of W found in the wear tracks of V6010 (Figure 4.4-7 (e)) are most possibly related to the micro-cutting of the WC-Co balls by the asperities of the superficial hard oxides. The initiation and growth of fatigue crack of the superficial oxides are due to the cyclic loading. When the crack propagated to a critical length, superficial oxides were flaked off. During the further sliding process, the relative motion of the tribo-pair ground the very thin oxide flaks into small sized abrasive particles. Consequently, abrasive wear occurred on the exposed ZrO_2 surface and hard oxides of V_2O_5 and PdO stopped cutting the WC-Co ball at this point, thus leading to the reduced CoF as shown in Figure 4.4-4 after 100 and 400 cycles for Pd6010 and V6010 respectively. The low content of V and Pd revealed by the EDX analysis for V6010 in Figure 4.4-7 (e) and Pd6010 samples indicates that the quantity of superficial oxides is low. The ZrO_2 ceramic layer underneath is hard and thick enough to resist the abrasive wear and to withstand the normal load applied. The wear rates for Pd6010 and V6010 are still low compared with that of the C2T sample, but are 20% and 80%, respectively, higher than that for the Au6010 and Ag6010 samples. Based on the results above, it can be deduced that the superior wear

properties of Ag6010 and Au6010 could be attributed to the formation of self-lubricating layers during the wear process.



Sample	Spectrum	O	Zr	Hf	Ag	V	Au	W
C2T	1	1.0	97.4	1.6				0.0
C3TAg	2	7.7	7.2	0.5	65.6			19.0
	3	18.0	78.3	2.0	0.2			1.5
C3TV	4	22.4	54.1	1.8		2.5		19.2
C3TAu	5	19.0	68.0	1.7			2.8	8.5

e)

Figure 4.4-7 The SEM observation on the wear tracks of (a) C2T; (b) Ag6010; (c) V6010; (d) Au6010; (e) Table summarises the EDX point ID chemical analysis results in wt% in the wear tracks in (a), (b), (c) and (d).

4.4.4 Load effect on wear behaviour

To investigate the effects of treatment conditions and wear testing load on the wear resistance of the ceramic conversion treated samples, the Au film pre-deposited Zr702 samples treated for 5 hours, 10 hours, 20 hours and 40 hours in air were selected for further wear tests under different loads. The 5 min treated sample was not included because of the thin oxide layer thickness formed and hence the low load-bearing capacity. The wear tests were performed on those samples under the same load of 21N as reported in Section 4.4.3(i.e., 21N, 30mins, 3600 cycles) and a higher load of 45N (i.e., 45N, 30mins, 3600 cycles). The results are compared with the C2T and Unt samples.

4.4.4.1 Wear factors

The wear factors were calculated, and the results are compared in Figure 4.4-8 and summarised in Table 4.4-1. It can be seen that both the untreated Unt and the short-time (10h) C2T treated C2T6010 samples exhibited very high wear factors when tested under loads of both 21N and 45N. Except for the untreated Unt sample, the wear factors for all the treated samples are higher when measured under 45N than under 21N.

When tested under the load of 21N, the Au6010 revealed a much lower wear factors as compared to the C2T sample treated under the same condition (i.e. C2T6010) mainly due to the increased surface oxide layer thickness (Figure 4.2-8) and the

surface hardness (Figure 4.4-1). Indeed, the wear factor of the Au6010 is slightly lower than that of the C2T sample treated at the same temperature for a much longer treatment duration (i.e., C2T6040) although the surface oxide thickness is slightly thinner for the Au6010 than for the C2T6040 (Figure 4.2-8). It can be also found from Figure 4.4-8 that the wear factors for all the Au pre-deposited samples treated under the same temperature of 600 °C for different treatment durations (i.e., Au6005, Au6010, Au6020 and Au6040) are very similar.

However, when tested under a higher applied load of 45N, the wear factors of Au6020 and Au6040 samples significantly outperformed short-time treated C3T sample of Ag6010. This should be attributed to the higher load bearing capacity of Au6020 and Au6040 samples due to their much higher surface hardness (Figure 4.4-2). The much high wear factors for the short-time treated Au6005 and Au6010 could be caused by the thin-ice nature of thin and hard oxide layers formed. Under a high applied load, the stress field can penetrate through the thin oxide layer to the soft substrate. This will lead to plastic deformation of the substrate and hence the thin and hard oxide film will collapse due to the lack of sufficient mechanical support from the substrate.

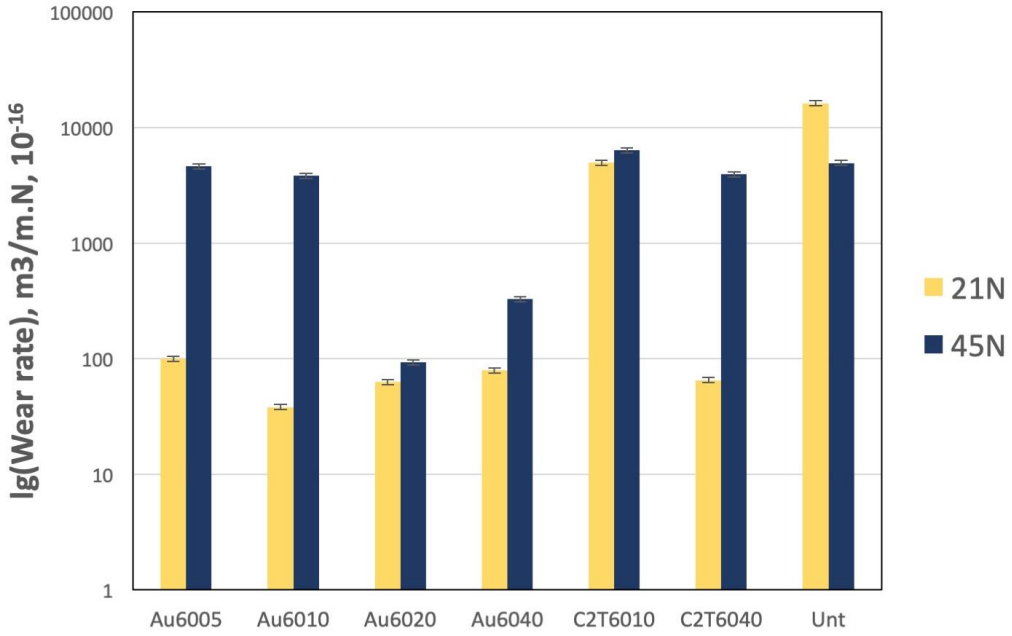


Figure 4.4-8 The effect of wear test loads on the wear factors (log) of Au pre-deposited C3T samples treated at 600 °C for 5, 10, 20 and 40 hours, C2T sample treated at 600 °C for 10 and 40 hours, and the untreated sample for comparison.

Table 4.4-1: The wear factor results of untreated Zr702, C2T and C3T (Au pre-deposited) samples under different load conditions (21N vs. 45N).

Wear rate, m^3/m.N, 10^{-16}	**Load 21N/30mins**	**Load 45N/30mins**
Au6005	99.74	4595.95
Au6010	38.07	3804.94
Au6020	62.83	92.46
Au6040	79.19	326.96
C2T6010	4950.71	6355.85
C2T6040	64.99	3913.95
Unt	16152.56	4922.28

4.4.4.2 Wear track morphologies

Figure 4.4-9 demonstrates the wear morphologies observed by SEM inside the wear tracks of the Unt sample tested at the load of 21N and on the counterpart WC-Co ball. After the wear test under the load of 21N, the surface inside the wear track of Unt sample is very rough (Figure 4.4-9 (a)). A large amount of Zr debris can be observed from the surface of the counterpart WC-Co ball after the wear test (Figure 4.4-9 (b)). The adhesive craters found in the site A in Figure 4.4-9 (a) and the substantial materials transfer to the counterpart WC-Co ball (Figure 4.4-9 (b)), indicated that the dominant wear mechanism for the Unt sample is adhesive wear. The adhesive craters were caused by the removal and transfer of the material from the adhesive joints formed by the zirconium asperities. A small area of grooves shown in the site B in Figure 4.4-9 (a) in the direction parallel to the grinding traces indicates the mild abrasive wear. These grooves were caused by the work hardened and oxidised zirconium materials in the sliding process transferred from the Zr702 sample surface on the counterpart WC-Co ball.

Figure 4.4-10 shows the SEM morphologies observed inside the wear tracks of the Unt sample wear tested at the load of 45N and on the counterpart WC-Co ball. The B sites in Figure 4.4-10 revealed the oxygen content via the EDX analysis but no oxygen content detected in A site. The high oxygen detected implies the formation of oxidised tribo-film layer. This is due to the high load induced high contact stress and high frictional temperature causing the plastic deformation and oxidation. Under the wear conditions, the formation of surface oxide might be responsible for reduced rather than increased wear factor of the untreated Unt sample when the applied load increased from 21N to 45N (Figure 4.4-8).

However, it should be indicated that the dominant wear mechanism for this sample is adhesive wear as evidenced by the severe materials transfer onto the counterpart WC-Co ball (Figure 4.4-10 (b)). Mild abrasive wear by oxide debris and oxidational wear may have also played a role indicated by the oxidisation found at B site and the oxygen content detected via the colour chem SEM images from the transferred material on the WC-Co counterpart surface.

As shown in Figure 4.4-8 the wear factor is slightly higher for the Unt sample when tested under 21N than tested under 45N. This is because the oxidation played a more role when tested under 45N, which can be evidenced by the colour chem SEM images in Figure 4.4-10 (b) showing more apparent yellow colour (indicating the oxygen content). In contrast, as shown in Figure 4.4-9 (b) limited orange colour (indicating the oxygen content) could be identified from the transferred materials on the WC-Co ball surface.

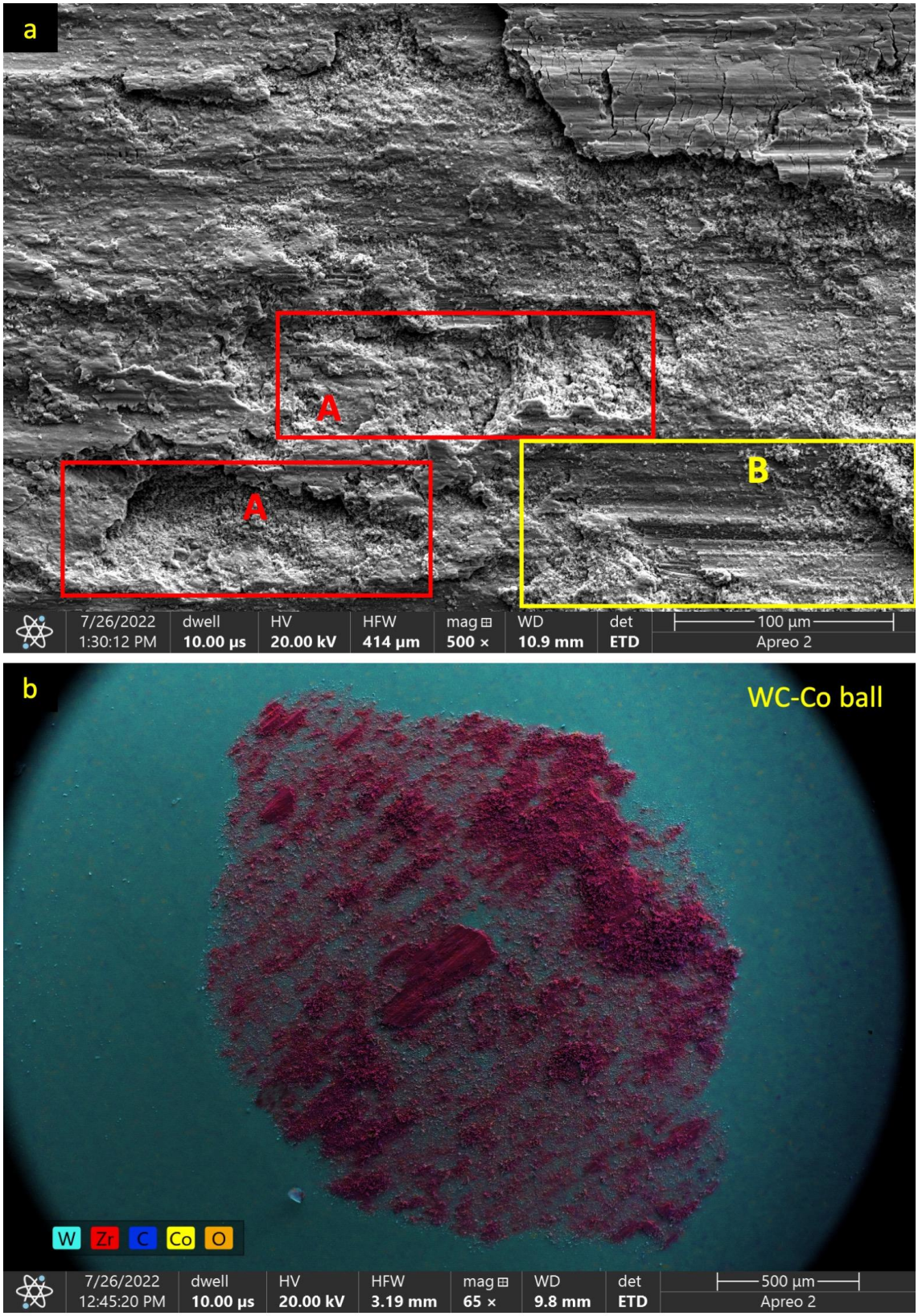


Figure 4.4-9 SEM images of samples Unt after wear test under 21N, (a) at the bottom of the wear track, (b) on the surface of the counterpart WC-Co ball with EDX elements distribution.

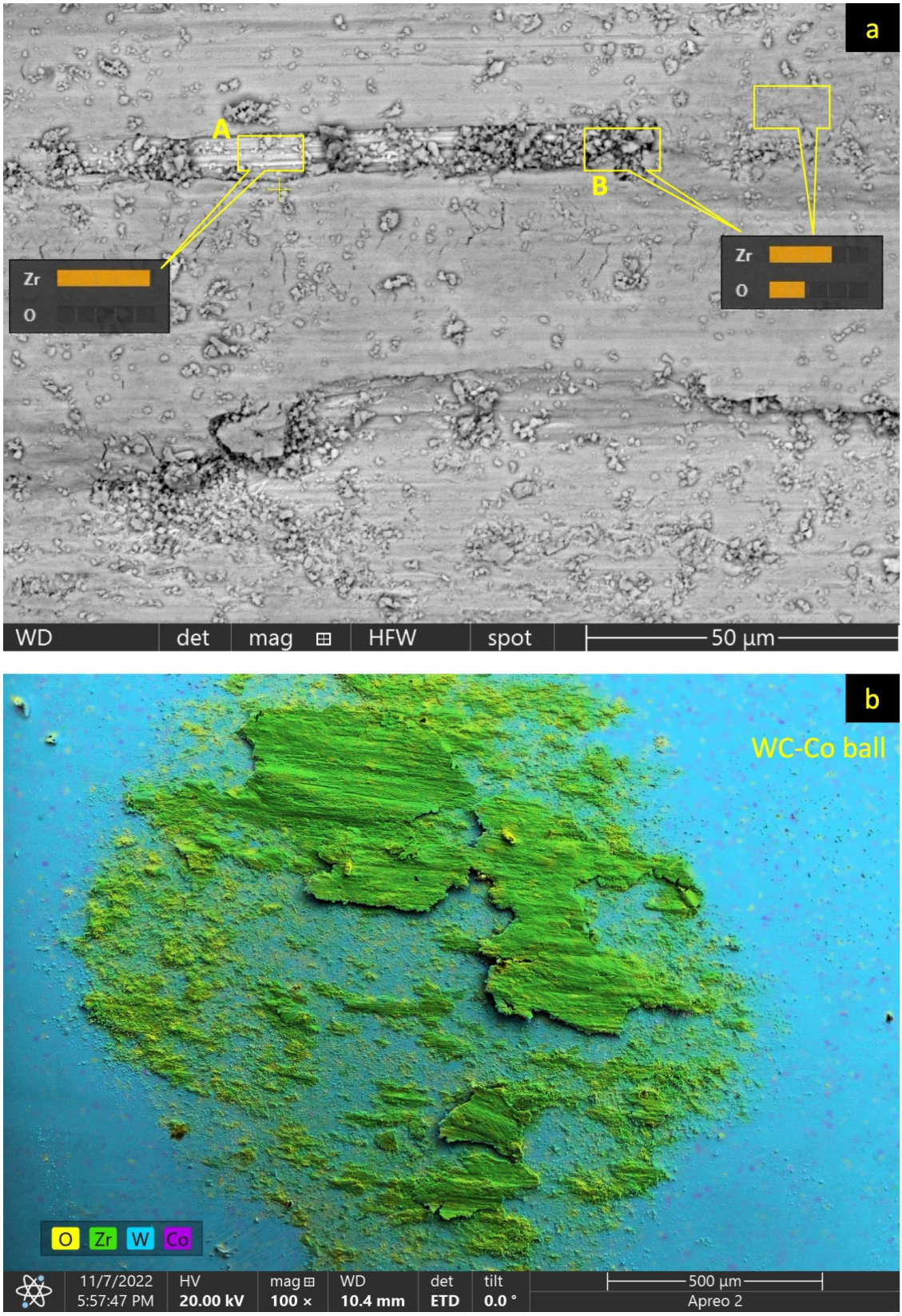


Figure 4.4-10 SEM images of samples Unt after wear test under 45N, (a) at the bottom of the wear track with EDX analysis, (b) surface of the counterpart WC-Co ball with EDX elements distribution.

a) Short time treated C3T samples

According to the wear factors, as summarised in Table 4.4-1 and Figure 4.4-8, both samples performed very well with relatively high wear resistance under the load of 21N but they are less effective under the high load of 45N. Despite of this, the Au6010 samples possess slightly better wear resistance in terms of wear factors under both low and high load wear conditions when compared to Au6005 samples. This is also evidenced by the wear tracks profile as shown in Figure 4.4-11. Although both samples show similar wear tracks in terms of the depth and width, Au6010 samples still produce marginally shallower wear tracks as compared to Au6005 samples under both conditions.

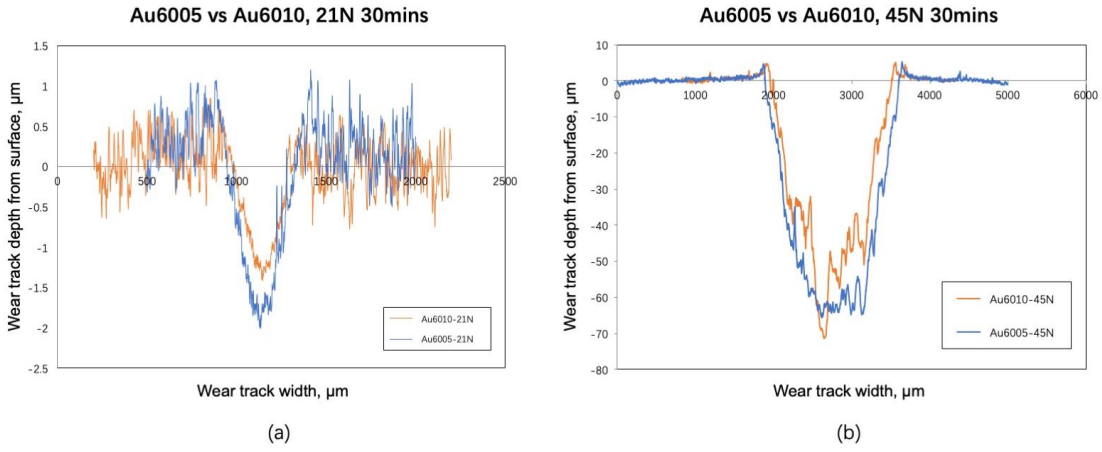


Figure 4.4-11 The wear track profiles of 5-hour and 10-hour C3TAu samples after wear tested under 21N (a) and 45N (b).

Figure 4.4-12 presents the comparison of the wear track morphologies of Au6005 sample wear tested under 21N ((a) & (c)) and 45N ((b) & (d)) together with the surface morphologies of the counterpart WC-Co balls after the tests. It can be seen from Figure 4.4-12 (a) that the wear of the Au6005 sample when tested under the 21N

is superficial and very mild. This is evidenced by the fact that the original grinding traces at an angle to the sliding direction could be seen within the wear track as shown in Figure 4.4-12 (c). In addition, Au (red) is still detected inside of the wear track as shown in Figure 4.4-12 (c). As depicted in Figure 4.4-12 (e), very little (if any) Zr (green) could be detected on the counterpart WC-Co ball surface. This implies the converted ceramic layer could still protect the substrate from wear because almost no material transfer from the zirconium substrate. However, when tested under the high load of 45N, the ceramic layer was worn through, and severe adhesive wear occurred to the substrate as evidenced by the adhesive wear craters observed within the wear track (Figure 4.4-12 (d)). Without the ceramic layer protection and self-lubricating film, transferred zirconium material was observed on the counterpart WC-Co ball surface (Figure 4.4-12 (f)), which is similar to the WC-Co ball counterpart after sliding against the Unt.

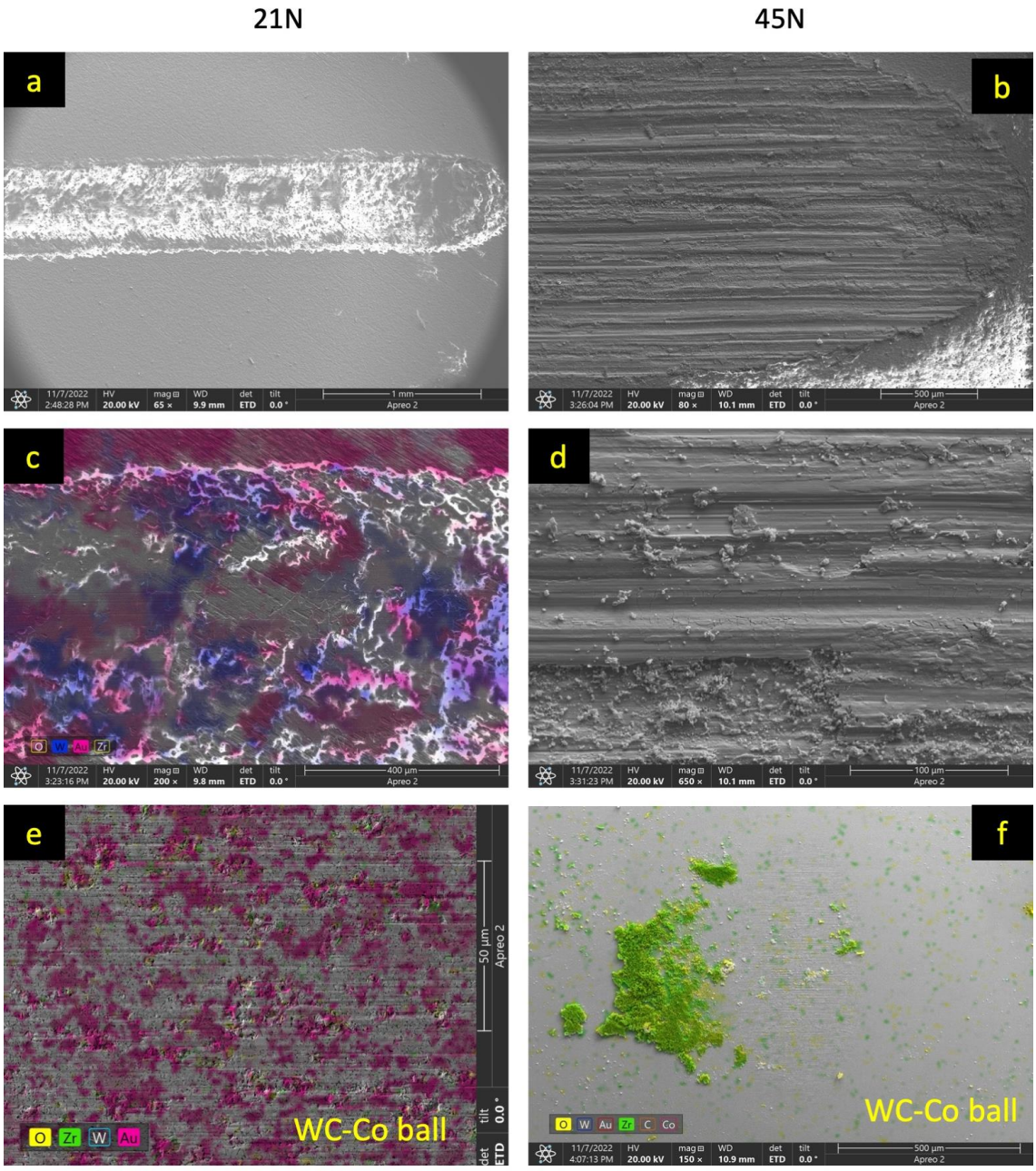


Figure 4.4-12 SEM images of the wear track of Au6005 sample wear tested under the normal load of 21N ((a), (c) and (e)) and 45N ((b), (d) and (f)).

b) Long time treated C3T samples

For C3T Au pre-deposited samples treated at relatively longer time (more than 10 hours), much thicker ceramic layers have been formed (Figure 4.2-8). As depicted in Figure 4.4-8, the long-time treated C3TAu samples still show good wear properties when tested under 45N. However, it is of interest to note that the wear factor of

Au6040 is larger than Au6020 although the oxide layer thickness is much thicker for the Au6040 (~17μm) than for the Au6020 (~7 μm).

Figure 4.4-13 shows the wear track of Au6020 sample after the wear test under the load of 45N. The sample exhibited superficial wear and has performed the best in all the C3TAu samples (Figure 4.4-8). Most probably, the ceramic layer was not worn through. Figure 4.4-13 (a) shows the mixture of the content of Au and W within the wear track, which is similar to the wear mechanism explained above for the Au6010 sample wear tested under 21N, and the self-lubricating film consisting of Au can reduce the wear damage. Only small amount of zirconium material transfer was found on the counterpart WC-Co ball as shown in Figures 4.4-13 (b) and (c).

For Au6040 sample, it still provided wear protection under the high load of 45N, but not as good as the Au6020 sample although its oxide layer is thicker on the Au6040 than on the Au6020. This could be attributed to the reduced quality of the surface oxide layer formed on the long-time treated sample. As evidenced in the Figures 4.4-14 (a) & (b), delamination and spallation of the ceramic layer occurred leading to thin layer delamination wear. The spallation and delamination of the layer occurred only at the top of the surface, which is evidenced by the high oxygen content in the spalled area. The spallation and delamination are most probably caused by the tangential force leading to the growth of the lateral cracks found at the top of the oxide layer formed on the surface of the long-time treated sample. More zirconium material transfer has been found on the counterpart WC-Co ball showing in Figure 4.4-14 (b) as compared to Au6020 (Figure 4.4-13 (c)) but still in a relatively small amount.

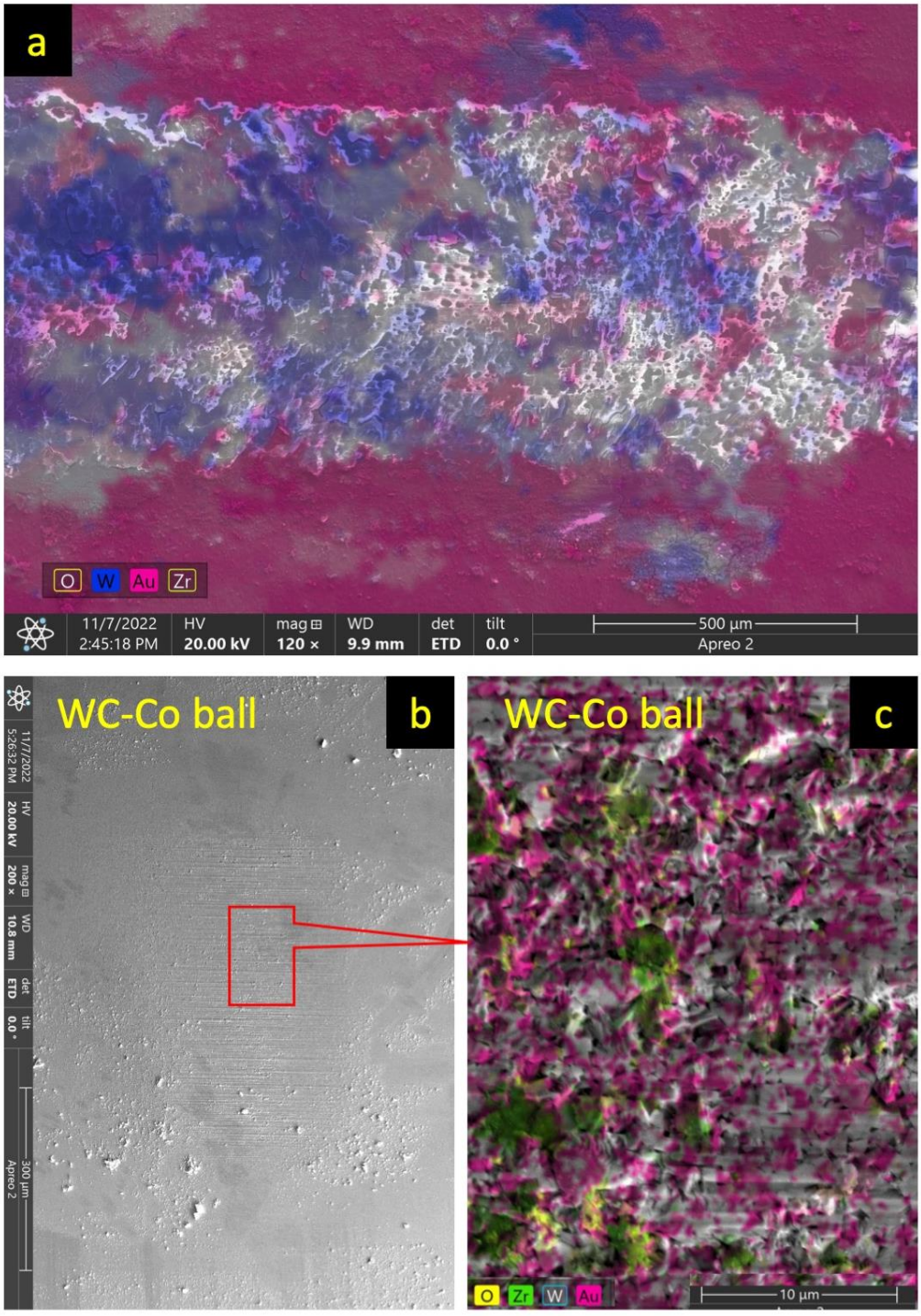


Figure 4.4-13 (a) The colour chem SEM image reveals the inside of the wear track for Au6020 sample wear tested under the load of 45N. (b) and (c) present the surface counterpart WC-Co ball and the EDX chemical analysis via colour chem SEM image.

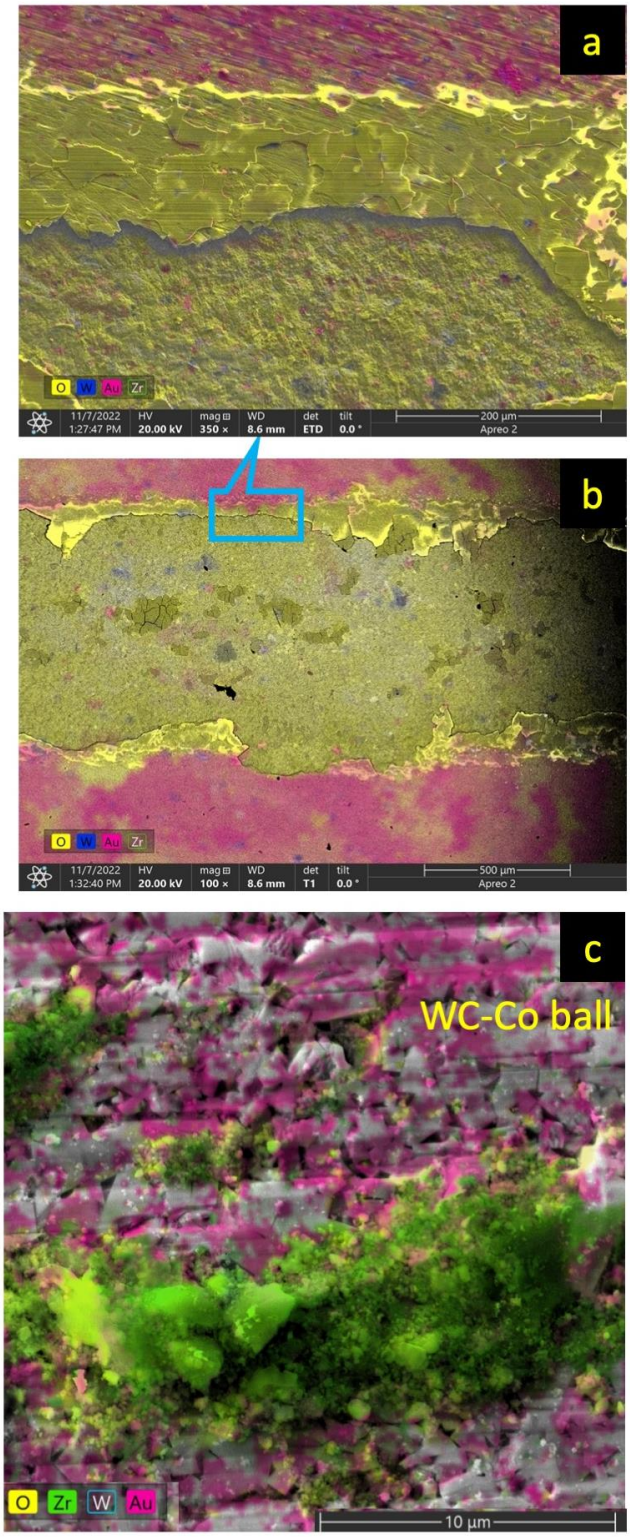


Figure 4.4-14 The colour chem SEM image reveals (a) & (b) the wear track of Au6040 sample wear tested under the load of 45N, (a) zooming in the part highlighted in (b) showing the wear features inside the wear track for Au6040 sample. (c) presents the surface counterpart WC-Co ball and the EDX chemical analysis via colour chem SEM image.

4.4.5 Wear behaviour of selected C3T samples in NaCl solution

The Unt, selected C2T and C3T Au samples were further tested under 21N load for 30 mins (3600 cycles) in 3.5wt% NaCl solution to investigate the effect of environment conditions on the wear resistance on these samples. In this section, the wear factors and the morphology of the wear tracks for these samples tested in NaCl solution ('wet condition' or 'corrosion wear') is compared with the samples tested in unlubricated condition ('dry condition').

4.4.5.1 Wear factors

The wear factors of samples in both 'dry' and 'wet' are summarised in Table 4.4-2 and visually compared in Figure 4.4-15. It can be seen that except for the untreated UNT and C2T6010 samples, all other ceramic conversion treated (C2T or C3T) samples exhibited very similar level of wear rates in both dry and wet conditions.

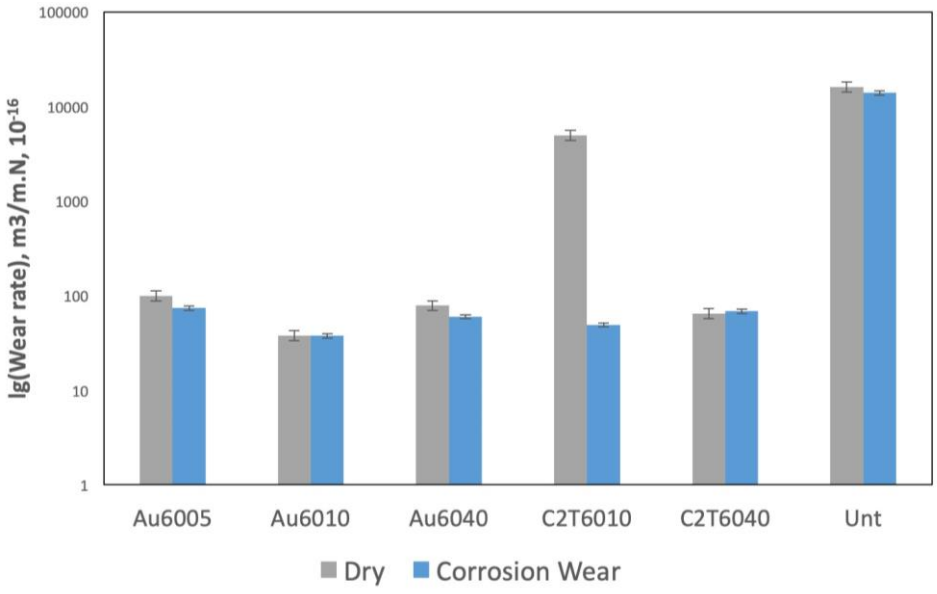


Figure 4.4-15 The wear factor (log) comparisons between Unt sample, C2T and C3T Au pre-deposited samples in different treatment time, tested in dry and wet conditions.

Table 4.4-2: The wear factor results of untreated Zr702, C2T and C3T Au pre-deposited samples under different wear conditions - Dry vs. Wet, with same normal load 21N and numbers of cycles (30min/3600 cycles).

Wear rates, $m^3/m.N, 10^{-16}$	**Dry**	**Corrosion Wear**
Au6005	99.74	74.20
Au6010	38.07	37.63
Au6040	79.19	59.99
C2T6010	4950.71	49.18
C2T6040	64.99	68.34
Unt	16152.56	13898.43915

4.4.5.2 Wear tracks

The wear mechanism of the Unt sample in wet condition is similar to the dry condition, both showing the mixture of severe adhesive and abrasive wear mechanisms. Figure 4.4-16 (a) shows that in the wet conditions, the materials transfer is obvious as high content of Zr can be seen on the WC-Co ball surface, indicating the severe adhesive wear. The adhesive wear features can also be seen in the wear tracks. Figures 4.4-16 (b) and (c) present the adhesive ploughing grooves and adhesive craters. The oxygen content showing in Figure 4.4-16 (d) indicates the oxidation, and the oxidation could also be seen on the counterpart WC-Co ball in Figure 4.4-16 (a). However, it can be seen from Table 4.4-2 that the wear factors change from 16152.56 $\times 10^{-16}$ m^3/mN for dry test to 13898.44 $\times 10^{-16}$ m^3/mN for wet test. The reduced wear factor could be explained by the lubricating effect of the solution used. However, the lubricating effect is very limited as the lubrication film cannot be established due to

the very rough surfaces caused by the severe wear at the beginning (Figure 4.4-16). In addition, as reported in Section 4.3, corrosion (especially pitting corrosion) was observed for untreated Zr702 (i.e., Unt) and therefore it is reasonable to assume that the negative corrosion effect may have to some extent reduced the positive lubricating effect of the NaCl solution for reducing wear.

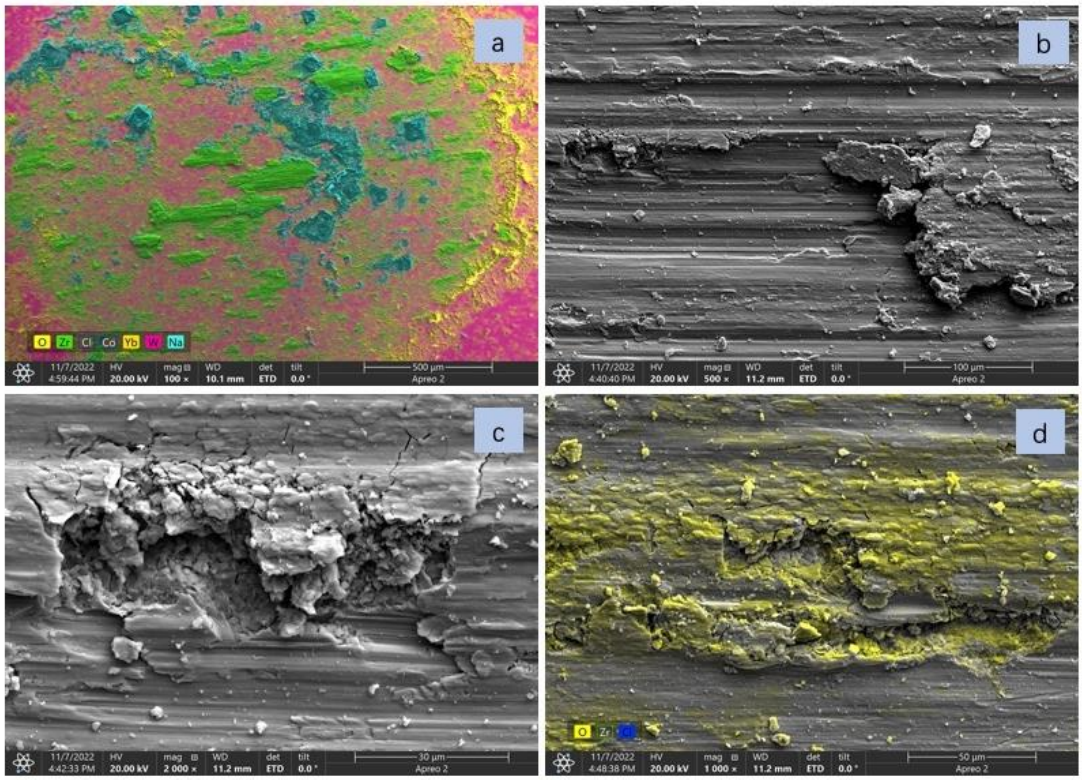


Figure 4.4-16 SEM images of (a) the WC-Co ball surface sliding against the Unt sample after the corrosion wear test; (b), (c) and (d) reveal the wear track and wear features of the untreated Zr702 sample after the corrosion wear test.

However, it is noted from Figure 4.4-15 that the wear factor of C2T6010 can be effectively reduced when tested under wet condition. Figure 4.4-17 presents the SEM observation of the wear crack after the corrosion wear tests of C2T6010 sample in dry and wet lubricated conditions. The width of the wear track formed in wet wear test (Figure 4.4-17 (b)) is ~400 μm, which is half the width of the wear track formed in

dry wear (Figure 4.4-17 (a)). As reported in Section 4.3, the ceramic layer formed during C2T possesses good corrosion resistance and hence no appreciable corrosion would be expected in NaCl solution. Instead, the solution acted as the lubricant during the wear process and the oxide layer can protect the surface from initial wear. Hence, significant reduced wear is expected.

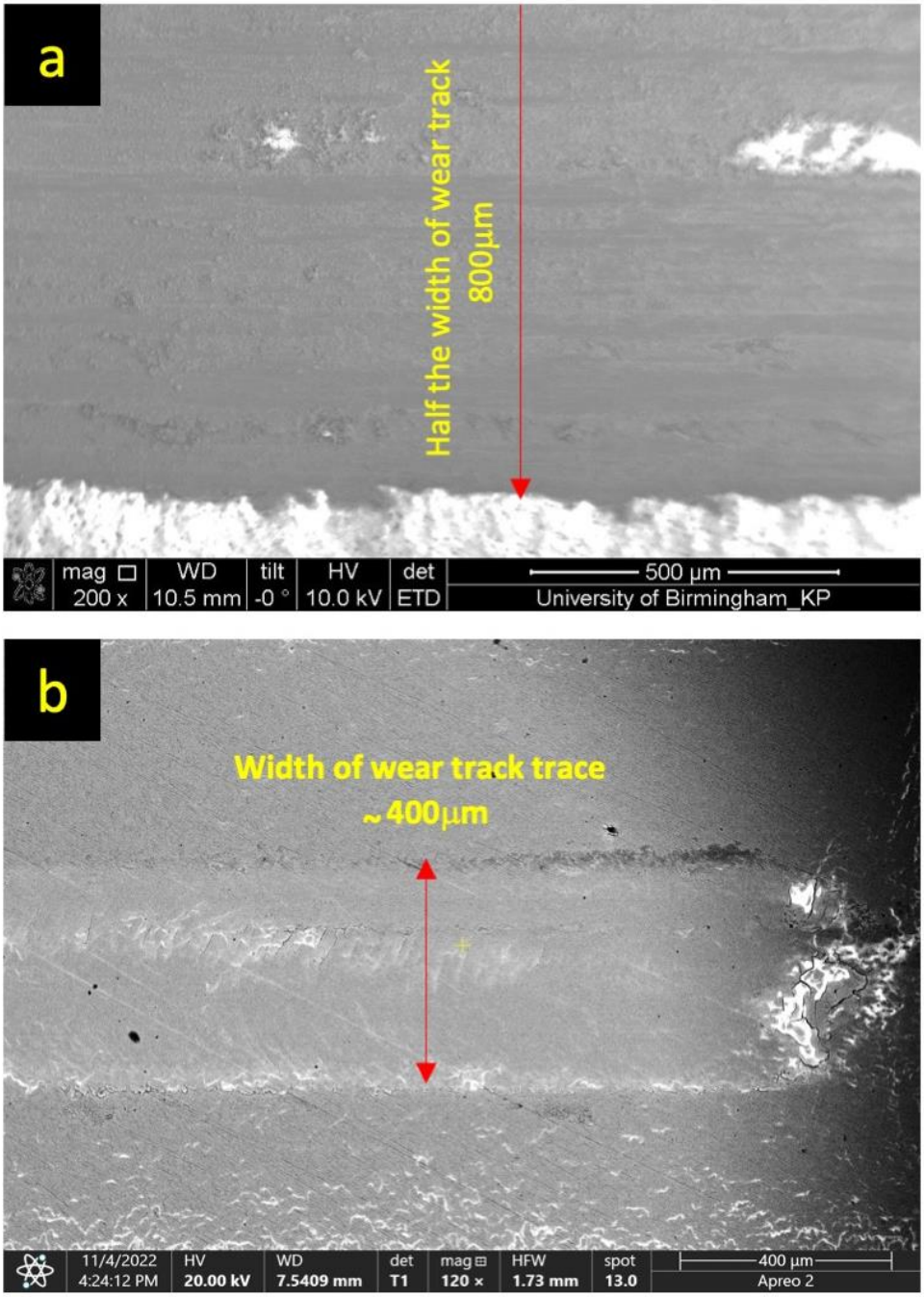


Figure 4.4-17 SEM images of the inside of the wear tracks and wear features of the C2T6010 samples after wear tests in dry conditions (a) and wet condition (b).

Chapter 5. Discussion

5.1 Catalytic effects and mechanisms

As has been reported in the last chapter, compared with no pre-deposition and ceramic conversion treated (C2T) samples, the pre-deposition of elements Ag, V, Pd or Au as well as the co-deposition of these elements (i.e., Ag/V, Ag/Pd) can accelerate the ceramic conversion process leading to so-called catalytic ceramic conversion treatment (C3T). However, it has also been noted that the catalytic effect depends on the pre-deposited elements and the treatment conditions (temperature in particular).

5.1.1 C3T with pre-deposition of Ag (C3TAg)

The naturally formed zirconia ceramic was reported to be similar to the colour of tooth [112], but it can also appear in various colours in synthesised cubic zirconia. For example, the cubic zirconia doped with vanadium dopant was reported to appear in the colour of green and such colour change could be affected by the concertation of the dopants as well as the oxidation states [113]. The colour of the C2T and C3T treated Zr702 samples has been reported in Section 4.1.2. As depicted in Figure 4.1-3, after 10-hour treatment at temperatures between 450 to 650°C, the surface of the C2T sample has changed from the metallic shining grey for the untreated sample to dark grey.

According to Wilkins [114, 115], the oxide layer thickness on zirconium could be measured by analysing the colour produced by optical interference. Therefore, the thickness of the oxide layer can contribute to the colour change appearing on the

surface. The higher the treatment temperature, the thicker the oxide layer, and thus the darker the surface colour appearing on C2T. According to Koski et al. [116], when the zirconium is fully oxidised to stoichiometric zirconium oxide in monoclinic structure, the zirconium oxide films are transparent and colourless. However, the films are in darker colour such as in black or brown when the zirconium oxide is substoichiometric. Hence, it is reasonable to deduce that the zirconium oxide layer formed during the C2T is most probably substoichiometric. The black colour is caused by the lattice defects (mainly oxygen vacancies) and lack of sufficient oxygen inside the layers [116], which indicates the low oxygen concentration in the oxidised surface during the ceramic conversion treatment, particularly when treated at higher temperatures with rapid growth of the oxide layer.

Although the C3T Ag pre-deposited sample changed to similar dark grey colour after treatment, close expectation revealed slightly silver-grey colour as compared with the dark grey for the C2T samples. This might be related to the silver particles observed on the C3T Ag surfaces (Figure 4.2-4) and identified by XRD (Figure 4.1-8). In addition, the XRD results also indicated the formation of the Ag_2O on the surface, which was reported to have a black or dark brown colour [117]. This may have also contributed to the darker colour of the high temperature treated Ag6010 C3T Ag sample.

It has been reported that at elevated temperature, silver can absorb up to 22 times its volume of oxygen and react with oxygen to form AgO and Ag_2O [118]. However, as shown in the Ellingham diagram (Figure 5.1-1), the $4Ag + O_2 = 2Ag_2O$ line locates at the top left of the diagram, therefore indicating the formation of Ag_2O at relatively

low temperatures [4] and also the easier reduction of the Ag_2O. The unstable Ag_2O is reported to decompose to metallic silver and oxygen atoms between 623 K and 673 K (i.e. between 349.85 °C to 399.85 °C), which effectively increase oxygen supply [119]. In addition, by providing extra electrons, Ag can also lower the energy for the conversion of oxygen, therefore increase the absorption and facilitate the diffusion of oxygen through the vacancies [120].

Meanwhile, the reduced Ag particles can pin the growth of ZrO_2 grains. Therefore, fine columnar grains will be formed as for C3TAu samples as shown in Figure 4.2-15. This is refining mechanism of Ag has also been observed in the C3T of Ti6Al4V alloy by Alexander et al. [4] The refined grains could facilitate the diffusion of oxygen to form the ZrO_2 oxide layer. Therefore, the catalytic mechanism of Ag in accelerating the formation of oxide layer could include: (i) Ag induced large absorption of oxygen and the formation of silver oxides at temperatures below 623K; (ii) decomposition of the unstable silver oxides between 623 K and 673 K to release Ag and O atoms; (iii) the formation of fine grains due to the pinning by the Ag embedded in the oxide layer; and (iv) rapid diffusion of oxygen due to the high oxygen level built up on the surface, short circuit diffusion via oxygen vacancies and the grain boundaries in the oxide layer; and thus lead to (v) fast formation of oxide layer.

The above catalytic mechanism is further supported by the experimental results. As shown in Figure 4.1-12, the pre-deposition of Ag can effectively increase the oxide layer thickness especially when treated at high temperature ≥550 °C. However, it is noted that only marginal further increase in the oxide layer thickness can be observed

when the treatment temperature is increased from 550 to 600 °C. This is dissimilar to the catalytic effect showing in this temperature range for other samples. The seemingly abnormal phenomena can be attributed to the Ag agglomeration at high temperatures as has shown in Figure 4.2-1, which hinders the catalytic effect of Ag on further promoting the growth of the oxide layer.

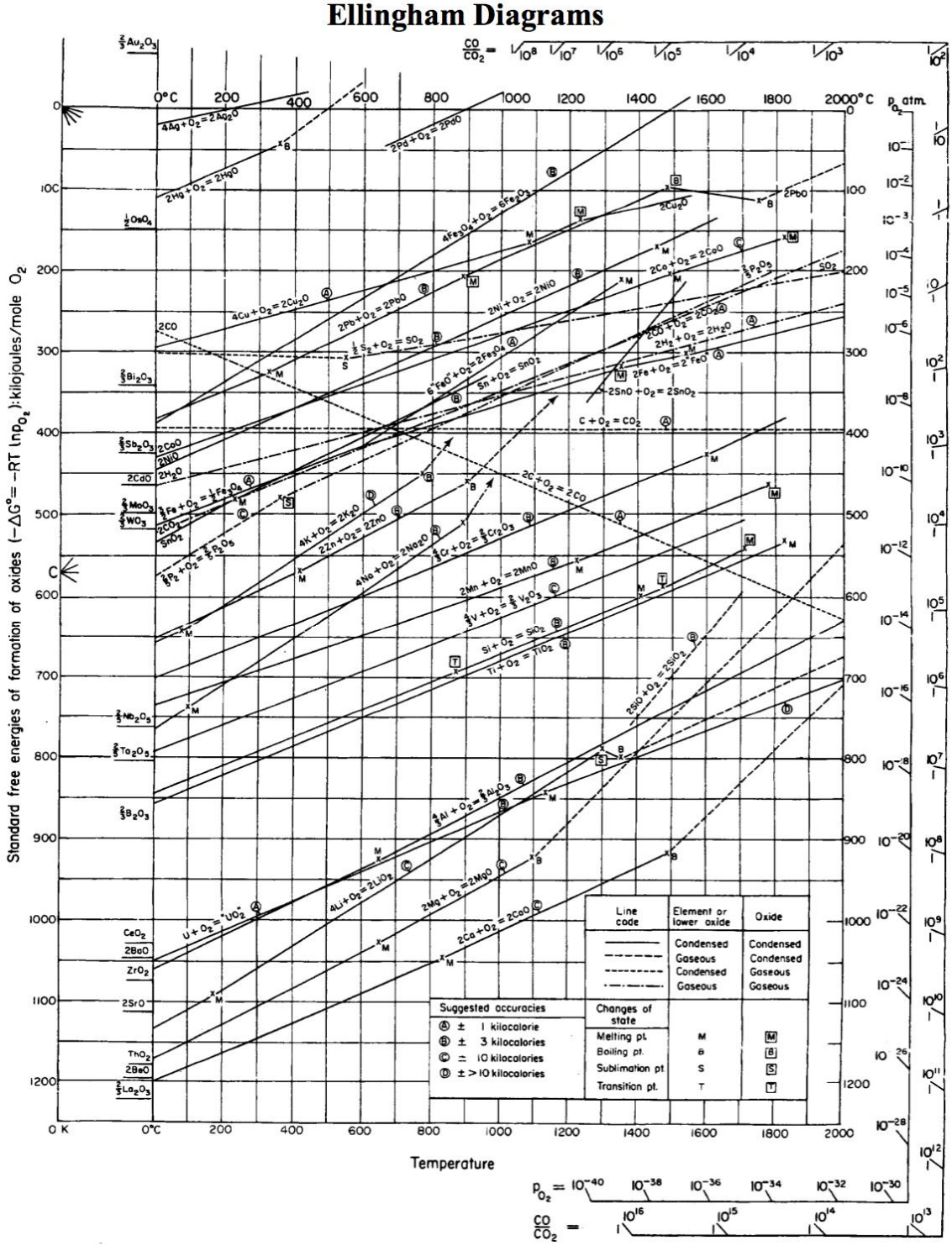


Figure 5.1-1 A more comprehensive Ellingham diagram showing the ease of the Ag_2O reduction [89].

5.1.2 C3T with pre-deposition of V (C3TV)

The C3T V pre-deposited (C3TV) samples underwent colour change from the blueish to purple colour at lower temperature of 450 °C and then appeared in a similar colour as other C3T samples treated at 600 °C. Vanadium pentoxide (V_2O_5) is identified on the Zr702 surface after the treatment according to the XRD results (Figure 4.1-9). The vanadium pentoxide (V_2O_5) is generally formed when the vanadium is heated in the environment of excessive oxygen. However, this formation of vanadium pentoxide (V_2O_5) is accompanied with the formation of other vanadium oxides. Heating the mixture of vanadium pentoxide (V_2O_5) and vanadium sesquioxide (V_2O_3) could form Vanadium dioxide (VO_2) [121]. The vanadium metal was reported to appear as grey with a bluish tinge, which explains the blueish appearance on the Zr702 sample after the pre-deposition but prior to the treatment. Vanadium pentoxide was reported to appear as brown/yellow [122] and vanadium dioxide (VO_2) was reported as dark blue solid [123]. The purple appearance of the 450 °C treated C3TV refers to the possible presence of vanadium pentoxide and vanadium dioxide when treated at the lower temperature.

Vanadium pentoxide (V_2O_5) was known as a catalyst in sulfuric acid production via the contact process oxidising the sulphur dioxide (SO_2) to sulphur trioxide (SO_3).

$$V_2O_5+SO_2 \rightarrow 2VO_2+SO_3 \qquad \text{(Equation 5.1)}$$

The catalyst is re-generated according to the following reaction of VO_2 with oxygen.

$$4VO_2+O_2 \rightarrow 2V_2O_5 \qquad \text{(Equation 5.2)}$$

The vanadium pentoxide (V_2O_5) on Zr702 surface implies the similar catalytic effect on promoting the oxidation in C3T process as the reaction to produce sulfuric acid is

in the temperature range of 400 °C to 620 °C [124, 125], which is the similar temperature range used in this study. The reason behind such temperature range for sulfuric acid production is that at temperatures below 400 °C-410 °C, the V_2O_5 will not perform its sustained catalytic activity [126]; but it will melt at the temperature 669.85°C (943 K) [127]. The temperature ranges used in this study suits the vanadium-based catalyst to perform its known catalytic activity, which has been supported by the existence V_2O_5 on the surface of C3T V samples.

The catalytic effect in terms of increasing the oxide layer thickness for C3T V samples is characterised by the steady improvement as the temperature goes from 450 °C up to 600 °C according to Figure 4.1-12. Particularly, when treated at the temperature of 500 °C, the V5010 sample formed the thickest oxide layer (3.3 μm) compared to all other single element pre-deposited sample treated at this temperature. When treated at 550 °C, the catalytic effect of V5510 was not as strong as Ag5510 and Pd5510, but was the 2nd best among all the single elements pre-deposited C3T samples after Ag6010 when treated at the temperature of 600 °C.

The catalytic effect of the pre-deposited V on Zr for the formation of ZrO_2 oxide layer during the ceramic conversion treatment is in line with the report that V can accelerate the oxidation of titanium alloys [128]. However, to date there has no report in the open literature on the catalytic mechanism of V for promoting the formation of ZrO_2 oxide layer on Zr or its alloys. As briefly discussed, the potential catalytic mechanism of the pre-deposited V could be related to the formation of needle-like V_2O_5. In addition, the potential catalytic mechanism of V could be related to the different diffusion of oxygen in V and Zr. The calculated diffusion lengths of oxygen

in Zr is about 12 nm at 400°C for one hour, which is 1.7 μm in vanadium [129]. Hence, the pre-deposited V could help to build up a high oxygen gradient to help form a large oxygen flux thus promoting oxide layer formation.

5.1.3 C3T with pre-deposition of Pd (C3TPd)

The C3T Pd pre-deposited (C3TPd) sample appeared blue when treated at 450 °C for 10 hours but the colour faded and turned to darker grey when treated at higher temperatures. Such colour change can be explained by the formation of the green-blue PdO at low temperature, and the formation of amber or black PdO [130] at high temperature with more substoichiometric zirconium oxide.

The catalytic effect of the Pd for promoting the oxidation process could be attributed to the increased oxygen coverage area caused by the lateral repulsion between the oxygen atoms and the Pd surface. This is because when the oxygen atoms are in contact with the Pd monolayer, the binding energy is therefore increased [131].

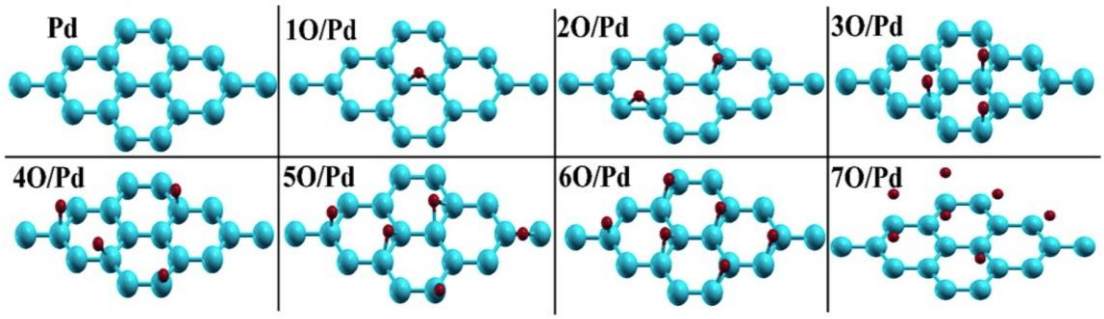


Figure 5.1-2 Schematic diagram showing the palladium monolayer with adsorbed oxygen atoms in relaxed structures [131].

As has been reported in Figure 4.1-12, the oxide layers for C3T Pd pre-deposited samples are thinner than the C3T samples pre-deposited with other elements when

treated at relatively low temperatures, i.e., 450 °C, and 500 °C. Indeed, the catalytic effect of Pd at these low temperatures is very limited as the thickness of the oxide layer formed is very close to that for the C2T None sample. However, a significant increase in the oxide thickness can be observed in Figure 4.1-12 when treated at 550 °C, increasing from 1.991 μm when treated at 500 °C to 4.554 μm when treated at 550 °C. When treated at 600 °C, the Pd6010 sample produced an oxide layer with the thickness of 5.8 μm, which is not as thick as that for Ag6010 and V6010 but thicker than that for Au6010. This indicates that the best treatment temperature for C3T Pd samples lies around 550°C. This is because the catalytic effect of Pd is very effective at 550°C and the relatively low treatment temperature could not only avoid or reduce the effect on bulk microstructure and/or properties but also reduce energy consumption and potential distortion of parts when treated at higher temperature.

5.1.4 C3T with pre-deposition of Au (C3TAu)

The Au deposited samples appeared in light green colour prior to the ceramic conversion treatment (Figure 4.1-2 (a)). Then the colour changed into darker gold after the ceramic conversion treatment (i.e., C3T Au), which can be explained by the mixed phases of Au and substoichiometric zirconium oxide after the C3T process.

According to the XRD results on Au6010 as shown in Figure 4.1-8, the Au (111) peak has been detected. The Au (111) surface has been known as an effective catalysts in promoting surface reactions including selective oxidation and oxidative coupling [125, 132]. Therefore, it is reasonable to assume that the detected Au (111) might have speeded up the oxidation process for Zr702.

However, it has been noted from Figure 4.1-12 that the catalytic effect of Au is not as strong as other elements of Ag, V and Pd in the temperature range from 550 °C to 600 °C. However, when treated for more than 20 hours, Au showed a stronger catalytic effect as compared to Ag pre-deposited samples (Figure 4.2-8), which will be further discussed in the next section.

The potential Au catalytic mechanisms involved in promoting oxide layer formation could be mainly attributed to the enhanced oxygen diffusion related to nano-crystallisation of columnar ZrO_2 grains by finely distributed Au particles (Figure 4.2-15).

STEM/EDX chemical composition mapping of the C3TAu6040 sample (Figure 4.2-16) demonstrates that the gold is not only rich in the top surface layer but also throughout the whole layer. Due to the strong affinity of Zr to O, when Zr diffuses outwards to meet inward oxygen and form ZrO_2, the stable Au particles act as doping elements that pin the ZrO_2 grains, thus preventing them from growing to a large size. This resulted in the formation of nano-crystalline columnar ZrO_2 (Figure 4.2-15). This formed nearly vertical (perpendicular to the surface) columnar grain boundaries between the nano-crystalline grains. Such vertical grain boundaries can act as oxygen diffusion channels, thus facilitating oxygen fast diffusion and boosting the growth of the dense ZrO_2 oxide. It is reported that the oxygen diffusion coefficient along grain boundary is 108 times greater than that of bulk diffusion [133]. In addition, the finely distributed Au particles within the ZrO_2 top layer increase the electrical conductivity of the oxide, allowing Zr $4e^-$ electrons transport and emitted to surface and further boost oxidation [134].

5.1.5 Treatment duration on the catalytic effects

As has been demonstrated in Figure 4.2-8, the catalytic effect of the Ag, V and Au pre-deposited C3T samples is also treatment time dependent although the thickness of the oxide layers formed for these C3T samples in general increased with the treatment time. Specifically, when increasing the treatment time from 10 hours to 20 hours, very limited layer thickness increase can be observed; however, when treated for 40 hours and 60 hours, the oxide thickness increased to 3 times and 6 times, respectively, that of the 10-hour treated samples. In contrast, the increase of oxide layer thickness for the C2T samples treated under the conditions are slowly. This implies that to maximise the catalytic effect of these elements (V and Au in particular), the final ceramic conversion treatment should be carried out at 550-600°C for 40-60 hours.

However, although the long treatment time has produced very thick oxide layer, the qualities of these layers were found to be compromised because some tiny pores and micro-cracks were observed within the extremely thick layers, as shown in Figures 4.2-9 (b), (d) and (f). The presence of these layer defects can be linked to the formation of the tetragonal ZrO_2 identified by XRD from the long duration treated surfaces (Figure 4.2-12). As described in Section 2.1.3, the phase transformation from the monoclinic zirconium oxide to tetragonal zirconium oxide is accompanied by 3-4% volume change, which could have caused the formation of these defects. The layer defects also affected the corrosion and wear performance of these samples, which will be discussed in the two sections.

5.2 Corrosion properties improvement

5.2.1 Corrosion behaviour of Unt sample

As demonstrated in Figure 4.3-1, the corrosion of untreated Unt sample started at about -0.54 V_{SCE}, and passivation occurred quickly with a relatively stable current density between 10^{-5} and 10^{-6} A and then pitting appeared as evidenced by the sudden increase of the current density at 0.54V (vs ref).

The corrosion of zirconium metals can be expressed as [135]:

$$Zr+2H_2O \rightarrow ZrO_2+2H_2 \qquad \text{(Equation 5.3)}$$

This corrosion reaction indicates the formation of oxide layer and hydrogen. Consequently, for the as prepared Unt sample (without intentionally formed ZrO_2 layer), passivation or the formation of ZrO_2 oxide layer will occur at the beginning of the corrosion process.

The observed poor corrosion behaviour of the untreated Unt sample is in line with the corrosion behaviour of pure Zr reported in the literature. Several studies by Motta et al. [134, 135] via SEM examinations on the cross section of the oxide layers formed on the pure zirconium and zirconium alloys explains why the oxides on pure zirconium is nonprotective to the Zr matrix. . It was found that the oxide layers formed on pure zirconium samples were very unstable because they contained lots of defects such as lateral cracks and veins. As a result, these oxides formed on pure zirconium in the corrosion process are believed to be non-protective. This phenomenon is demonstrated in Figure 5.2-1 showing the cross section of the sponge zirconium after 69 days exposure in the corrosion testing condition (Figure 5.2-1 (a)),

and crystal bar Zr after 3 days exposure under the same testing condition (Figure 5.2-1 (b)), comparing with the Zircaloy-4 after 75 days exposure under the same testing condition (Figure 5.2-1 (c)). The oxide layer formed on Zircaloy-4 was therefore believed to be protective to the Zr metal matrix underneath [134, 135]. With the protective oxide layer formed, the zirconium alloys become passive during the corrosion process in water. However, this passivity will lose when exposed to a testing solution of NaCl.

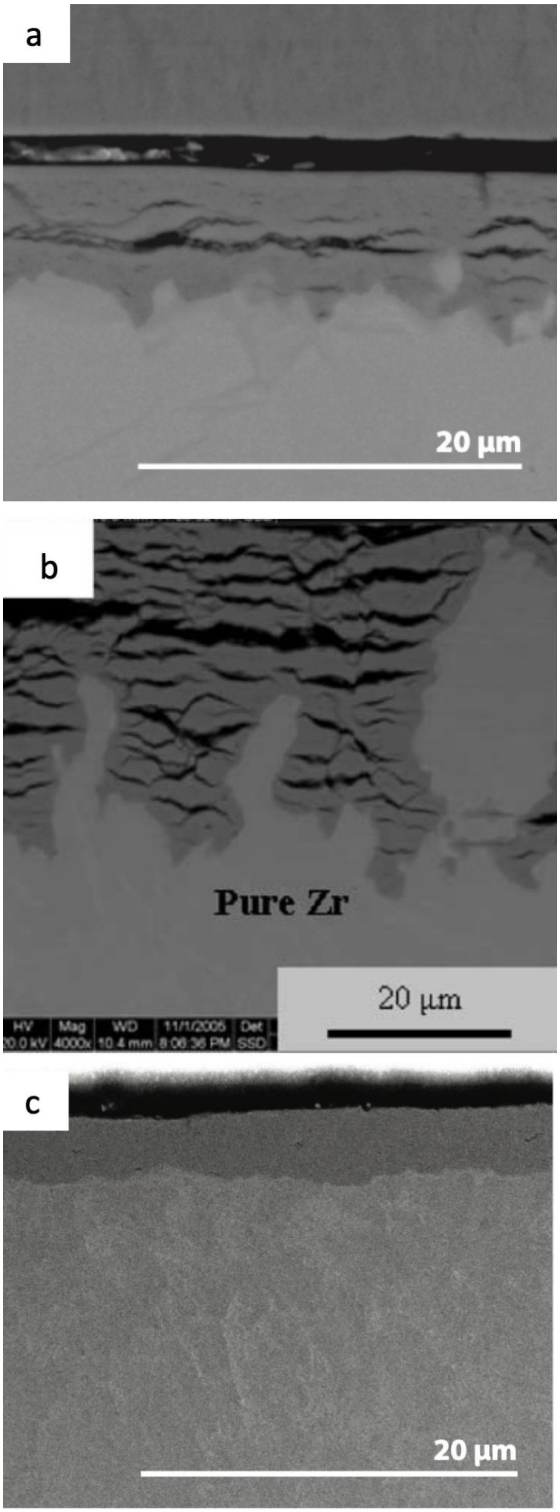


Figure 5.2-1 SEM image of oxide layer formed on (a) sponge zirconium during the corrosion process after 69 days exposure in hot water (360 °C); (b) crystal bar Zr after 3 days exposure and (c) Zircaloy-4 after 75 days of exposure [134, 135].

In the corrosion testing process in this research using 3.5 wt% NaCl solution, with the presence of chloride anions, the passivity of the zirconium alloys achieved by the protective oxide layer became unstable. The breakdown of the passive films occurred and then caused pitting of the zirconium alloys [136]. Particularly for the Zr702 alloy, pervious research has found that the pitting potential decrease as the chloride anions concentration increases [137]. The corrosion pit was formed on the Unt sample surface as shown in Figures 4.3-2 (b) and (c) under the pitting potential of 0.54 V_{SCE}.

At the initial stage before the formation of the passive oxide layer, the untreated zirconium surface directly contacts the aggressive chloride anions. The aggressive chloride anions attack the zirconium alloy and dissolve the Zr material into the corrosion solution. Then, oxide layer starts to form but it contains pinholes and cracks, which were also observed in this research as evidenced in Figure 4.3-2 (a). The defects of the oxide layer allow the chloride anions containing corrosion solution to easily penetrate through and contacts the zirconium matrix at the metal/oxide interface. The localised acidification at the site of these defects makes the pitting occur. The pitting observed on the tested Unt sample surface is considered as the mixture of penetration mechanism through thin oxide layer and film breaking mechanism as schematically shown in Figure 5.2-2.

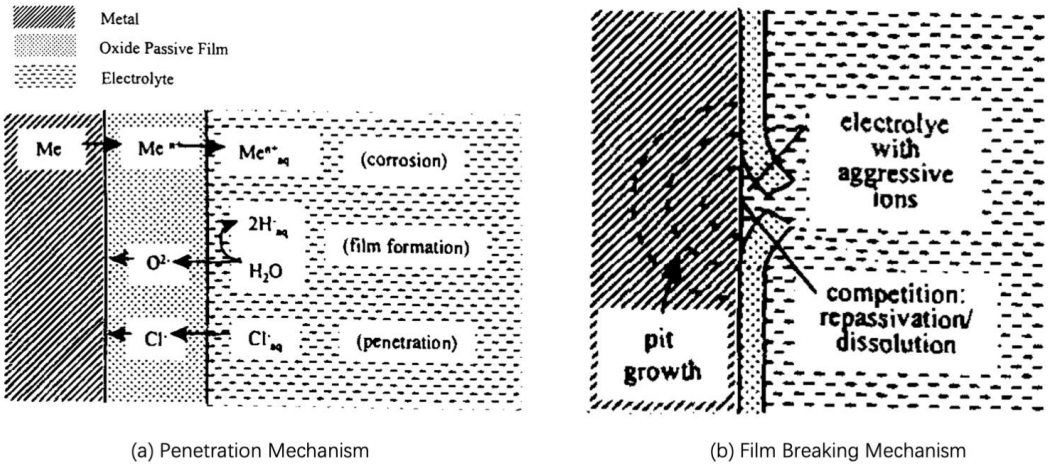


Figure 5.2-2 Schematic diagrams of initiation of pitting via (a) penetration and (b) film breaking mechanisms [138].

5.2.2 Anti-corrosion performance of C2T sample

As has been demonstrated in Figure 4.3-1 and Table 4.3-1, the overall corrosion behaviour of the C2T treated Zr702 sample C2T6010 is better than the untreated Unt counterpart. A large passivation plateau without pitting was found on the polarisation curve (Figure 4.3-1) for the C2T6010 sample, and the Tafel calculation revealed reduced I_{corr} and corrosion rate as compared with that for the Unt sample (Table 4.3-1)

The enhanced corrosion performance of the C2T treated samples as compared with the untreated Unt samples can be attributed to the dense and uniform oxide layer converted from the original Zr702 surface by C2T prior to the corrosion test, as shown in Figure 4.2-3 (a). The oxide layer formed prevents the direct contact of the corrosion solution containing chloride anions. In addition, the dense oxide layer can retard the diffusion of oxidising species to reach the zirconium matrix [135]. The corrosion protection from the ceramic layer is evidenced by the passivation plateau

extended to the end of test (0.9V) without showing any sign of pitting for the C2T6010. SEM observation on the corroded surface only revealed uniform corrosion (Figure 4.3-3), which fully support the above explanation.

It has also noted from Figure 4.3-1 that the corrosion potential E_{corr} of C2T sample is slightly lower than that for the untreated Unt. This could be attributed to the increase surface roughness following the C2T treatment. As shown in Figure 4.2-2, the R_a and R_t of the C2T surface increased from 0.20 and 1.58 μm for the untreated Unt surface to 0.25 and 1.81 μm respective. The deeper valleys would provide vulnerable sites for corrosion attack.

5.2.3 Anti-corrosion performance of C3T samples

As has been reported in Section 4.3, the corrosion behaviour of the C3T samples seems complex depending not only on the types of catalytic elements used but also the ceramic conversion treatment conditions. However, some common features can be extracted by careful analysis of the polarisation curves given in Figure 4.3-4, Figure 4.3-7 & Figure 4.3-9: (i) clear passivation with wide passivation plateau; (ii) much lower current density of the passivate state i_p as compared with that of C2T samples; and (iii) no pitting occurred. These desirable corrosion characteristics of the C3T samples are mainly related to the thicker oxide layers formed during catalytic ceramic conversion treatment (C3T) than formed during conventional ceramic conversion treatment (C2T) as demonstrated in Figure 4.2-8.

According to corrosion theory [139], the corrosion of a metal with a dense oxide layer in NaCl containing solution depends mainly on the penetration of the chloride anions

containing corrosion solution through the oxide layer through the defects and/or the grain boundaries to reach the metal/oxide interface. Accordingly, the corrosion rate was reported to be affected mainly by the oxide layer thickness of the zirconium alloys, if the quality of the oxide layer is high without containing large pores and cracks [135]. This is also supported by the effect of treatment duration on the corrosion behaviour C3T samples. For both C3T Ag (Figure 4.3-7) and C3T V (Figure 4.3-9) samples, the i_p of the 10-hour treated samples is similar to that of C2T sample but it is gradually reduced when increasing the treatment time from 10 hours to 20 hours and 40 hours in particular. Similar trend has also been observed for C3T Au (Figure 4.3-4) but the critical treatment time changed from 20 hours for C3T Ag and C3T V to 10 hours for C3T Au.

The overall anti-corrosion performance of C3T Au is better than C3T Ag and C3T V. This can be exemplified by the comparison of the polarisation curves of the 10-hour treated C2T and C3T samples in Figure 5.2-3. Clearly, the Au6010 outperformed Ag6010, V6010 and C2T with the lowest current density in the passive region (i_p) and it's the smallest corrosion rate of $1.114 \times e^{-3}$ mpy (Table 4.3-1), which is in line with the very identical surface morphologies observed under SEM for the corroded surface and uncorroded surface (Figure 4.3-5). Indeed, the Au6010 sample significantly reduced the corrosion rate to only 2.4% and 3.2% that of the Unt and C2T samples respectively.

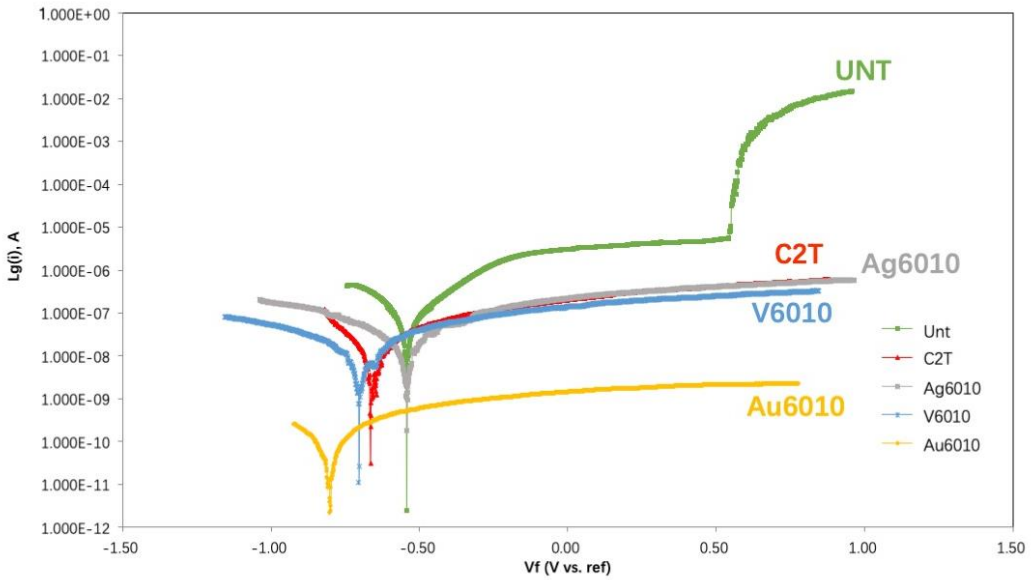


Figure 5.2-3 The polarisation curves of selected treated (Ag6010, V6010, Au6010, C2T6010) and untreated Zr702 samples.

The outstanding corrosion performance of C3T Au as compared with C3T Ag and C3T V can be linked to the distribution of the catalytic elements in the treated surface cases. As has been reported in Section 4.2, Ag and V are mainly concentrated in the very surface of the oxide layer converted; in contrast, Au is distributed across the whole oxide layer although it is rich in the near surface area. Therefore, better corrosion performance is expected for the C3T Au sample than for the C3T Ag and C3T V as it is well known that Au is a noble element.

The above hypothesis is supported by the very low i_p of Au6060 samples (Figure 4.3-4), although superficial thin oxide layer corrosion was observed on the Au6060 sample as shown in Figure 4.3-5 (f). The corrosion features found could be assumed to be related to the defects of the oxide layer after long time oxidation. These cracks could act as crevices allowing the corrosion solution flow in, leading to crevice corrosion and stress corrosion cracking. However, the oxide formed is thick enough

and Au is distributed across the superficial and main oxide layers and therefore the corrosion solution could not penetrate through these cracks all the way down to the metal/oxide interface, thus preventing the further corrosion to the Zr matrix.

5.3 Improved mechanical and tribological properties

5.3.1 Mechanical and tribological properties of Unt and C2T samples

5.3.1.1 Hardness improvement

The surface hardness of the untreated Zr702 alloy is measured to be 180HV0.05 (178HV0.1). After the C2T process, the surface hardness can be improved to 400HV0.05, as depicted in Figure 4.4-1, which is much lower than the hardness value of 941HV5 reported by Shukla et al. [140] for bulk ZrO_2 ceramics. The measured hardness of the C2T sample surface is a complex hardness of the surface ZrO_2 layer and the substrate below the oxide layer. This is because the ZrO_2 oxide layer formed on the C2T sample is so thin (~3.5μm) that the stress field produced by the loaded indenter can penetrate through the thin oxide film to the soft substrate (180HV0.05). This is supported by the reduced surface hardness of 380HV0.1 when the applied load is increased to 0.1kgf (Figure 4.4-1). In order to probe the hardness of the thin ZrO_2 layer itself, the load is reduced to 0.025kgf and the measured surface hardness can reach 1000HV0.025, which is higher than the measured hardness for bulk ZrO_2 ceramics. This extremely high hardness of the ZrO_2 oxide layer could be partially due to the fine grains formed in the C2T induced oxide layer and partially due to the indentation size effect [141]. In short, the effectively improved surface hardness by

C2T could therefore be mainly attributed to the thin hard ZrO_2 ceramic layer formed on top of the Zr matrix.

5.3.1.2 Tribological property enhancement

As has been demonstrated in Figure 4.4-4, the Unt sample is characterised by high value of coefficient of friction (CoF) (up to around 0.65), which is in line with the reported high CoF values for zirconium and its alloys [142]. The wear factor of the Unt sample is high ($16152.56 \times 10^{-16}\ m^3/m \cdot N$) as well when tested under 21N for 3600 cycles.

The observed poor tribological properties of Zr702 in terms of high CoF and low wear resistance are related to its low hardness, high plasticity and strong adhesive wear tendency. As shown in Figure 4.4-5 (a), the depth profile on the cross-section of the wear track is very rough with large high peaks and deep valleys. This implies that severe plastic deformation and adhesion might have dominated the wear of untreated Zr702 material. The observation of the wear track provided further supporting evidence that the wear track produced (as shown in Figure 4.4-6 (a)) are not only wide but also rough. Closer observation revealed typical adhesive wear features including adhesive craters, micro-cracks and some parallel grooves (Figure 4.4-9). The strong adhesion tendency of the untreated zirconium alloys is due to the ductile zirconium and its alloy having low surface hardness, high chemical activity (low d-bond character (~31)) and high metallurgical compatibility with most metals affecting the adhesive wear tendency [2, 43]. The materials transfer from the surface of Unt to the WC-Co counterpart ball has provided strong evidence of adhesive wear. The

transferred Zr material on the ball will be work hardened during the reciprocating sliding and then abrade the Zr producing the parallel grooves at the bottom of the wear track.

It is of interest to note that when tested under a higher load of 45N, the wear factor of the Unt sample was reduced to $4922.28 \times 10^{-16}\ m^3/m \cdot N$, which is lower than that ($16152.56\times 10^{-16}\ m^3/m \cdot N$) of Unt sample tested under 21N. This seemingly abnormal finding can be explained by the change of the dominating wear mechanisms when the applied load is increased from 21 to 45N. As discussed above, adhesive wear dominated the wear process of untreated Unt sample. In contrast, highly oxidised tribo-film was identified inside the wear track formed under 45N as shown in Figure 4.4-10 site B and the area with high oxygen contents area in Figure 5.3-1. This suggests that oxidation wear have played an important role during the wear of Unt sample when tested under a high load of 45N. The high load and hence high contact pressure will produce high frictional temperature leading to oxidation and the formation of the oxide films. The highly oxidised tribo-film therefore reduced the wear at 45N as compared to the wear at 21N.

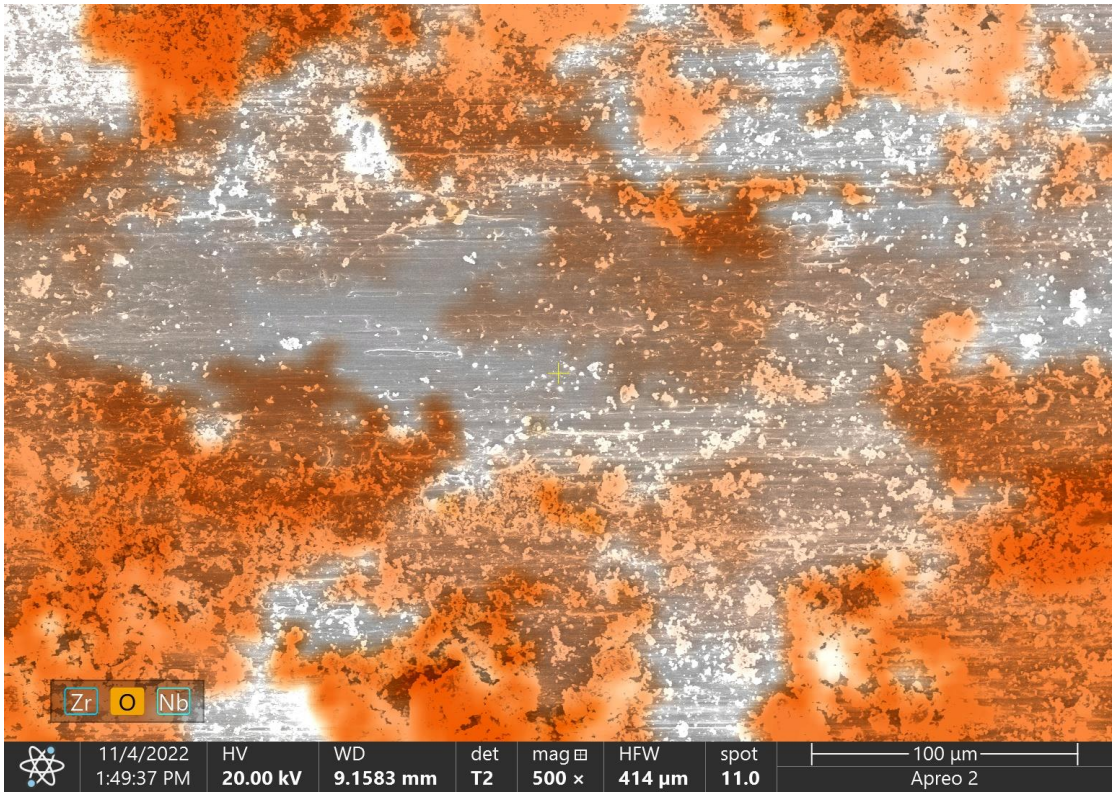


Figure 5.3-1 The colour chem SEM image showing inside of the wear track of Unt sample under 45N, indicating high oxygen contents.

The C2T and C3T techniques are found to be effective to improve the tribological properties in terms of reduced CoF and increased wear of Zr702 alloy, which can be attributed to the in-situ conversion of the soft metallic zirconium into the hard ZrO_2 ceramics during the ceramic conversion treatment process (The C3T will be discussed separated in the next section).

As has been summarised in Table 4.4-1, when tested under the same load of 21N, the wear factor can be effectively reduced from 16152.56× 10^{-16} $m^3/m \cdot N$ of Unt to 4950.66 × 10^{-16} $m^3/m \cdot N$ for C2T6010 and only 64.99 × 10^{-16} $m^3/m \cdot N$, for much longer time treated C2T6040 sample. The low plasticity and low metallurgical compatibility of surface ceramic layer to metallic surfaces improve the adhesive wear resistance of zirconium alloys as no cold weld and adhesion is expected to take place

[43]. The reason for the lower wear factor of 40-hour treated C2T6040 as compared with 10-hour treated C2T6010 can be attributed to the thicker oxide layer formed on C2T6040 (6.3 μm) than that on C2T6010 (3.2 μm). This is supported by careful observation of the wear track formed on C2T6010 samples. It can be seen that while the majority of the wear track might be still within the oxide layer, some areas would most probably worn through as evidenced by a few furrows with low level of oxygen content (Figure 4.4-7).

The above interpretation is supported by the fact that when tested under 45N, the wear factor of C2T6010 (6355.85×10^{-16} $m^3/m \cdot N$) is higher than that (4922.28×10^{-16} $m^3/m \cdot N$) of Unt (Table 4.4-1). This is because the thin oxide layer on C2T6010 sample is unable to withstand the high applied stress when tested under 45N. The oxide layer was broken, and these hard debris acted as the third body to abrasively wear off the soft zirconium substrate, thus leading to severe abrasive wear.

Consequently, the 40-hour treated C2T6040 has shown reduced wear factor even tested under 45N because the thick oxide layer, which is 1.69 times of the thickness for C2T6010 sample, can effectively withstand the high contact stress.

5.3.2 Mechanical and tribological properties of C3T samples

5.3.2.1 Hardness improvement

As demonstrated in Figure 4.4-1, after the 600°C/10-hour treatment, all C3T samples exhibited more significant improvements on the surface hardness as compared with the surface hardness improvements by C2T. As discussed above, the thicker oxide

layer is most likely correlative to the larger surface hardness improvement. As shown in Figure 4.1-12, the oxide layers formed by C3T is about 30-50% thicker than that by C2T.

For the 600 °C/10h treatment, the pre-deposition of V and Pd produced the largest surface hardness enhancement to 1380 and 1280 HV0.05 respectively. However, the oxide layer thickness is quite similar for all the C3T samples if the experimental error bars are considered. Indeed, if the average oxide layer thickness is taken into account, the oxide layer formed on C3T Pd sample is slightly thinner than that formed of C3T Ag.

This discrepancy suggests that in addition to the layer thickness, other factors could have also contributed to the surface hardness of C3T samples. Referring to XRD phase analysis results (Figure 4.1-9 & Figure 4.1-10), the variation of the surface hardness could be attributed to the formation of V_2O_5 and PdO on the C3T sample surfaces. The hardness of V_2O_5 was reported to be in the range of 300-700 HV [143], which is not as hard as ZrO_2 ceramics. However, Chen et al. [144] have demonstrated that adding 2 wt% V_2O_5 to the diamond composite can successfully increase hardness by 23.7% as compared with no V_2O_5 addition. This is due to the reduced porosity of the composites with the V_2O_5 addition and hence the density and hardness of the composite can be improved. The work of Rafieerad et al. [145] has also demonstrated that the addition of PdO can significantly improve the hardness of Pd/PdO coating on titanium based implant surface due to the formation of compact structures by inter diffusion of Pd /PdO between substrate and the coating. The V_2O_5 and PdO could

therefore have the similar roles in the ceramic layer formation for the hardness enhancement.

5.3.2.2 Tribological property enhancement

As has been shown in Figure 4.4-4, the CoF of the untreated Unt sample was increased after about 400 cycles quickly to a value above 0.65, which was also fluctuated due to the adhesive wear nature of the Unt sample. In general, the CoF of the C3T samples is lower than that of the Unt sample although relatively high and unstable CoF was recorded for V6010 and Pd6010 samples at the beginning as shown in Figure 4.4-4. Then the CoF values became stable and remained low after 400 cycles and 100 cycles for Pd6010 and V6010 samples, respectively. This implies that the dominant wear mechanisms may have changed after 400 cycles for the Pd6010 sample and after 100 cycles for the V6010 sample.

Therefore, it is reasonable to assume that the high CoF of these two samples at the beginning could be related to the hardness of the superficial layers formed on the surface of these two samples. For example, as shown in Figure 4.4-1, the surface of V6010 sample is very hard (~1400HV0.05). However, when the load is increased from 50gf (HV0.05) to 100gf (HV0.1), the measured surface hardness drastically dropped from ~1400HV0.05 to below 1000HV0.01. This indicates that this hard layer is very thin located at the very surface.

Therefore, the high CoF at the early stage of the test of V6010 could be related to the formation of very hard superficial layer consisting of needle-like surface

microstructure (Figure 4.2-5). At the beginning of the wear process, the asperities of the superficial hard oxides would interact with the asperities on the WC-Co balls in form of micro-cutting because the superficial layer is harder than WC-Co (HV1300). During the process, the thin superficial layer was also worn by the WC-Co counterpart due to the close hardness values. When the superficial layer becomes even thinner, it would be flaked off by the cyclic loading, and then ground into small sized abrasive particles in the process of the relative motion of the tribo-pair. [125] Consequently, the CoF is reduced after 400 cycles.

The CoF of Au6010 is the most stable and the lowest as compared with the CoF for all other C3T samples (Figure 4.4-4). This could be attributed to the lubricant effects of Au [125, 146] because Au is a soft metal with low shear strength. . However, it can be seen from Figure 4.4-4 that the CoF of Ag6010 is higher than that for Au6010 although it is know that Ag is even softer than gold. This seemingly contradiction could be explained by referring their surface roughness. As shown in Figure 4.2-2, the surface roughness (especially R_t) of Ag6010 is much higher than that of Au6010 because of the formation of large Ag particles and the coarse microstructure (Figure 4.2-1).

As has reported in Figure 4.4-5, all C3T treated samples can further reduce the wear factor by about two orders of magnitude as compared with C2T samples. This clearly demonstrates the effectiveness of pre-depositing catalytic elements in reducing the wear factors of the Zr702 alloy. Such significant improvement of wear properties for C3T samples could be attributed to the catalytic roles of these pre-deposited elements in promoting the formation of thick and dense oxide layer during the final ceramic

conversation treatment as discussed in Section 5.1. As evidenced in Figure 4.1-12 and Figure 4.4-1, the C3T treatments can effectively increase not only the layer thickness but also the surface hardness. The thick and hard surface oxide layer formed on the top of the surface after the C3T can increases the wear resistance and hence the durability of the oxide layer. This can ensure the ceramic/metal contact and avoid metal/metal contact thus reducing adhesive wear tendency. Furthermore, the thick ceramic layer formed by C3T can increase the load bearing capacity thus supporting the surface oxide layer to survive the sliding process. The wear mechanisms for these samples changed from severe adhesive wear of untreated Zr702 alloy to mild abrasive wear.

It is interesting to note that for the 600 °C/10h treated C3T samples, the best anti-wear performance when tested under 21N was seen for the Ag6010 sample and Au6010 sample but their surface hardness HV0.05 is lower than V6010 and Pd6010 (Figure 4.4-1) and the oxide layer of the Au6010 sample is thinnest among these four C3T samples (Figure 4.1-12). This hints that there would be other factor may have contributed to the significantly improved wear properties of C3T samples in addition to the increased thickness and hardness of the oxide layers. As has discussed above, Ag and Au are soft metals and could be used as solid lubricant when oil or grease lubrication is impracticable such as in vacuum or in space. Such lubricating effect has also been observed especially for C3T Ag. As has been shown in Figure 4.4-4, the frictional behaviour of the C3T Ag as well as the C3T Au is better than C3T Pd and C3T V. Therefore, it is reasonable to assume that the pre-deposited Ag and Au may have also contributed to the improve tribological properties of C3T Ag and the C3T Au samples.

The above analysis has also supported by the further wear tests under a higher load of 45N. When tested under 45N, the wear performance of the C3T Au pre-deposited samples with short treatment time (no more than 10 hours) was worsen because the oxide layer thickness is relatively thinner compared to the C3T samples with long treatment time (more than 10 hours). As expected, the thickness of the thin ceramic layer will reduce by the wear process; more importantly, the stress field crated by the high load of 45N will penetrate through the very thin oxide layer into the soft substrate leading to macro plastic deformation and collapse of the thin oxide layer. It has been reported that the plastically deformed substrate layer thickness affects the mean size and volume of fragments [146, 147]. Indeed, the fragments of the hard surface oxide could serve as abrasives thus leading to severe abrasive wear. Consequently, when the thin oxide layer formed on the short treatment time C3T samples under the high load applied was worn through, the ceramic layer protection and self-lubricating effects from Au were no longer exists and the hard wear debris would make the wear even worse. The above proposed wear mechanism is strongly supported by the adhesive craters and the grooves shown in Figure 4.4-12 indicating the severe adhesive and abrasive wear. In contrast, only superficial wear observed for the long time treated C3T samples because the thick ceramic layer can still provide wear protection and self-lubrication. Au6020 sample performed the best under both low load and high load, indicating the optimal treatment condition for the wear resistance improvements.

5.3.3 Wear in NaCl solution

In view of potential application of Zr702 in Cl^{-1} containing solutions (such as for body implants etc.), wear tests were also carried out in 3.5 wt% NaCl solution (i.e., under wet corrosion conditions). During the wet corrosion wear process, the WC-Co ball counterpart was immersed in the 3.5 wt% NaCl corrosion solution. As has reported in Figure 4.4-15, except form C2T6040, the wear factors are more or less reduced for all other samples when tested in 3.5 wt% NaCl solution.

According to tribo-wear theory, the addition of the 3.5 wt% NaCl solution could provide both positive lubrication effect and negative corrosion effect. Hence, the reduced wear in 3.5 wt% NaCl solution should be attributed to the positive lubrication effect provided the oxide layers are dense and smooth before the tests. For example, the oxide layer formed on the short-time treated Au6005 is extremely dense without appreciable defects. Defects such as pinholes may gradually form when increasing the treatment time.

However, it is known that defects in ceramic coatings could serve as the short circuit for the corrosive solution to penetrate through the oxide layer and reach the substrate thus leading to corrosion of the substrate beneath the oxide layer. Hence, the Au6010 showed less increase in corrosion-wear resistance as compared with Au6005 because pinhole induced corrosion would counteract the beneficial lubricating effect of the solution. When further increasing the treatment time to 40 hours for Au6040 sample, although the number of pinholes may increase with time, the oxide layer formed is so thick that no or only limited number of pinholes could go through the thick oxide

layer. Accordingly, the thick oxide layer could eliminate the negative corrosion effect due to pinholes.

It should be also indicated that the positive lubricating effect would be also related to the surface roughness. According to the lubrication theory, it is very difficult, if not impossible, to form effective lubrication film given the low sliding speed and the low viscosity of water-based solution. For instance, the wear factor for the untreated Unt sample tested in the 3.5 wt% NaCl solution is still very high. This is because the untreated surface was worn quickly, and surface became very rough. Therefore, the solution would provide very limited lubricating effect. This is supported by the fact that the wear tracks of untreated samples still showed the mixed wear mechanisms of severe adhesive wear and abrasive wears after test in wet condition. This is almost the same as for the Unt sample tested in dry condition, as the wear craters, grooves, and materials transfer on the counterpart WC-Co ball could still be seen (Figure 4.4-16).

The negative effect of surface roughness is also supported by the wear of C2T6010 in wet and in dry conditions. As shown in Figure 4.4-15, the wear factor of C2T6010 tested in dry is very high. This is because the oxide layer formed by short-time C2T is very thin, which can provide only limited wear protection at the beginning. Then the hard wear debris will lead to severe abrasive wear. However, the surface of the C2T6010 is very dense with almost no pinholes and hence no or limited corrosion effect is expected when tested in 3.5 wt% NaCl solution. In addition, the surface of the thin oxide layer is smoother on C2T (None) than on C3T Ag (Figure 4.2-2). Therefore, the lubrication by the solution could reduce the direct interaction between

the asperities from the surfaces of the tribo-pair. This is evidenced by the residual surface features within the wear track formed during wet wear (Figure 4.4-17 (b)) whist the width of the wear track formed in dry is doubled without any original surface features (Figure 4.4-17 (a)).

However, C2T6040 revealed slightly increased corrosion-wear, which could be related to increased defects in the oxide layers and the increased surface roughness. As shown in Figure 4.4-3, the defects formed especially within the first half of the oxide layer led to the relatively low nanohardness. As discussed above, defects in ceramic coatings could serve as the short circuit for the corrosive solution to penetrate thus leading to corrosion of the substrate; increased surface roughness would reduce the benefit lubricating effect. Consequently, the potential beneficial lubrication effect of the solution would be fully cancelled by the defects facilitated corrosion and reduced lubricating effect due to increased surface roughness.

Chapter 6. Conclusions and future Work

6.1 Summary and conclusions

A novel catalytic ceramic conversion treatment (C3T) for Zr702 alloy has been developed to successfully reduce the ceramic conversion treatment (C2T) time by pre-depositing a thin catalytic film prior to the C3T treatment. Detailed microstructural characterisation and property evaluation have demonstrated that the novel C3T technique can not only reduce the treatment time and the energy consumption but also effectively improve the hardness, corrosion and tribological properties of Zr702 as compared with conventional C2T treatment. Based on the results reported and discussion in the previous two chapters, the following conclusions could be drawn:

Catalytic effects:

1. By introducing a thin (50-500 nm) specific catalytic film (Ag, V, Au, Pd, Ag/V, Ag/Pd), all the C3T samples outperformed the C2T samples in terms of the surface oxide layer thickness when treated under the same ceramic conversion conditions.
2. In the temperature range (450-600 °C) investigated in this study, in general the catalytic effects increase with the treatment temperature. The oxide layer thickness produced by C3T at 600 °C is 2 - 3 times that produced by C3T at 450 °C.
3. For all the four catalytic elements investigated in this research, when treated at 600°C for 10 hours, the catalytic effects from the single element pre-

deposition are in the order of Ag>V>Pd>Au, judging by the surface oxide layer thickness.

4. When treated at 600°C, the C3T samples pre-deposited with mixed elements (Ag/V and Ag/Pd) show a marginal increase of oxide layer thickness over the C3T samples with pre-deposited single element. However, the former does not show appreciable advantage over the latter if both the process complication and the element costs are considered.
5. Au shows the weakest catalytic effects among the three (Ag, V and Au) elements when treated for a short period of time (10h) but Au outperforms Ag and V when treated for 40 and 60 hours.

Microstructure and layer structure:

6. The surface morphologies of the C3T samples depend on the types of pre-deposited catalytic elements. For the 600 °C/10h C3T samples, fine Au particles were observed on the Au6010 surface, multi-directional needle-shaped V_2O_5 was observed form the V6010 surface, and agglomerated Ag was observed from the Ag6010 surface. Pd6010 sample shares the similar surface morphologies as for Au6010 with extremely fine particles evenly covering the whole surface.
7. XRD phase identification work revealed the formation of monoclinic zirconium oxide for C2T6010 samples and for all the C3T samples investigated in this research. In addition to the monoclinic ZrO_2 phase, Ag_2O, V_2O_5, AgO_3V, PdO, PdO & $(Pd, Ag)_3O_4$ are also identified from the surfaces of the Ag6010, V6010, AgV6010, Pd6010 and AgPd6010 samples, respectively. Tetragonal zirconium oxide is identified only for the longer time treated samples (i.e., Au6040).

8. The surface average roughness value R_a of the C3T samples is more or less increased as compared to that of the untreated and the C2T samples with the Ag6010 showing the largest R_a value. With regard to the value of R_t, the V6010 possesses the smallest R_t whist the Ag6010 shows the largest R_t. The formation of agglomerated Ag particles is responsible for the highest R_a and R_t values, and the formation of PdO and presence of fine Au particles have led to the slightly increase of the R_t values of the Pd6010 and Au6010 samples.
9. SEM characterisation shows that the overall cross-sectional layer structure of the C3T sample is similar to that of CT sample consisting of a top oxide layer, an interface layer and a diffusion layer at top of the substrate. Although the oxide layer formed on both the C2T and the C3T samples is columnar structured, the column size of the C3T induced oxide layer is much finer than that formed by C2T.
10. Cross-sectional TEM (XTEM) further confirms that the surface layer is composed of a fine columnar structured layer, oriented in perpendicular to the sample surface, and a horizontally grown grain interface layer along the oxide/matrix interface. The substoichiometric phase $ZrO_{0.35}$ with a preferred orientation of $[2\bar{1}\bar{1}0]_{ZrO_{0.35}}$ // $[0001]_{Zr}$, (0002)//($\bar{1}$010) can be identified. For C3T Au sample, the top layer is rich in gold and Au is distributed throughout the layer.
11. Very thick oxide layers produced from long time (>40h) C3T contain defects such as tiny pores and micro-cracks, which are related to the volume change of the phase transformation from the monoclinic zirconium oxide to tetragonal zirconium oxide under very high stress within the oxide layer.

Potential catalytic mechanisms:

12. The catalytic mechanism of Ag promoting the oxidation would follow the following 5 steps: (i) large absorption of oxygen induced by Ag and the formation of silver oxides; (ii) decomposition of the unstable silver; (iii) the formation of fine grains; and (iv) rapid diffusion of oxygen due to the high oxygen level on the surface, short circuit diffusion via oxygen vacancies and the boundaries of the fine columnar grains in the oxide layer and (v) fast formation of oxide layer.
13. The potential catalytic mechanism of V promoting the oxidation and the formation of the oxide layer is most probably related to the formation of needle-like V_2O_5 and fast diffusion of oxygen in V than in Zr. This would rapidly build up the high oxygen gradient, form a large oxygen flux and thus speeding up the oxidation process.
14. The potential catalytic mechanism of Pd promoting the oxidation and the formation of oxide layer could be attributed to the increased oxygen coverage area due to the lateral repulsion between the oxygen atoms and the Pd surface, thus facilitating the fast formation of the oxide layer.
15. The potential catalytic mechanism of Au promoting the oxidation is attributed to the enhanced oxygen diffusion facilitated by the very fine columnar ZrO_2 grains. The finely distributed Au particles can effectively pin the lateral growth of the zirconium oxide layer, thus refining microstructure and promoting oxygen diffusion.

Corrosion properties:

16. Pitting corrosion occurred to the untreated sample under the pitting potential of 0.54 V_{SCE} due to the breakdown of the passive films, attacked by the aggressive chloride anions. The dense and uniform oxide layer of C2T sample

can prevent the direct contact of the chloride anions to the zirconium matrix, thus reducing corrosion.

17. All the C3T samples have shown effective passivation with reduced passive current density as compared with that for the C2T samples although the corrosion potential is slightly reduced for long-time treated C3T samples. Comparatively speaking, the overall anti-corrosion performance of C3T Au is better than C3T Ag and C3T V because the corrosion rate of Au6010 is only 2.4% and 3.2% that of the untreated Unt and C2T samples respectively.

Mechanical and tribological properties:

18. The short-time treated C2T6010 sample showed limited surface hardening from 180HV0.05 to 400HV0.05 because of the thin ZrO_2 formed. More significant hardness improvements up to 1400HV have been achieved for all the C3T samples because of the formation of thick and hard oxide layers promoted by the catalytic effect of the pre-deposited elements.
19. The C3T samples have showed two orders of magnitude reduction of wear factor and reduced coefficient of friction from 0.65 to <0.25. The C3TAg and the C3TAu samples possess the highest wear resistance and the lowest CoF mainly because of the self-lubricating films formed during the wear testing process in addition to the wear resistant thick oxide layer.
20. Au6020 sample outperformed all other samples under both low load (21N) and high load (45N), indicating the optimal treatment conditions for the wear resistance improvements.
21. The lubricating effects of the NaCl solution reduced the corrosion-wear factors particularly for C2T6010 and Au6005 samples; however, Au6010,

C2T6040 and Unt sample showed similar corrosion-wear factors most probably the corrosion effect has cancelled the lubricating effect.

6.2 Suggested future work

This study has revealed that the novel C3T technique developed form the PhD project can effectively speed up the formation of surface oxide layers through catalytic metal promoted rapid ceramic conversion for zirconium and its alloys, resulting in the significant improvements in the mechanical, corrosion and tribological properties of Zr702 alloy. Consequently, the novel catalytic C3T technique can extend the application of zirconium-based alloys to body implants and valves. In addition, the developed C3T technique can also promote economical growth and sustainability due to the cost-effectiveness and effectively reduced energy consumption. However, more work is needed to transfer this novel C3T technique to industrial surface modification processes, which is linked to the proposed future work below.

The proposed future work would focus mainly on extending the novel C3T technique to other types of zirconium alloys, selecting different deposition elements or combinations and evaluating the properties for potential industrial applications, which include:

1. The catalytic effects of the novel C3T techniques could be applied to other zirconium alloys, such as Zr705 alloys and nuclear grade zirconium alloys.
2. The anti-bacterial properties of the C3T treated zirconium alloys could be evaluated for their potential biomedical applications as compared to C2T and untreated samples.

3. A more systematic investigation into the duplex co-deposition including the selection of element combinations and optimisation of C3T conditions is suggested.

References

1. Zirconium, Zr: MatWeb - Material Property Data; [Available from: https://www.matweb.com/search/datasheet.aspx?matguid=6e8936b3ad994f13bfb29923cc1506a9.
2. Zhang S. Improving the tribological and corrosion properties of Zr702 and Zircaloy-4 alloys by ceramic conversion treatment [Doctoral dissertation]: Univerisity of Birmingham; 2016.
3. Zhang Z, Zhang Y, Li X, Alexander J, Dong H. An enhanced ceramic conversion treatment of Ti6Al4V alloy surface by a pre-deposited thin gold layer. Journal of Alloys and Compounds. 2020;844:155867.
4. Alexander J, Dong H, Bose D, Hassan AA, Soo SL, Zhang Z, et al. Novel Catalytic Ceramic Conversion Treatment of Ti6Al4V for Improved Tribological and Antibacterial Properties for Biomedical Applications. Materials. 2021;14(21):6554.
5. Zirconium: Royal Society of Chemistry; [Available from: https://www.rsc.org/periodic-table/element/40/zirconium
6. Lide DR. CRC handbook of chemistry and physics: CRC press; 2004.
7. Stwertka A. A Guide to the Elements: Oxford University Press; 2002.
8. Emsley J. The A–Z of zirconium. Nature Chemistry. 2014;6(3):254-.
9. Emsley J. Nature's building blocks: an AZ guide to the elements: Oxford University Press; 2011.
10. Van Arkel A, de Boer JH. Darstellung von reinem Titanium-, Zirkonium-, Hafnium-und Thoriummetall. Zeitschrift für anorganische und allgemeine Chemie. 1925;148(1):345-50.
11. Oestberg G, Perez A. Fabrication of zirconium sponge. 1973.
12. Krishnan R, Asundi M. Zirconium alloys in nuclear technology. Proceedings of the Indian Academy of Sciences Section C: Engineering Sciences. 1981;4(1):41-56.
13. Rickover HG, Geiger LD, Lustman B. History of the development of zirconium alloys for use in nuclear reactors. Energy Research and Development Administration, Washington, DC (USA). Div …; 1975.
14. Rudling P, Strasser A, Garzarolli F, van Swam L. Welding of Zirconium alloys. IZNA7 special topic report Welding of Zirconium Alloys. 2007.
15. Technical Data Sheet-Reactor Grade Zirconium: Allegheny Technologies Incorporated; [Available from: https://www.atimaterials.com/Products/Documents/datasheets/zirconium/alloy/Zr_nuke_waste_disposal_v2.pdf
16. Zirconium and Zirconium Alloy Tubes (ZR 702/ ZR 704/ ZR 705): Aircraft Materials; [Available from: http://aircraftmaterials.com/data/nuclear/zirconiumtubes.html.
17. Lemaignan C. 2.07-Zirconium alloys: properties and characteristics. Comprehensive nuclear materials. 2012:217-32.
18. Jayaraman A, Klement Jr W, Kennedy G. Solid-solid transitions in titanium and zirconium at high pressures. Physical Review. 1963;131(2):644.
19. Usikov M, Zilbershtein V. The orientation relationship between the α-and ω-phases of titanium and zirconium. Physica status solidi (a). 1973;19(1):53-8.
20. H. Nielsen R, H. Schlewitz J, Nielsen H, Staff Ub. Zirconium and zirconium compounds. Kirk-Othmer Encyclopedia of Chemical Technology. 2000:1-46.
21. Saridag S, Tak O, Alniacik G. Basic properties and types of zirconia: An overview. World Journal of Stomatology. 2013;2(3):40-7.

22. Mihai LL, Parlatescu I, Gheorghe C, Andreescu C, Bechir A, Pacurar M, et al. In vitro study of the effectiveness to fractures of the aesthetic fixed restorations achieved from zirconium and alumina. Rev Chim(Bucharest). 2014;65:725.
23. Hobbs LW, Rosen VB, Mangin SP, Treska M, Hunter G. Oxidation microstructures and interfaces in the oxidized zirconium knee. International Journal of Applied Ceramic Technology. 2005;2(3):221-46.
24. Lee DB, Roberts M, Bluchel CG, Odell RA. Zirconium: biomedical and nephrological applications. Asaio Journal. 2010;56(6):550-6.
25. Northwood DO. The development and applications of zirconium alloys. Materials & design. 1985;6(2):58-70.
26. Slobodyan M. Resistance, electron-and laser-beam welding of zirconium alloys for nuclear applications: a review. Nuclear Engineering and Technology. 2021;53(4):1049-78.
27. Why Is Zirconium Used In Nuclear Reactors? : Advanced Refractory Metals; [Available from: https://www.refractorymetal.org/why-is-zirconium-used-in-nuclear-reactors/.
28. The Use Of Zirconium In Nuclear Reactors: Advanced Refractory Metals; [Available from: https://www.refractorymetal.org/the-use-of-zirconium-in-nuclear-reactors/
29. How is used nuclear fuel managed? : World Nuclear Association; [Available from: https://world-nuclear.org/our-association/publications/technical-positions/how-is-used-nuclear-fuel-managed.aspx.
30. Mehjabeen A, Song T, Xu W, Tang HP, Qian M. Zirconium alloys for orthopaedic and dental applications. Advanced Engineering Materials. 2018;20(9):1800207.
31. Hanawa T. Metal ion release from metal implants. Materials Science and Engineering: C. 2004;24(6-8):745-52.
32. Hieda J, Niinomi M, Nakai M, CHO K, NAGAI S. Acta Biomater. Acta Biomater. 8, 3888-3903, 2012. Acta Biomater. 2012;8:3888-903.
33. Nomura N, Tanaka Y, Kondo R, Doi H, Tsutsumi Y, Hanawa T. Effects of phase constitution of Zr-Nb alloys on their magnetic susceptibilities. Materials transactions. 2009;50(10):2466-72.
34. Oetzel C, Clasen R. Preparation of zirconia dental crowns via electrophoretic deposition. Journal of materials science. 2006;41(24):8130-7.
35. Hoppe V, Szymczyk-Ziółkowska P, Rusińska M, Dybała B, Poradowski D, Janeczek M. Assessment of mechanical, chemical, and biological properties of Ti-Nb-Zr alloy for medical applications. Materials. 2020;14(1):126.
36. Haygarth JC, Fenwick LJ. Improved wear resistance of zirconium by enhanced oxide films. Thin Solid Films. 1984;118(3):351-62.
37. Devaraju A. A critical review on different types of wear of materials. Int J Mech Eng Technol. 2015;6(11):77-83.
38. Popov VL. Is tribology approaching its golden age? Grand challenges in engineering education and tribological research. Frontiers Media SA; 2018. p. 16.
39. Archard JF, Hirst W. The wear of metals under unlubricated conditions. Proceedings of the Royal Society of London Series A Mathematical and Physical Sciences. 1956;236(1206):397-410.
40. Buckley DH. Surface effects in adhesion, friction, wear, and lubrication: Elsevier; 1981.
41. Tanzi M-C, Farè S, Candiani G. Foundations of biomaterials engineering: Academic Press; 2019.

42. Dohda K, Yamamoto M, Hu C, Dubar L, Ehmann KF. Galling phenomena in metal forming. Friction. 2021;9:665-85.
43. Ji R, Li X, Dong H. Ceramic conversion treatment of zirconium alloys to combat corrosion wear. Surface engineering. 2010;26(1-2):30-6.
44. Khruschov M. Principles of abrasive wear. Wear. 1974;28(1):69-88.
45. Kato K. Abrasive wear of metals. Tribology International. 1997;30(5):333-8.
46. Wanklyn J, Britton C, Silvester D, Wilkins N. Influence of environment on the corrosion of zirconium and its alloys in high-temperature steam. Journal of the Electrochemical Society. 1963;110(8):856.
47. Farina S, Duffo G, Galvele J. Stress corrosion cracking of zirconium and Zircaloy-4 in halide aqueous solutions. Corrosion Science. 2003;45(11):2497-512.
48. Nagano H, Kajimura H. The stress corrosion cracking performance of pure zirconium and zirconium alloys in highly oxidizing nitric acid. Corrosion science. 1996;38(5):781-91.
49. Chevalier J. What future for zirconia as a biomaterial? Biomaterials. 2006;27(4):535-43.
50. Thakare V. Progress in synthesis and applications of zirconia. International Journal of Engineering Research and Development. 2012;5(1):25-8.
51. Lawson S. Environmental degradation of zirconia ceramics. Journal of the European ceramic society. 1995;15(6):485-502.
52. Komotori J, Lee B, Dong H, Dearnley P. Corrosion response of surface engineered titanium alloys damaged by prior abrasion. Wear. 2001;251(1-12):1239-49.
53. Wang L, Hu X, Nie X. Deposition and properties of zirconia coatings on a zirconium alloy produced by pulsed DC plasma electrolytic oxidation. Surface and Coatings Technology. 2013;221:150-7.
54. Goto T. Thermal barrier coatings deposited by laser CVD. Surface and Coatings Technology. 2005;198(1-3):367-71.
55. Peng D, Bai X, Chen X, Zhou Q. The air oxidation behavior of lanthanum ion implanted zirconium at 500 C. Nuclear Instruments and Methods in Physics Research Section B: Beam Interactions with Materials and Atoms. 2003;201(4):589-94.
56. Rawers J, Reitz W, Bullard S, Roub E. Surface and corrosion study of laser-processed zirconium alloys. Corrosion. 1991;47(10):769-77.
57. Mattox DM. Physical vapor deposition (PVD) processes. Metal Finishing. 2002;100:394-408.
58. Sikdar S, Menezes PV, Maccione R, Jacob T, Menezes PL. Plasma electrolytic oxidation (PEO) process—processing, properties, and applications. Nanomaterials. 2021;11(6):1375.
59. Johansen O, Dontje J, Zenner R. Reactive arc vapor ion deposition of TiN, ZrN and HfN. Thin Solid Films. 1987;153(1-3):75-82.
60. Molarius J, Korhonen A, Harju E, Lappalainen R. Comparison of cutting performance of ion-plated NbN, ZrN, TiN and (Ti, Al) N coatings. Surface and Coatings Technology. 1987;33:117-32.
61. Penttinen I, Molarius J, Korhonen A, Lappalainen R. Structure and composition of ZrN and (Ti, Al) N coatings. Journal of Vacuum Science & Technology A: Vacuum, Surfaces, and Films. 1988;6(3):2158-61.
62. Harsha KS. Principles of vapor deposition of thin films: Elsevier; 2005.
63. Wiiala U, Penttinen I, Korhonen A, Aromaa J, Ristolainen E. Improved corrosion resistance of physical vapour deposition coated TiN and ZrN. Surface and Coatings Technology. 1990;41(2):191-204.

64. Schickner W, Beach J, Faust CL. Electroplating on Zirconium. Journal of The Electrochemical Society. 1953;100(6):289.
65. Dini J, Johnson H, Jones A. Plating on Zircaloy-2. Journal of the Less Common Metals. 1981;79(2):261-70.
66. Schlesinger M, Paunovic M. Modern electroplating: John Wiley & Sons; 2011.
67. Aliofkhazraei M, Macdonald D, Matykina E, Parfenov E, Egorkin V, Curran J, et al. Review of plasma electrolytic oxidation of titanium substrates: Mechanism, properties, applications and limitations. Applied Surface Science Advances. 2021;5:100121.
68. Simchen F, Sieber M, Kopp A, Lampke T. Introduction to plasma electrolytic oxidation—An overview of the process and applications. Coatings. 2020;10(7):628.
69. Cengiz S, Uzunoglu A, Stanciu L, Tarakci M, Gencer Y. Direct fabrication of crystalline hydroxyapatite coating on zirconium by single-step plasma electrolytic oxidation process. Surface and Coatings Technology. 2016;301:74-9.
70. Peng A. Guide To Plasma Electrolytic Oxidation (PEO): DEK; 2020 [Available from: https://www.dekmake.com/guide-to-plasma-electrolytic-oxidation/.
71. Liang H, Wan Y, He F, Huang Y, Xu J, Li J, et al. Bioactivity of Mg-ion-implanted zirconia and titanium. Applied surface science. 2007;253(6):3326-33.
72. Tang G, Choi B, Kim W, Jung K, Kwon H, Lee S, et al. The characteristics of surface oxidation and corrosion resistance of nitrogen implanted zircaloy-4. Surface and Coatings Technology. 1997;89(3):252-7.
73. Lee S, Kwon H-S, Kim W, Choi B. Effects of compositional and structural change on the corrosion behaviour of nitrogen implanted Zircaloy-4. Materials Science and Engineering: A. 1999;263(1):23-31.
74. Lee S, Park C, Kwon H, Choi B. Corrosion resistance of nitrogen-implanted Zircaloy-4 in high-temperature water. Journal of nuclear materials. 2000;282(2-3):223-31.
75. Reitz W, Rawers J. Effect of laser surface melted zirconium alloys on microstructure and corrosion resistance. Journal of materials science. 1992;27(9):2437-43.
76. Lee S, Park C, Lim Y, Kwon H. Influences of laser surface alloying with niobium (Nb) on the corrosion resistance of Zircaloy-4. Journal of Nuclear Materials. 2003;321(2-3):177-83.
77. Chen K, Zeng L, Li Z, Chai L, Wang Y, Chen L-Y, et al. Effects of laser surface alloying with Cr on microstructure and hardness of commercial purity Zr. Journal of Alloys and Compounds. 2019;784:1106-12.
78. Goto T, Ishigaki H, Ito Y. Electrochemical surface nitriding of zirconium in LiCl–KCl–Li3N systems. Materials Science and Engineering: A. 2004;371(1-2):353-8.
79. Huang H, Jiang M, Yan J. The coupling effects of laser thermal shock and surface nitridation on mechanical properties of Zr-based metallic glass. Journal of Alloys and Compounds. 2019;770:864-74.
80. Hong J, Qian Y, Zhang L, Huang H, Jiang M, Yan J. Laser nitriding of Zr-based metallic glass: An investigation by orthogonal experiments. Surface and Coatings Technology. 2021;424:127657.
81. Banerjee S, Mukhopadhyay P. Phase transformations: examples from titanium and zirconium alloys: Elsevier; 2010.
82. Selmi N, Sari A. Study of oxidation kinetics in air of zircaloy-4 by in situ X-ray diffraction. Adv Mater Phys Chem. 2013;3:168-73.

83. Debuigne J. Contribution to Study of Zirconium Oxidation and oxygen Diffusion into the Oxide and the Metal: PhD Thesis, Faculté des sciences de Paris; 1966.
84. Rosa C. Oxidation of zirconium—A critical review of literature. Journal of the Less Common Metals. 1968;16(3):173-201.
85. Hussey R, Smeltzer W. The oxidation kinetics of zirconium in the temperature range 400°–600° C. Journal of The Electrochemical Society. 1964;111(5):564.
86. Ellingham HJ. Reducibility of oxides and sulphides in metallurgical processes. J Soc Chem Ind. 1944;63(5):125-60.
87. Hasegawa M. Ellingham diagram. Treatise on Process Metallurgy: Elsevier; 2014. p. 507-16.
88. Stratton P. Ellingham diagrams–their use and misuse. International Heat Treatment and Surface Engineering. 2013;7(2):70-3.
89. Ellingham Diagrams: MIT; [Available from: https://web.mit.edu/2.813/www/readings/Ellingham_diagrams.pdf.
90. Dong H, Bell T. Enhanced wear resistance of titanium surfaces by a new thermal oxidation treatment. Wear. 2000;238(2):131-7.
91. Dong H. Development of novel surface engineering technologies for Ti6A14V alloy: University of Birmingham; 1997.
92. Dong H, Bloyce A, Morton PH, Bell T. Surface oxidation of a titanium or titanium alloy article. Google Patents; 2001.
93. Baufeld B, Van der Biest O. Mechanical properties of Ti-6Al-4V specimens produced by shaped metal deposition. Science and technology of advanced materials. 2009.
94. Li X, Dong H. Ceramic conversion treatment of titanium-based materials. Surface engineering of light alloys: Elsevier; 2010. p. 475-500.
95. Zhang Y. Silver-promoted rapid ceramic conversion of titanium alloys surfaces [MScT Report]: University of Birmingham; 2016.
96. Chen M, Goodman D. The structure of catalytically active gold on titania. science. 2004;306(5694):252-5.
97. Kotobuki M, Leppelt R, Hansgen DA, Widmann D, Behm RJ. Reactive oxygen on a Au/TiO2 supported catalyst. Journal of Catalysis. 2009;264(1):67-76.
98. Liu K. Rapid ceramic conversion of titanium surfaces with a pre-deposited V/V-Ag metal layer [MScT Report]: University of Birmingham; 2017.
99. Kiryukhantsev-Korneev PV, Phiri J, Gladkov V, Ratnikov S, Yakovlev M, Levashov E. Erosion and abrasion resistance, mechanical properties, and structure of the TiN, Ti–Cr–Al–N and Cr–Al–Ti–N coatings deposited by CFUBMS. Protection of metals and physical chemistry of surfaces. 2019;55(5):913-23.
100. Quick Guide to Surface Roghness Measurement: Mitutoyo; [Available from: https://www.mitutoyo.com/webfoo/wp-content/uploads/1984_Surf_Roughness_PG.pdf.
101. Brundle CR, Wilson L, Evans CA, Wilson S, Wilson G. Encyclopedia of materials characterization: surfaces, interfaces, thin films: Gulf Professional Publishing; 1992.
102. HighScore(Plus). V3.X database PDF - 2 Release 2004. HighScore(Plus) 2004.
103. Electrochemical Techniques for Corrosion Measurement: Gamry Instruments; [Available from: https://www.gamry.com/assets/Uploads/Echem-Corrosion-Measurement.pdf.

104. Adamovic D, Zivic F. Hardness and Non-Destructive Testing (NDT) of Ceramic Matrix Composites (CMCs). Journal: Encyclopedia of Materials: Composites. 2021:183-201.
105. Tejland P, Andrén H-O. Origin and effect of lateral cracks in oxide scales formed on zirconium alloys. Journal of Nuclear Materials. 2012;430(1-3):64-71.
106. Yilmazbayhan A, Motta AT, Comstock RJ, Sabol GP, Lai B, Cai Z. Structure of zirconium alloy oxides formed in pure water studied with synchrotron radiation and optical microscopy: relation to corrosion rate. Journal of Nuclear Materials. 2004;324(1):6-22.
107. Preuss M, Frankel P, Lozano-Perez S, Hudson D, Polatidis E, Ni N, et al. Studies regarding corrosion mechanisms in zirconium alloys. Journal of ASTM International. 2011;8(9):1-23.
108. Parise M, Foerch R, Cailletaud G. Coupling between diffusion and mechanics during the oxidation of zircaloy. Le Journal de Physique IV. 1999;9(PR9):Pr9-311-Pr9-20.
109. Parise M, Sicardy O, Cailletaud G. Modelling of the mechanical behavior of the metal–oxide system during Zr alloy oxidation. Journal of nuclear materials. 1998;256(1):35-46.
110. Zhang X, Liang J, Liu B, Peng Z. Preparation of superhydrophobic zinc coating for corrosion protection. Colloids and Surfaces A: Physicochemical and Engineering Aspects. 2014;454:113-8.
111. Zirconia (ZrO2) - Applications of Zircalon Ceramics: AZO Materials; [Available from: https://www.azom.com/article.aspx?ArticleID=4507.
112. Manicone PF, Iommetti PR, Raffaelli L. An overview of zirconia ceramics: basic properties and clinical applications. Journal of dentistry. 2007;35(11):819-26.
113. Nassau K. Cubic zirconia: an update. Gems and Gemology. 1981;17(1):9-19.
114. Wilkins N. Infra-red interference measurements on oxide films on zirconium. Corrosion Science. 1964;4(1-4):17-24.
115. Wilkins N. Optical measurement of oxide films on zirconium in the range of wavelengths from 2000 to 2· 5 μ. Corrosion Science. 1965;5(1):3-18.
116. Koski K, Hölsä J, Juliet P. Properties of zirconium oxide thin films deposited by pulsed reactive magnetron sputtering. Surface and Coatings Technology. 1999;120:303-12.
117. Burstein GT. The tarnishing conundrum of silver. 2019.
118. Hossein-Babaei F, Rahbarpour S. Titanium and silver contacts on thermally oxidized titanium chip: electrical and gas sensing properties. Solid-State Electronics. 2011;56(1):185-90.
119. Waterhouse GI, Bowmaker GA, Metson JB. The thermal decomposition of silver (I, III) oxide: A combined XRD, FT-IR and Raman spectroscopic study. Physical Chemistry Chemical Physics. 2001;3(17):3838-45.
120. Setvín M, Aschauer U, Scheiber P, Li Y-F, Hou W, Schmid M, et al. Reaction of O2 with subsurface oxygen vacancies on TiO2 anatase (101). Science. 2013;341(6149):988-91.
121. Brauer G. Handbook of Preparative Inorganic Chemistry V2: Elsevier; 2012.
122. Sediri F, Gharbi N. From crystalline V2O5 to nanostructured vanadium oxides using aromatic amines as templates. Journal of Physics and Chemistry of Solids. 2007;68(10):1821-9.
123. Ding J, Gao H, Zhao K, Zheng H, Zhang H, Han L, et al. In-situ electrochemical conversion of vanadium dioxide for enhanced zinc-ion storage with large voltage range. Journal of Power Sources. 2021;487:229369.

124. Lokkiluoto A, Taskinen PA, Gasik M, Kojo IV, Peltola H, Barker MH, et al. Novel process concept for the production of H 2 and H 2 SO 4 by SO 2-depolarized electrolysis. Environment, development and sustainability. 2012;14:529-40.
125. Xiong X, Li X, Alexander J, Zhang Z, Dong H. A Novel Catalytic Ceramic Conversion Treatment of Zr702 to Combat Wear. Materials. 2023;16(5):1763.
126. Muller TL. Sulfuric acid and sulfur trioxide. Kirk-Othmer Encyclopedia of Chemical Technology. 2000.
127. Wu Y-D, Zhang G-H, Xu R, Wang Y, Chou K-C. Fabrication of pure V2O3 powders by reducing V2O5 powders with CO-CO2 mixed gases. Ceramics International. 2019;45(2):2117-23.
128. Takahashi T, Minamino Y, Hirasawa H, Ouchi T. High-Temperature oxidation and its kinetics study of Ti–Al and Ti–V alloys in air. Materials Transactions. 2014;55(2):290-7.
129. Wu M, Lemettre S, Mansour D, Plante M-P, Bosseboeuf A, Seok S, et al., editors. Evaporated Zr-V, Zr-Ti and Zr-Co getter thin films: Activation temperature and microstructure. 2016 Symposium on Design, Test, Integration and Packaging of MEMS/MOEMS (DTIP); 2016: IEEE.
130. Palladium oxide: ChemBK; 2022 [Available from: https://www.chembk.com/en/chem/Palladium%20oxide.
131. Shah J, Kansara S, Gupta SK, Sonvane Y. Oxygen adsorption on palladium monolayer as a surface catalyst. Physics Letters A. 2017;381(36):3084-8.
132. Spurgeon PM, Lai KC, Han Y, Evans JW, Thiel PA. Fundamentals of Au (111) Surface Dynamics: Coarsening of Two-Dimensional Au Islands. The Journal of Physical Chemistry C. 2020;124(13):7492-9.
133. Godlewski J, Gros J, Lambertin M, Wadier J, Weidinger H, editors. Raman spectroscopy study of the tetragonal-to-monoclinic transition in zirconium oxide scales and determination of overall oxygen diffusion by nuclear microanalysis of O 18. Zirconium in the Nuclear Industry: Ninth International Symposium; 1991: ASTM International.
134. Motta A, Da Silva MG, Yilmazbayhan A, Comstock R, Cai Z, Lai B. Microstructural characterization of oxides formed on model Zr alloys using synchrotron radiation. Journal of ASTM International. 2008;5(3):1-20.
135. Motta AT, Couet A, Comstock RJ. Corrosion of zirconium alloys used for nuclear fuel cladding. Annual Review of Materials Research. 2015;45:311-43.
136. Ghosal S, Palit G, De P. Corrosion of zirconium alloys in nuclear applications-A review. Mineral Procesing and Extractive Metallurgy Review. 2001;22(2):519-46.
137. Malik F. The pitting corrosion of zirconium and zirconium-niobium alloys in sulphate solutions containing chlorides at 300–373 K. Surface and Coatings Technology. 1990;43:511-20.
138. Frankel G. Pitting corrosion of metals: a review of the critical factors. Journal of the Electrochemical society. 1998;145(6):2186.
139. Stansbury EE, Buchanan RA. Fundamentals of electrochemical corrosion: ASM international; 2000.
140. Shukla PP, Lawrence J, Wu H. Fracture toughness of a zirconia engineering ceramic and the effects thereon of surface processing with fibre laser radiation. Proceedings of the Institution of Mechanical Engineers, Part B: Journal of Engineering Manufacture. 2010;224(10):1555-69.
141. Pharr GM, Herbert EG, Gao Y. The indentation size effect: a critical examination of experimental observations and mechanistic interpretations. Annual Review of Materials Research. 2010;40:271-92.

142. Attia MH. On the fretting wear mechanism of Zr-alloys. Tribology international. 2006;39(10):1320-6.
143. Mirabal-Rojas R, Rodil SE, Ramirez G, Polcar T, Camps E, Erdemir A. Effect of the addition of Si into V2O5 coatings: structure and tribo-mechanical properties. Surface and Coatings Technology. 2018;349:111-8.
144. Chen S-p, Liu X-p, Wan L, Gao P-z, Zhang W, Hou Z-q. Effect of V2O5 addition on the wettability of vitrified bond to diamond abrasive and grinding performance of diamond wheels. Diamond and Related Materials. 2020;102:107672.
145. Rafieerad A, Bushroa A, Nasiri-Tabrizi B, Vadivelu J, Baradaran S, Mesbah M, et al. Mechanical properties, corrosion behavior and in-vitro bioactivity of nanostructured Pd/PdO coating on Ti–6Al–7Nb implant. Materials & Design. 2016;103:10-24.
146. Miyakawa Y. Friction and wear performance of gold and gold alloy films. Gold bulletin. 1980;13(1):21-30.
147. Soda N, Kimura Y, Tanaka A. Wear of some FCC metals during unlubricated sliding Part II: Effects of normal load, sliding velocity and atmospheric pressure on wear fragments. Wear. 1975;35(2):331-43.